University of Southampton
School of Medicine

Southampton NHS
University Hospitals NHS Trust

UNIVERSITY OF SOUTHAMPTON

School of Medicine

and

SOUTHAMPTON UNIVERSITY HOSPITAL NHS TRUST

Department of Medical Physics and Bioengineering

SIMULATION AND ITS ROLE IN THE DEVELOPMENT AND ASSESSMENT OF QUANTITATIVE RADIONUCLIDE IMAGING OF THE BRAIN

by

Tony Ward B.Eng. (Hons.) AMIEE

Submitted in support for the award of Doctor of Philosophy in Medical Physics

June 2006

UNIVERSITY OF SOUTHAMPTON

ABSTRACT

FACULTY OF MEDICINE, HEALTH AND BIOLOGICAL SCIENCE
SCHOOL OF MEDICINE

Doctor of Philosophy

SIMULATION AND ITS ROLE IN THE DEVELOPMENT AND ASSESSMENT OF QUANTITATIVE RADIONUCLIDE IMAGING OF THE BRAIN

by Tony Ward

Functional imaging is a powerful tool in dementia research. Combined with molecular imaging using radiotracers, we gain useful insight into the mechanisms behind dementia. However, the imaging method is only as powerful as the methods used to detect abnormal data. An early and defining goal of this study was to create a method of effectively allowing a comparison of imaging systems and analysis methods, with the aim of providing an effective validation. To this end, a simulated audit data set has been created specifically for SPECT imaging with ^{99m}Tc-HMPAO, and is shown to realistically represent variation in parameters. An in depth analysis using *statistical parametric mapping* (SPM99) has been performed, and the results are compared to an analysis using *brain registration and analysis of SPECT studies* (BRASS). The results show that if analysis parameters are carefully selected, then both methods can produce identical results. The data set is being used in a national pilot audit study of semi-quantiative analysis techniques, and has been distributed to participating centres. A full analysis will be performed once results are collated.

Analysis and validation remains a long term goal of the project, and a lot of the work has focused on the production of ground truth models that can be used in this task. Due to analytical simulation limitations, remaining work to date has focused on developing full Monte Carlo simulation models to supersede analytical simulation methods. The Zubal phantom model has been updated for use in this task and has been used with iterative biodistribution estimation procedures. The data are used as simulation objects for SimSET simulation to generate normal datasets, and methods are suggested for creating realistic physiological and anatomic variation. Analysis of simulated data using statistical methods and comparison to real normal data shows good approximation, although errors are present. These errors are systematically defined and characterised, and shown to be correlated with discrepancies between the updated Zubal phantom and normal anatomy.

We conclude that the method is feasible for the production of normal data sets, and suggest that if the phantom model is further updated such that existing errors are corrected, then the model would be valid for the production of accurate and realistic SPECT simulation data. The simulation system can then be used to supersede analytical methods for the production of audit data sets.

Table of Contents

List of Figures (Shortened captions)

List of Tables (Shortened captions)

Acknowledgments

First and foremost I would like to thank my three supervisors, Prof. John Fleming, Dr. Sandra Hoffmann and Dr. Paul Kemp for all of their help, advice and direction in the four years of the project, and their knowledge and help in the production of this thesis. I would also like to thank them for providing me with the opportunity to work at the department and improve my understanding of routine clinical methods and my waning bank balance! Specifically, I would like to thank Prof. Fleming for his help with my theoretical education in medical physics and helping me to improve my (poor) writing skills, to Dr. Hoffmann for her practical education and information on everything statistical, and to Dr. Kemp for his clinical medicine teachings. To these three great teachers, I owe nearly all of my understanding of the subject. I would also like to thank Robin Holmes of the United Bristol Healthcare Trust for the useful discussions, direction and practical issues, and also for being an able and keen pub-goer, where much of the discussion took place.

Thanks are also extended to the authors of SimSET, in particular to Robert Harrison and Tom Lewellen for their help in getting the software working, and for improving my understanding of the basic principles of Monte Carlo simulation. Thanks also go Nuclear Fields for their help with creating an accurate model of our Gamma camera.

Peer Reviewed Publications

Ward, T., Fleming, J. S., Hoffmann, S.M. and Kemp, P.M.
Simulation of Realistic Abnormal Brain Perfusion SPECT: Application in Semi-quantitative analysis.
Phys. Med. Biol. 50 (2005) 5323-5338

Not Primary Author

Kemp P.M., Hoffmann, S.A., Holmes C., **Ward T.**, Holmes R.B. and Fleming J.S.
The contribution of statistical parametric mapping in the assessment of precuneal and medial temporal lobe perfusion by ^{99m}Tc-HMPAO SPECT in Alzheimer's and Lewy Body dementia
Nucl. Med. Comm. 26 (12), December 2005, pp. 1099-106

Abstract Only

Ward T., Hoffmann S.M.A., Fleming J.S., and Kemp P.M.
Comparison of SPM and BRASS Using Clinically Realistic Simulated Abnormal Images.
Proceedings of the European Association of Nuclear Medicine annual meeting
Istanbul, October 2005

Ward T., Hoffmann S.M.A., Fleming J.S., and Kemp P.M.
Simulation of Realistic Abnormal SPECT Brain Perfusion Images: Methods and Applications.
Proceeding of Medical Imaging Understanding and Analysis 2004.
Imperial College, London, September 2004

Ward T., Fleming J.S.F., Hoffmann S.M.A. and Kemp P.M.
A Simulation Method for Realistic Abnormal SPECT Brain Perfusion Images
Proceedings of the 32nd Annual Meeting of the British Nuclear Medicine Society
Brighton, April 2004
Nucl. Med. Comm. 25 (4), April 2004, pp. 406 (supl.)

Ward T., Holmes R., Kemp P.M., Hoffmann S.M.A., Bolt L. and Fleming J.S.F
The Importance of Age Adjustment in an SPM HMPAO rCBF database
Proceedings of the European Association of Nuclear Medicine annual meeting
Amsterdam, August 2003

Glossary

Anisotropic	Non-invariant with respect to direction. (see *isotropic*)
Atrophy	A decrease in the size of an organ caused by disease or disuse
Cognition	The psychological result of perception, learning and reasoning
Control group	A group of individuals with some pre-defined common characteristic (e.g. normality). The characteristic is well defined and enforced, allowing its use for comparison with a study group. A normal control group is also referred to as a *normal database*.
Differential Diagnosis	The determination of which of two similar symptomatic presentations is the underlying problem.
flux	The rate of flow of photons. In *Monte Carlo* simulation, we are effectively estimating the flux to produce the image.
inter-	Between, e.g. inter-subject is between subjects.
intra-	Within, e.g. intra-modality is within the modality
in-vivo	Within the living body
isotropic	Invariant with respect to direction. Used to describe an image (component) with equal parameters in its three orthogonal planes.
MNI Space	Oriented in the space defined by the Montreal Neurological Institute, that has many similarities with the *Talairach Atlas*
Monte Carlo	A common term used to refer to random sampling, taken from the place name due to the similarity with a game of random chance
Normal Database	Used to describe a collection of data that has been independently verified as exhibiting no abnormal characteristics, or more loosely, no confounding effects.
pixel	From *pi*cture *el*ement. A single element of a two-dimensional image (picture).
Protocol	A common set of procedures applied (usually) to the same task to provide a repeatable method.
Radionuclide	Any atom that is radioactive
Radiopharmaceutical	A drug containing a radioactive substance
Sensitivity	A measure of how well a method correctly identifies disease
Specificity	A measure of how well a method correctly identifies normality
Study group	See *subject group*
Subject group	A group of individuals under study. In quantitative analysis, the group (individually or collectively) is compared to a control group to detect significant difference.
Talairach space	Oriented in the space described by the Talairach atlas [Talairach and Tournoux, 1988]
t-test	Basic statistical test based on the normal distribution
voxel	From *vo*lume *el*ement. A single element of a three dimensional image (volume), and the three dimensional analogue of a *pixel*.

Abbreviations

3D-FA	**3** **D**imensional **F**ractal **A**nalysis
3D-SSP	**3** **D**imensional **S**tereotactic **S**urface **P**rojection
^{99}Mo	**M**olybdenum-99
^{99m}Tc	**T**echnetium-99 (meta state)
AC	Anterior Commissure
AD	**A**lzheimer's **D**isease
ART	**A**lgebraic **R**econstruction **T**echnique
Bq	Becquerel
BRASS	**B**rain **R**egistration and **A**nalysis of SPECT **S**tudies
Ci	Curie
CMRg	**C**erebral **M**etabolic **R**ate of **G**lucose
COR	**C**entre **O**f **R**otation
CSF	**C**erebro-**S**pinal **F**luid
CT	**C**omputed **T**omography
DCT	**D**iscrete **C**osine **T**ransform
ECD	**E**thyl **C**ysteinate **D**imer
EEG	**E**lectro-**e**ncephalo**g**ram
EM	**E**xpectation **M**aximisation
ET	**E**mission **T**omography
FBP	**F**iltered **B**ack **P**rojection
FDG	Fluoro-deoxy-glucose
FLD	**F**rontal **L**obe **D**ementia
fMRI	**F**unctional **M**agnetic **R**esonance **I**maging
FTD	**F**ronto-**T**emporal **D**ementia
FWHM	**F**ull **W**idth at **H**alf **M**aximum
FWTM	**F**ull **W**idth at **T**hird **M**aximum
GM	**G**rey **M**atter
HMPAO	**H**exa**m**ethyl **p**ropylene**a**mine**o**xime
IPEM	**I**nstitute of **P**hysics and **E**ngineering in **M**edicine
LBD	**L**ewy **B**ody **D**ementia
LEUHR	**L**ow **E**nergy **U**ltra **H**igh **R**esolution
MID	**M**ultiple **I**nfarct **D**ementia
MLEM	**M**aximum **L**ikelihood **E**xpectation **M**aximisation
MMSE	**M**ini **M**ental **S**tate **E**xamination
MNI	**M**ontreal **N**eurological **I**nstitute
MRI	**M**agnetic **R**esonance **I**maging
MTLE	**M**edial **T**emporal **L**obe **E**pilepsy
OM	**O**rbital **M**eatal
OSEM	**O**rdered **S**ubset **E**xpectation **M**aximisation
PC	**P**osterior **C**ommissure
PCA	**P**rincipal **C**omponent **A**nalysis
PDF	**P**robability **D**ensity **F**unction
PET	**P**ositron **E**mission **T**omography
PHG	**P**hoton **H**istory **G**enerator
PMT	**P**hoto **M**ultiplier **T**ube
PSF	**P**oint **S**pread **F**unction
PV	**P**artial **V**olume

QA	**Q**uality **A**ssurance
QC	**Q**uality **C**ontrol
rCBF	**r**egional **C**erebral **B**lood **F**low
ROI	**R**egion **o**f **I**nterest
SD	**S**tandard **D**eviation
SPECT	**S**ingle **P**hoton **E**mission **C**omputed **T**omography
SPM	**S**tatistical **P**arametric **M**ap
SSE	**S**um of **S**quared **E**rrors
VaD	**Va**scular **D**ementia
VOI	**V**olume **o**f **I**nterest
WM	**W**hite **M**atter

Chapter 1 Introduction to Imaging in Dementia

The practical methods described in this thesis are based on nuclear medicine imaging techniques, which is a powerful and commonly used tool in dementia research. This chapter covers the background to dementia and pertinent imaging based methods used in its research.

1.1 Dementia

It is estimated that there is a total of 750,000 people in the UK suffering with dementia and approximately 18 million worldwide, a figure expected to rise to 34 million by 2025 due to the increase in birth rate and ever increasing longevity. The diseases incur costs in excess of 6 billion UK pounds per annum, which puts considerable strain on the national health system resources. The dementias affect approximately 18,000 people under the age of 65 in the UK. 5% of the over 65 population is affected, a figure that rises above 20% when considering post 80 year old subjects[i]. Onset becomes ever more likely with increasing age and the relationship suggests approximately 27% prevalence in post 90 year subjects in Europe [Berr *et al.*, 2005]. Alzheimer's dementia (AD) accounts for 55% of all occurrences of dementia.

Dementia is the progression of symptoms that occur with functional deterioration of the brain, resulting in a decline in cognitive and intellectual function. The most common symptoms of dementia are memory loss, confusion, language problems, deterioration in visual-spatial skills and behavioural changes. These symptoms are usually bought on by some progressive biological change in the brain, usually caused by an underlying disease. The dementing process is a direct result of the disease causing loss of neuronal activity. There is no method of curing dementia, and current treatment concentrates on slowing down the progression of symptoms.

[i] Figures taken from The Alzheimer's Society - www.alzheimers.org.uk

Figure 1.1 is a diagram indicating the major brain lobes, and Table 1-1 indicates the largely functional aspects of the lobes, and the effective dementia. Predominantly, in all right handed people and most left handed people, the left half of the brain is the dominant side. Right sided dominance is only found in some left handed people.

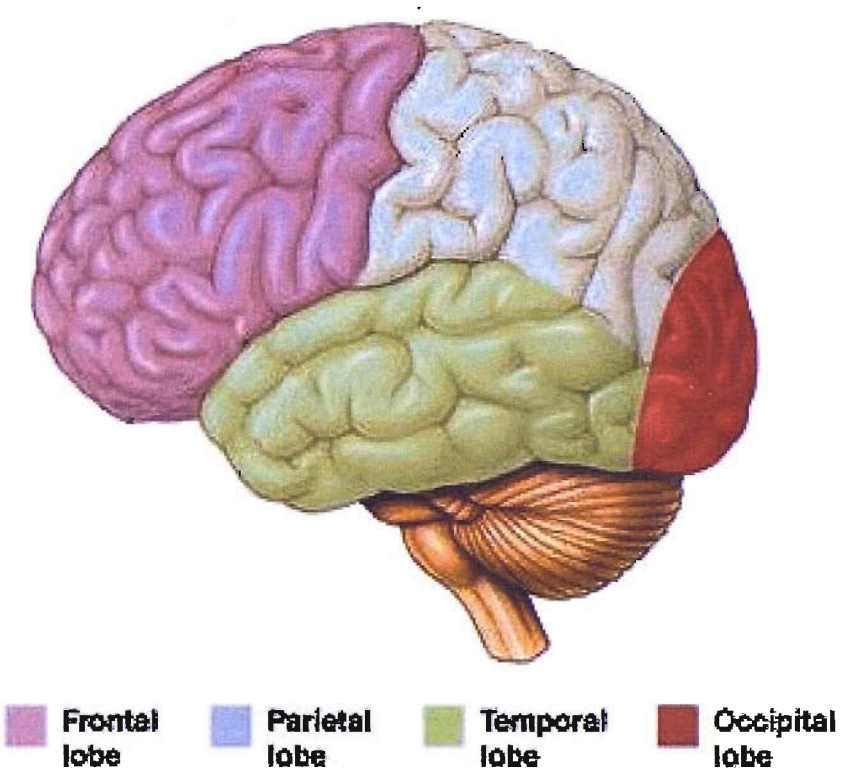

Figure 1.1. The major subdivisions of the human brain, indicating the approximate positions of the lobes

Brain Lobe	Side	Function	Affective Dementias
Frontal	Both	Executive and Management Planning/learning tasks Motivation Behavioural regulation Inhibition	Fronto-temporal Vascular Advanced Alzheimer's Lewy body
Parietal	Dominant	Structuring / ordering Sentence construction / language Coordination Learned purposive movement	Alzheimer's Lewy body Vascular
	Non dominant	3D recognition Visual spatial skills	
Temporal	Dominant	Verbal memory	Alzheimer's Fronto-temporal Lewy body Vascular
	Non dominant	Non-verbal memory (visual)	
Occipital	Both	Visual interpretation	Lewy body Alzheimer's Vascular

Table 1-1. The major brain lobes, associated cognitive aspects and effecting dementia. The affecting dementias are organised by prevalence.

1.1.1 Dementia Types

There are over a hundred different types of dementia, characterised by different pathophysiological defects, but of these the following are the most common.

1.1.1.1 Alzheimer's Dementia (AD)

Alzheimer's dementia is the most common form of dementia, affecting approximately 55% of the demented population. Its prevalence is the reason that the majority of an enormous research effort is put into diagnosis and treatment of the disease. The disease is biologically characterised by the presence of amyloid plaques and neurofibrillary tangles, and also by synapse loss and neuronal death as hallmark lesions. The result is the death of brain cells, atrophy and a loss of function in the affected area. The regions of the brain primarily affected by AD are the medial temporal lobes (in particular the hippocampal formations affected by neurofibrillary tangles), posterior tempo-parietal regions, and the parieto-occipital regions. The disease is irreversible and clinically progressive, and mostly characterised by loss of memory and word finding difficulty due to the changes in the medial temporal areas. Disease onset and progression is correlated with a combination of factors, of which age is the most prevalent. AD has been shown to be hereditary.

1.1.1.2 Vascular Dementia (VaD)

Vascular dementia is the second most common type of dementia affecting around 25% of the demented population. VaD is caused by impaired regional cerebral blood flow leading to oxygen deprivation to brain cells leading to the death of neurons. Risk factors include alcohol, smoking, high blood pressure, and the disease can also be hereditary. Stroke is a common form of VaD, where the blood vessels in the brain become blocked or burst. Multiple infarct dementia (MID) is the combination of several minor strokes. The major other form is sub-cortical vascular dementia. Disease onset is stepwise, irreversible and degenerative. It can be difficult to make a differential diagnosis between AD and VaD clinically, although VaD is generally indicated by large number of focal lesions where AD affects entire regions.

1.1.1.3 Dementia with Lewy Bodies (DLB)

Dementia with Lewy bodies accounts for around 15% of all dementia sufferers. Lewy bodies are very small spherical protein deposits found in the nerve cells in the brain, and cause disruption of the chemical signalling between neurons, including acetylcholine and dopamine transport. Lewy bodies are also found in people with Parkinson's disease and LBD also shares characteristics with Alzheimer's disease, which causes difficulty in making the differential diagnosis. Affected areas of the brain are similar to Alzheimer's disease, but often also include moderate neuron loss in the occipital regions. The cause of the protein deposition is still unknown. LBD onset is usually gradual, irreversible and degenerative, and sufferers usually find that their cognitive function varies greatly with time. Diagnosis is usually based on clinical tests and symptomatic presentations.

1.1.1.4 Fronto-Temporal Dementia (FTD)

Fronto-temporal dementia is a term given to a group of degenerative conditions concerning deterioration of the frontal and temporal lobes. The disease accounts for a very small percentage of the dementias, but covers a large group of different diseases, of which Pick's disease and frontal lobe degeneration are the most common forms. FTD affects the frontal and temporal aspects of the brain, or a combination. The disease is not age related, and younger people are more at risk of developing FTD than older people. As with Alzheimer's dementia, the disease is gradual in onset,

irreversible and degenerative. The disease affects the areas of the brain largely associated with behaviour, personality and language, while memory is relatively well preserved. The condition will become similar to Alzheimer's dementia as the disease progresses and becomes more widespread and generalised.

1.1.1.5 Other Causes of Dementia and Confounding Conditions

There are many other causes of dementia that are far less common. There are also a large number of confounding conditions that mimic the onset of dementia, such as vitamin deficiencies, thyroid problems and depression. Parkinson's syndrome and Lewy body dementia (LBD) are two common confounding conditions, where LBD's characteristic Lewy body's are also found in the nerve cells of Parkinson's sufferers. Multiple sclerosis (MS) can also cause mild dementia and cognitive difficulties in individuals. Prion diseases are similar to LBD in that proteins (prions) are laid down in the brain and can cause jerky movements similar to those of Parkinson's disease. Creutzfeldt-Jakob disease (CJD) is one such disease. The disease is transmitted through the prions, which are transmissible agents, although little is known of the mode of transmission. Acquired immune deficiency syndrome (AIDS) is known to cause dementing processes due to the virus either directly attacking brain cells or by an infection taking advantage of the bodies reduced immunity level. With all of the different dementias and related diseases, and the unclear pathology due to underlying elements from more than one type of dementia, it is often difficult to form the differential diagnosis. This has led to the continually increasing number of alternative and complimentary analysis adjuncts being used in the clinical diagnosis of the dementias.

1.1.2 Diagnosing Dementia

Traditionally, dementia is diagnosed by a clinical examination conducted by a consultant in old age psychiatry, after eliminating all other possibilities. This would typically involve the assessment of the individual symptomatic presentation, taken with the patients understanding of his/her condition and that of a personal witness. Cognitive function testing would also be employed to ascertain which areas, if any, of cognition were being affected. This is ascertained through the use of a various

psychometric testing of mental state (e.g. the mini-mental state examination (MMSE) [Folstein *et al.*, 1975]) which offers a crude but useful clinical test.

Most dementia's are well characterised by groups set up with particular interests, such as the NINCDS-ADRDA (National Institute for Neurological and Communicative Diseases and Stroke/Alzheimer's Disease and Related Disorders Association) criteria for possible and probable AD, or the DSM IV (Diagnostic and Statistical Manual of Mental Disorders) criteria. These tests rely on the subject fulfilling criteria characteristic of the dementing process. However, many methods have been established as offering useful information to aid in and complement clinical diagnosis methods by employing image and non-image related techniques.

The electroencephalogram (EEG) is a less common method used for diagnosing dementia. The EEG is a record of the summed post-synaptic potentials measured in the brain, acquired by passive electrodes placed on the subjects scalp in positions adjacent to the lobes of the brain. The EEG was traditionally recorded on paper using an electrically controlled mechanical stylus, and has been replaced by digital recording methods that offer more information. Interpretation of the EEG can aid in the detection of a variety of brain problems including dementia, by using digital techniques to analyse the EEG and return advanced information on the data that indicates abnormal results. The data can then be used as a useful indicator of cortical dysfunction. EEG abnormalities do not differ much across the different types of dementia but can be used as a useful indication of an underlying dementia. The main disadvantage of the method is that the differential diagnosis is unclear.

The majority of the more recent developments involve creating an image of the brain that represents some effect of interest, which can be subjectively or objectively interpreted to aid in the clinical diagnosis of dementia. Section 1.2 deals with these methods.

1.1.3 Treatments for Dementia

Currently, there are no treatments for any of the dementias that will actually permanently stop the progression of the disease, and furthermore, there are no treatments that will repair the damage caused. A very large research effort is applied

to dementia, primarily targeting AD. The main research effort is based largely on: improving the diagnostic accuracy of detection methods, to characterise the disease and its onset, to find causes for the disease, and develop and test treatments for the disease. To date, several treatments have become available, or are currently being evaluated. However, the treatments available are primarily preventative, which necessitates early diagnosis to obtain maximum efficacy.

The primary treatments for AD are acetylcholinesterase inhibitors. This drug causes the brain to stop breaking down acetylcholine, which is used for chemical signalling between brain cells. The result is higher levels of communication between nerve cells and improved function. In this group are Aricept (donepezil hydrochloride), Exelon (rivastigmine) and Reminyl (galantamine). Recent research also suggests the use of cholinesterase inhibitors in the treatment of DLB and VaD, although the drugs are not yet licensed for use as this treatment. Ebixa (memantine) works in a different way, by blocking the excessive release of glutamate from damaged brain cells, the drug can prevent the cells damaging themselves further. The overall effect of all of the drugs is to temporarily slow down the onset of the disease, and occasionally can temporarily improve the condition of the subject. Eventually the effect of the treatment will weaken and disease onset will continue. Large research trials are underway to assess the effectiveness of current and new treatments, and rely heavily on image analysis for quantifying the results.

Vascular dementia can be treated by attacking the source of the vascular events, whether small vessel problems, excessive blood fat or high blood pressure, controlling the cause can usually result in limiting or delaying the severity of the damage. As yet, there are no treatments for fronto-temporal dementias.

1.2 Medical Imaging and its Role in Detecting Dementia

There are several imaging techniques that can be used to provide useful information on dementia and its progression. It has been reported that these methods are generally slightly less sensitive than clinical criteria although offer an increase in specificity [Dougall *et al.*, 2004]. These methods are usually based on imaging of the brain, either anatomically or functionally. This gives an insight into deterioration associated

with biological brain death and decay or lack of function associated with neuron loss. Many studies exist showing correlations between these effects and both cognitive impairment and the onset of specific types of dementia [Dougall *et al.*, 2004]. Imaging methods are continually evolving and technological advances are improving the image quality of the systems. The result is an overall improvement in the diagnostic capability of the imaging system, resulting in earlier, faster and more accurate detection and diagnosis of dementia and dementia related illness.

Medical imaging forms a very large section of medical research, and is the subject of a large number of projects. The main reason for the growth is the diagnostic ability of the imaging modalities, offering predominantly non-invasive methods of imaging internal structures using a number of techniques. Anatomical imaging techniques allow high-resolution imaging of in-vivo systems and functional imaging allows visualisation of function on a number of levels. The methods also generally allow three-dimensional reconstruction, which can be analysed using conventional tomographic display methods or interactively using real time volume rendering systems. Anatomical and functional techniques are finding application in all areas of medicine, from basic x-rays or radiographs on film for diagnosing problems with bones, through measuring the activity of the thyroid gland or the ejection fraction of the heart, to 3-dimensional volume rendering to aid in surgery planning.

Imaging methods exist for studying the brain. Anatomically, the methods are used to indicate problems with structure due to atrophy or abnormal growth, which could be associated with dementia or a tumour. Functionally, tracers are used to indicate regions of abnormal activity which are usually associated with disease. Functional methods can also be used to detect the presence or lack of neuronal activity in response to external stimulation.

1.2.1 Anatomical Imaging Modalities

There are two common anatomical imaging modalities used for providing accurate three-dimensional anatomical information. Computerised tomography (CT) relies on x-ray transmission and tomographic reconstruction, while magnetic resonance imaging (MRI) uses super conducting magnets along with magnetic pulses, radio waves, antenna and complex reconstruction methods to obtain anatomical images.

Both modalities offer an accurate method of non-invasive anatomical imaging of the brain, which combined with either qualitative or quantitative interpretation, allows the differentiation of atrophy associated with normal ageing and that caused by disease onset. This is particularly relevant in the amygdala hippocampal complex structures in AD and normal ageing, where volumetric measurements aid in the differential diagnosis [Fotenos *et al.*, 2005]. Frontotemporal lobe degeneration can also be diagnosed using similar methods. Other methods using advanced magnetic resonance imaging (MRI) techniques can also be used to diagnose other forms of dementia.

1.2.1.1 Computerised Tomography

Computerised tomography (CT, or sometimes referred to as computerised axial tomography or CAT) images are constructed from a set of x-ray transmission measurements (projections) taken from equally spaced positions around the subject. An electrically controlled generator is used to create the source emissions. Each projection is formed from the measurement of the resultant energy of x-rays after attenuation by the materials in the path of the radiation (usually assumed to be a straight line). Each projection represents the total attenuation cross-section. The projections can be combined using reconstruction methods to estimate the attenuation at any point in the image, and provide a voxel-wise tomographic representation of the attenuation within the object of study. The voxels of the tomograph represent the Hounsfield units, indicating the attenuation at any point. The attenuation index is effectively constant across different tissue types, and the reconstructed CT image can be used to accurately indicate the anatomy of the volume being scanned. CT imaging offers improvements over conventional planar x-ray imaging through the added depth measurement, which allows precise measurement of object boundaries and volumes.

CT imaging is faster than MRI imaging and offers a higher imaging resolution of ~1mm. CT is very effective at distinguishing between different tissues. However, CT investigations result in the subject and the camera operator being exposed to ionising radiation. The attenuation measurements are useful for correction of degrading effects in nuclear medicine imaging (see section 2.1.4). MRI can offer similar anatomical information to CT systems without the associated dose, and are consequently being used in more and more applications in place of CT. This form of imaging also has application in other areas.

1.2.1.2 Magnetic Resonance Imaging

Magnetic resonance imaging (MRI) takes advantage of one of the main constituents of the body – water. Water consists primarily of hydrogen, whose nuclei are usually spinning randomly. The method incorporates large magnetic fields to polarise the hydrogen nuclei in the body, such that they are all spinning in alignment with the magnetic field. The protons can then be excited by electromagnetic radiation (radio frequencies), and if the frequency of the excitation is equal to the frequency of the nuclei rotation, causes them to flip direction because of the resonance effect. When this signal is removed, the nuclei will realign with the magnetic field, and the resultant realignment will result in a very small electromagnetic discharge (called an echo) from the nuclei, which can be picked up by an antenna or coil on the MRI scanner. Measuring the amplitude of the echo results in a proton density measurement, and gives a reading of the amount of hydrogen present in a particular region that is indicative of anatomy. T1 and T2 weighted images indicate the rate of decay of the echo, and offer other discriminative information. The technique can be carried out to measure this information for whole volumes of the human body at once.

The method, like CT, is very useful for obtaining volumetric anatomical models of the area being studied. MRI has a better theoretical resolution (~0.5mm), but is more prone to noise and resolution is worse in practise. Very small structures can be easily discriminated within the result, and the high resolution allows very accurate measures of structure volume, which is useful in detecting some dementing diseases. MRI is most effective in the discrimination of different types of soft tissue through T1 and T2 type imaging, such as in the brain, where it offers much better contrast than CT. This allows discrimination between grey and white matter, which is a useful property for imaging of the brain. There is no ionising radiation source with MRI, however, the scanner uses very large magnets, and so no metal objects can be used during scanning. This includes medical devices such as pacemakers or implanted metal support structures, which makes it impossible for some subjects.

1.2.2 Functional Imaging Modalities

Functional imaging refers to, in general terms, the imaging of function as opposed to anatomy such as the activation of a particular brain region in a sensory-motor task.

Functional imaging relies primarily on nuclear medicine imaging modalities, although other techniques are used with contrast agents, such as fluoroscopy and CT for imaging the act of swallowing. Functional MRI (fMRI) can be used to measure changes in blood flow within the brain, indicating activation during a sensory-motor task. Functional brain imaging can be used in aiding the detection of dementia by supporting the clinical diagnosis, particularly where anatomical imaging appears normal in light of contradictory psychiatric data. All of the functional imaging modalities measure brain activity through the use of some surrogate marker for localised activity.

Correlation has been shown between decline of the functional aspect of particular regions of the brain and different dementia diseases. This extends to all types of dementia and brain related illnesses, all of which appear to be characterised by functional decline in associated cortical regions. Functional imaging methods are used to detect these deficits with an ever-increasing sensitivity and support a differential diagnosis in dementia, or dementia related illness.

1.2.2.1 Nuclear Medicine Techniques

Nuclear medicine imaging employs radioactive sources for the tracing of some function of interest. The primary concern is that of emission tomography, where specific radioactive chemical compounds are used intravenously with a deposition rate proportional to function. The emission of radiation can then act as a marker for neuronal activity allowing functional deficits to be localised. The radiotracer (or radionuclide) is usually a chemical compound with some useful property, which is labelled with a radioisotope to act as a surrogate marker for some function. This allows an internal image to be obtained non-invasively. The administered substance is termed a radiopharmaceutical; a pharmaceutical consisting of a radioactive compound used as a diagnostic or therapeutic agent.

Firstly, a radiopharmaceutical is administered to the subject, usually intravenously, and allowed time to reach the system under study. The pharmacokinetics of the radiopharmaceutical are chosen so as to be taken up by the functional system of interest. The emissions from the radionuclide pass through the surrounding structures and leave the body, where they can be detected using an external detector.

There are two main nuclear imaging modalities used in modern day functional imaging. These are single photon emission computed tomography (SPECT) and positron emission tomography (PET). Both methods rely on the administration of radiopharmaceuticals and subsequent detection of radioactive emissions. The methods differ only in the type of radioactive emission and the method used for detection.

Dementia can be indicated using nuclear medicine methods, by carefully choosing the required radiopharmaceutical to trace either the cerebral metabolic rate of Glucose or Oxygen (CMRg or $CMRO_2$), or the regional cerebral blood flow (rCBF). All of the measures act as surrogate markers for local functional activity. The resulting images can be analysed either qualitatively or quantitatively. Different patterns of abnormality are indicative of the dementing process in different diseases.

1.2.2.2 Functional Magnetic Resonance Imaging and MRI related techniques

fMRI is based on MRI. An increase in metabolic activity in a region of an activation results in an increase in rCBF resulting in a region of highly oxygenated blood. When a magnetic field is applied, the decreased level of deoxyhaemoglobin (which is paramagnetic, meaning it becomes more magnetic as the field increases) leads to the echo decaying faster because less of the protons are in phase coherence (reducing the resonant effect). The method is therefore effective in detecting a decrease in deoxyhaemoglobin, which is indicative of functional activity (oxygen metabolism).

fMRI is generally used to measure differences in the oxygenation of blood over time, allowing changes (indicating cerebral activation) to be monitored. It cannot offer information about the normality of the original state of the organ, and therefore an abnormally low level of activity. Although fMRI can be used for functional activation studies, it is subject to several limitations. The signal itself could be caused by a high haemodynamic response, which itself is a combination of a number of energy requiring processes. The response measured is used as a surrogate marker for neuronal activity, but actually measures the haemodynamic response that is much slower acting. However, constant experimentation and research are moving the technique towards becoming the standard for neuronal activation studies.

MRI can also be used with tracers to indicate uptake. Tracers can be administered (Gadolinium-DTPA is used as a contrast) to the subject under study, and ultra fast MRI methods (echo planar imaging or EPI) can be used to measure the rate of delivery of the tracer to particular regions of the brain, a technique called perfusion MRI. The results can be interpreted to indicate blood flow through brain vessels, and show whether blood flow is normal.

1.3 Functional Brain Imaging Methods Using Radionuclides

This section deals more substantially with radionuclide imaging of the brain, as this technique is the imaging method on which this thesis is based.

1.3.1 SPECT and PET Imaging

1.3.1.1 SPECT

Single photon emission computed tomography (SPECT, sometimes called SPET) relies on the emission and subsequent detection of gamma photons from decaying radioisotopes. The images are then reconstructed to create a three dimensional image and converted to tomographic data. An Anger camera is used to obtain planar images of the source. Various reconstruction techniques exist using basic back projection methods and more complex iterative methods based on statistical models.

SPECT imaging can be used to estimate the level of cerebral perfusion through the use of lipophilic tracers, which bind to oils and fats. The tracers are able to cross the blood-brain barrier where they are metabolised into more hydrophilic (water bound) forms, and generally become trapped within 5 minutes of injection. The resultant distribution is a surrogate marker of the rCBF in the region during extraction from blood. The two most commonly used tracers are hexamethyl propyleneamineoxime (HMPAO) and ethyl cysteinate dimmer (ECD), with the most common radiolabel being Technetium 99m (^{99m}Tc). Another application of SPECT imaging of the brain is Ioflupane-123 FP-CIT (DaTSCAN^{TM}, GE Healthcare), which can be used to image the dopamine transporters in the brain and is used to diagnose dopaminergic dysfunction in Parkinsonian syndromes, and to differentiate it from essential tremor.

1.3.1.2 PET

When decay occurs in a positron-emitting isotope, a positron is emitted which begins moving along a randomly changing path (termed a random walk), until it encounters an electron. The path length of the photon is usually only a maximum of a few millimetres. The interaction results in the annihilation of both the positron and electron, and the emission of two gamma rays of equal energy in opposite directions, called pair production. An event is indicated by the simultaneous detection of photons on both sides of the activity, using scintillation devices in different configurations. A detected event is recorded if both gamma rays are detected within a time period, and the event is assumed to have occurred on the line joining the location of the two events, termed coincidence imaging. Generally, the detection is carried out using a continuous ring of static detectors, although gamma camera PET can be carried out using a pair of revolving Anger cameras (with or without collimators). The acquired data is similar to that for SPECT and can be reconstructed into a 3 dimensional representation of the source distribution using the same methods.

PET imaging can be used to measure either glucose metabolism or rCBF using one of two techniques. The first technique uses fluorodeoxyglucose (FDG), an artificial form of glucose, which is radiolabeled with Fluorine-18 (^{18}F). The uptake of FDG provides an estimation of cerebral glucose metabolism, as it is partly metabolised by the brain. The second technique uses oxygen-15 (^{15}O) incorporated into other compounds ($C^{15}O$, $^{15}O_2$ and $C^{15}O_2$) and is administered by inhalation to indicate cerebral oxygen or glucose metabolism. The count rate from any voxel or region in the image can then be used with kinetic modelling to quantify the level of metabolism or rCBF in the voxel or region accurately.

1.3.1.3 PET vs. SPECT

Although PET is available clinically in an ever-growing number of locations, helped by the emergence of mobile PET scanners, its implementation in dementia studies remains primarily a research tool. This is due in the main to the unavailability of isotopes, which itself is due to the requirement of a cyclotron for production of isotopes such as ^{18}F and ^{15}O, on which PET techniques are based. This can be slightly alleviated by a centrally based cyclotron and a distribution network, although this could not be extended to short lived isotopes such as ^{15}O with a half life of only 2

minutes. The installation of a cyclotron requires, apart from substantial costs, a considerable amount of room. However, PET offers sensitive quantitative measurement of brain function, which is not offered by other functional imaging methods. System spatial resolution approaching 5mm FWHM is obtainable using PET, resulting in more accurate quantification of brain metabolism. SPECT camera resolution is lower than that of PET. Also, apart from the usual problems associated with gamma emissions, the positrons emitted by the PET isotopes undergo a random walk before annihilation, which results in the photons being emitted from the position of the annihilation and not the precise location of decay, a factor which limits the theoretical maximum obtainable resolution.

SPECT tracers are relatively inexpensive and easy to prepare and administer when compared to PET, because of the wide availability and relatively long half-life of the isotopes. Most SPECT radiopharmaceuticals are readily obtainable in kit form, which allows preparation in the average nuclear medicine laboratory. Furthermore, SPECT uses a simpler detector technology than PET, hence more widely available (i.e. most hospitals are equipped with a gamma camera) and cheaper purchase costs. The effective operator dose is about ten times smaller in SPECT, due to higher energy levels (in the region of three times), the production of twice as many photons from the decay and longer preparation and scanning times. Therefore SPECT systems are generally considerably cheaper to install, maintain and operate than PET, and also offer safer operator environments. When considering the options, the relatively high costs and restricted availability associated with PET has to be traded off against the technical limitations of SPECT.

1.3.2 Gamma Radiation, Transport and Detection

Functional brain imaging methods in nuclear medicine rely on the detection of emitted photons from a radioactive source within the brain. The properties of gamma radiation are ideal for functional imaging of the brain, and are: The emissions should be such that the photons pass through the various tissues of the head and skull without being absorbed, while being capable of being stopped by the detector without passing through in large quantities.

Gamma camera imaging relies on the emission and subsequent detection of gamma radiation, which is a form of electromagnetic radiation emitted during a radioactive decay or produced via electron-positron annihilation. The emissions are able to travel many feet in air and many centimetres in human tissue. During transport, the photons are subject to several types of interaction with the material through which they are travelling. The major interactions and photon paths are summarised in Figure 1.2. The photoelectric effect (a) takes place when a gamma photon interacts with an orbiting electron, resulting in the electron being ejected from the atom with a kinetic energy equal to the energy of the gamma photon minus the binding energy of the electron. The gamma photon transport ends here, and this is the primary mechanism used in scintillation materials to indicate an event. Compton scatter (b) also occurs when the gamma photon interacts with an orbiting electron, resulting in ejection from the atom. However, only part of the photon energy is transferred to the electron, and the gamma photon will continue its transport with a reduced energy level and at a deflection angle related to the decrease in energy. A third interaction, called pair production, occurs when the photon passes close to the nucleus, resulting in the energy of the gamma photon being converted directly into mass, as an electron and positron. The resultant mass equivalent energy of the pair is 1.02MeV and this is the minimum energy level required by the incident gamma photon to obtain pair production. Any excess energy is converted to kinetic energy of the pair. This form of interaction is not usually witnessed in gamma radiation transport in medical imaging applications due to the low energy of the emissions.

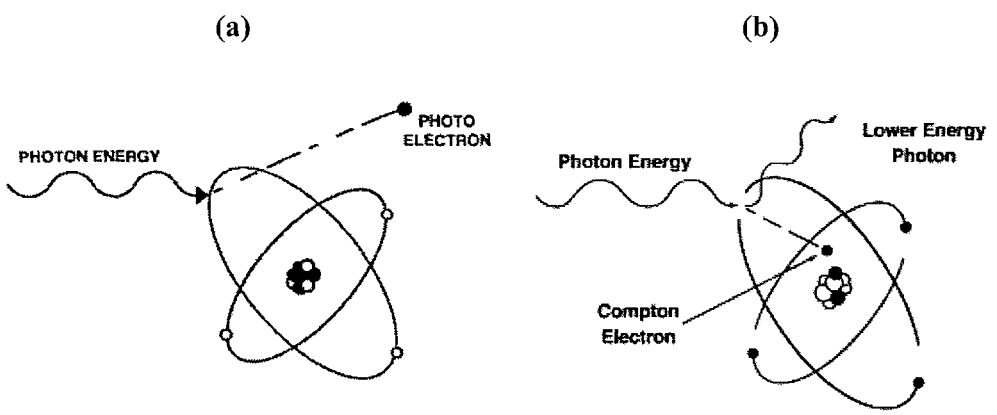

Figure 1.2. Illustration of different photon interactions with atoms; (a) The photoelectric effect and (b) Compton Scatter

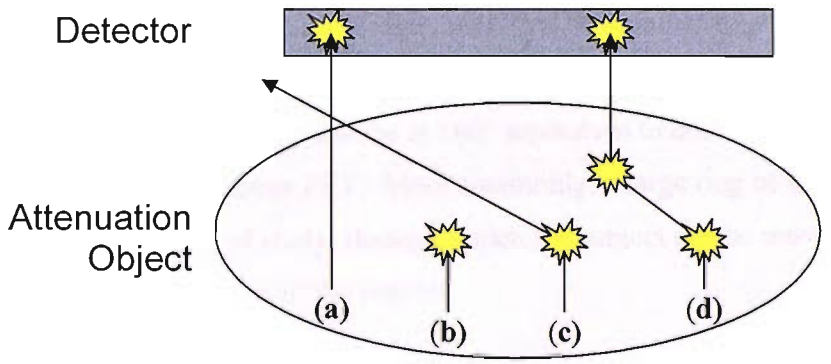

Figure 1.3. Overview of gamma radiation transport and detection; (a) No interaction resulting in a correctly detected event, (b) the photoelectric effect resulting in no detection of the event, (c) a single Compton interaction resulting in no detection, (d) two Compton interactions resulting in a detected event, in an erroneous position.

Of the photons that reach the detector those that have undergone interaction prior to detection are termed scattered photons or events, whereas photons that have not undergone interactions are termed primary photons or events. The interactions produce errors in the imaging system; the assumed location of the photon emission is calculated based upon the detected energy level and the position of the detected interaction. If a photon undergoes any interaction in the source object, then the photon properties (i.e. energy and direction) are likely to change in a random manner. This is illustrated in Figure 1.3 where (a) shows a photon detected on a straight line from the source with no interaction in the matter. (b) The photoelectric effect resulting in total absorption of the photon energy. (c) A photon undergoes a single Compton scatter resulting in a deflection away from the detector. (d) (possibly multiple) Compton scattering where the photon is eventually detected.

The location of the interactions, if any, on their path is random, and so photons that are scattered are undesirable, particularly if detected. The end result is uncertainty in the acquired image.

1.3.3 Gamma Camera Imaging

Emitted photons can be detected using the devices described below, and several methods exist for capturing images using arrays of these detectors. The three acquisition modes are planar, SPECT and PET. Single photon imaging in nuclear medicine relies on the detection of a single photon using gamma cameras positioned around the target of study. Positron imaging is similar in that detectors are placed

around the subject of study, but the images are based on simultaneous detection of two photons at opposite sides of the subject (called coincidence imaging). PET can be implemented using at least two cameras at 180° separation to detect coincident photons, called Gamma camera PET. More commonly, a large ring of detectors placed around the subject of study, through which the subject can be moved to image individual (or multiple) slices of the subject.

Single photon imaging is based on using arrays of detectors, usually arranged in a rectangle, to image the source. Planar imaging relies upon a single camera placed to obtain a single discretised view of the source activity in two-dimensional format. SPECT imaging uses a series of planar images taken from equally spaced locations around the subject (usually 64 or 128), which can be reconstructed into a three-dimensional voxel representation that can be displayed as a tomograph.

1.3.3.1 The Anger Camera and Alternatives

The Anger camera, named after its inventor Hal Anger [Anger, 1958] and still largely unaltered to this day, forms the basis of most single photon cameras used in current nuclear medicine. The camera consists of three main parts, a collimator, a scintillation crystal that acts as a detector and a set of photo multiplier tubes that detect scintillation events in the crystal. Positional electronics are used to determine the location of the interaction. Figure 1.4 shows a basic block diagram of the Anger camera.

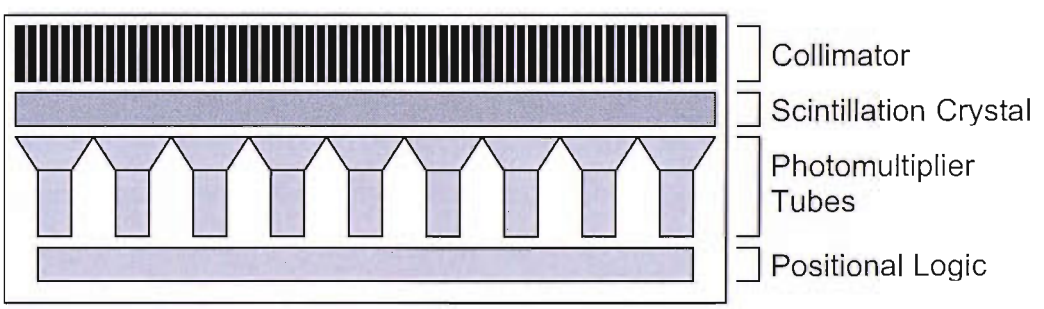

Figure 1.4. The basic Anger camera design

The collimator is a large block of highly attenuating material in a hexagonal lattice arrangement (septa) with very small channels (holes) running through it. It is designed to stop photons impinging upon the scintillation crystal from an unwanted direction. The collimator attempts to ensure the image is created only from photons

travelling in certain prescribed directions. The collimator can be of different design depending on the required use. The most common types are parallel hole, converging and diverging as well as pinhole for study of very small regions. The scintillation crystal (typically Sodium Iodide – NaI) is positioned behind the collimator. The crystal should have a high attenuation coefficient such that photons are stopped and generate a detectable event, rather than pass straight through. The material is selected such that it emits a burst of light (due to interactions causing electron emission) when an impinging photon interacts with the crystal. The resultant light event is then picked up by photomultiplier tubes (PMT) that are coupled to the surface of the crystal and generate a current that is proportional to the energy of the interaction. Arrays of PMT's allow positional circuitry to obtain the location of the event, with an intrinsic resolution of approximately 3mm.

There are several variations on the standard Anger camera, as well as other different methods of detection. Progressions in recent years are heading towards replacing the NaI crystal and PMT's with semiconductor alternatives. These methods would offer more compact design and greater energy and spatial resolution and hence better contrast and quantitative measurements. However, the poor stopping power of the detectors leads to an overall decrease in system sensitivity. Of current solid-state devices, Cadmium Telluride (CdTe) and Cadmium-Zinc-Telluride (CdZnTe) appear to be the most promising gamma radiation detectors at room temperature [Darambara and Todd-Pokropek, 2002].

An alternative method for the detection and imaging of radionuclides is the Compton camera, first introduced by Todd *et al* [Todd *et al.*, 1974]. The camera is based on a two-detector design, where the first detector maximises the likelihood of Compton scatter, and the second detector is designed to absorb the remaining energy. The energy of the detected events in the first detector allows accurate calculation of the scatter angle. The second detector location can be matched to the first detector location and the scatter angle to extrapolate a range of possible source positions, which would lie on a cone prescribed by the detection parameters. The result is an electronic collimation of events. This overcomes the major limitation of the gamma camera and improves the spatial resolution and sensitivity. The method is not in use

in radionuclide imaging due to the poor sensitivity of the detection elements, although it has found use in astronomy.

1.3.3.2 Gamma Camera Limitations

Gamma cameras have an inherent trade-off between sensitivity and resolution, which is mainly influenced by the construction of the collimator. The necessity of a collimator, and the combination of its required properties results in the biggest operating limitation. An increase in the spatial resolution of the camera (longer and narrower septa), reduces the sensitivity of the detector (less detected counts per decay). The trade off must be optimised to limit the patient exposure, allowing the acquisition of a useful number of counts with the smallest possible dose. The collimator can resolve source activity to approximately 10mm resolution when using the highest resolution collimators. The scintillation crystal is capable of resolving the location of events to approximately 3mm resolution, but the collimator resolution predominates, thus the overall system resolution of the gamma camera is relatively poor. Septal penetration, where photons travel straight through the collimator septa, is not a problem with low energy photons such as those emitted by ^{99m}Tc.

The scattering of photons within the attenuating material (Figure 1.3), introduces error in the calculation of the photon source. This problem is significant, although the loss in photon energy can be used partly as a discriminating factor between primary and low energy scattered photons. Accurate removal of scattered photons is not possible due to the random location of the scatter interactions. Several techniques exist for scatter correction, and have been shown to improve analysis [Buvat *et al.*, 1995]. Several techniques exist using either the energy data for the detected events [Shiga *et al.*, 2002] or by generating a model and estimating the scatter before subtracting it from the image.

Attenuation is the term given to the effect of photons that are not detected due to interaction in the material (Figure 1.3 (b,c)). The probability of a photon undergoing an interaction is a function of the distance the photon has to travel through the attenuating material, and the attenuation coefficient of that material. This causes lower numbers of detected events for photons originating from deeper within the source object, as a scatter interaction is more likely. Accurate correction for this

effect is possible using models of the attenuating objects and generating a voxelwise correction map based on the average attenuation coefficient over all projections.

The total measured counts from a single element of the acquired image are assumed to be linearly distributed about the source element. This is usually not true and the result is termed the partial volume effect. The effect is particularly evident where atrophy widens the fissures between folds in the brain producing an apparent reduction in neuronal activity that is actually due to a reduced source volume. Correction for partial volumes can be achieved through the use of an anatomical map of the source object, where the actual detected activity can be adjusted according to the amount of source activity in that region. For example, if a voxel is assumed to be entirely within the cortex, but is only half so, then the detected count level is only half of the actual count level.

The level of activity decreases with time due to radioactive decay, which results in fewer counts for each subsequent planar view. This can be easily and accurately corrected for if the half life of the radioisotope is known. Image quality degrades with distance to the camera surface due to resolution loss as photons paths diverge.

A major source of degradation of image quality is statistical noise. Due to the random nature of the emission and detection process, a planar gamma camera image element is subject to random statistical variations in counts, and the noise can be accurately modelled using the Poisson distribution. The standard deviation of repeated measurements of counts per pixel is the square root of the number of counts. This gives rise to a speckled effect in the images, which becomes less marked as the number of counts in the image increases. Figure 1.5 illustrates the effect of noise for the gamma camera dependent on the average number of counts in a voxel. Image quality is substantially lower for a lower number of counts. The image does not include any other effects.

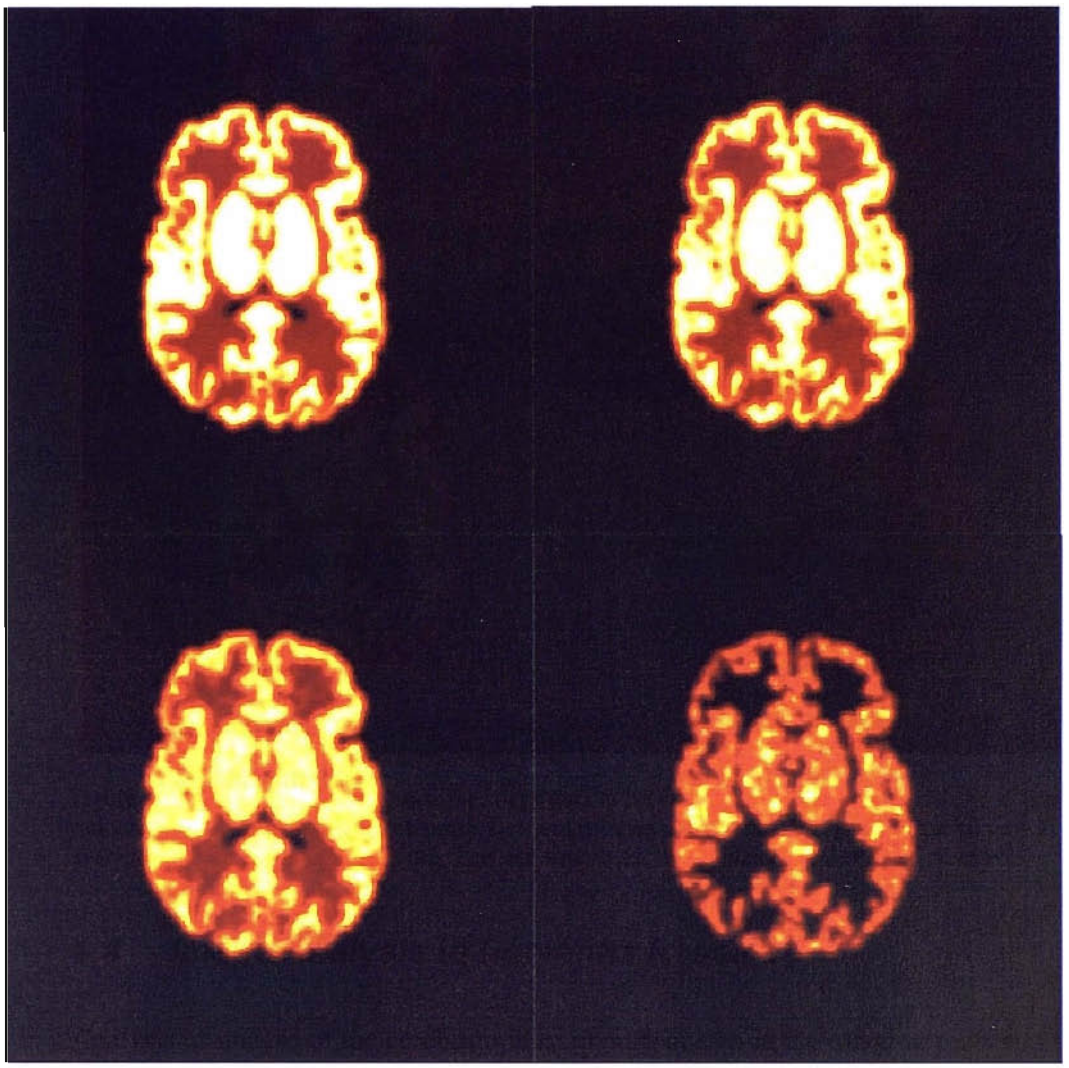

Figure 1.5. Effect of statistical noise on image quality for different average count levels for a 4:1:0 ratio of grey to white matter; a) no noise, b) average count value = 50, c) average count value = 10 d) average count value = 1. Images are Gaussian smoothed, and contain no other physical effects.

1.4 Image Analysis in Dementia Research

Analysis of images of the cerebrum is an important step in the imaging process. Analysis serves to provide some inferences based on the actual acquired image, which can be used to indicate problems caused by underlying pathology. This can be carried out either visually (qualitative methods), automatically (quantitative methods) or by a combination of both (semi-quantitative methods). All of the methods produce data that indicate regional deficits in some form. It is ultimately the job of a consultant to infer a diagnosis based upon the results of the analysis and other data. The analysis method should therefore be as sensitive to the presence of disease as possible while being completely specific to normal data. This data can be used, for example, to

measure the effectiveness of a drug during a trial treatment period, by assessing the disease progression.

Pre-processing (and occasionally post-processing) is an essential step for all analysis methods, such that the acquired data is comparable to normal data. The main aim of the pre-processing step is improve the accuracy of analysis by conditioning of the data. The method used is specific to the equipment, acquisition type, image format and analysis method and occasionally the subject under study. Specific methods are given where applicable.

1.4.1 Visual inspection

Visual inspection is the most basic and natural method for detecting the presence of dementia. Visual inference is based on viewing by an experienced person to determine if and where defects exist. Visual inspection involves viewing the data and determining if an abnormality exists, such as the presence of atrophy in a CT or MRI image or the presence of functional defects in a CMRg tomograph. This makes the pre-processing stage an important factor in analysis. The overall accuracy of visual inspection is low when compared to other methods, as it relies on the prior knowledge of the analyst. The method is also subjective and prone to inter and intra analyst variability.

1.4.2 Semi-quantitative

Semi-quantitative analysis methods attempt to combine qualitative and quantitative analysis methods. This is carried out by obtaining a qualitative measure and applying a quantitative analysis (e.g. when applying count analysis on manually defined regions), or *vice-versa* (e.g. using a scale to quantify the level of medial temporal lobe atrophy in AD). Semi-quantitative analysis methods usually involve a degree of subjectivity associated with the qualitative part of the analysis. Semi-quantitative analysis broadly covers volume of interest (VOI) and region of interest (ROI) analysis. The measurement is usually the mean detected perfusion in a region, and the diagnosis is usually based on how these regional values compare to normal ranges. The method has the advantage of allowing quantitative comparison of any region of two (or more) images.

1.4.3 Quantitative

Quantitative analysis involves generating some measure of an image feature in an attempt to correlate this with disease progression. For example, the normalized volume or perfusion of a particular region of the brain could be compared to a normal range using statistical tests, and pronounced abnormal if exceeding a set limit. These tests effectively allow the measure of the certainty in a particular result. The methods are predominantly automatic and objective, although there are some qualitative aspects to all methods. The majority of the methods require normalisation so that the quantitative measure is most accurate, and can be compared to known normal ranges. Many methods for analysing the quantitative results exist, and complex, partly validated analysis methods are available (section 2.2). The major drawback is that the user is 'left out of the loop' and any errors are easily propagated throughout the system. Complete validation of the software is not possible due to a lack of known ground truth, thus the quantitative analysis methods are used mainly as research tools, or as an adjunct to clinical evaluation.

Quantitative analysis of brain SPECT imaging is as also a useful tool in the early diagnosis of functional brain disease due to its ability to diagnose small functional defects. This helps to improve the confidence in the clinical diagnosis, and the results of such a study can often prompt a re-assessment of the original SPECT data.

1.5 SPECT Functional Brain Imaging

1.5.1 So Why SPECT imaging

SPECT imaging has the ability to capture the function of the brain nearly instantaneously due to a high first pass extraction rate, where PET offers an image, averaged over tens of minutes. This allows the function of the brain at time of administration to be analysed some time later. This is particularly useful when an instantaneous measure of the brain activity is required during special circumstances, e.g. an epileptic seizure.

While PET offers superior imaging resolution over SPECT, PET incurs large installation and subsequent running costs, where SPECT remains relatively

inexpensive in terms of imaging equipment and production of radioisotopes for brain imaging. There has also been extensive research into functional brain imaging using SPECT tracers in the dementias, and studies have demonstrated repeatable results that show only slightly lower sensitivity than that of FDG PET, while maintaining a higher specificity. SPECT is widely available in the clinical community, which outweighs its lower sensitivity relative to PET. While the sensitivity of SPECT imaging in very early disease has not yet reached the levels achievable with PET, the prognosis in the majority of dementia cases is unaltered by the progression of disease at time of diagnosis. Functional MRI imaging can be used to indicate functional activations within the brain at a given time, when compared to a baseline measurements (e.g. stimulus versus no stimulus), but does not offer information on the steady state level of perfusion, and as such is not a useful tool for diagnosing functional defects within the brain.

1.5.2 SPECT Imaging Tracers

While ^{99m}Tc offers an almost ideal radioisotope for in-vivo brain imaging using SPECT, the choice of pharmaceutical tracer is less simple. Hexamethylpropylene amine oxime (HMPAO, Ceretec®, GE Healthcare, UK) is the most established and commonly used tracer in brain SPECT perfusion imaging, although more recently and continually increasing, ethyl cysteinate dimer (ECD, Neurolite®, DuPont Pharmaceuticals Ltd., Brussels, Belgium) has come into use as a tracer for rCBF. Both tracers are lipophilic and enter the brain by diffusion across the blood brain barrier, where they are rapidly converted or bound to hydrophilic forms and cannot diffuse back across the barrier, resulting in stable images shortly after administration. Table 1-2 gives a comparison of the main properties of the two tracers.

HMPAO, unlike ECD is very unstable in-vitro, which requires administration with a freshly prepared radiopharmaceutical. The lower level of ECD extraction leads to an underestimation of rCBF, and tends to be more so at high flow levels. HMPAO appears to overestimate low flow slightly, while underestimating areas of high flow. ECD is taken up by the brain and rapidly cleared from the blood resulting in a higher uptake to background ratio than with HMPAO. ECD is rapidly excreted to urine, allowing higher doses to be used than with HMPAO, resulting in higher count levels. ECD has been compared to HMPAO in imaging of age matched Alzheimer's disease

patients with the results reporting an increase in the contrast between affected and unaffected areas with ECD over HMPAO, and similar levels of sensitivity and specificity [van Dyck *et al.*, 1996].

Parameter	Tc-HMPAO	Tc-ECD
1st pass extraction	80%	60-70%
Peak activity	1 min	2 min
Brain uptake (% dose)	5%	5-7%
Washout	12-15% over 2 minutes	12-14% 1st hour; then 6%/hr
Excretion (+48 hrs)	50% liver-gut; 40% kidneys	15% liver-gut; 75% kidneys
Grey-to-white matter ratio	2.5:1	4:1
Imaging time window	Up to 4 hours	Up to 2 hours

Table 1-2. Comparison of the properties of Tc-HMPAO and Tc-ECD radiopharmaceuticals

1.5.3 Technetium 99m – The Ideal Radioisotope

Technetium only exists in radioactive form and has 22 isotopes with atomic mass ranging from 90 to 111. Technetium 99m (^{99m}Tc) is a synthetic radioisotope that has a half-life of 6.01 hours, and is generated as a meta-state isotope from its mother element, Molybdenum-99 (^{99}Mo) that has a half-life of 2.7 days. ^{99m}Tc decays into ^{99}Tc with the emission of characteristic gamma radiation with an energy of 140KeV, and the resulting beta emitting isotope is nearly stable with a half-life of 21,000 years.

^{99m}Tc is the most widely used radioisotope in nuclear medicine because of the combination of its properties. ^{99m}Tc is particularly easy to generate using readily available kits, and its mother element, ^{99}Mo, can be synthetically produced by irradiating Uranium-235 (^{235}U) foil. ^{99}Mo has a half-life of 2.7 days, which allows a single generator to be used for an entire week without the need for excessive activity concentrations. The half-life of ^{99m}Tc is suitably small to allow it to decay quickly in vivo which minimises the dose to the patient while being long enough for metabolic studies. The gamma emission accompanying the decay of ^{99m}Tc is of a high enough energy to pass easily through human tissue while being low enough to be easily stopped by the denser detector. Furthermore, the isomeric transition produces no high-energy gamma rays or x-rays, further reducing subject dose. The isotope also has a very versatile chemical structure allowing it to be used to form tracers in a wide variety of active substances, which allows its use in a wide range of target organisms. Figure 1.6 shows the decay scheme for ^{99}Mo.

This process can be controlled in a $^{99}Mo/^{99}Tc$ generator, where the relatively much shorter half-life of the daughter nuclide allows the generator to be 'milked' every 6-12 hours approximating to 50-75% equilibrium level. Alumina is used in the generators to absorb the ^{99m}Tc, which can then be eluted into a saline solution that is pulled through the stationary Molybdenum to produce Sodium Pertechnetate; a Technetium concentrate that can be used for labelling and administration.

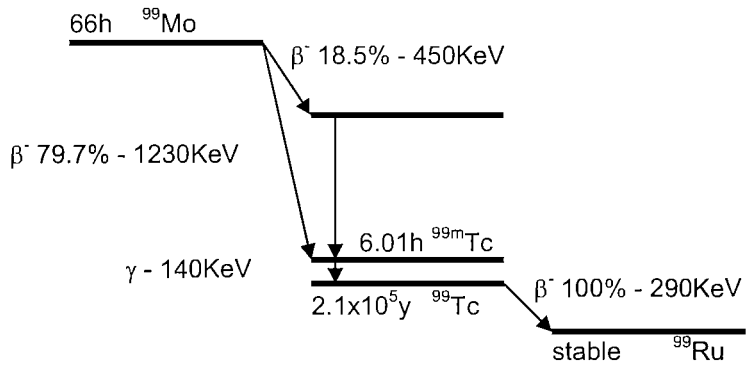

Figure 1.6. ^{99}Mo decay scheme

1.6 *Image Simulation in Dementia Research*

While medical imaging offers us the ability to obtain data that vastly reduces the errors involved in diagnosis, no *in-vivo* analysis methods used are 100% sensitive and specific. With the life changing implications of a misdiagnosis, it is important to assure the accuracy of the results. This is impossible to assess unless a definite diagnosis can be made, and where this is possible it is only so by post-mortem examination. The problem comes from uncertainty regarding the deposition of the administered radiopharmaceutical within the subject, and often a lack of information regarding the subjects' anatomy. The problem is further confounded by inter subject variability and the lack of comparative data (known normal subject images).

Accurate simulation of an imaging system can be used to generate realistic data that allows assessment of the actual performance of any analysis method, be it visual, quantitative or semi-quantitative. This provides three major benefits;

An adaptable and safe method of providing realistic data. The ethical concerns around administering a radioisotope to the patient are a fundamental limitation to the

general use of nuclear medicine techniques, and the major reason for the shortage of large normal data sets. The simulation can be re-performed using different parameters to mimic a range of settings, e.g. between different imaging devices.

A method for validation of analysis methods. Analysis proceeds based on assumptions about the response of the imaging and processing systems. Simulation allows these assumptions to be validated by supplying comparative data and known ground truth. Increasing knowledge of the analysis method increases the certainty in the results obtained.

A greater understanding of the imaging and processing systems. Simulation can be used to test the variability in system responses, including parameters that may be inaccessible when using physical systems. Parameters can be altered to allow a direct theoretical comparison for different system settings and physical parameters, and their effect on the results. This facilitates a method of optimising the imaging and analysis process.

The major shortfall of simulation as a tool is the lack of realism provided by the simulation system. This can arise due to a number of factors, including the digital representation of the object under study, assumptions about the physical processes involved and the uncertainty involved in modelling a random process. Realistic simulation is only commonly available using Monte Carlo codes which usually require a large amount of processing time for a single simulation.

However, as processing power increases through advancements in technology and the event of multi-processor dedicated environments for running simulations, the use of simulations is quickly gaining a large share of imaging research.

Chapter 2 SPECT Functional Brain Imaging, Analysis and Validation

This chapter provides a discussion of single photon emission computed tomography (SPECT) imaging and its application in studies of the human brain. It explores the options for the analysis and study of functional imaging and the associated advantages and disadvantages. Physical and theoretical system modelling and simulation are discussed in view of their use in the analysis of SPECT studies.

2.1 SPECT Imaging of the Brain

SPECT imaging of the human brain is not simply an acquisition problem, but also relies heavily on the methods used to extract useful information from a predominantly noisy measurement. Errors due to erroneous assumptions or inaccurate modelling can have a large effect on analysis results and consequent interpretation.

This section deals with the different methods available for use in the formation of functional images of the human brain from SPECT measurements, and discusses practical implementation issues.

2.1.1 Image Formation

It is necessary to incorporate a set protocol when forming images for comparison, such that the final images have similar characteristics. The following is the general method applied to creating an image from acquired SPECT planar data, and is also applicable to PET imaging, although the reconstruction methods differ slightly.

Spatial filtering is often applied to SPECT imaging during the image formation process, either prior to or after reconstruction. For example, image smoothing is performed by spatially filtering the voxels in an image with a low pass filter based on their detected count rate (or intensity). The process improves the signal to noise ratio by decreasing the magnitude of random variations by averaging counts over many voxels (as count variation is random and Poisson distributed). Common smoothing filters are the Butterworth, Hamming and Gaussian filters. Filter shaping can also be

applied to the smoothing filter to improve certain characteristics of original image, and a trade-off exists for optimal filter design. The Metz and Wiener filters are commonly used in this process.

Inter-subject variation is a particular problem with SPECT brain imaging, and it is essential that brain images are reoriented to limit the risk of error due to misalignment of internal structures. This is particularly important when performing automated quantitative comparison. While complex automatic methods exist for image reorientation for quantitative analysis (see section 2.1.2), simple individual re-orientation is usually sufficient for qualitative analysis. The data is usually reoriented into a standard tomographic view such that it aligns with some predetermined standard, most commonly along the line connecting the anterior and posterior commissure, the AC-PC line. This is often carried out manually by describing a set of vectors based on the perceived human anatomy, and transforming the entire image based upon this.

Count normalisation is usually carried out as the last step prior to analysis. It is used to scale the average activity level in the brain to correct for overall haemodynamic differences between subjects.

2.1.2 Image Reconstruction

Image reconstruction aims to solve the problem of obtaining an accurate estimate of the original source activity from acquired data, while incorporating knowledge of the physical processes of the imaging system. There are several methods used for reconstruction, each with advantages and disadvantages. These can be broadly divided into two groups; statistical and non-statistical reconstruction methods. An in-depth study of all available methods is itself an active research area [Brambilla *et al.*, 2005, Cot *et al.*, 2005, Baete *et al.*, 2004, Yokoi *et al.*, 2002, Vandenberghe *et al.*, 2001], and beyond the scope of this thesis.

The reconstruction problem in its simplest form aims to estimate the amount of activity in image voxel i, λ_i, from the acquired projections, p_j. p_j can be expressed as an expected number of counts ($\tilde{p}_j$) plus a noise term (n_j). The expected response is a

function of λ_i and the unknown transition matrix c_{ij}, which relates the activity at each voxel to each bin in the acquired projection (or some other measured variable);

$$p_j = \tilde{p}_j + n_j = \sum_i c_{ij}\lambda_i + n_j \qquad \textbf{(2.1)}$$

Where i is the object voxel, and j is the projection number. Thus the reconstruction problem is straightforward; solve the above for λ_i given p_j and c_{ij}. It is clear from 2.1 that the determination of λ_i is dependent on the accuracy of the transition matrix. It is difficult to solve the reconstruction problem directly for large data sets, owing to the large number of simultaneous variables. Iterative methods are particularly suited to this problem, where a solution is updated each iteration, based on forward-back projection.

A major limitation of the reconstruction methods is the amount of storage required for the transition matrix, given that it contains a mapping between each pixel in the source distribution and each bin in each projection. The amount of space required can be reduced by reducing the resolution of the input and output images. The reconstruction process requires a forward projector for providing the expected response, and accuracy is dependent largely on these components. The computational power required for accurate modelling of all physical effects is another limitation of the reconstruction process.

2.1.2.1 Filtered Back Projection (FBP)

One of the most common and easily implemented methods of reconstruction is filtered back projection (FBP). Each planar image is projected backwards using its original angular displacement through the 3D tomograph space. The individual back projections are then summed to create a three dimensional tomograph. FBP relies on the assumption that a detected event originated along the angle of projection i.e. the collimator response is perfect. Thus pre-filtering is essential, and this is commonly carried out using a ramp filter, although the high pass nature of the filter results in amplification of the high frequency noise in the image. Post filtering is also required to remove the unsharpness introduced by the back projection. The Wiener filter is commonly used in FBP of SPECT images, as it contains a combination of a ramp filter and a low pass filter.

The FBP method is the most widely used method of reconstruction in brain SPECT imaging, and is relatively quick to perform on modern computers. Thus FBP is particularly suited to routine analysis. However, FBP introduces variation in image resolution at points further from the detectors centre of the rotation, and also introduces a streak artefact.

2.1.2.2 3D Algebraic Reconstruction Technique (ART)

ART is an example on non-statistical reconstruction method that uses an iterative approach to estimate the original source distribution λ. This is achieved by updating the estimate based on the difference between the measured true distribution, at_j, and an estimated (usually simulated) distribution as_j. These parameters are effectively measured and simulated activity distributions, and equation 2.2. shows a formula for three-dimensional reconstruction using ART;

$$\lambda_i^{n+1} = \lambda_i^n + r.\lambda_{ij}^n \frac{\left(at_j - as_j\right)}{at_j} \qquad \textbf{(2.2)}$$

Where r is a relaxation parameter (typically 0.25), n is the iteration number, i is the voxel in the forward-back projection, and j is the estimated voxel number. The process updates the forward projection parameters for every iteration; this again requires an accurate forward-projector.

ART is not often used for reconstruction as it is usually performs worse that statistical methods for the same number of iterations. However, ART is simple to understand and easy to implement quickly.

2.1.2.3 Statistical Image Reconstruction

Practical iterative reconstruction methods in PET and SPECT are usually based around expectation maximisation (EM), which involves an iterative statistical approach, where the estimator converges to a result for the source distribution that makes the acquired data most likely, based on Poisson models for the data. This is usually carried out by first estimating an initial source distribution (the parameters) for the acquired image data. The result is then simulated using this source distribution, and the difference is used to adjust the parameters before repeating the

process. A method based on obtaining a maximum likelihood distribution is given by the MLEM algorithm, as shown in 2.3.

$$\tilde{\lambda}_i^{k+1} = \frac{\tilde{\lambda}_i^k}{\sum_j c_{ij}} \sum_j \left(\frac{c_{ij} p_j}{\sum_i c_{ij} \tilde{\lambda}_i^k} \right) \quad \textbf{(2.3)}$$

The main advantage of using statistical methods is the accuracy of the results obtained, as an accurate system model can be incorporated into the forward projection. However, the method takes a considerable length of time to achieve a useful number of iterations when using accurate models, as each iteration requires the data be re-simulated. There are variations based around EM such as the use of ordered subsets of data (OSEM) that improve on the efficiency of the estimator by using subsets of the original projection data. This allows reconstruction time to be substantially reduced as only a small number of forward projections have to be simulated each iteration. Efficiency improving techniques produce only a very small reduction in the accuracy of the reconstruction process. Thus this form of reconstruction is best suited to situations where high quality and accuracy is essential, high computer power is available, and/or time is not a major constraint, such as in a typical research environment.

2.1.3 Image Standardisation

Image standardisation is a prerequisite to quantitative inter or intra-subject comparison in functional brain imaging. The main aim of image standardisations is to transform a reconstructed image into a predefined template to facilitate comparison. In brain SPECT, the standardisation process is used to transform the subject image to the template using a spatial transformation and count normalisation.

2.1.3.1 An Essential Tool

In brain SPECT imaging, it is desirable to quantify the neuronal activity in a particular region of the brain such that its level can be compared to known normal levels to diagnose abnormalities. It is usually difficult to find the exact correspondence between regions on two independent images, due to anatomical and physiological variations that occur naturally between subjects. The result without standardisation is a level of subjectivity in the measured parameter, leading to difficult and inaccurate

comparison. The template represents a reference space in which images can be compared effectively. This also allows one or many images to be compared with many other images, which increases the statistical test power. There are many methods that can be used to transform an image into a standard reference space, including manual and automatic methods. Manual methods are time-consuming and suffer from poor reproducibility, so the emphasis is on accurate automatic methods as the gold standard in image standardisation.

2.1.3.2 Spatial Normalisation

The ultimate aim of spatial normalisation or registration is to establish an exact point-to-point correspondence between the voxels of two images, making direct comparison possible. The main operation of most automatic spatial normalisation techniques (non-label based) follows. The algorithm usually attempts to fit an image to a template by adjusting a spatial image transformation until some predefined criteria is met that provides the optimal fit (given the limitations). A difference operator has to be defined in a quantifiable way such that we reach a maximum similarity (or minimum cost) when the images are perfectly aligned. The definition of the similarity measure is usually study based, and can be based on homologous spatial structures, landmarks in the images or overall distribution of activity [Hutton *et al.*, 2002].

Extrinsic markers can be used to aid in normalisation tasks. Their use is limited in brain studies and rarely reported due to the presence of large inter-subject variability, and the inability to attach the markers to the brain itself. Anatomical landmarks, as with other landmarks or features (such as surfaces) that can be extracted from the images, are useful but reserved primarily for high-resolution anatomical imaging where a structure can be accurately defined. The majority of SPECT based spatial normalisation methods rely upon measures of the voxel intensities and the transformation is based upon the distribution of these values.

Several different methods of image registration have been suggested in SPECT imaging, including; finding a centre of mass and the orientation of the objects, minimising intensity differences between objects and maximising mutual information and cross correlation [Hutton *et al.*, 2002]. More recent methods involve the use of the voxel intensity histogram to generate similarity measures between images, which

work on the principle that there should be a correlation between groups of voxels that have similar values.

There are several different types of transformation that can be applied to the original image to provide a solution for the registration problem, broadly divided into linear and non-linear transformations. The number of parameters required for the transformation increases with the level of complexity. Rigid body transformation applies a six-parameter linear transformation consisting of a rotation and a translation along each of the three primary axes, and assumes that the original image sizes are the same, as is the case with intra-subject registration. Further parameters can be included in the transformation to represent either global or anisotropic scaling, with a parameter required for each axis.

An affine transformation is as described above with the inclusion of a shear parameter for each of the primary axes, and Figure 2.1 illustrates the effect of each component part separately. A useful feature of these linear transforms is that they can be operated upon using matrix algebra, allowing transformations to be precisely decomposed, combined, operated upon and reversed. The twelve- parameter affine transformation is capable of transforming one image to a template with a moderate accuracy, but lacks the ability to take into account local variations in anatomy, which can be an important feature when performing quantitative analysis.

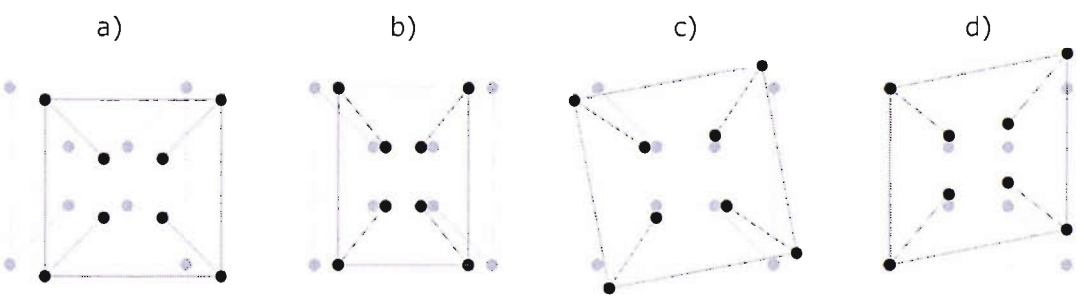

Figure 2.1. Examples of the four component parts of the affine transformation, where the grey image represents the original image and the black image represents the transformed image; a) translation in x and y dimensions, b) scaling in the x dimension, c) a rotation about the z dimension and d) a shear in the y dimension. Note that lines remain parallel after applying the shear.

Warping is a collective term used to define a non-linear operation on a subject image, used to take account of local anatomical variations between subjects. It is necessary to include well-chosen constraints when performing image warping, as severe

warping can cause a loss of underlying data. Thus the warping process is used to correct only gross differences between subjects. Non-linear global approaches include the use of constrained fields that apply a transformation to each voxel individually using an underlying basis function or describable model.

Image deformation can be carried out locally by progressive coarse to fine sampling of a region, and the application of a (usually rigid) transformation for each iteration [Slomka *et al.*, 2001]. Further parameters allow the transformation parameters to be selected based on a model of the expected response. For example, SPM99 uses a linear combination of discrete cosine transforms (DCT) as the basis functions to create the deformation field, applied separately along the three orthogonal axes. The automatic iterative algorithm then attempts to estimate the best fit parameters using a Bayesian framework. Section 6.3.3 describes examples for forward and reverse transforms for both the affine type and the DCT method. The more complex a transformation becomes, the more parameters are required to describe it and the more time required to compute it. As the number of parameters increase, so too does the noise in the parameter estimates. Furthermore, transformation introduces interpolation errors, and iterative approaches can propagate and increase these errors when sampling and interpolating more that once.

All registration methods require that the cerebrum be segmented from extraneous activity prior to registration, and all of the effects are confounded when attempting to spatially transform an abnormal image to a template. The effect of abnormal perfusion on registration has been evaluated for brain SPECT imaging [Radau *et al.*, 2001], and reported to have only a small effect on quantification.

2.1.3.3 Count Normalisation

For inter-subject comparison, it is also necessary to transform the image voxel intensities prior to performing analysis, to account for global differences in blood flow. This ensures that the voxel intensities in both (groups of) images are similar. The spatial normalisation methods are generally unaffected by differences in the mean image counts, and can therefore be performed without the need for count normalisation, although it is generally essential for image analysis or comparison. Methods for intensity normalisation adjust the counts globally depending on the ratio

between some function of counts in the images. This could be the mean count level in a particular region, cortex, structure or the whole brain. The most commonly used methods in SPECT analysis are normalisation to the cerebellum, and this has been shown to be a reliable reference region [Soonawala *et al.*, 2002], and validated for analysis of AD using SPECT [Pickut *et al.*, 1999]. Iterative approaches can be used to account for abnormal voxels by masking and normalising to the mean of the within limit voxels.

Filtering is usually also a necessary step in the standardisation procedure, carried out (usually) by convolving the data with a low-pass three dimensional filter kernel to reduce the effect of noise. Low-pass filtering is effective as noise contains higher spatial frequencies than the variation in rCBF signal. Filtering also provides a method of reducing the variation caused by errors in the registration procedure or to reduce the signal to noise ratio prior to registration. Filtering can also be used to condition data for statistical analysis. For example, SPM99 uses a Gaussian smoothing kernel such that the data more readily conforms to the Gaussian field theory, making inference based upon it more powerful.

2.1.4 Factors Affecting Image Interpretation and Analysis

While some of the factors that influence the quality of the image data are physically well defined and easily corrected, others contain a high level of uncertainty. Results are heavily influenced by the physics of the imaging system, and the ultimate goal is to accurately correct the image for all of the degrading physical effects. However, corrections provide at best, the most likely solution based on the probabilistic behaviour of the underlying system, and can significantly influence results in both qualitative and quantitative analysis.

Radioisotope decay results in a reduction in the amount of decays occurring over time, with a rate proportional to the isotope half-life. This is an example of a well defined physical process and a simple and accurate correction is achievable by artificially increasing (or decreasing) the acquired count level in each planar image. The level is based on the time of acquisition and the original isotope concentration.

Statistical noise causes uncertainty in the emission and detection of photons. The number of decays for any radioactive source in a given time interval is Poisson distributed. Therefore subsequent time periods are unlikely to yield the same number of detected events. For Poisson variables, the variance is equal to the number of events, $\sigma^2 = \lambda$, and the SD, $\sigma = \sqrt{\lambda}$. Thus the noise is related to the square root of the mean number of detected events, and $\frac{\sigma}{\lambda}$ approaches zero as $\lambda \to \infty$. For example, a mean detected count of 1×10^6 has SD = *0.001*, whereas a mean detected count rate of 1000 has SD of *0.032*. It is therefore desirable to detect as many events as possible to minimise image noise, while maintaining a safe operating environment. Obtaining more counts is only possible by increasing the activity level (and dose) or by imaging for a longer period, which increases the probability of movement. It is not possible to explicitly correct for imaging noise as the variable is random, but a model can be incorporated into reconstruction algorithms to attempt to reduce its contribution.

Attenuation correction is used to correct for difference in counts in an image caused by photons being stopped or scattered on their path to the detector. The correction is performed by applying an attenuation map to correct the counts in each voxel within an image. Ideally, exact representation of the source object in terms of materials should be available, and the attenuation at each voxel for each projection can be accurately calculated. This is often not the case as anatomical information is not usually available. The result is an over- or under-adjustment when the attenuation map is not accurate.

For simplicity, the head is often assumed to be a uniform cylinder, although methods of acquiring more accurate attenuation maps are available, such as generating a map from the observed counts in back projection [Fleming *et al.*, 2002]. A CT transmission image can be used to provide accurate measurements of the Hounsfield units, which can be converted to SPECT attenuation coefficients [Fleming, 1989]. This can be acquired at the time of SPECT imaging using a low power CT scanner. The same method can be applied using dual isotope imaging to obtain simultaneous emission and transmission images [Bailey *et al.*, 1987]. The advantages in using these methods are that attenuation measurements are reasonably accurate at the cost of

a small increase in dose to the subject. Another method has been suggested [Stodilka *et al.*, 2000] using a segmented brain atlas, and registering subject images to a Monte Carlo simulation using the atlas. The original atlas could then be used to infer an attenuation coefficient based on the location within the atlas. The study reported a sufficient accuracy for the method, and a 92% correlation with transmission methods. The same method was used to compare six transmission and transmission-less attenuation correction methods [Zaidi *et al.*], and reported good correlation with other methods. Attenuation correction can also be included as part of the reconstruction process when using statistical methods, by adjusting the algorithm to include the object shape [Beekman *et al.*, 1997], giving the most likely estimate of the original source activity in the presence of the attenuating material.

Attenuation correction factors are often generated using the Chang method [Chang, 1978], which suggests calculating the attenuation factor for each voxel, $C(x,y)$, based on the following formula.

$$C(x,y)=\left[\frac{1}{M}\sum_{i=0}^{M} e^{-\mu l(x,y,\theta_i)}\right]^{-1} \qquad \textbf{(2.4)}$$

Where $l(x,y,\theta_i)$ is the distance a photon has to travel through the attenuating material in directions x and y and projection angle θ_i, i is the projection number, M is the number of projections and μ is the attenuation coefficient. The result is an average attenuation over all projections, and is easy to calculate, allowing a simple attenuation correction to be carried out quickly. The standard Chang attenuation correction method provides only an approximation, and accurate attenuation correction can be achieved by iteratively forward-back projecting the image and recalculating the attenuation coefficients.

Normal, and to some degree abnormal anatomical and physiological variation is well characterised in SPECT imaging within the brain for a given radiopharmaceutical. However, tracer uptake in extraneous regions, particularly the sinuses and fatty facial tissue, is highly variable in both inter- and intra-subject studies, and dependent on a large number of factors. It is difficult to characterise or predict this effect and it is necessary to remove this confounding effect. This can be achieved by manually masking out the areas on reconstructed images on a tomograph, and attempts have

also been made to automate this process through the inclusion of heuristic data [Radau *et al.*, 2001]. This is still however highly subjective and can introduce variation that is difficult to detect and correct.

Fundamental to qualitative analysis is the choice of output display filter used. The properties of the filter are selected to attempt to reduce the noise in the image while preserving image features. The filter selection is crucial to the identification of image abnormalities that are characteristic of the dementing process. Too much smoothing results in the boundaries between regions disappearing and a loss of anatomical information, too little smoothing results in noisy images that are difficult to interpret, and too sharp a filter cut-off introduces ringing artefacts that could be misinterpreted as abnormal perfusion.

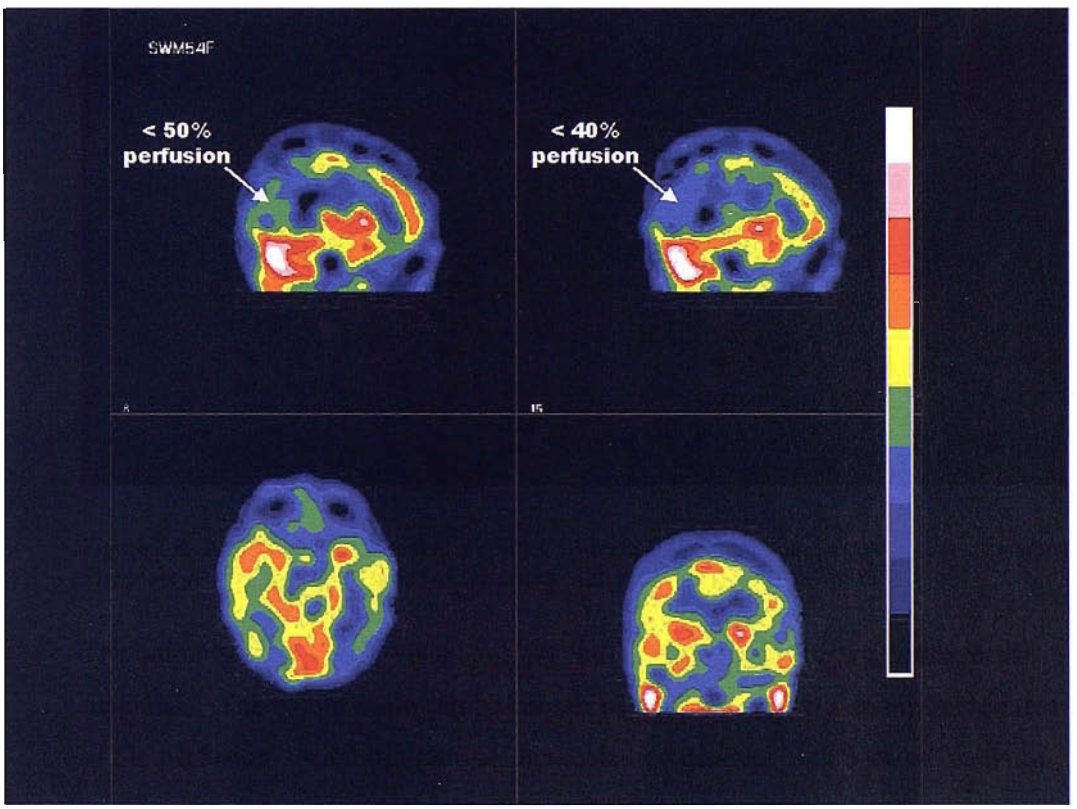

Figure 2.2. An example abnormal rCBF SPECT image of the brain using a quantitative colour scale. The scale clearly indicates regions of the cortex with abnormally low perfusion.

The colour scale used for visual analysis has a large impact on the consequent diagnosis. The colour scale can be chosen to effectively give a quantifiable measure of the perfusion, by splitting the colour scale into discrete high contrast intervals representing the perfusion levels. Figure 2.2 shows one such quantitative colour scale

where each division represents a 10% interval relative to the count in the reference region.

2.1.5 The Effect of Age

There is conflicting published work available in the literature on the effect of ageing on SPECT studies. Furthermore, the reported location and extent of the effect varies considerably between the reports.

A PET study on healthy volunteers suggested that the ageing effect could be explained and corrected for by partial volumes and atrophy [Meltzer *et al.*, 2000]; covariance analysis has demonstrated that the effect of age on rCBF was greater than the effect of atrophy [Imran *et al.*, 1999b]. These results suggest that the ageing process is a combination of many factors. Thus an analysis of uncorrected data can be performed assuming that the overall effect, be it atrophy, age or other, is characterised by a heterogeneous and widespread reduction in rCBF. The level of reduction is thus correlated with age. The age effect on rCBF in healthy subjects has been shown to be heterogeneous and most significant in the frontal and temporal cortex [Van Laere *et al.*, 2001].

Age has also been demonstrated to have a variable effect on the progression of AD [Hanyu *et al.*, 2003]. The pre cuneus and posterior cingulate are known to be preserved in late onset AD [Salmon *et al.*, 2000, Kemp *et al.*, 2003]. If this is accompanied by normal ageing, then it is important to be able to distinguish between the two effects to maintain maximum specificity.

The homogeneous effect of age was experimentally assessed to attempt to quantify its effect in normal data. A regression analysis was performed on the normalised global rCBF value using two different models, and assuming no gender differences in rCBF pattern. A linear model was used to take account of a linear decline in brain function, and an exponential model was used to take into account an accelerated decline in brain function with ageing. Regression analysis revealed that the linear fit was significantly in error. The model indicated an overall decrease in rCBF of 15% over the entire age range (40-96 yrs), with a small and approximately linear relationship up

to 75yrs. The relationship is then used to correct the global count value for each control subject.

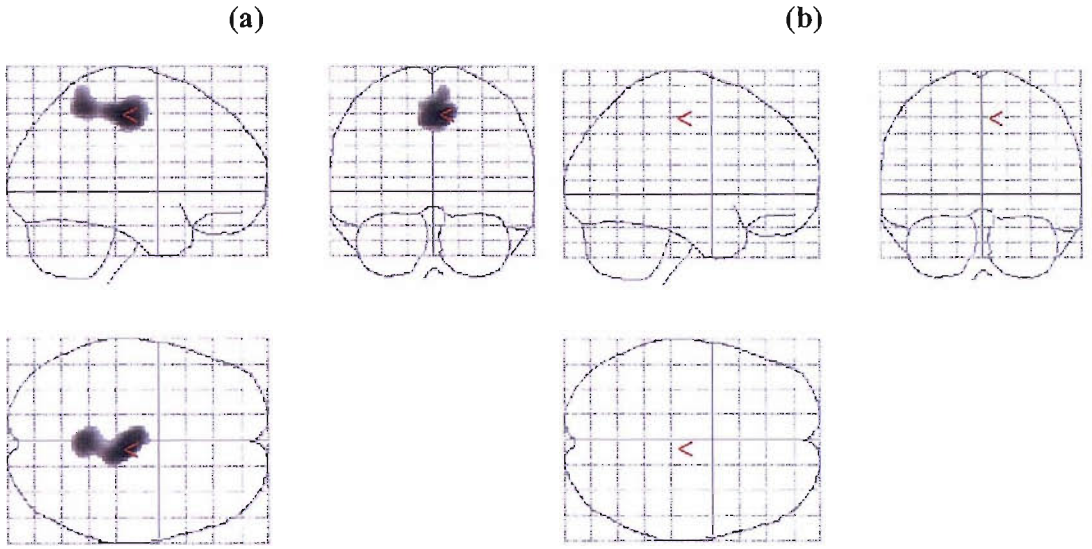

Figure 2.3. The glass brain output from SPM showing clusters of significant hypoperfusion. Results are for a post 80 year old subject (a) without and (b) with the inclusion of a correction for age, demonstrating a reduction in the significance of abnormality.

It was found that the method created a reduction in variance of the normal database, and effectively reduced the effect of the natural age-related decline. Leave one out analysis of the corrected group indicated that subjects in the age group 80-90 years presented normally with the inclusion of age correction, where previously they presented abnormally. Figure 2.3 shows an example of a post 80 year old subject analysed using SPM99 with and without the inclusion of age correction.

2.2 Quantitative SPECT Image Analysis Techniques

This section deals with the most widely used methods for quantitative analysis in brain SPECT imaging.

2.2.1 Brain Registration and Analysis of SPECT Studies (BRASS)

Brain registration and analysis of SPECT studies (BRASS, Nuclear Diagnostics, Hägersted, Sweden), is a commercially available tool specifically designed for routine

clinical analysis of both SPECT and PET images, and has been developed as an addition to the HERMES workstation (Nuclear Diagnostics, Stockholm, Sweden).

The method is based on a voxel-wise statistical comparison of spatially standardised images with a pre-compiled normal database. Registration is performed using an iterative approach in an attempt to maximise a similarity measurement (normalised mutual information, or other), using sub-sampling to improve efficiency. The images are by default registered to the standard spaced described by Talairach and Tournoux [Talairach and Tournoux, 1988].

Analysis is carried out using a standard statistical test, such as the t-test, on either a voxel by voxel or regional basis. Bonferroni correction is applied to the results to correct for multiple comparisons. The software also includes a labelled stereotactic template for localisation, and supports the creation and import of databases based on external templates. Clusters of voxels that meet size and standard deviation thresholds can be automatically reported by the software, and displayed on the atlas along with volume statistics.

BRASS has been reported to be capable of discriminating Alzheimer's dementia from normal controls, using the parietal lobe to cerebellum count ratio as a diagnostic discriminator, and have shown sensitivity and specificity of 91% and 94% respectively [Slomka *et al.*, 2001]. Another study [Van Laere *et al.*, 2002b] used the BRASS software to analyse SPECT studies of patients with traumatic brain injury (TBI), moderate to severe cognitive impairment of different types and healthy controls. The study reported BRASS to be more accurate than SPM99 and visual approaches. Results reported in Chapter 5 demonstrate contradictory findings, and suggest that both methods produce identical results when analysis parameters are well controlled.

The incorporation of both voxel-wise and regional analysis in BRASS overcomes the problems associated with poor sensitivity to small defects in ROI analysis and over-sensitivity to registration errors in voxel-wise analysis. This also results in an increase in the amount of effort and time required to analyse the data. The commercial nature of the software reduces the availability of the package, due to cost considerations.

2.2.2 Three Dimensional Stereotactic Surface Projection (3D-SSP)

Three-dimensional stereotactic surface projection (3D-SSP) is a fully automatic method of data analysis, originally developed at the University of Michigan, USA for use as a stereotactic atlas of the human brain to aid in visual interpretation of PET functional brain images [Minoshima *et al.*, 1994]. The method was later updated and applied to the study of PET images in AD [Minoshima *et al.*, 1995].

Spatial normalisation is carried out using automatic registration involving rotations, linear scaling and non-linear warping into a standard stereotactic space. Cortical perfusion is indicated through the use of predetermined surface pixels based on the template. Each surface pixel is assigned a three-dimensional vector perpendicular to the surface, and the pixel value obtained by searching for the maximum along the vector up to the depth of the grey matter cortex (approximately 13.5mm), and projecting this value onto the surface pixel. Comparison is through statistical methods using a normal control database and by averaging Z scores over cerebral cortices. The use of such a measurement reduces the effect of partial volumes, as well as reducing registration errors and anatomical variation. Resolution is limited and the method offers no information about the white matter of the brain.

[Hirsch *et al.*, 1997] incorporated the method as an observer-independent diagnosis tool for Alzheimer's disease using ECD SPECT imaging, reporting significant correlation between cognitive dysfunction and decreases in rCBF. The method has also been reported to produce significant results in the study of age affect in AD [Hanyu *et al.*, 2003] and the distribution of rCBF in small vessel vascular disease [Yoshikawa *et al.*, 2003b].

2.2.3 Three Dimensional Fractal Analysis (3D-FA)

Three-dimensional fractal analysis 3D-FA is a relatively newly discovered method of image analysis, based on a measurement of the scalability of the image. rCBF distribution is statistically scale invariant within limits, and can be characterised by a non-integer dimension termed the fractal dimension, which represents the heterogeneity of a data set as a single value. Variable patterns of abnormality increase

the heterogeneity of the underlying rCBF data, resulting in increased fractal dimensions, with larger fractal dimensions representing larger abnormalities [Nagao *et al.*, 2001].

The fractal dimension is calculated by taking a threshold value (percentage) and the number of voxels above a threshold level as variables in the fractal geometry relationship shown below.

$$M(a) = k.a^{-D} \tag{2.5}$$

Which expresses the relationship between a measure, M, and the scale, a. k is a scaling constant and D represents the fractal dimension. a is the threshold level and the measure, $M(a)$, is taken as the total number of voxels in the defined region. The equation can be solved for D by taking natural logarithms and then performing linear regression, with the gradient of the line representing the fractal dimension. The fractal dimension is highly correlated with the original data for the range of threshold levels representing 35-50% of the maximum value and significant differences have been reported between normal and demented groups [Nagao *et al.*, 2001, Yoshikawa *et al.*, 2003a]. The method can also be applied regionally by image masking.

The method is simple to incorporate and requires no image normalisation making it applicable to routine clinical use. 3D-FA may be a useful observer-independent method for objectively identifying the progression of dementia and may also offer an aid in the differential diagnosis of dementia. However there is currently very little published work on the incorporation of 3D-FA, and more complex studies on regionally specific fractal dimensions are required.

2.2.4 Principal Component Analysis (PCA)

The PCA technique is a well-known method for reducing the dimensionality of a data set, such as functional images of the brain. The method allows data to be expressed as a set of variance images representing decreasing levels of importance, which illustrate different levels of correlation within a group of images. That is each variance image explains a decreasing percentage of the data set variance. Statistical tests can be performed by computing a best fit image for the subject from a subset of the principal components, and comparing this with the control group standard deviation map.

Cross validation of the method has been reported to be 100% sensitive in discriminating Alzheimer's disease and 92% sensitive in identifying infarcts [Houston *et al.*, 1994]. The method was also used to study the effects of age and gender on rCBF and reported a significant decline with increasing age [Pagani *et al.*, 2002], and has also been used in depression studies using SPECT [Pagani *et al.*, 2004].

2.2.5 *Statistical Parametric Mapping (SPM)*

Statistical Parametric Mapping (SPM, Wellcome department of cognitive neurology, London) is designed for the analysis of brain imaging data sequences, by statistically assessing spatially registered images and time series on a voxel by voxel basis. The software is also applicable to the analysis of SPECT images, where the data sequence is a set of normal data.

Images are spatially normalised to a standard template space (Talairach or MNI), using linear and/or non-linear transformations. Gaussian smoothing is also performed to reduce noise and condition the data for analysis. Standard univariate statistical tests can then be performed on a voxel by voxel basis, comparing images and groups of images. The methods used involve parameter estimation to incorporate error in the system (the general linear model), and inference is based on the Gaussian field theory. Significance values can be obtained for voxels and clusters of voxels. A multiple comparisons correction is also applied. A full discussion of the theory of SPM can be found in [Frackowiak, 1997].

SPM is freely available in the public domain via the Internet, and is strongly supported by its authors and the neuroimaging community. There is also an extensive database of custom written third party additions to the standard software. The software offers extensive voxel-wise comparison, and as such lends itself to most forms of individual or group comparison.

The literature on the implementation of SPM in brain SPECT imaging is extensive, and outnumbers that for all of the other quantitative analysis methods described here. SPM99 analysis was compared to BRASS and a semi-quantitative VOI analysis for assessing ECD SPECT images, and has been reported to be overall less diagnostically accurate than other methods, as defined by an ROC analysis [Van Laere *et al.*,

2002b]. However, SPM had been reported to be sensitive enough for use in imaging AD [Varrone *et al.*, 2002, Kemp *et al.*, 2003, Salmon *et al.*, 2000], in Parkinson's disease [Ito *et al.*, 1999] and head injury [Stamatakis *et al.*, 2002]. SPM has also been used in the study of rCBF in normal subjects [Van Laere *et al.*, 2001, Hyun *et al.*, 2001]. At the time of writing, SPM99 was the most widely used version of SPM in HMAPO SPECT, and has been rigorously evaluated within the research community. However, very few validation studies actually exist [Stamatakis *et al.*, 1999, Van Laere *et al.*, 2002a].

2.2.6 Other Quantitative Analysis Tools

Many other methods of quantitative analysis based on specific methods have been suggested. Most are based on automatic image registration and standardisation and subsequent custom statistical based analysis [Imran *et al.*, 1999a, Imran *et al.*, 1999b, Ito *et al.*, 1996] to detect statistically abnormal perfusion levels. Other techniques have been suggested and validated based on more general region of interest (ROI) and volume of interest (VOI) approaches [Takeuchi *et al.*, 2002]. A more complicated method has been suggested based upon multiple measurements [Pagani *et al.*, 2003], and reported that a combination of five factors produced 100% accuracy in discriminating FLD from normal controls, 97% accuracy in AD from normal controls and 99% accuracy in discriminating between the AD and FLD groups. These methods however, all lack comprehensive assessment.

2.3 Physical Phantoms

Physical phantoms are useful tools in the measurement and analysis of the physical parameters of SPECT systems. The results can be considered as, or compared to a gold standard thus establishing a protocol for common performance measurement on different systems. The choice of phantom is selected based on the application, for example a standard cylindrical water filled phantom (see section 2.3.2) can be used to measure the point spread function of a source within an attenuating material. Physical phantoms offer a method of image acquisition that greatly simplifies the experimental considerations.

The major shortfall of physical phantoms is the difficulty associated with engineering complex or realistic physical phantoms. Nearly all require filling with radioactive liquid to represent the activity levels, which makes variable or heterogeneous activity levels impossible. Thus physical phantoms are particularly suited to quality control and quality assurance, where the source object is usually arbitrary and does not represent any real world equivalent. The following sections describe some commonly used physical phantoms.

2.3.1 The Williams Phantom

The Williams phantom is not particularly useful in brain studies, although it has use in quantification of system parameters. The Williams phantom can be used to perform qualitative and quantitative measurements of imaged data. The phantom has a background activity level and four hot and cold spots of different sizes. The activity is encased in Perspex and represents a uniform activity level, with hot spots of double the activity level where there are deeper holes in the Perspex, or of no activity in areas of Perspex only. Section 3.5.1 contains a detailed description of the Williams phantom.

2.3.2 The Cylindrical Phantom

While this is not a dedicated brain phantom, it has particular importance in brain imaging experiments. The cylindrical phantom is a cylinder with a compartment at the centre in which an activity can be placed. The volume surrounding the phantom can be filled with water (or activity) to act as an attenuating material, which is approximately equivalent to the main constituency of the brain. If the diameter of the phantom is selected to be approximately equal to the diameter of the head (around 200 mm), and filled with water, the object can be used as a crude approximation to the human head. This allows an approximate PSF measurement to be made.

2.3.3 The Hoffman Brain Phantom

The Hoffman brain phantom [Hoffman *et al.*, 1991] was primarily developed to offer a method of physically imaging an activity distribution that was similar to normal PET and SPECT images of the brain. The phantom consists of three sections that can

be used to contain different ratios of activity; using a liquid for the white matter, thin layer of Lucite for the cortex and nothing for CSF structures, without the inclusion of the cerebellum. The levels can be selected to give a 5-1-0 ratio of activity to mimic normal distribution, allowing cross-comparison with ideal data and quantitative evaluation of errors. The phantom is routinely used in research environments and represents the only commercially available dedicated brain PET/SPECT phantom.

2.3.4 The Inkjet Phantom

The paper phantom was first suggested by [Larsson *et al.*, 2000] for use as an attenuation and scatter free physical distribution for use in SPECT imaging. The method was modified by [Van Laere *et al.*, 2002a] to closer represent real images.

The general principle is to create a sub-resolution, digital discrete representation of the required activity distribution, as a set of stacked planes. The discrete representation of each plane is then printed to a sheet of paper using radioactive ink in a specially modified printer, with activity proportional to the grey scale. The images can then be stacked using an arbitrary spacing material, e.g. air or plastic to provide a variable level of attenuation.

The phantom is configurable to any arbitrary activity distribution, allowing complexity to be easily managed. A major advantage is the ability to perform physical experiments using digital data, allowing direct comparison to simulation results. The method has been shown to produce very high reproducibility (0.7%) and uniformity (1.2%) of the printed paper sections.

2.4 Simulation in HMPAO Brain SPECT

2.4.1 Introduction to Simulation

Simulation systems offer the user a method of synthetically recreating a physical process, effectively allowing testing of many aspects of the imaging and analysis procedure in a reproducible manner with no specialist hardware. This gives two distinct advantages; 1) the process can be studied in scenarios that would usually be unfeasible to perform using the physical process, offering the ability to assess

performance without the associated effort of running such a system, and 2) parameters that would be impossible to measure physically can be monitored and analysed, allowing a better understanding of the cause of physical effects.

Simulation can be performed on a number of levels, with each level requiring more complicated modelling of real world characteristics, usually accompanied by fewer assumptions and more variables. The top level would assume total modelling of all aspects of the physical system. In nuclear medicine imaging this would involve modelling of the tracer decay, and individual photon transport and interactions with the matter and the gamma camera. The camera would also be simulated, with simulated interactions in the collimator, scintillation crystal, and subsequent detection by the PMT's and binning. Complete simulation would be infinitely complicated and time consuming to perform. Making assumptions based on observed real world data is essential to reduce the complexity of the simulation system. System complexity can also be reduced by the inclusion of measured data in the simulation system. So called analytical simulation systems, and described in more detail in section 2.4.2.

It's clear that the validity of the simulated data is entirely dependent on the model used for the simulation. Accurate modelling of the decay, transport and acquisition process can offer invaluable tools for the creation of realistic data, although run times currently constrain this to research environments. Time constraints can be overcome through the inclusion of model generalisation, at the cost of reduced accuracy.

2.4.2 Analytical Simulation Methods

Analytical system modelling and generalisation has been successfully implemented to achieve huge improvements in simulation time over Monte Carlo methods. On a microscopic scale, radioactive decay is inherently stochastic and the behaviour of individual photons is unpredictable. However, macroscopically, the behaviour becomes increasingly predictable, and distribution of detected photons from a single point source of activity (the point spread function or PSF) approximates a characteristic distribution. The generalisation can be made that the whole gamma camera response can be described by a model (e.g. a Gaussian distribution) on a per point source basis, and the source distribution could be described as a collection of

individual point sources. These methods are, however, sensitive to the accuracy of the model used.

These methods can also be extended to the simulation of abnormal images. Abnormal image simulation is not a new technique for the validation of the performance of analysis methods in functional brain imaging. Artificial lesion simulation has been employed to test the sensitivity of SPM96 [Stamatakis *et al.*, 1999], to determine the thresholds for visual detection of cerebellar abnormalities in SPECT images [Stapleton *et al.*, 1994], and to evaluate the effect on automatic registration [Radau *et al.*, 2001]. A more complicated method described in [Grova *et al.*, 2003] used quantitatively measured perfusion data to perform simulation of medial temporal lobe epilepsy (MTLE). To our knowledge, this is the only method that uses quantitatively acquired functional distributions and accurate anatomical support data for the production of pathological simulated images.

Analytical simulation systems use system generalisation to simplify the process of simulating the image, vastly reducing run times at the cost of a decrease in accuracy. A suggested method uses a summation of mathematical models for primary and scattered photon distribution based on a library of PSF measurements to create the simulated PSF of the camera [Fleming and Simpson, 1994]. Two more general methods described in [Ma *et al.*, 1993] and [Yokoi *et al.*, 2002] used approximation of Gaussian functions to model the PSF, and similarly, data was simulated in [Yokoi *et al.*, 2002] while incorporating distance dependent variation in the PSF. Analytical simulation has also been used to test the sensitivity of SPM96 [Stamatakis *et al.*, 1999], to determine the thresholds for visual detection of cerebellar abnormalities in SPECT images [Stapleton *et al.*, 1994], and to evaluate the effect of lesions on automatic registration [Radau *et al.*, 2001].

2.4.3 Monte Carlo Simulation Methods

Monte Carlo simulation methods are widely used to solve problems where the system can be modelled as a statistical process, such as radioactive decay, transport and detection. Von Neumann named the method after the gambling centre in Monaco because of the similarity of the simulation methods to a game of chance and random sampling; the method employs sequential random sampling to perform the simulation.

The basic principle of Monte Carlo simulation is to model the response of a system as a set of probability density functions (PDF). The PDF is the relative frequency of the distribution of a random variable, as a smooth histogram over its entire output range, expressed in terms of integrals. Random sampling of this PDF can then be used to produce an accurate random response for the system. The major components of a Monte Carlo simulation system include the PDF's describing the physical system, a uniformly distributed random number generator, sampling rules for the PDF's and an estimator for the error. Monte Carlo methods have been employed in many aspects of nuclear medicine; including detector modelling, design of imaging systems and collimators, the validation and analysis of reconstruction and registration methods, analysis of image correction techniques, dosimetry, treatment planning and pharmacokinetic modelling [Zaidi, 1999].

In previous years, the introduction and expansion of Monte Carlo systems has been hindered by the available computer power of the times. For nuclear medicine applications, each photon has to be tracked individually from conception, through its transport and up to subsequent detection or to the point where it escapes. This requires very large number of calculations due to the very large number of decays required to obtain a single image. However, the recent huge increase in available computing power has seen the emergence of Monte Carlo methods as viable simulation systems for use in nuclear medicine applications.

2.5 Monte Carlo Simulation Systems for Emission Tomography

Monte Carlo simulation can be applied to the nuclear emission imaging process to generate hypothetical image data of a source distribution inside of a known attenuating object, for a given camera configuration. This is based on simulating random decays within a source, simulating the resultant gamma emission transport through the source object and up to the collimator surface and into the crystal where detection takes place. The accuracy is entirely dependent on the models used for the simulation as the entire imaging system has to be described. In emission tomography, it is necessary to model the decay and emission transport through the source materials and air to the detector, through the collimator and into the crystal. This requires

accurate models that allow the photons to interact with the simulated transport medium in a realistic manner. This in turn also requires that the medium through which the transport is simulated be accurately modelled. So while the accuracy of the simulation method is key, it is still important to ensure that the models on which a particular simulation is based are realistic. Figure 2.4 gives a basic overview of a Monte Carlo simulation system for a single photon originating in the source object, and is described below.

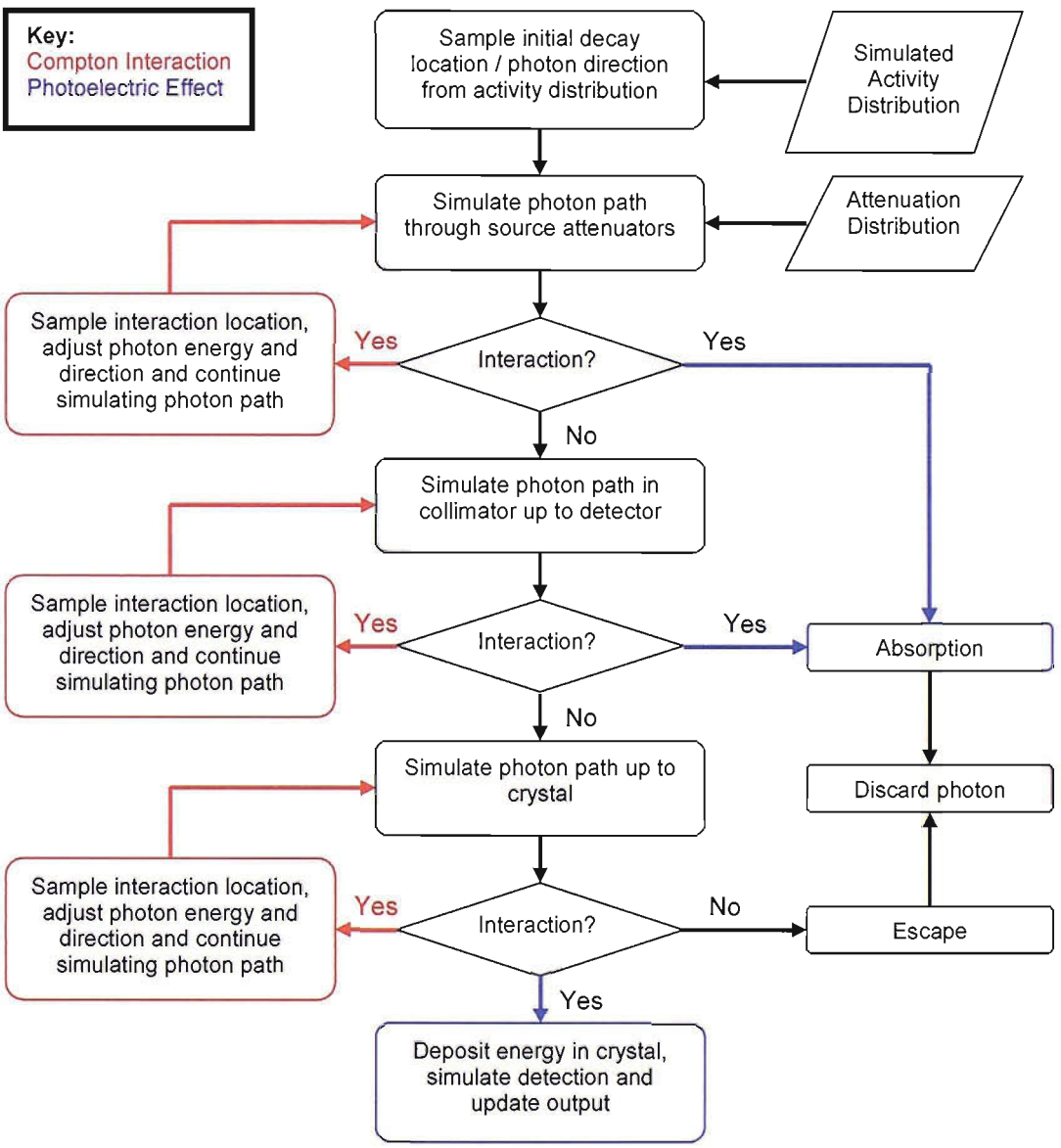

Figure 2.4. Basic overview of the Monte Carlo photon-by-photon simulation. The flow chart illustrates the simulation of each photon for each simulation, and the possible outcomes at each stage

For a given model, two inputs must be supplied for each simulation. The first input to the simulation system is an activity map, representing varying levels of activity across the object. Each photon is then tracked in a random direction through the material in which the activity is distributed. This requires a map of the attenuation coefficients to describe the source object, which is the second input. The attenuation map describes the distribution of materials within the object, and density and energy cross-sections for commonly used materials are usually pre-defined as part of a Monte Carlo simulation system.

The activity and attenuation maps together form the anthropomorphic phantom. The phantom can be described using one of several methods depending on the simulation system being used. It is usually possible, and desirable, to define the phantom arbitrarily as a voxelised image, to enable phantoms to be generated from real anatomical images, allowing very accurate anatomical modelling. Other methods rely on describing the maps as geometric shapes, and combining these to produce more realistic distributions. Geometric object descriptions simplify photon tracking by reducing the complexity of the source objects, removing necessary calculations at the edge of each voxel. However, most geometric anthropomorphic phantoms suffer from a lack of realism, and are not supported by all systems.

The number of published articles on Monte Carlo applications in medical radiation physics has risen from approximately 100 in 1970 up to over 1500 in 2000 [Buvat and Castiglioni, 2002], mainly due to the ever increasing computer power, and availability and complexity of the codes. General purpose Monte Carlo simulation codes exist for the simulation of transport of radiation through matter, developed for high-energy physics and dosimetry. The advantage of these codes is that they are usually well documented and tested due to the large community that they serve, and are generally freely available. These codes however, are not usually aimed at emission imaging, and extensive programming is required to fully simulate the imaging system. There are, however, several codes dedicated to emission tomography using SPECT and/or PET that differ in their features and applications. The most well known are SIMIND [Ljungberg and Strand, 1989], SIMSPECT, MCMATV and SimSET.

True random sampling is essential for accurate Monte Carlo simulation, to accurately model true random events. Any statistical correlation between results from a random

number generator would produce non stochastic behaviour, which can cause problems when using statistical reconstruction or analysis. Generally, random number generation on a computer system is employed through the use of a random number generator, which relies upon an algorithm that is usually repeatable. The generators are actually pseudo-random as such, although the run length is usually long enough to be considered random. The random number is used to sample the PDF for the current aspect of the simulation, and the result is a number that indicates the probability of an event having occurred, such as the interaction of a photon with an attenuating material. The reproducibility of the random numbers allows simulations to be repeated using exactly the same set of calculations, which is useful in finding problems with simulated data.

For realistic simulation, the pharmacokinetics of radiopharmaceuticals has to be estimated to synthesise the source activity in-vivo. This can be measured or estimated from retrospective or specifically acquired data using the physical imaging system. When using acquired data, the original data are also subject to random variations associated with imaging, which creates difficulty in determining the relative or absolute level of uptake accurately. This is particularly true of the partial volume effect. Errors in the measurement of the original source distribution are propagated and altered by the simulation system in a complex manner, making it essential to provide an accurate source description to achieve normal results.

2.5.1 *Properties of Simulation Systems for Emission Tomography*

It is desirable to accept both geometric and voxel-based phantoms as input to the simulation systems. Further enhancements have included the use of patient images for source objects. It is common for a system to support the simulation of planar detectors for 2D emission imaging, and it is often also desirable to simulate transmission imaging for generating theoretical attenuation maps. Most methods support binning of events as non-scattered and scattered photons and energy spectra. Compton and photoelectric scatter simulation is common in ET simulation systems, although coherent scatter can be assumed negligible in SPECT.

Parallel processing is natively supported with some Monte Carlo ET codes to improve computational efficiency by employing more that one processor to perform the computations.

The collimator is generally modelled using geometric transfer functions only, as collimator complexity would result in a dominant impact on simulation time. In this method, each photon undergoes a weight alteration which is determined by the probability of the photon passing through the collimator without interacting, based on the physical collimator parameters and the photon angle of incidence. Septal penetration is partly modelled by the geometric transfer function, but scatter in the collimator is not simulated at all. Septal penetration and scatter in the collimator are almost negligible in ^{99m}Tc SPECT, where the low energy of the photons and the high stopping power of the collimator predominantly result in absorption of photons. However, this becomes a problem for other higher energy isotopes such as ^{123}I, where septal penetration is significant. When using geometric collimator models, the distribution of detected events is not Poisson distributed. Thus where the statistical properties of the data set are to be used to aid analysis, a solution can be obtained by simulating relatively noise free projections (very large number of counts), scaling to the correct levels and adding analytical Poisson noise. This process is described in section 3.5.4.

The interactions within the crystal are always modelled as a point spread function, whose parameters are dependent on the component parameters of the camera back compartment, as well as the energy of the incoming photon and also on the type of crystal used. The dead time of the detected light events in the crystal is usually not simulated. The non-perfect energy resolution of physical detectors causes an increase in the number of scattered photons and a decrease in the number of primary photons that are detected. It is therefore desirable to model non-perfect energy resolution, and this can be achieved by blurring the incident photon energy with a Gaussian function.

2.5.1.1 The Effect of Variance Reduction

Variance reduction techniques are useful for improving the speed of simulation by reducing the variance of simulated events. This is achieved by forcing the simulation to sample the events that are more likely to occur in a detected event more often. This

can realise an increase in speed ranging from 3 times to 100+ times. Stratification (or importance sampling) forces the sampling of event outcomes that are more likely to result in a detected event more often, forced detection forces the resultant photon direction after a scatter to be in the direction of the detector, and forced non-absorption stops photons becoming absorbed in the attenuating material. The inclusion of variance reduction techniques requires that the weight of each event be adjusted to indicate the probability of that event having occurred. Photon rejection criteria can also be applied, such as stopping the simulation of photons whose energies drop below a pre-defined cut-off, or where the angle of incidence on the collimator is above a set level. Variance reduction techniques, however, generally result in a decrease in the accuracy of the results obtained and alter the statistical properties of the data. This can have a severe impact when dealing with techniques that depend on the random statistical nature of the data, such as statistical reconstruction algorithms. The inclusion of variance reduction techniques has been validated for PET imaging [Buvat *et al.*]. Forced detection cannot be used under SimSET when using the SPECT collimator modelling, as it is not supported. Furthermore, the weight windowing technique relies upon the use of forced detection and is therefore also not supported.

The greater the spread of the weights in a given simulation (indicated by a lower quality factor), the higher the variability of the flux estimate [Haynor *et al.*], which introduces a level of uncertainty in the simulated result. It is desirable to maintain minimal variation in the flux estimate to ensure simulation results accurately depict their intended model. However, geometric collimator modelling is based on updating photon weight depending on the properties of the photon, and is highly variable with the incident angle of the photon, which is a random variable. Thus for geometric collimator models, the variation in weight will be large, and the flux variability will be high. This can be improved by incorporating other variance reduction techniques to improve the distribution of weights, although is the most difficult parameter to control.

In all cases where photon probabilities are non-uniform, i.e. when using geometric collimator modelling or variance reduction techniques, the count image represents the number of detected events in a projection bin, and an additional weight image is

created that represents the summed 'weight' of each photon, which is the probability of that photon being detected. For summed weights, the variance can be approximated by summing the square of the weights. Thus for N events from a Poisson distribution, having weight described by w, we get $\sigma_w = w\sigma_n$, and as $\sigma_n = \sqrt{N}$, the variance is approximated by $\sigma_w^2 = w^2 N$. This approximation is correct asymptotically, and provides an estimate of variance that is useful for evaluating noise in a system.

2.5.2 Multi-Processor Environments

It is often possible to perform Monte Carlo simulations using multiple processors, either organised discretely or as a connected group. This is possible as physical decay is an independent and random event. Thus each decay and associated photon path can be simulated separately. Multi-processor environments allow large numbers of heterogeneous processors to work on the same task, allowing a proportional increase in computational power and decrease in simulation time with each added processor. This allows complex simulation to be achieved with relatively fast run times. There are several techniques available for generating simulated data using more than one processor, with varying degrees of involvement. The term *node* is often used to describe a single processing unit in a connected environment.

2.5.2.1 Discrete Multiple Processing

The simplest technique for using a multiple processor environments is to partition the simulation into discrete, sub-simulations and performing each simulation on a different processor running the same software. The simulation results can then be combined to create the final output data set. This technique is the simplest to implement and offers near minimum overhead for each additional node. However, the simulation must be manually partitioned into individual jobs prior to execution, which creates difficulty in maximizing efficiency. Physically, the method is unreliable as failure of any node has to be detected and corrected manually, which can have a dramatic effect on simulation time.

Problems can exist when using multiple nodes as the user has to ensure that each independent simulation is discrete to ensure no repetition in random number

generation. It is often desirable to partition the simulation according to individual projections, allowing each projection to be simulated as an individual image.

2.5.2.2 *Managed Clusters and Parallel Processing*

A managed cluster is a group of discrete nodes, networked such that each node has communication with a management program that has knowledge of all current simulation statuses. Communications between nodes allow dynamic allocation of resources prior to and during simulation, and offer an increase in reliability. This requires co-ordination of individual simulations, under software control, for maximum efficiency.

Parallel processing is the term given to running a single simulation on a set of nodes simultaneously, and each node reporting its status until the simulation is complete. The main difference is that the cluster is effectively running individual parts of one large simulation, as opposed to running many smaller simulations. The result is a performance increase for each additional node, although there is also an additional overhead as each node must also report its status.

Reliability and efficiency is much better when using clusters or parallel processing as a failure at any node can be detected and alternative resources allocated. Parallel processing requires that the simulation system has inherent support, and managed clusters require supervisory software.

2.5.2.3 *Computational Grids*

A computational grid is a (usually) large collection of nodes and/or clusters, arranged as a heterogeneous and ubiquitous network. The philosophy of the computational grid is the distribution of computational power as an on-demand resource, or "commodity", in a similar way as users utilise electricity from a power grid. This is a similar configuration to managed clusters, although the emphasis is on the use of general purpose networks with the ability to perform ad-hoc computations with the help of additional software. The end user requests CPU cycles from the grid. Grid technology has been successfully implemented to perform SPECT simulation using a localised grid [Thomason *et al.*, 2004], and reported negligible overhead with each additional node. Globally oriented grids via the internet would allow users access to

many teraflops of computational resource at any time, using a very reliable network infrastructure.

2.5.3 Simulation System for Emission Tomography (SimSET)

SimSET (**Sim**ulation **S**ystem for **E**mission **T**omography) [Lewellen *et al.*, 1998] is a Monte Carlo model of the physical processes and instrumentation used in emission imaging. The software was developed at the Division of Nuclear Medicine at the University of Washington, as a dedicated simulation package for emission tomography, with application in both SPECT and PET. The method was first released into the public domain in 1993, and is under continual development and is supported by a growing community of researchers. The code is comprehensive, well documented and is also freely available for download.

The software consists of a simulation system and several independent utilities. These include an object editor for the creation of attenuation and activity objects using either voxel or simple geometry based methods. Parameter files and data tables are included for different materials and tissue types common in SPECT imaging. The main software component is the photon history generator (PHG), responsible for generating and tracking individual photons through their transport during the simulation. As well as the standard binned output files, the software allows the recording of photon statistics (such as energy and direction) at various other stages during transport, such as interaction locations.

2.5.3.1 User Interface and Text Files

The SimSET software is a compiled command line tool. Parameters for each of the modules are specified in standard ASCII text files pointed to by a simulation parameter file, which is passed to the software as a command line argument. All additional utilities are also provided as separate interactive command line tools.

The main interface with the software is provided via text files for each part of the physical system. Text files exist to define the following: the collimator type and parameters, the detector type and parameters and the binning method for detected events. Additionally, the simulation parameter file contains all of the data pertaining to the PHG as well as pointers to the location of the other files.

2.5.3.2 *Simulation Objects*

Objects used in SimSET simulation are described two voxelised three-dimensional images for the spatial distribution of activity and attenuating materials. These files, along with an index file and look up tables, are then used by the PHG to simulate photon transport. Index tables are used to allow changes to activity levels and attenuating materials without the need to change the object or the associated table. The attenuation object indicates the type of attenuating material at a given voxel from a list of materials provided with the software. The index is used to look up the correct cross-sectional energy distribution. The activity object is similar, but the look-up table contains absolute activities for each index. The object discretisation is specified in the PHG file, and voxel sizes can differ across image slices.

2.5.3.3 *The Photon History Generator (PHG)*

The PHG is the major part of the SimSET package, responsible for the creation, simulation and transport of photons. The PHG uses the attenuation and activity objects along with their data files and simulation options to perform photon tracking through the materials. The basic operation of the PHG is summarised in flow chart form in Figure 2.5, and the components are described in the following sections.

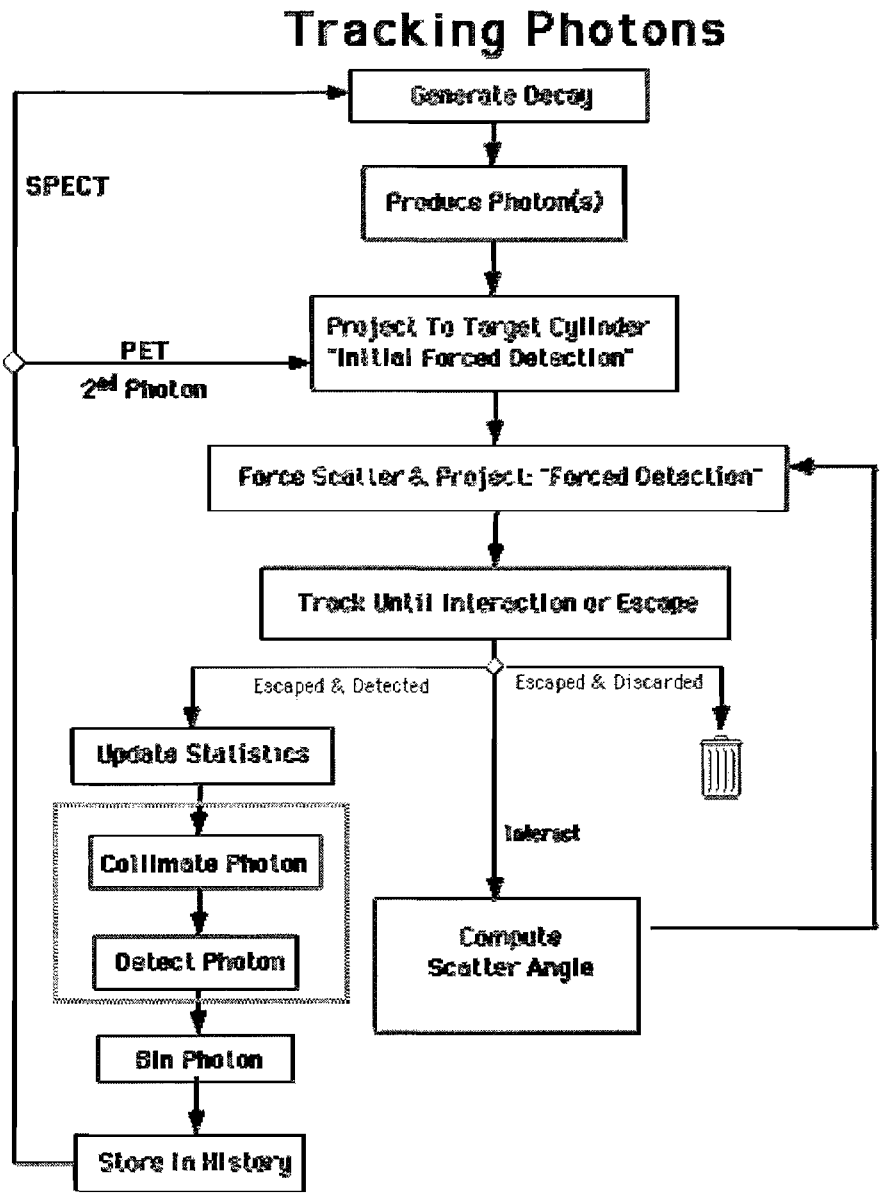

Figure 2.5. The photon history generator tracking algorithm. Decays are simulated on a voxel by voxel basis starting at a randomly selected decay location.[ii]

2.5.3.4 Collimators

The collimator module in the simulation is optional to allow the study of events in the absence of a collimator. The collimator is specified by the following parameters; the type of collimator to be modelled, the type of modelling for the collimator, the position and geometry of the collimator, and the septal thickness and hole radius. Options are available for collimator modelling for both PET and SPECT in a number

[ii] Reprinted with permission

of different configurations. PET collimators are modelled using Monte Carlo methods whereas the SPECT collimators are modelled using geometric transfer functions, supporting parallel, fan beam and cone beam models. The output from this module, when included, is used as the input to the detector model.

2.5.3.5 Detectors

The detector module receives photon path information from the collimator module or directly from the PHG module, and tracks them through the detector, before passing the output to the binning module. Importance sampling can be used in the detector module, forcing every photon to undergo an interaction in the detector, termed forced interaction. Two models are offered for the detector type in SPECT. The SPECT model is either a basic Gaussian energy blurring for each interaction or a planar detector where interactions with the detector geometry are modelled using Monte Carlo techniques. The planar method performs full simulation using layers of active and non-active materials, with additional Gaussian blurring available to simulate the limited energy resolution of the detector. Output can include statistics for all photons entering the detector. The number of layers, material and the geometry of the detector must be specified in the text file along with a description of each layer.

2.5.3.6 Binning

The binning module is responsible for binning the event data from the detector module into discrete ranges for output. Results can be output in any order of parameters, over any ranges specified, allowing for the creation of histograms or images from the resultant data. Furthermore, binning can be performed on qualitative basis, such as the binning of sinograms or energy into primary and Compton scatter.

Chapter 3 Imaging Methods

The methods presented in this chapter are general methods used throughout the rest of this thesis. The values of parameters described for the different methods have been used for all implementations unless specifically stated otherwise.

3.1 The Subject Groups

Two set of data are available, representing a known normal group (the normal database), and a group diagnosed with mild to moderate AD. In all following methods, the normal database or AD database refers to the group, or a subgroup, of the subjects described in these sub-sections.

There are several reasons why a particular subset of the normal database would be used, usually divided by demographic factors. For example, group variance can be lowered by reducing the age range of the subjects.

3.1.1 Normal Database

The subjects were originally chosen based on exclusion criteria to ensure no relevant history of neuropsychiatric impairment. Subjects were also screened to ensure no obvious evidence of cognitive impairment and no history of head injury.

The group consists of 34 subjects, and the demographics are given in Table 3-1.

	Number	Min / Max age	Mean age (SD)
All	34	40 / 96	68.9 (12.5)
Male	18	40 / 96	69.9 (13.5)
Female	16	47 / 90	67.7 (11.6)

Table 3-1. Normal Database demographics

3.1.1.1 Audit Group Sub-set

A subset of subjects was chosen retrospectively from the normal database. The group consisted of 28 normal subjects (16 male, 12 female) between the ages of 40 and 80 years (Mean = 65.43, SD = 10.00). The post 80 year subjects were excluded from this study to avoid the production of false positives due to the decline in function

associated with age. The studies were randomly divided into two groups representing a normal database (group 1, n=20) and a group of subjects to be used for abnormality simulation to represent the unknown population (group 2, n=8). Table 3-2 shows the demographics of the subject groups.

	Number	Number M/F	Mean age (SD)
Group 1	20	11/9	67.4 (8.9)
Group 2	8	5/3	60.6 (11.6)

Table 3-2. Audit group demographics

3.1.2 AD Database

As there are known differences between early and late onset AD [Kemp *et al.*, 2003], it is convenient to sub-divide AD database into two groups to account for this. These are termed the early onset group and the late onset group, and the age relationship is $Age_{early} < 65 < Age_{late}$. Table 3-3 shows the demographics for the two AD groups.

The AD subjects were selected based upon them having fulfilled the NINCDS-ADRDA clinical criteria for possible or probable AD. The subjects also had a MMSE score of $\geq$ 20/30 for late onset and $\geq$ 10/30 for early onset AD [Folstein *et al.*, 1975]. This was assessed at the time of or subsequent to the SPECT examination.

	Number	Mean MMSE (SD)	Mean age (SD)
Early Onset	20	18.8 (4.9)	57.9 (4.2)
Late Onset	31	23.4 (2.1)	77.0 (4.6)

Table 3-3. AD Database demographics

3.2 The Standard Acquisition Process

All subjects are injected with approximately 500MBq of freshly prepared ^{99m}Tc labelled Hexamethylpropyleneamine oxime (HMPAO) intravenously, while lying in a supine position with eyes closed in a quiet, dimly lit room. All imaging was carried out on a dual headed SMV DST-XLi (GE Medical systems) gamma camera equipped with low energy, ultra high-resolution parallel hole collimators. 128 projection images are acquired over 64 steps for 25 seconds per step, with a zoom of 1.33. The resultant data size is 128 x 128 pixels at 3.38mm per pixel. An example of a standard circular brain acquisition is shown in Figure 3.1. This output projection data is used as the input to the methods of image analysis described in section 3.3.

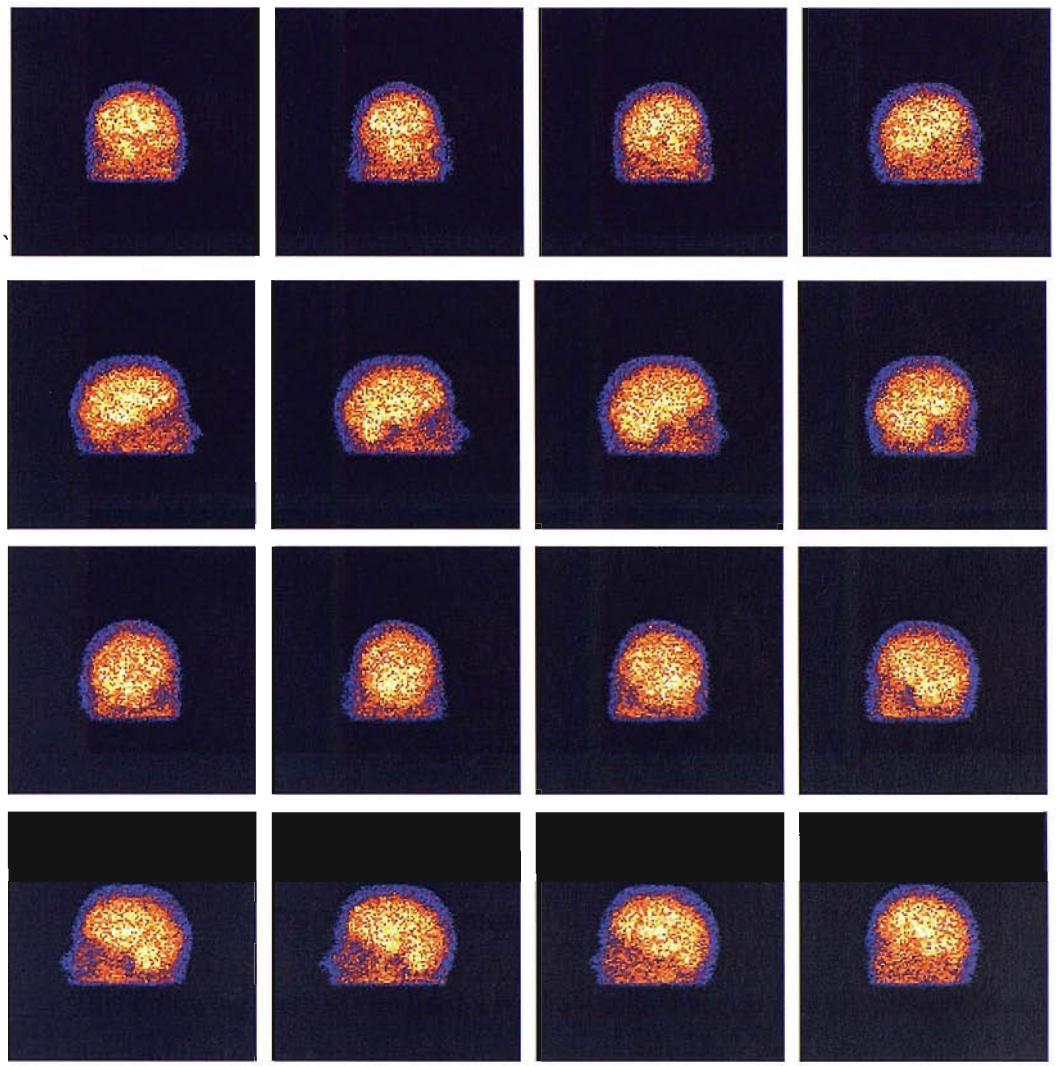

Figure 3.1. Example projection data for a standard brain acquisition for the Zubal head phantom. Images are taken from the complete data set and show every eighth image.

3.2.1 PSF Measurement

This following method was used with the standard acquisition process to obtain a standard image of a point source of activity inside of an attenuating object.

A 200 mm diameter, cylindrical water filled phantom was used to contain the point source of activity. A 2.3MBq point source measuring approximately 1 mm^3 was placed at the centre of the phantom. A SPECT acquisition was performed with a radius of rotation of 15 cm. The data was then processed using the same method as described above. FWHM measurements were performed on the data to ensure conformity with the manufacturer's specifications. The measured PSF was then

scaled such that $\int PSF = 1$. Approximately 2.5 million counts were acquired to ensure maximal signal to noise ratio in the acquired images. The PSF image is assumed to represent the reconstructed and corrected image contribution due to a point source of activity inside the brain.

3.3 Image Analysis Methods

3.3.1 SPECT Visual Inspection

This is the process used for generating SPECT images that are subsequently used for visual display and analysis. The process is designed to produce relatively smooth and noise-free images that can be used in the visual analysis of clinical brain images.

The planar data were smoothed using a Butterworth filter of order 10, cut-off 0.2 cycles/pixel, and then reconstructed using filtered back projection (FBP). The reconstruction included a Weiner filter of FWHM 7mm, resulting in 128 slices of 128x128 voxels with an isotropic voxel size of 3.38 mm. The data were attenuation corrected using the Chang method with a uniform attenuation coefficient of 0.112 cm^{-1}, and using a cylinder to approximate the head shape. The selected value of the attenuation coefficient was acquired empirically by filling a cylindrical phantom with constant activity. The phantom was imaged and reconstructed using different attenuation coefficients and the attenuation coefficient giving the most uniform cross section was used. No scatter correction is applied.

The image is then manually reoriented using the rotations along the three major axes, to create a symmetrical image tomograph oriented along two views. Firstly, orientation is along the AC-PC line to give an approximation to the OM line. Secondly, the OM image is rotated 20° (posterior down) along the sagittal axis to dissect the medial temporal lobes axially.

Axial slice summing is used to reduce the amount of output data and to reduce the noise in the image, and is carried out independently along each of the primary axes, summing every two slices. Count normalisation is performed using the maximum mean of a 5 pixel diameter circular region within the cerebellum, on any of the two axial slicing methods, or either side of the brain. Firstly, the axial slices are

convolved with a 5 pixel (16.9 mm) diameter circular ROI to find the maximum within the cerebellum, for the two axial slicing methods. The values are converted to a mean for the ROI and the maximum found on each side of the cerebellum region for both image sets. The largest value for each side is used, and an average of both is taken and the image normalised to 100 counts in this ROI. Figure 3.2 shows graphically how the regions are selected.

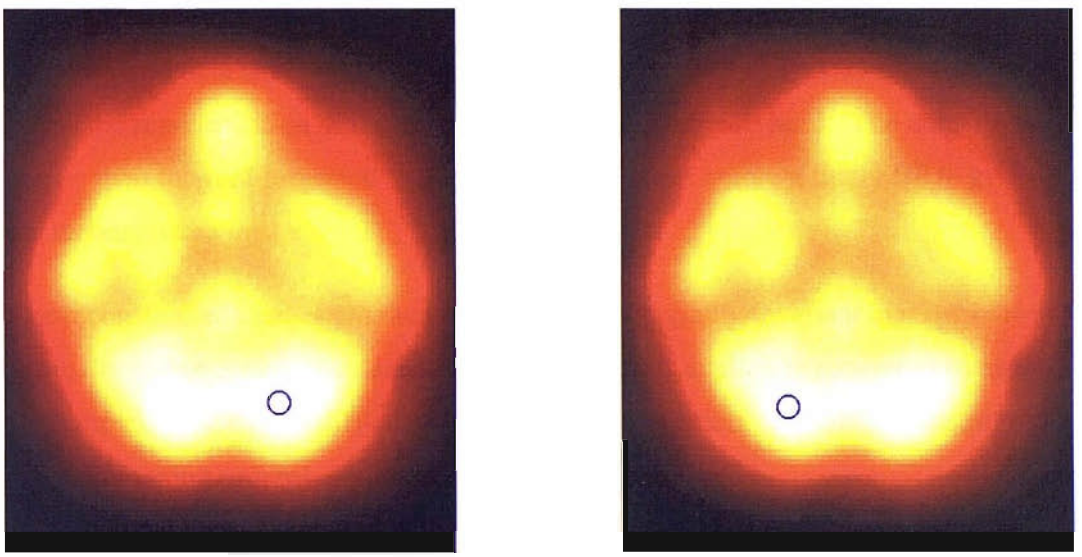

Figure 3.2. Cerebellum normalisation method. The images show the selected ROI location (not to scale) for the respective left and right side of the brain. The selected region represents the location where convolution with the circular ROI produces the maximum value. The mean of the two values is used for the normalisation parameter.

For clinical reporting purposes the 16 most central cerebral images for sagittal and coronal views were used with the two axial views. Data is displayed using the quantitative colour scale shown in Figure 2.2.

3.3.2 SPM99

SPM99 was used for all studies in this thesis. While SPM2 and SPM5 were available at the time of writing, initial experiments with SPM2 reveal that it is less specific to defects in SPECT. Also, SPM99 is the most widely reported version of SPM, which was released in January 2000. Very little published research was found using SPM2 or SPM5 in SPECT imaging studies.

3.3.2.1 *Pre-processing*

The data is initially converted to standard Analyze format images (Biomedical Imaging Resource, Mayo Foundation). The data is attenuation corrected using the first order iterative Chang method (two iterations) with a uniform attenuation coefficient of 0.112 cm^{-1}. No scatter correction is applied. The attenuation map is generated by thresholding the planar data at $1/20^{th}$ of the maximum image intensity, reconstructing using filtered back projection (FBP) and then thresholding the reconstructed data at $1/14^{th}$ of the maximum image intensity. This was found to give a realistic representation of the size and shape of the subjects head. The attenuation map is then forward projected to correct the projections before a final FBP to generate the reconstructed image.

The reconstructed images are then masked using a sagitally invariant mask, which is manually drawn around the central slice. The mask is applied to remove extraneous facial uptake that causes difficulty in automatic registration. Figure 3.3 illustrates the manual masking process.

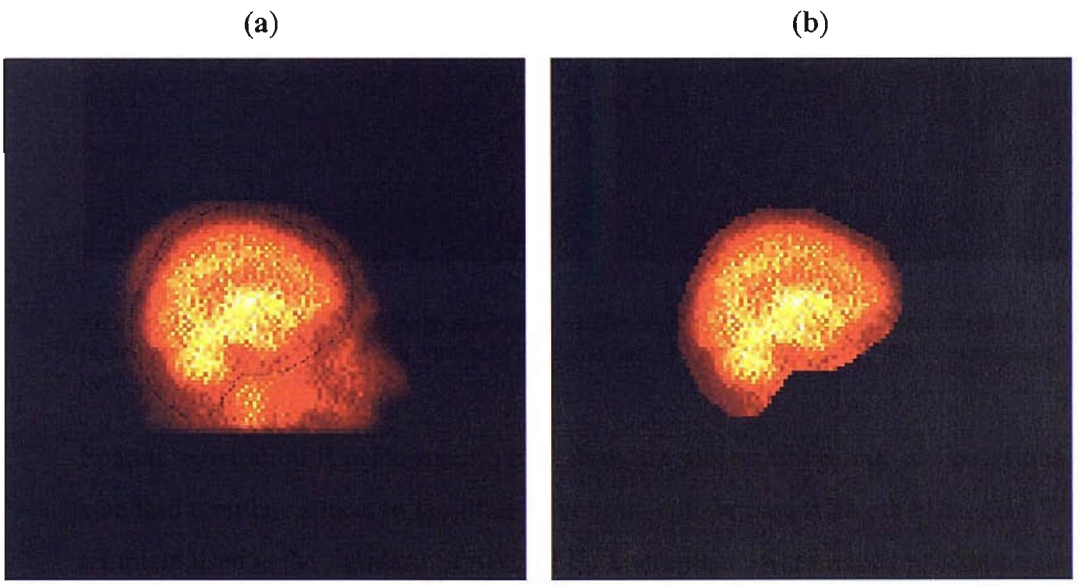

Figure 3.3. Example of brain image masking. (a) The original image as a maximum intensity projection with the defined mask shown as a broken line, (b) is the same image after the masking has been applied.

Spatial registration is performed to transform the subject image into a pre-defined standard template space, to facilitate voxelwise comparison with other images. The template used is the standard SPM99 SPECT template. Automatic registration uses a

12-parameter affine transformation, and where required, a 12 iteration non-linear warping algorithm, using 4x5x4 DCT basis functions and bi-linear interpolation. Registered and interpolated images have dimension of 91x109x91 and an isotropic voxel size of 2 mm.

Smoothing is then performed, usually using a Gaussian smoothing kernel of user defined size. This kernel is usually isotropic with a 16 mm FWHM, although anisotropic smoothing can be applied to account for differences in resolution along the three primary axes. The final step is count normalisation to the cerebellum, and is achieved using the automatic method described in section 3.7.4.

3.3.2.2 SPM Tests

SPM analysis is used to compare a subject SPECT image with a set of known normal images in an attempt to detect abnormal perfusion levels, and is achieved by performing statistical tests. More specifically the two sample t-test is performed on a voxel-wise basis. No image count normalisation or grand mean scaling is applied at this stage. The analysis threshold is applied at 70% of the global, where the global is mean voxel value within a mask, with a threshold defined at one eighth of the full image mean.

Model estimation is then performed, attempting to estimate the p-value at each voxel. The output from SPM is the statistical parametric map, which describes each voxel as a probability. Inferences can then be made based on this map. Multiple comparisons correction is performed based on the number of resolvable elements (resels) in the image. Voxels are assumed to be abnormal at $p < 0.001$ (uncorrected). Sub-threshold voxels are grouped into clusters and sets, and significance is indicated at $p < 0.05$.

3.3.2.3 MarsBaR

MarsBaR performs statistical analysis using a summary function for homologous regions (i.e. the lobes of the brain). Analysis is then performed by comparing the summary function for regions between the subject and a control group (i.e. normal subjects), and assessing the significance of the difference between them. The summary function is commonly the mean or the median of the VOI under study. A Bonferroni correction is applied to take account of the number of individual regions

being tested. A significance threshold of $p < 0.05$ is used to indicate an abnormal volume.

3.4 The Talairach Daemon and Regions

VOI analysis provides a method of quantitatively assessing the level of perfusion in predefined volumes of the brain. A wide range of VOI sets have been described in the literature [Greitz *et al.*, 1991, Slomka *et al.*, 2001, Van Laere *et al.*, 2002b, Minoshima *et al.*, 1994, Takeuchi *et al.*, 2002]. The space defined by Talairach and Tournoux [Talairach and Tournoux, 1988] is a commonly used reference space for the anatomical sub-division of the brain. The regions presented here are based on standardised segmentation of the brain, and therefore each volume represents an anatomically distinct region. A full set of VOI's has been generated, hereon termed "Talairach space", stored in digital format.

The Talairach Daemon [Lancaster *et al.*, 1997] is a stereotactic, probabilistic brain atlas based upon Talairach space. The daemon splits the Talairach atlas into 5 levels consisting of cerebral organisation, associated lobe, associated gyrus, the tissue type and cytoarchitecture, consisting of 7, 12, 58, 3 and 71 independent regions within each level. The full set of anatomical labels was extracted from the daemon for all 1mm isotropic voxels within the image. Matching labels were then combined by grouping voxels to form the independent VOI's. Each region was separated into left and right-sided regions. A further database is defined by transformation to the space defined by the Montreal Neurological Institute (MNI space, as used by SPM99) using a transformation derived by [Brett *et al.*, 2001].

Figure 3.4 shows slices of part of the MNI database demonstrating the grey matter in different lobes of the brain as different colours for three axial slices.

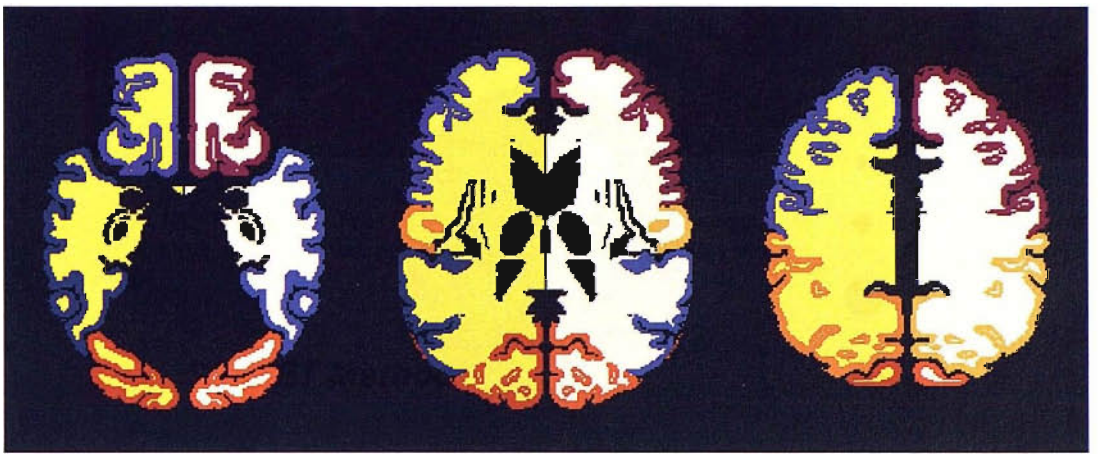

Figure 3.4. Three axial slices of an example Talairach atlas image. The different colours represent different regions, as the various lobar cortex regions. The large central areas are the white matter of the brain.

3.5 SimSET Methods

Simulation using Monte Carlo techniques is a complex process. While several studies have been carried out to validate the method for use in simulation, the accuracy and precision cannot be guaranteed for every implementation due to changes in software, hardware and implementation specific parameters. Thus it is necessary to perform a basic validation using simple models to ensure correct operation. The Williams phantom is well suited to such a validation.

3.5.1 Digital Williams Phantom

A digital representation of the Williams phantom was created on a PC in bitmap format with an isotropic voxel size of 1 mm. 13 slices of 1 mm were drawn for the attenuation and activity map.

Figure 3.5 illustrates the three components of the digital Williams phantom, which were used as the basic building blocks for both the attenuation and activity objects.

The attenuation map was generated using the slices with white modelled as Perspex and black as water. Everything outside the phantom was modelled as air. The activity object is generated by assigning a set level of activity within the black area setting the rest of the object to no activity. The generated objects are used in subsequent simulations involving the Williams phantom.

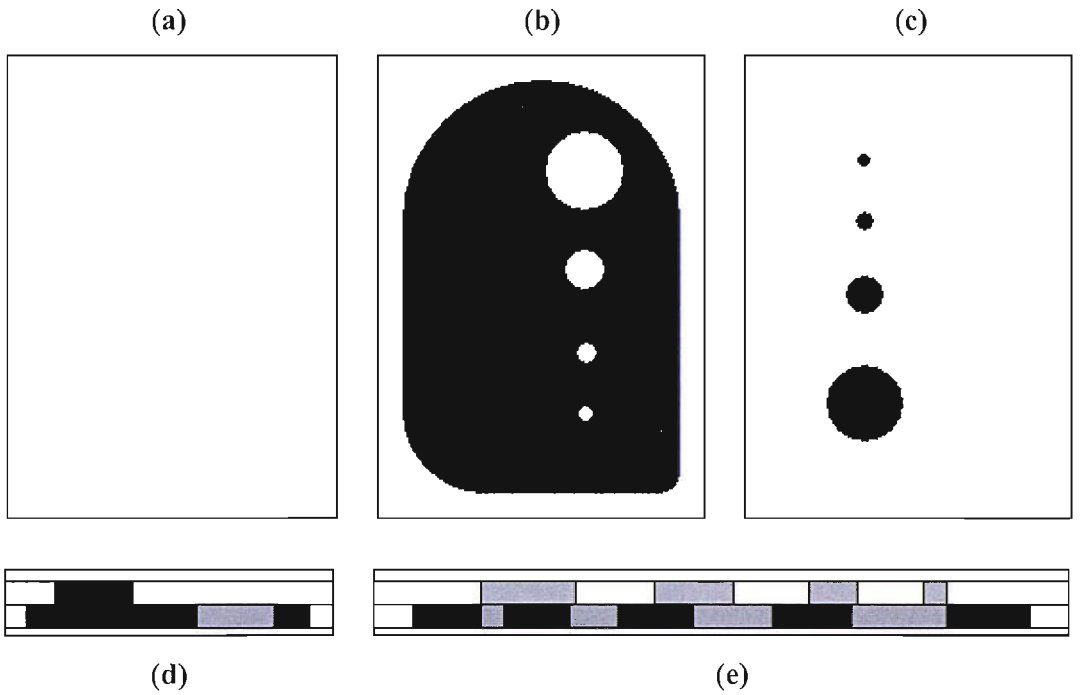

Figure 3.5. The actual digital Williams phantom slices used to construct the activity and attenuation objects. (a,b,c) are purely binary, to scale and bounded by the edge of the Perspex, with white representing Perspex and black representing activity; (a) is the Perspex only, (b) shows the uniform object activity with cold spots and (c) is the uniform Perspex with hot spots. Images (d, e) represent maximum intensity projections for orthogonal views of the three sandwiched slices, and are not to scale.

3.5.2 *The Camera Model*

As well as providing an accurate description of the source activity and attenuation distribution, it is equally important to accurately model the imaging system under study to provide valid results. For all experimentation in subsequent chapters using SimSET, a camera model is defined based on the physical imaging system in use at our site. This camera is a dual head SMV DST-XLi equipped with low energy ultra high resolution (LEUHR) collimators.

For simulation, accurate models are defined for the gantry, collimator, detector and binning modules. The bed is not modelled in the simulation system. The gantry is modelled via individual simulation parameters and SPECT datasets are acquired by imaging (usually 128) discrete steps around the subject.

Photon tracking is not carried out in the collimator model. Instead a geometric transfer function is used to provide an average spatial resolution response, based on geometrically collimated photons [Tsui and Gullberg, 1990]. For each incident

photon, the probability of the photon passing through the collimator is calculated, and the photon weight updated accordingly. If the probability is zero, the photon is absorbed in the collimator.

The geometric collimator model in SimSET is based on hexagonal arrays of circular holes. The actual collimators used are created from corrugated foil that is moulded into a hexagonal honeycomb array, and thus the apertures are actually hexagonal. This difference is illustrated in Figure 3.6.

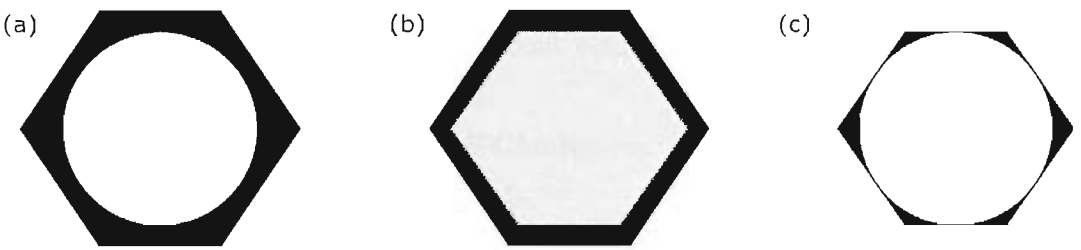

Figure 3.6. The difference between the collimator model used in SimSET and the physical collimator. (a) The geometric collimator model used in SimSET. (b) The geometry of the physical septa. (c) The difference image illustrating the area of aperture that is incorrectly modelled as septa.

The septal thickness for collimator models quoted by manufacturers is usually based on the combination of two adjacent septa. For the SimSET simulation system, the specified septa size is actually equivalent to half of the septa thickness between two adjacent holes.

The result is a decrease in the area of the apertures and an increase in the area of the septa, reducing the sensitivity of the imaging system. It has been shown that there is only minor difference in the transfer function model between the hexagonal and circular aperture geometries, providing the septa/aperture area ratio is the same [Metz *et al.*, 1980]. Therefore, an approximation to this is sought by increasing the aperture size and decreasing the septa size, such that the septa/aperture area ratio is the same as in Figure 3.6 (b).

The physical collimator is a 47 mm deep, 400x500 mm square array. Septa are 0.1 mm thick and holes are 1.9 mm wide. The cross-sectional area of a single honeycomb cell is 3.82 mm^2. The area of the physical collimator aperture is 3.13 mm^2. If the standard measurements are used for the SimSET collimator model, the cross sectional area of the hole is 2.84 mm^2 or approximately 10 % too small. Likewise, the area of

the septa would be approximately 40 % too large. To correct this problem, the hole radius was adjusted to 1.00 mm to give an aperture area of 3.13 mm^2, and the septal thickness was adjusted to 0.052 mm to give a cross-sectional septal area of 0.69 mm^2.

The detector is modelled as a continuation of the collimator model, and full Monte Carlo simulation is performed in the detector. The detector is the same size as the collimator, and is made up of two layers; a 0.5 mm deep copper shield and a 9.5 mm ($^3/_8$") deep Sodium Iodide (NaI) crystal. Gaussian energy blurring at 9.8 % of the incident photon energy is simulated in the detector to model non-perfect energy resolution. No modelling of the camera back compartment is performed.

3.5.3 IRIDIS 2 – Beowulf Cluster

As Monte Carlo simulation is a very processor intensive task, each simulation was run on the University of Southampton Iridis 2 network. The network is a Beowulf cluster and consists of 600 2.2GHz AMD Opetron and 214 1.8 GHz Intel Xeon processors, capable collectively of over 3.4 $x10^{12}$ floating point operations per second (flops). Access to the processors is via a queuing system via a remote job submission interface.

For the simulation of a large number of photon histories, the job is sub-divided and submitted as a number of smaller jobs that can run in parallel. The results from each individual simulation can then be combined to realise the final result. Each individual simulation is assigned a different random seed to ensure that sub-jobs do not use the same set of pseudo-random numbers.

3.5.4 Simulating Poisson Noise

SimSET simulation using geometric collimator modeling or variance reduction techniques produce data that is not Poisson distributed and requires that Poisson noise is added (see section 2.5.1). The following describes the method used to add artificial Poisson noise to simulated images using the inverse transform method.

Simulation is performed for a very large number of detected events, N, producing total weight, W, such that the images have very high signal to noise ratio and can be assumed to be practically noise free. The projection bins are then normalised such

that W represents the average weight for a standard acquisition, and rounded to the nearest integer value. The normalised and rounded weight value for each projection bin i, w_i, is then assumed to be the mean value of a Poisson distribution and the cumulative probability is calculated as shown in equation 3.1.

$$cp(n) = \sum_{a=1}^{n} e^{-w_i} \left[\frac{w_i^a}{a!} \right] \tag{3.1}$$

Where $cp(n)$ is the cumulative probability of obtaining n counts in voxel i. A uniformly distributed random sample in the range [0.0, 1.0] can then be substituted for $cp(n)$, and equation 3.1 can be solved for n. In practice, it is unlikely that a solution exists for an integer value of n given a random sample, and thus the integer value of n that gives the numerically closest result is used. w_i is then replaced with the estimate n. Figure 3.7 shows the effect of adding simulated Poisson noise.

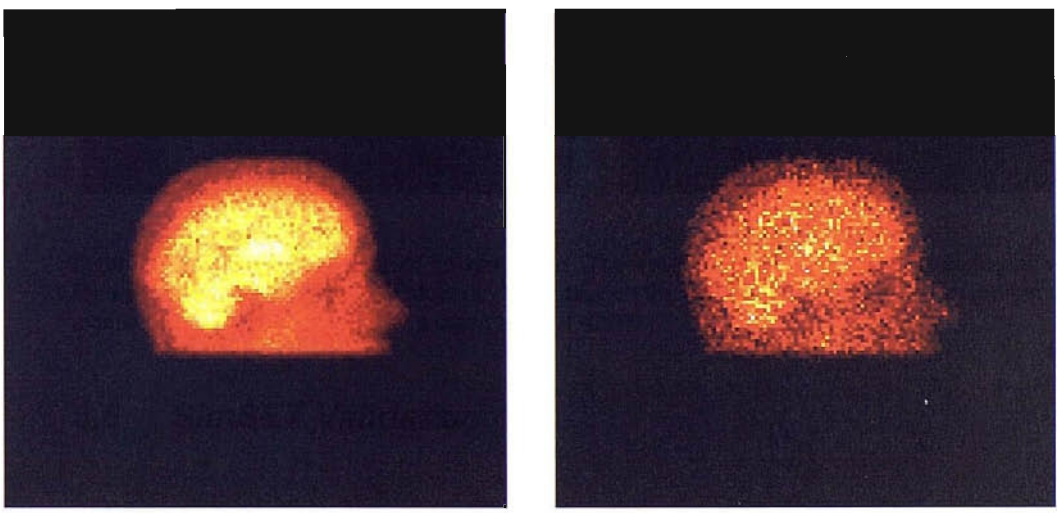

Figure 3.7. Example simulation of Poisson noise. The image on the left represents a single projection for a simulated image with 6×10^9 decays. The image on the right represents the same projection with manually added Poisson noise for a count level of 42000.

3.6 SimSET Validation

SimSET validation is performed as a preliminary step to ensure correct operation of the system at a lower level. This provides data that can be compared to physically acquired data and used as a validation method. There are no publications in the current literature covering a thorough and complete validation of the SimSET code. However, the models used in SimSET have been validated for SPECT, and shown to

be sufficiently accurate to model the process [Buvat *et al.*, 2005]. Further validations are presented in [Buvat and Castiglioni, 2002] for SimSET in PET

There is obviously a level of error for any simulation due to non-perfect modelling of real world data and assumptions necessary for reduced complexity. As the SimSET system is intended to simulate random photon paths, its very nature makes it difficult to verify correct operation. Validations proceed in an attempt to ascertain whether the data being produced is adequately representative of the output from the process being simulated. Simulation is performed and data is compared to published specifications or physically acquired test data. Further validation is also required to ensure the data sets are free from random and recurrent errors that could be generated by the models used for simulation. Validation of the detector response without collimation is not performed, as the effect of linearity and uniformity is small for the physical imaging system. A software validation preceded simulation for all systems, and confirmed correct operation.

3.6.1 Point Source

A point source simulation was performed to assess the properties of the basic element of the simulation system. The output data was used to compare the basic properties of the physical process being simulated. The changes to the collimator model are validated, as output response is highly variable with collimator parameters. This is performed by comparison of measurements of simple simulated data to the manufacturer's specifications. The results also provide a method of assessing the resolution of the imaging system in comparison to the physical system.

A standard simulation was performed for a point source. The point source was modelled as a single 1 mm^3 source voxel at the centre of the field of view, modelled as water without any surrounding attenuating material. The point source contained $27x10^{-3}$ mCi, equivalent to 1 MBq of activity with $1x10^6$ decays per second. $100x10^6$ decays were simulated resulting in effectively 1 MBq of activity imaged for 100 seconds. A standard simulation was run using the models described earlier for a single planar acquisition, without any applied variance reduction techniques. The collimator is modelled at a distance of 10 cm from the source.

Of the 100 million simulated decays, the deposited photon weight was 6165 which represents a sensitivity of 61.65 c/s/MBq. The experimentally measured specifications for sensitivity is 70-75 c/s/MBq. The difference between the simulated and physical sensitivity can be partly described by septal penetration and collimator scatter, which are not modelled in the collimator. Further errors may be due to scattering in objects that are not included in the simulation, such as the subject headrest and bed, and the camera gantry.

The FWHM of the simulated point source was measured at 7.4 mm. This compares well to manufacturer's specifications of 6.8 mm, and differences can be explained in the low resolution of the acquisition with FWHM being only twice the pixel size.

3.6.2 Validation Using the Williams Phantom

This experiment was performed to validate the operation of the SimSET code for more complex models. A digital representation of the Williams phantom was created from measurements obtained from the physical phantom. Attenuation and activity objects were created from this and used to simulate a planar view for comparison with physically acquired data.

3.6.2.1 Physically Imaged Phantom

The Williams phantom was filled with 39MBq of freshly prepared ^{99m}Tc-HMPAO, and topped up with water to avoid air bubbles. The phantom was agitated and allowed 30 minutes to mix properly. The phantom was then placed on a headrest and imaging was performed. A single projection was acquired at a distance of 85mm from centre of field of view to the collimator surface. The camera used was a General Electrics DST XLi equipped with LEUHR parallel hole collimators, as modelled in the SimSET simulation system. 70,000 counts were acquired over approximately 30 seconds.

3.6.2.2 Phantom Simulation

All methods are based on using the weights image. Validations could proceed by attempting to normalise the mean acquired counts to the mean simulated weights by adjusting the number of simulated decays while maintaining the correct simulation parameters (simulation time, activity etc.). However, the resulting variance estimate

would be substantially lower for the simulation ($\sum N < \sum w^2$) as generally w is less than unity. To achieve an accurate comparable simulation, the number of detected events must also be equal to the variance of those events, as in analogue Monte Carlo simulations. This can be achieved by either simulating noise free images and adding analytical Poisson noise, or by updating the simulation parameters such that the variance in both simulations is equal, $\sum N = \sum w^2$. Individual photons are assigned a starting weight based on the length of scan and initial activity levels, thus affecting the variance estimate. This allows us to use the 'length_of_scan' parameter to easily adjust the photon starting weights to allow some control of the variance of the simulated photons.

Simulation proceeded using the digital Williams phantom and the following parameters. No method of variance reduction or importance sampling was used. The number of decays to simulate was calculated to obtain a similar measure of variance to the original image, i.e. 70,000, thus ensuring noise characteristics were similar. 450×10^6 decays were simulated, based on filling the phantom with 39MBq of activity and imaging for 30 seconds, as performed in the physical experiment. ^{99m}Tc imaging was simulated by using photon energy of 140KeV and a lower and upper threshold of 10%: 126KeV and 154KeV respectively. The camera was simulated at a distance of 8.5cm from the centre of the field of view to the face of the collimator, and the updated collimator model was used.

The simulated data has a total of 131156 detected events, with total weight 69805 and estimated variance, $\sigma_w^2 = \sum w^2 = 68212$. The quality factor for the simulation is 5.45×10^{-1}, which when multiplied by the number of detected events, gives an equivalent real world acquisition of 71480 photons.

3.6.2.3 Comparison

Figure 3.8 shows two projections from qualitative comparison of acquired and simulated data from the Williams phantom experiment. For the simulation, the weight and variance of the simulation are equal to the physical acquisition. Both images appear comparable visually, with the size of the images and the apparent distribution of counts approximately the same. Figure 3.9 shows a comparison of acquired data and simulated data, with an additional Gaussian smoothing.

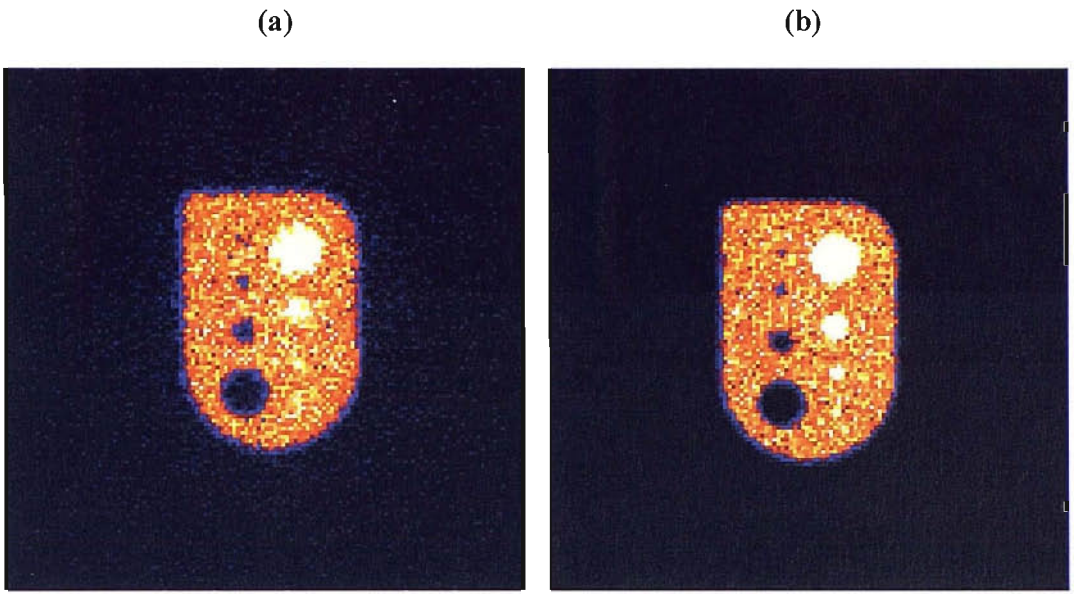

Figure 3.8. Qualitative comparison of Williams's phantom for a) acquired data with 70000 counts and b) simulated data with approximate variance 70,000.

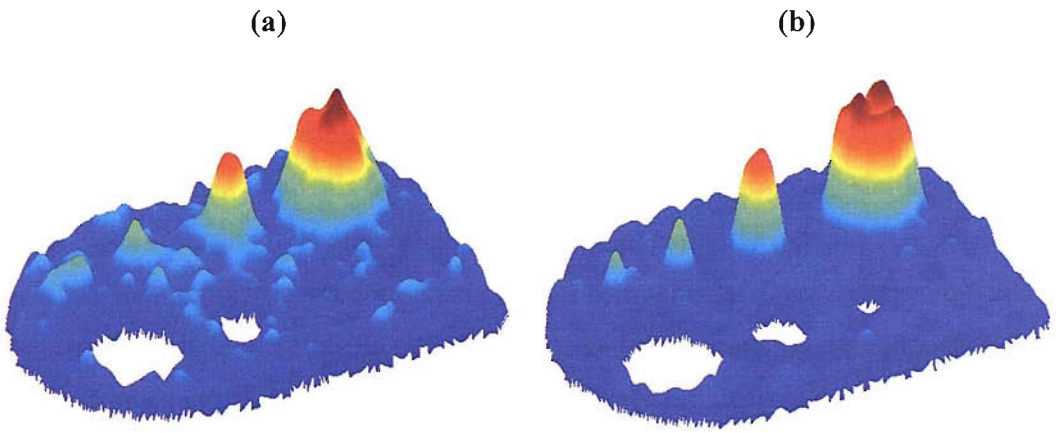

Figure 3.9. Qualitative comparison of Williams's phantom for a) acquired data with 70000 counts and b) simulated data with approximate variance 70,000. The data are smoothed with a two-dimensional 7mm FWHM Gaussian kernel, and displayed as a three dimensional surface plot, thresholded at 20 counts.

It can be seen that the simulated data has less noise than the physically acquired data, and the physically acquired activity peaks have larger scatter tails (indicated by a wider base). The differences in the image can be directly attributed to lack of a model for septal penetration and scatter. Additional errors could be present in the estimate of variance obtained, due to the large variation in image weights. A fraction of the detected events in the original image are created from effects that are not modelled in

the simulation (septal penetration and scatter), thus the simulated source activity contributes more flux per detection element to the image than the physical source activity. Therefore, it is also likely that the simulated image will have lower noise, as the process includes the acquisition of more real world equivalent photons. The total effect is difficult to estimate as it is the combination of a number of smaller effects. The results are comparable when these effects are taken into account.

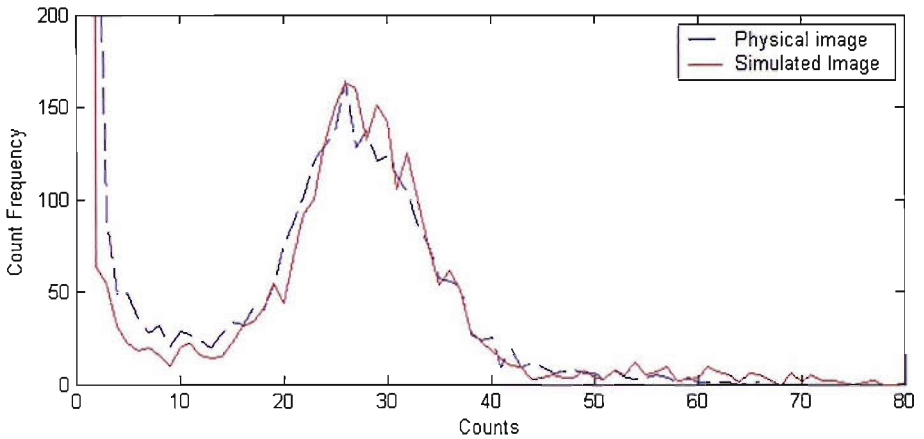

Figure 3.10. Histogram of counts against frequency for the images show in Figure 3.9.

Figure 3.10 shows the histogram for the images shown in figure 3.4. It can be seen that the distribution of counts by frequency for the images have very similar profiles. Differences are evident due to collimator modelling, particularly in the low count regions which represents predominantly scatter components. Overall, the simulated data compares well qualitatively with that acquired from scanning of the physical phantom, even in the presence of the differences between the two data sets.

These results indicate the validity of the simulation system, and while some differences are present, the use of the software for Monte Carlo simulation was considered a sufficiently good representation of gamma camera performance for our implementation.

3.7 MATLAB and MATLAB Based Tools

Matlab version 6.5 (The Mathworks Inc., Natick, MA, USA) was used extensively for most aspects of this project where solutions did not previously exist. As well as general purpose utilities, the software was used for the following: Parameter file and

object generation for the SimSET simulation system, generation of the VOI's described in section 3.4 as well as the Zubal phantom regions, combination and editing of VOI sets for use in VOI analysis. Also several stand alone software tools were created for use within the project that are useful in their own right, as described below.

3.7.1 Biodistribution Estimation

The distribution of the radioisotope within the brain is of key importance when analysing SPECT data, as this is the actual surrogate marker used in analysis that determines how active (or non-active in the case of dementia studies) a particular region is. The use of SPECT to measure the tracer uptake is variable on a number of different levels, and the imaging and reconstruction process produces variation in the perceived results. The biodistribution of the tracer can offer more information than the SPECT data, as it is not subject to variability introduced by the imaging process.

Custom software has been generated to aid in the generation of the biodistribution data. This is used for both PSF and SimSET based extraction methods, for both ART and MLEM iterative algorithms. The software improves repeatability and reduces human errors in the system, and also ensures that the same method is applied to each subject or iteration of the system. The software is used to: generate the Zubal regions for simulation and analysis, normalise and extract counts from the control subjects including any necessary processing, generate the f_{ij} matrix for use in the iterative process, perform the iterative ART and MLEM algorithms and to generate the required files for simulation.

3.7.2 Abnormal Image Simulation

The abnormal image simulation system described in section 4.1 was developed and written entirely using the Matlab programming language. The software is designed to operate as a stand alone program, allowing the generation of abnormal image subjects within an interactive environment by automating common tasks. The user provides an input image and generates an abnormal distribution before simulating. This software includes tools for pre-processing (masking, smoothing and count normalisation), creation and editing of abnormality distributions and providing information on the

distribution. Interactive slice editing is also supported, allowing the user to add geometrically defined abnormalities manually. The software also includes a separate interface for the generation of VOI's through the combination of existing VOI's using standard processes such as masking etc.

3.7.3 Anatomical Labelling

Spatial normalisation is essential to any voxel-wise comparison and quantification study. As the template used for normalisation is stereotactically defined, this leads to the possibility of incorporating anatomical labelling in the reporting of these images to aid in detection of regionally specific effects in SPECT, PET and MRI studies. Previously, a third party electronic database was used to determine the position of an abnormality by inputting coordinates and manually recording the label.

An improvement to this method has been made by the introduction of a fully automatic method, using the atlas described in section 3.4. The database is used to reference a set of text labels indicating the associated areas, which are then used to form the anatomical text label. The result is a text label indicating the anatomical position of a voxel in Talairach (or MNI) space. This has been incorporated as a toolbox into SPM99 to give a text label output on the results, indicating the current position of the pointer in real time, along with the nearest grey matter. Validation was performed on the software by selecting random coordinates, and comparing the results achieved using the attachment to that achieved using the daemon, and perfect concordance was observed. The adaptation allows the user to discriminate between affected regions, which facilitate a more accurate differential diagnosis based on stereotactic data. Wherever specific labels are quoted within this text, they are generally derived using this method.

3.7.4 Automatic Count Normalisation

Cerebellar count normalisation is implemented as an SPM99 toolbox. The method involves using a spherical VOI of user definable size, and three dimensional convolutions with a masked subject image of the cerebellum. The result is a value representing the average in the VOI at each position. The maximum values for both

sides of the cerebellum are then averaged to produce a global scaling factor, which can be applied to normalise the counts in a subject to a standard reference value.

Chapter 4 Analytical Simulation: Creating an Audit Dataset

A method is described here that allows the creation of abnormal distribution through the synthesis of realistic and stereotactic hypoperfusion inside a known normal brain. Validation of the method is described using SPM99. The method is applied to a subgroup of the normal database to generate an abnormal data set that could be applied to the audit of HMPAO SPECT analysis techniques.

4.1 Analytical Simulation

This section describes a fast method for the simulation of realistic abnormal data, incorporating an experimentally measured, spatially uniform 3D PSF (see section 3.2.1) and existing normal reconstructed hexamethylpropyleneamine oxime (HMPAO) SPECT brain scans. Simulation is performed by convolution of the PSF with an arbitrary abnormal source distribution. The method can be used for the production of realistic simulated data sets that can mimic pathological hypoperfusion in normal subjects, by using the Talairach atlas to synthesize the anatomical position of abnormalities in a variety of disease specific regions. Physiologically accurate simulation of dementia is achieved through the use of heuristic knowledge on functional deficits in dementia progression.

The input to the simulation system is the PSF described in section 3.2.1 and a normal image, both of which are processed and reconstructed using standard methods. Manual image masking is carried out on the reconstructed images to remove extraneous facial activity. Spatial registration is then performed on the subject image using SPM99, and a 12 parameter affine transformation only. The affine transformation mapping the subject image to the template space is stored for future use.

Each abnormality is defined by selecting an anatomical region of the brain from a list of segmented VOI's defined in standard space as described in section 3.4, by adding user defined regions in standard space, by arbitrary construction in subject space or by

a combination of these. The majority of simulated abnormalities are located in the grey matter lobes of the brain, as this is the primary focus of the dementing process. The regions to be simulated are selected and combined and/or masked with other regions to produce a pattern of abnormality, I^{ab} in which the intensity at each voxel represents the percentage perfusion reduction in that voxel. The stored normalisation matrix for the subject is then reversed and applied to the standardised abnormality to produce an abnormality defined in the original subject space. The effect of partial volumes (PV) in the transformed distribution is corrected by calculating the mean activity for a whole voxel through sub-sampling of the transformed region at <1 mm^3 resolution using tri-linear interpolation. Activity defined outside of the brain is removed from the abnormality by applying a brain mask generated from the histogram of the original SPECT image. The abnormality map is then convolved with the measured PSF to generate a simulated abnormality distribution, representing the contribution of the abnormality distribution to the overall image. The simulated abnormal distribution image is subtracted from unity (1 - I^{PSF}) and multiplied by (as opposed to subtracted from) the normal image. This process preserves features of the original image, such as the natural image noise, at a relative level. The resultant image is representative of the simulated abnormal image with a known abnormality distribution. Equation 4.1 shows the mathematical equation for the generation of the simulated image I^{sim}.

$$I^{sim} = I^{sub} \times \left(1 - \left(I^{ab} \times I^{mask}\right) \otimes I^{PSF}\right) \tag{4.1}$$

Where I^{sub} is the original subject image used, I^{ab} is the image representing the abnormality contribution in subject space (relative to 1), I^{mask} is a mask representing brain only and I^{PSF} is the normalised point spread function ($\sum I^{PSF} = 1$). This method allows the rapid creation and simulation of wide range of scenarios. In house software has been developed under MATLAB to facilitate the process of simulating the images. Figure 4.1 illustrates the steps in an example abnormal image simulation procedure for a single transaxial slice showing the simulation of an abnormality defined over the entire occipital and temporal cortex on both sides of the brain.

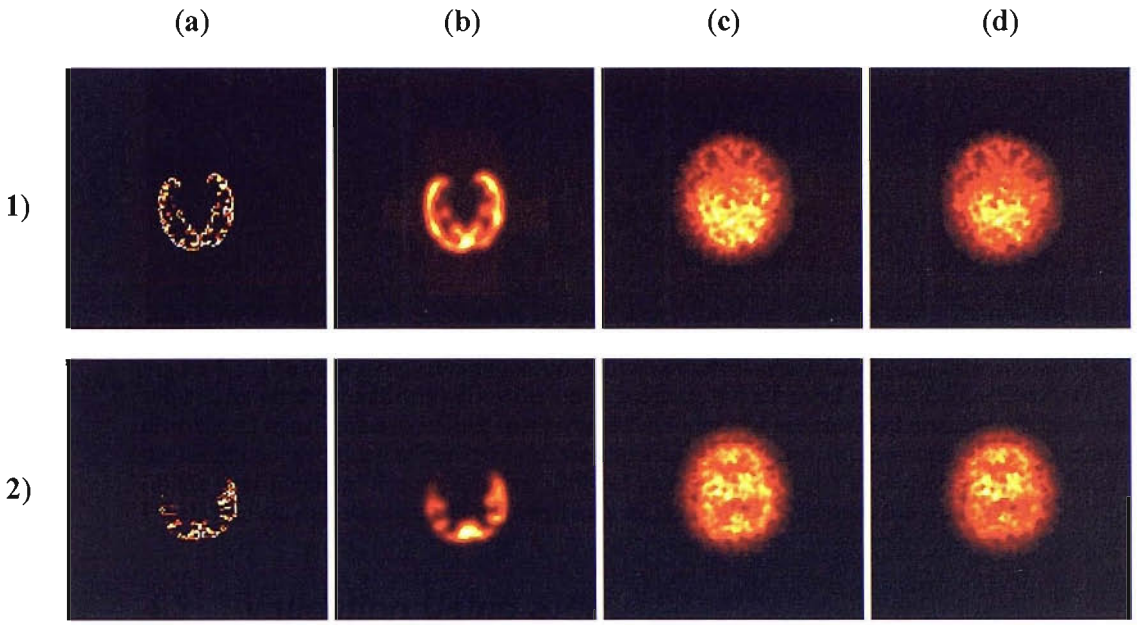

Figure 4.1. The basic simulation procedure for two different image slices (1,2) from an example subject, for an abnormality covering the entire occipital and temporal cortex; (a) the abnormal distribution transformed to subject space, corrected for partial volumes and masked with brain only, (b) the result of convolution of the PSF with the abnormal distribution, (c) the original normal image and (d) the final simulated abnormal image. Subject images are Gaussian smoothed (isotropic, 8mm FWHM) to aid visualisation and demonstrate a single axial slice through the abnormal region.

4.2 Validation Using SPM

Statistical Parametric Mapping (SPM) can be used in single photon emission computed tomography (SPECT) of regional cerebral blood flow (rCBF) to obtain a quantitative measure of the extent of abnormal perfusion. The simulation system is assessed here using SPM99 for two reasons. Firstly, it is important to ensure that the simulation system is producing results that are similar to those that would be acquired under normal operating conditions. This also ensures that unknown errors are not being introduced into the simulated images. Secondly, it is important to understand the sensitivity of a test for a given imaging and analysis technique. This method provides a qualitative analysis of parameters such as resolution and sensitivity.

The system is used to study the detection threshold of SPM99 in our clinical setting, and to validate the simulation system in the production of abnormal data. Validation is performed using the same subset of controls as described in section 3.1.1.1. The simulated images were assessed using standard SPM99 processing methods. The variation of sensitivity of abnormality detection with volume of perfusion deficit was determined for each abnormality, and inter-subject variation was assessed. Inference

proceeds on a cluster level for each abnormality. Results are obtained for cluster levels where a group of 100 or more significant voxels are connected.

4.2.1 Part 1 – Detection Thresholds

For the first part, a single subject image was used for simulation with comparison to a pre-defined control group. This ensures parameters are maintained constant wherever possible, and removes variability associated with inter-subject differences.

Four symmetrically paired abnormalities were stereotactically defined in the grey matter of the four major brain lobes in the reconstructed data. The abnormalities were defined directly in subject space and then constrained to GM by applying a mask in subject space. Volume growing was then applied to obtain the desired volume size. No partial volume correction or brain only mask was applied. The size of the abnormality was varied from 5.8cc to 17.4cc in four steps, and the intensity from 25% to 100% for each abnormality. Simulation was performed on the resultant distributions. Table 4-1 details the abnormalities simulated, along with actual sizes and Table 4-2 contains the detection characteristics for significant groups of voxels and significant clusters.

	Frontal		Temporal		Parietal		Occipital	
	Left	Right	Left	Right	Left	Right	Left	Right
5.8 ml	158	152	159	146	151	149	145	144
9.7 ml	255	255	260	254	251	244	258	241
13.5 ml	358	340	344	359	348	347	345	353
17.4 ml	460	467	456	447	451	459	456	449

Table 4-1. Individual abnormality description, showing the actual sizes of the simulated abnormalities in whole voxels.

	Left				Right			
	5.8 ml	9.7 ml	13.5 ml	17.4 ml	5.8 ml	9.7 ml	13.5 ml	17.4 ml
25 %	0	0	0	0	0	0	0	0
50 %	0	2	2	3 (1)	0	1	2	2
75 %	2	3	4 (2)	4 (3)	0	2	4 (2)	4 (3)
100 %	2	4 (2)	4 (4)	4 (4)	2	4 (2)	4 (4)	4 (4)

Table 4-2. Detection sensitivity for simulated abnormalities of different sizes at different intensities. The number of detected abnormalities at voxel level is shown, and the number detected abnormalities at cluster level is shown in brackets.

SPM analysis required a reduction of 50% for subsequent detection of significant abnormalities of all sizes, and similarly a minimum abnormality size of 9.7cc to detect

all levels of significantly reduced perfusion. 100% sensitivity was only achieved for abnormalities larger than 13.5cc with a complete reduction in perfusion. Sensitivity was considerably higher for the temporal and occipital lobe abnormalities compared to the frontal and parietal lobes. No abnormalities were detected at less than 50% perfusion reduction, and only one abnormality was assessed as significant at 50% reduction. The simulated to detected abnormality size is correlated for all regions with $r > 0.89$. The correlation coefficient was highest for the temporal lobes for 50% intensity and above ($r > 0.992$). No meaningful difference was witnessed between the two hemispheres of the brain.

4.2.2 *Part 2 – Inter-subject Variation*

The second part of the validation uses the same methods to simulate the same pattern of abnormality in eight different simulated abnormal subjects. This is performed to assess the reproducibility for the simulation with respect to the simulated abnormality distribution in different subjects, and also serves as a method of assessing the abnormal control group (see section 5.1.4 for a discussion). Abnormalities are simulated using an abnormality map defined in standard space and transformed independently to each subject, and are simulated using the full simulation system. The introduced abnormality is the complete grey matter region for the left side of the brain, has a volume of 266 ml, and is illustrated in Figure 4.2.

Subject Number	Transformed PV (ml)		Brain Only Masking (ml)			SPM99
	Size	weight	size	weight	% Red.[iii]	Detected
1	416	208	382	194	6.8	1520
2	354	181	345	171	5.3	929
3	417	209	395	200	4.1	1372
4	392	195	367	185	5.1	1429
5	370	184	359	180	2.1	1637
6	446	220	420	211	4.4	1503
7	407	204	387	196	3.7	1316
8	450	228	414	212	6.9	1808
Mean	406	203	384	194	4.8	1439
SD	34	16	26	14	1.6	258

Table 4-3. The results for the inter-subject variation for the same abnormality transformed to the different subjects. The results indicate the abnormality size and weight for different stages of the transformation process, along with the detected size using SPM99 and standard processing.

[iii] This is the relative percentage size difference for the abnormality image after applying brain only masking, with respect to the transformed and partial volume corrected image.

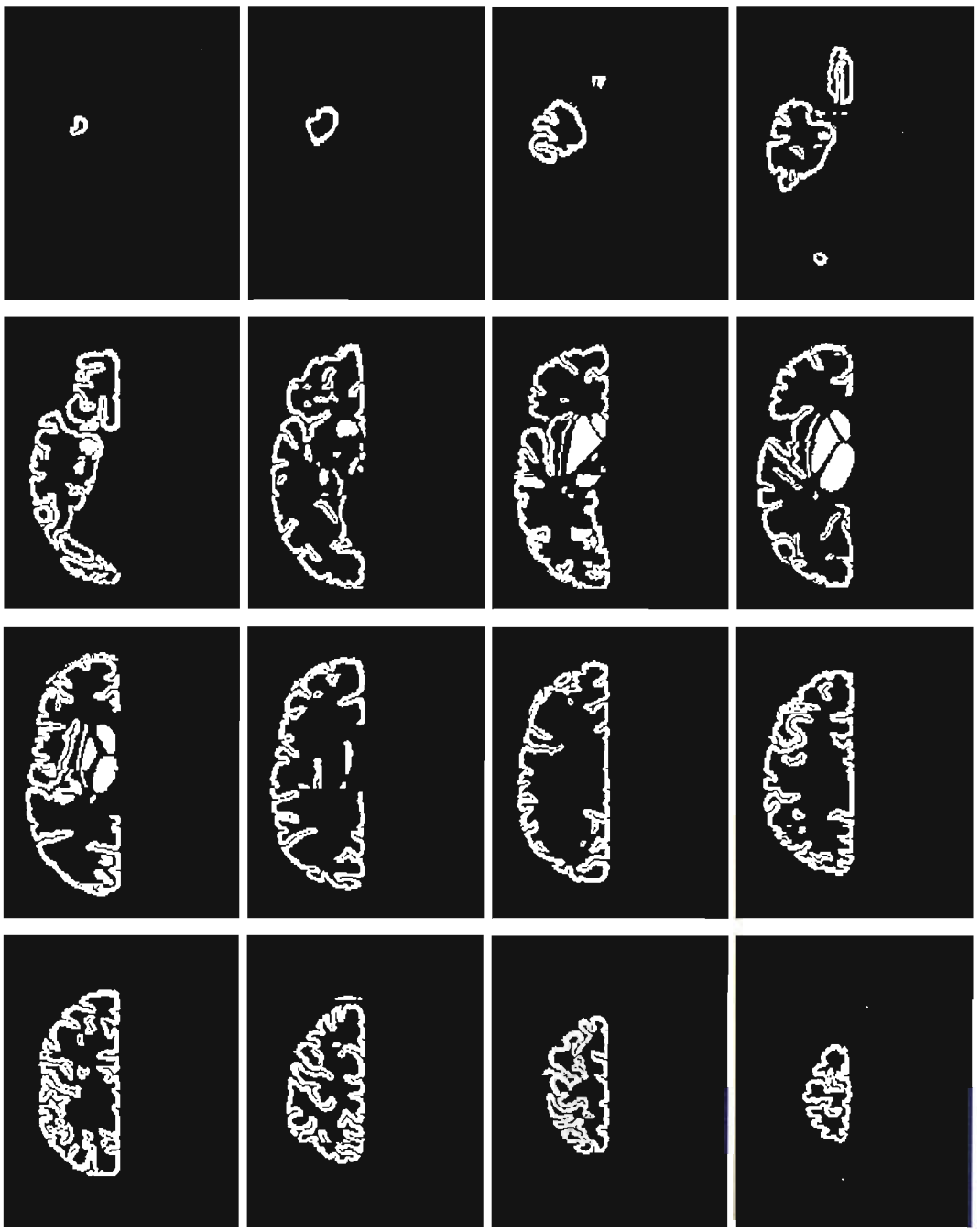

Figure 4.2. The ROI used to measure the inter-subject variation. Images are of axial slices every 8 mm for the valid range of the VOI.

Table 4-3 shows the results for abnormality definition and SPM99 analysis. The average transformed and PV corrected abnormality size was 203 ml, showing the atlas to be approximately 30% larger than the subject images. Applying the brain mask to the transformed input data caused an average of a 5% (maximum 7%, minimum 2%) reduction in the overall weight of the simulated abnormality. The small reduction in

the abnormal weight for all subjects demonstrates that the brain mask is quite accurate, and possibly too tight.

The weight lost during brain only masking should be zero in an ideal case, and the evidence of a reduction illustrates the necessity of this step. The loss is due to automatic spatial normalisation errors, using only affine transformation. Approximations are also evident in the conversion between Talairach and MNI space. The application of a brain mask reduces these errors, but introduces errors in the simulated count levels. These errors tend to influence how large an abnormality is perceived to be using SPM (at voxel level), although rarely changes the significance at cluster level. The results suggest that the threshold is over-sensitive, although results reported in section 5.1 show that this level of sensitivity is also attributable to the average defect intensity of the underlying abnormality.

The results also indicate that applying the brain mask results in a reduction in the variance of total abnormality weight across subjects. Reduction due to masking was acceptable in all cases as the magnitude of the deficit is much lower than the perfusion reduction required to be detected initially. There is large variation in the size of the detected abnormality when using SPM, which can be attributed to registration errors and the effect of specifying abnormalities near to the detection threshold.

4.3 An Audit Dataset for HMPAO Brain SPECT

The purpose of this experiment was to generate a set of abnormal subject images that could be used in the audit of cross centre analysis methods, facilitating a method of testing the efficacy of the methods. The subjects used for the generation of the data set are those described in section 3.1.1.1.

4.3.1 HMPAO Brain SPECT Audit Data

The abnormal group is subdivided to represent the three major dementia diseases, including Alzheimer's dementia (AD), fronto-temporal dementia (FTD) and dementia with Lewy Bodies (DLB). Two representations for each of the diseases were generated, and two subjects were used as normal subjects. Normal subjects were included to allow an objective assessment of the specificity of the applied analysis

method. The severity of the condition was randomised across the group. The regions used in the simulation are chosen to represent those associated with the dementia progression represented by the simulation. The data were repeatedly simulated and assessed to iteratively reach a realistic representation of the true disease. This was carried out with the help of a medical consultant in assessing the closeness to a clinically realistic result.

Table 4-4 gives a description of the representative data set, including the disease type, the severity, and a description of the simulated abnormalities. Figure 4.3 illustrates an example of abnormality distribution as used for simulation 1. Note that Figure 4.3 shows the underlying transformed distribution and not the simulated distribution.

Subject Name	Disease Type	Disease Severity	Affected Regions. (Left/right side, GM/WM involvement, region growing, attenuation)
Abnormal 1	DLB	Moderate/ Severe	Inf. Occipital Gyrus (L&R, GM, 1, no) Mid. Occipital Gyrus (L&R, GM, 1, no) Sup. Occipital Gyrus (L&R, GM, 1, no) Pre-cuneus (R, GM, 1, no)
Abnormal 2	Normal		None
Abnormal 3	Pre-senile AD	Mild/ Moderate	Inf. Parietal lobe (L&R, GM, 1, no) Sup. Parietal lobe (L&R, GM, 1, no) BA 39 (L&R, GM, 1, no)
Abnormal 4	FTD	Moderate Widespread	Med. Frontal gyrus (L, GM&WM, 0, 70%) Med. Frontal gyrus (R, GM&WM, 0, 50%) Mid. Frontal gyrus (L, GM&WM, 0, 60%) Mid. Frontal gyrus (R, GM&WM, 0, 40%) BA 21,28,34,38 (L&R, GM, 0, no) BA 8 (L, GM, 0, no) BA 22 (R, GM, 0, no)
Abnormal 5	DLB	Mild	Mid. Occipital gyrus (L&R, GM, 1, no) Inf. Occipital gyrus (L, GM, 1, no) Sup. Occipital gyrus (R, GM, 1, no)
Abnormal 6	FTD	Mild Widespread	Mid. Frontal gyrus (L&R, GM, 0, 60%) Sup. Frontal gyrus (L, GM, 0, 60%) BA 27,28,34 (L&R, GM, 0, no) Inf. Frontal gyrus (R, GM, 0, no) Uncus (L&R, GM&WM, 0, no) Hippocampus (L&R, GM&WM, 0, no)
Abnormal 7	Normal		None
Abnormal 8	Senile AD	Severe Widespread	Parahippocampal gyrus (L&R,GM&WM,0,no) Uncus (L&R, GM&WM, 0, no) Sup. Temporal gyrus (L&R, GM&WM, 0, no) Sup. Parietal lobe (L&R, GM&WM, 0, 75%) Inf. Parietal lobe (L&R, GM&WM, 0, 60%) BA 7 (L, GM, 0, no)

Table 4-4. Audit data group simulated parameters. The table indicates type of disease, the severity of the disease and lists the volumes that were affected, Left (L) or Right (R) hemisphere, grey matter (GM) or white matter (WM) involvement, region growing in pixels and applied overall percentage reduction. DLB = Dementia with Lewy Bodies, AD = Alzheimer's disease, FTD = Fronto-temporal lobe dementia.

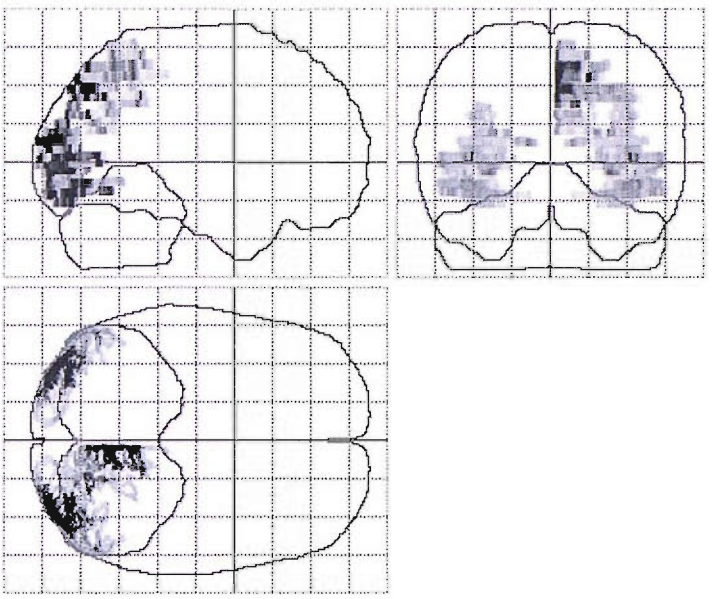

Figure 4.3. Abnormality distribution for abnormal simulation 1 normalised to MNI space and displayed as a maximum intensity plot on orthogonal planes. The brain overlay is a maximum intensity outline of the MNI database image. The image shows the original perfusion reduction at each voxel prior to transformation to subject space and convolution with the PSF.

Summary data is calculated as follows for each of the abnormal subjects, I_i^{ab}.

Equation 4.2 shows the effective volume (V_{eff}) for each abnormal subject image I^{sim}. This is calculated as the sum of intensities for each voxel, i, expressed in units of millilitres. This measure is used to incorporate the extent of a simulated abnormality into the volume measurement.

$$V_{eff} = v\sum_{i=1}^{N}\left(I_i^{ab}\right) \tag{4.2}$$

Where N is the number of voxels in the image and v is the volume of each voxel in ml. The mean simulated weight (MSW) for each abnormal simulation was also calculated using the abnormal distribution as shown in equation 4.3. This measure attempts to quantify the 'spread' of the simulated abnormality as a single value. A smaller value indicates that the abnormality is more dispersed, and a larger value indicates a more concentrated distribution.

$$MSW = \sum_{i=1}^{M} I_i^{ab} \Big/ M \tag{4.3}$$

Where i is a voxel such that $I_i^{ab} > 0.05$ [iv], and M is the total number of super-threshold voxels. The threshold was used to avoid counting voxels with negligible effect on the abnormal distribution. Table 4-5 shows the summary data for the abnormal subjects.

Simulation number	1	2	3	4	5	6	7	8
Total abnormal volume (ml)	128.1	0	176.9	264.4	79.7	144.8	0	237.7
Effective Volume (ml)	45.1	0	55.5	104.7	21.4	48.0	0	146.5
Mean simulated weight	0.172	0	0.187	0.153	0.147	0.115	0	0.212

Table 4-5. Summary of the simulated abnormal group

4.3.2 *Example Subject; Abnormal 3*

Figure 4.4 shows a comparison between a pre-senile AD simulation (abnormal 3) and an example of a routine clinical investigation of a 56 yrs male subject referred with probable Alzheimer's dementia. Both images show significant detected hypoperfusion voxels overlaid on orthogonal glass brain projections. The figure demonstrates the closeness of the simulation to a clinically realistic presentation of dementia, and illustrates the use of the method for generating realistic abnormal data.

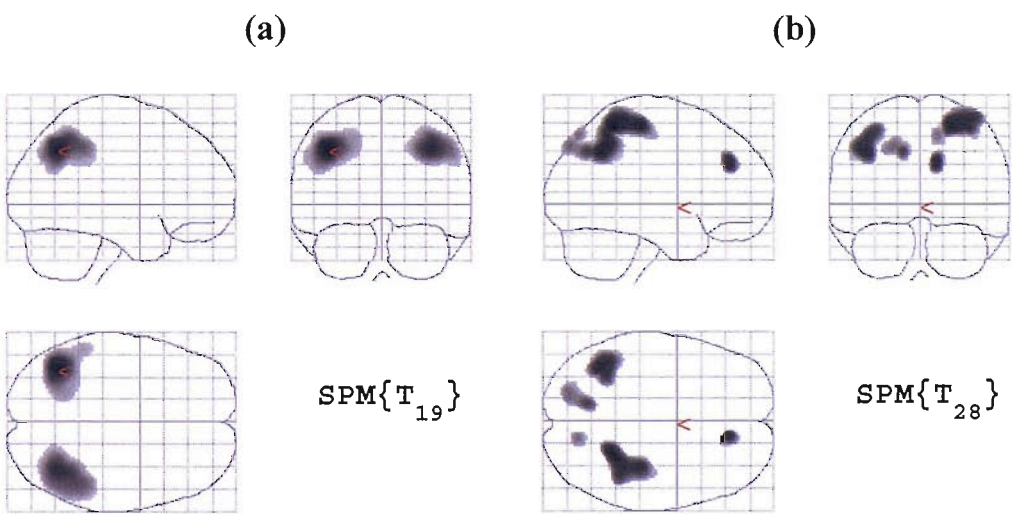

Figure 4.4. Comparison of (a) simulated result of analysis and (b) actual clinical data of an Alzheimer's disease, highlighting areas of statistically significant hypoperfusion

[iv] This value is chosen to reduce the large effect of small signal voxel intensities created by the tails of the PSF function.

4.4 Discussion

This simulation method using measured PSF data and existing patient images, offers fast simulation that cannot be achieved using less analytical approaches, such as Monte Carlo simulation, with complete simulation times in the order of 10 minutes. The inclusion of a stereotactic atlas and image registration allows for accurate anatomical positioning of abnormalities, enabling the simulation of realistic disease presentation through the use of prior information regarding disease pathology. As the images are based on real subjects, anatomical and physiological variation is already included within the images, and utilised though registration.

Abnormality position using an atlas of the human brain improves on the less realistic models of activity distribution discussed in [Radau *et al.*, 2001, Stamatakis *et al.*, 1999, Stapleton *et al.*, 1994]. When implemented with spatial normalisation and transformation the method allows for the anatomical positioning of the abnormalities within any subject space. Anatomical variation is thus included as part of the simulation system and real subject images can be simulated with arbitrary abnormal anatomic distribution, allowing realistic pathological variability to be included. However, the Talairach daemon is based on an atlas that was first derived using methods where exact region boundaries were assumed and registration errors are present. The error is minimised due to the poor resolution of the SPECT imaging technique. Manual mapping has been reported to be 85% accurate for within ±5 mm [Lancaster *et al.*, 2000], which is below brain SPECT resolution. Realistic anatomical supports have previously been used in simulation studies [Grova *et al.*, 2003] to produce data, though no method has been reported that produces realistic abnormal pathological data that is directly applicable to the audit of analysis methods. The simulated abnormality is introduced into the image through multiplication offering a method of preserving the noise in the image at a level relative to the intensity of the abnormality. This provides an approximation to the true noise level in the reconstructed image, which removes the need to incorporate a model for noise into the simulation system. One advantage of the method is its relative simplicity. While the method improves on simulation techniques for system analysis such as [Radau *et al.*, 2001, Stamatakis *et al.*, 1999], generic methods are used with simple models to create a system that is reproducible with minimal technical knowledge. Furthermore, the

method is easily expanded for use in different environments or different processing and analysis methods. Methods such as that described by [Grova *et al.*, 2003] require considerable effort to implement any change in the source or simulation system.

The results from the SPM99 validation (section 4.2) show that generated abnormalities are detectable, and that the detected size of the abnormality is correlated with the size of the simulated abnormality when sufficiently large or intense. The results also indicate that the sensitivity of the analysis method is highly variable and correlated with both location and intensity. This is thought to be predominantly due to differences in anatomy that cause variation in the physical properties of emissions, and also errors due to the registration process. After applying the brain mask, similar size results were achieved for a large abnormality, indicating that the simulation process is valid across different subjects.

There are currently several limitations of the simulation system, most notably the type of output data. As is, the method is not applicable to production of planar projection data, which is the usual starting point for analysis protocols, which limits its use in analysing reconstruction methods. However, more advanced methods exist to obtain this type of simulated data [Ma *et al.*, 1993, Yokoi *et al.*, 2002]. This limitation may also require that standard protocols are adjusted. While the effects of noise are minimised through the use of high counts in the PSF measurement, these effects cannot be totally removed, which introduces errors. This could be approached by using three-dimensional mathematical modelling of the PSF incorporating these parameters [Yokoi *et al.*, 2002]. It is well known that the PSF is position variant, and dependent on the amount and constitution of surrounding attenuating material. This variability in the PSF is considerably reduced when using reconstructed data from a 360° acquisition as the partial volume effects are averaged over each planar acquisition. Thus a position invariant PSF was used for this study. Scatter correction is not employed in the image reconstruction process for the PSF, as the original data was selected retrospectively and had no applied correction when acquired. While these effects are clearly a limitation of this implementation, the principle of the methods described remains the same.

Affine registration is used to transform the abnormality into the subject space, which does not take into account individual local anatomical differences, and errors may be

evident in the positioning of the abnormalities. It is possible to use the inverse of the SPM non-linear warping algorithm to transform an abnormality while incorporating warps, but this method introduces large levels of interpolation when using a small set of basis functions, and isn't used in the simulation system. The errors associated with affine transformation are generally small compared to the FWHM of the PSF.

The method discussed here produces data that are directly comparable to routine studies, as the simulated images are based on clinically acquired data. The basic principles of the method can be applied to generate abnormal functional data for any SPECT or PET system configuration by using existing normal images. A set of HMPAO brain SPECT data has been generated that will be used in a cross-centre audit of analysis methods. This procedure is currently being successfully implemented in lung perfusion studies [Fleming *et al.*, 2004] and is governed by the Nuclear Medicine Software Quality Group of the Institute of Physics and Engineering in Medicine (IPEM), whose role is to evaluate concordance across various software packages designed for the same routine clinical task. Initial viewing of the dataset by an experienced nuclear medicine consultant has confirmed the images to be representative of the intended disease pathology, and that the results show variation in the detection of the introduced abnormalities. The data set is intended to be used as a reference for the comparison of analysis methods, and also to offer a method of improving these methods through the establishment of ground truth. Generated data can also be used in the optimisation of different analysis methods for individual sites, by synthesising abnormalities and adjusting the parameters of the analysis methods to achieve the optimum representation of the original distribution.

The generated dataset could be used in a cross-centre audit of analysis methods. Collation of the data across centres will reveal problems arising from different methods of analysis and different aspects of the analysis procedure, and provide a method of systematically rectifying problems and approaching overall conformation in the area of HMPAO brain SPECT analysis and reporting.

4.5 Conclusions

A method has been described for the fast simulation of realistic abnormal images through the use of known normal data and a measured point spread function. The method provides anatomical and physiological variation in the simulation results, and includes a method for stereotactically positioning abnormalities within any subject. We have demonstrated that the method is useful in the fast generation of realistic abnormal images which makes the method feasible for large datasets. These results suggest that the simulation system is valid for use in the simulation of data sets that can be used to test the sensitivity and specificity of a given analysis method, with reference to normal range.

Chapter 5 Analysis and Cross-Validation of Quantitative Analysis Techniques

We concentrate here on the use of the audit data set in the validation of SPM99. We present a thorough analysis using SPM99, and a cross comparison to the BRASS method.

The use of the data set is demonstrated using SPM99 for voxelised whole brain analysis and the MarsBaR toolbox [Brett *et al.*, 2003] for VOI analysis. The data set is also analysed using BRASS for regional analysis. Finally, a cross-comparison of the two analysis methods is presented.

5.1 Analysis of SPM99 and MarsBaR

5.1.1 Control Subject Processing

Pre-processing was carried out using the standard methods described in section 3.2.

Two image sets were created by smoothing using a 16 mm and 13.8 mm FWHM Gaussian kernel representing the standard clinical procedure and the measured system resolution of the camera respectively. For subsequent statistical analysis, both sets of images were compared with like images.

Cerebellar normalisation was then implemented using a 14 mm (for 13.8 mm smoothed) and 16 mm (for 16 mm smoothed) diameter spherical VOI as described in section 3.7.4.)

5.1.2 SPM and VOI Analysis

Analysis was performed on the pre-processed images by comparing a single individual subject image to the control group on a voxel by voxel basis using a two-sample t-test. The analysis threshold was set at 70% of the global mean. Leave one out analysis was performed on control subjects for both the 13.8 mm and 16 mm smoothed data sets to ensure the analysis method was not introducing false positives

into the results. Uncorrected voxelwise SPM maps were generated for each subject image and analysed at different threshold p-values. Results were obtained showing clusters of voxels below threshold values of $p< 0.05$, 0.01, 0.005, 0.001, 0.0005 and 0.0001 (uncorrected), for clusters with more than 100 connected supra-threshold voxels. For SPM analysis, a subject was considered to be abnormal if the analysis showed significant hypoperfusion at cluster level ($p<0.05$ corrected) within the brain. The threshold levels were then evaluated by comparing the total effective volume of simulated abnormalities for each subject, j, V_{effj} (from equation 4.2), to the total supra-threshold detected volume DV_j in ml for that subject. For each threshold, k, the sum of squared errors (SSE) was calculated from the following;

$$SSE_k = \sum_{j=1} \left(Veff_j - DV_j \right)^2 \qquad \textbf{(5.1)}$$

VOI analysis was performed on all studies to resolve abnormal regions on an anatomical basis, as the full extent was unavailable using voxelwise results alone (i.e. large abnormal regions covering more than one area). Sensitivity and specificity were calculated for both the 13.8 mm and 16 mm smoothed data sets, and used to indicate the accuracy of the methods. This was carried out using the MarsBaR SPM toolbox [Brett *et al.*, 2003], and subsets of the anatomical VOI's as described below. The results were based on treating the lobes and major subdivisions of each lobe independently, and assessed the ability of the respective method to identify a simulated defect in each volume. Three different sets of left and right sided VOI's were independently analysed;

1. 16 independent left and right whole brain regions, termed *lobar VOI's* defining the major lobes consisting of frontal, parietal, occipital, temporal, limbic, sub-lobar and midbrain regions.

2. 66 independent left and right gyri, termed *gyral VOI's* as subdivisions of each lobe consisting of:

    a. 14 frontal lobe gyri; white matter, middle, inferior, medial/paracentral lobe, rectal/orbital and precentral gryi

b. 12 parietal lobe gyri; white matter, superior, inferior, pre-cuneus, angular/supramarginal and postcentral gyri

c. 10 occipital lobe gyri; white matter, superior/middle, inferior/fusiform, cuneus and lingual gyri

d. 8 temporal lobe gyri; white matter, superior/transverse, middle/inferior and fusiform gyri

e. 10 limbic lobe gyri; white matter, posterior cingulate, cingulate, anterior cingulate/hippocampus and Parahippocampal gyri

f. 12 sub-lobar; extra nuclear/undefined, corpus callosum/lateral ventricle, thalamus, putamen/globus pallidus, caudate brain and insula

3. Independent VOI's representing the actual simulated defects for each of the simulated data set, termed *abnormal VOI's*.

A Bonferroni correction was applied for each of the three sets of VOI's. For 3 above, each simulated abnormality was defined as an independent VOI and analysed with respect to the relevant image. This was carried out to allow assessment of the detection of individual abnormalities. For 1 and 2 above, sensitivity and specificity were calculated for each subject independently using each lobe of the brain as an individual measurement, where any significant detected abnormality inside of a lobe indicated an abnormal lobe. For specificity measurements, all regions where no abnormality was simulated were treated as a single region. Sensitivity is given as the ratio of correctly identified abnormalities to total simulated abnormalities and specificity is given as the ratio of correctly identified unaffected regions to total unaffected regions.

5.1.3 SPM and VOI Analysis Results

Both 13.8 mm and 16 mm smoothed data sets have been analysed using SPM99. Figure 5.1 shows the resultant detected abnormality distributions for the example distribution given in Figure 4.3 for SPM99 analysis of 16 mm and 13.8 mm data, illustrating regions of detected significant hypoperfusion ($p<0.001$) compared to the control group using a two sample t-test. The results show that both methods detected

all simulated defects, and illustrates slight differences in the shape of the detected defects.

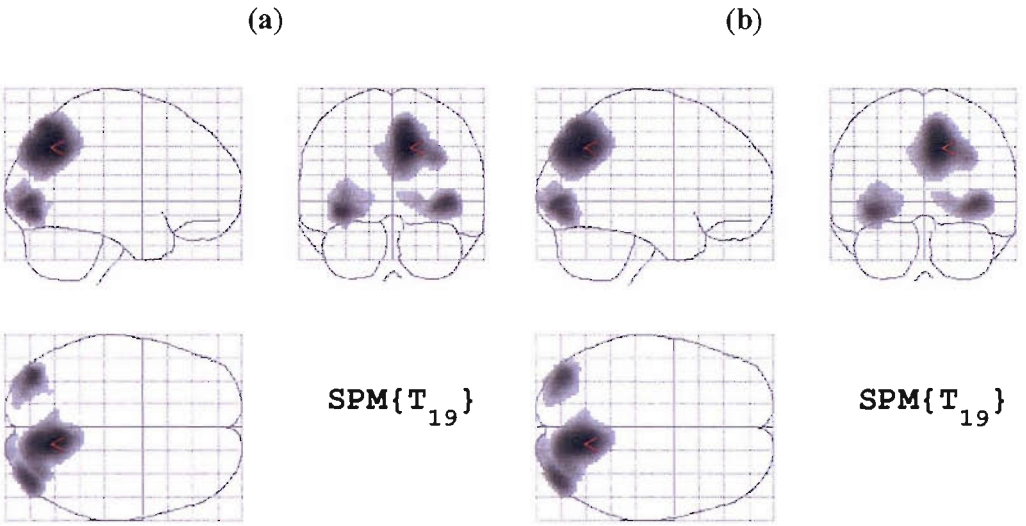

Figure 5.1. Result of SPM99 analysis on the simulation from data in Figure 4.3. Areas of significant hypoperfusion are shown as a maximum intensity projection for a) 13.8 mm smoothed image and b) 16.0 mm smoothed image.

Using the detection of at least one abnormal cluster with $p<0.05$ as the basis of an abnormal image, SPM analysis gave a sensitivity of 67% (4/6 TP) and a specificity of 100% (0/2 FN) for both the 13.8 and the 16 mm smoothed data sets.

In comparing the detected size of abnormalities in each subject with the effective volume, the sum of squared error (SSE) was found to reach a minimum at a threshold of $p<0.0005$ (uncorrected) for both the 16 mm (SSE=5918) and 13.8 mm (SSE=4606) smoothed data, and the difference between the results was shown to be significant ($p<=0.0625$, Wilcoxon matched-pairs signed-rank test). Analysis of the 13.8 mm smoothed images produced a closer correspondence to simulated defects than the 16 mm smoothed data for the routinely used threshold ($p<0.001$ uncorrected). The SSE was 10938 for 16 mm smoothed and 6139 for 13.8 mm smoothed data. Table 5-1 shows the abnormal volume detection characteristics for the simulated dataset for 13.8 mm smoothed data, indicating the total volume of the abnormality, its effective volume, the mean weight for the simulated distribution and the significantly hypoperfused volume determined by SPM99 analysis at $p<0.001$. Figure 5.2 shows the data graphically, and also illustrates the correlation between the mean simulated weight and the detection error for each subject. Significant correlation is shown

between the effective volume and the total detected abnormal volume ($r=0.932$, $p < 0.001$) and between the mean simulated weight of the abnormality and the error in the size of detection ($r=0.954$, $p<0.001$).

Simulation number	1	2	3	4	5	6	7	8
Total abnormal volume (ml)	128.1	0	176.9	264.4	79.7	144.8	0	237.7
Effective Volume (ml)	45.1	0	55.5	104.7	21.4	48.0	0	146.5
Mean simulated weight	0.172	0	0.187	0.153	0.147	0.115	0	0.212
Detected volume ($p<0.001$)	54.1	0	55.4	89.9	3.2	0	0	203.1

Table 5-1. Detection of significantly hypoperfused abnormal voxels showing the size of the total abnormal volume against the significant detected size using SPM99 for 13.8 mm smoothed data at $p<0.001$ (uncorrected). The effective volume is calculated as the sum of the simulated abnormal voxel intensities, and the mean simulated weight is the 5% threshold mean weight of the simulated distribution.

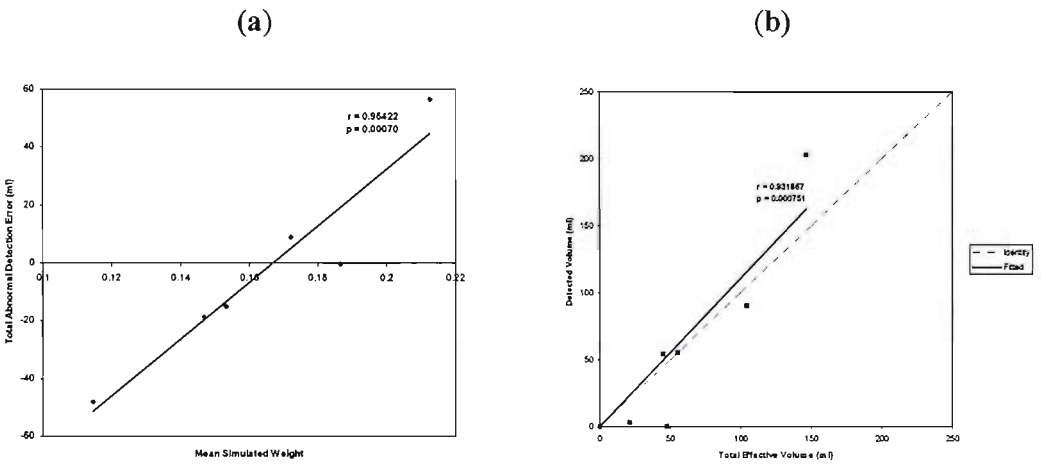

Figure 5.2. Graphs showing correlation between (a) detection error and mean simulated weight for each subject, and (b) total detected abnormal volume and total effective abnormal volume (size × intensity). Both graphs are for the simulated data group for 13.8 mm smoothed data at $p<0.001$.

Table 5-2 shows the sensitivity results of the MarsBaR analysis for the 13.8 mm and 16 mm smoothed images for the mean and median comparison. All analyses gave a specificity of 100%. An increase is sensitivity is evident when using the median over the mean values and when using gyral or abnormal analysis over lobar. However no significant difference was found between any of the groups. The results are presented for the three groups of analyses described in section 5.1.2, and are the results for successfully detected simulated abnormality. At patient level, irrespective of the type of region or summary function, the method was 66 % sensitive and 100 % specific. The abnormal regions had a higher sensitivity of 83 %, although was less sensitive when using the median at 16mm.

	13.8 mm smooth			16 mm smooth		
	Lobar	Gyral	Abnormal	Lobar	Gyral	Abnormal
Mean	30.43	56.52	55.88	30.43	52.17	55.88
Median	34.78	56.52	55.88	43.48	56.52	55.88

Table 5-2. MarsBaR sensitivity results in percentage for the two sets of smooth data, showing the detection characteristics for the entire data set for each set of VOI's using the mean and the median.

5.1.4 Discussion

The SPM99 leave one out analysis for both the 16 mm smoothed and 13.8 mm smoothed data detected significant hypoperfusion in control 16, in the right anterior sub-lobar region. The abnormality could be explained by a widening of the ventricles. The leave one out analysis for the 13.8 mm smoothed data also showed control 17 to contain a significant abnormality in the posterior-inferior aspect of the right occipital lobe. This discovery is consistent with a widening of the fissure between the cerebellum and the occipital lobe being detected due to the reduction in the size of smoothing. Both subjects can be explained by normal ageing and had normal clinical presentation according to the NINCDS-ADRDA criteria. Therefore they are assumed to be normal while exhibiting abnormal characteristics and are not omitted from the control group.

Results obtained using SPM99 analysis can often be difficult to interpret on a regional basis when a large number of significant voxels are detected and results of independent regions analysis are required. This is due to larger clusters overshadowing the neighbouring clusters, possibly when the original abnormal distributions are distinct. The SPM result contains information on local maxima and as such the results will usually report only the cluster maximum and a few local maxima (where they exist). In this case, inference within the region of interest can only proceed on a voxel-wise basis, which considerably reduces the power of the statistical test. VOI analysis can alleviate these problems by analysing distinct regions independently and inferring statistics on these alone, which also limits the number of multiple comparisons. VOI analysis is powerful when analysing functional data with an accurate functional or anatomical atlas. This can be seen when comparing the accuracy of detection between lobar and gyral analysis, showing a substantial increase in sensitivity with no cost to specificity (Table 5-2). As expected, these differences were not shown to be significant due to the relatively small size of

the group, and a larger study would be necessary to fully explore the significance of this finding.

SPM99 analysis was used to assess the detection characteristics for the whole brain volume. Confirmation of abnormality detection was achieved by analysis of correlation showing the size of abnormality detection to be significantly and highly correlated with the effective volume of the inserted abnormality. The detected size of an abnormality can be directly related to the severity of the underlying hypoperfusion, and SPM was shown to underestimate the extent of mild abnormalities and overestimate the extent of severe abnormalities (Figure 5.2). Current routine analysis using SPM99 employs a 16 mm FWHM Gaussian smoothing kernel. However, the results of this study show that using a 13.8 mm (in line with the system resolution) generates results that more accurately reproduce the original abnormal distribution. This is contrary to reported results in [Van Laere *et al.*, 2002a], which state an optimum at around 18 mm. However, the optimum was selected by achieving a maximum t-statistic to show evidence of an activation, where SPECT brain studies are aimed at producing an accurate representation of the underlying dysfunction. Smoothing at 13.8 mm improves the significance of the individual detected abnormalities for gyral anatomy, although lobar abnormalities are more easily detected when using 16 mm smoothing. Using a 13.8 mm kernel also improves the detection size to simulated size relationship for SPM99 over the 16 mm smoothed images. This indicates that the current clinical protocol could be improved by including a smaller smoothing kernel. The use of $p<0.0005$ (uncorrected) as the significance threshold for voxel-wise analysis further improves the detection accuracy of the original distribution extent. Using the median over the mean in MarsBaR analysis has a similar but less pronounced effect for individual abnormality detection, particularly for large volumes. Combining the larger smoothing kernel with the median produced the best results for larger VOI's due to the effect of spreading out of the abnormality resulting in more small value voxels, and hence a lower median value. When attempting to determine abnormal gyri within a lobe, an improvement is witnessed when using the median compared to the mean, once again particularly for large VOI's. Overall, the median performed better than the mean when analysing the dataset using MarsBaR.

The abnormal VOI's were included to assess how well abnormalities were being detected and to offer a method of determining the characteristics that made detection difficult. As the same spatial registration (without non-linear warping) was used for the insertion of the abnormalities as well as the detection of the abnormalities using MarsBaR, the method should offer near point to point correspondence between the simulated defect location and the location of the VOI, although registration errors may be pronounced in abnormal regions [Radau *et al.*, 2001]. The only other factor affecting the registration is the application of the brain mask, which may result in a larger summary value (i.e. mean or median) than expected. As a result, small abnormalities on the edge of regions (such as in surface grey matter) were difficult to detect. Detection problems existed primarily for Brodmann areas, particularly where defined in relative isolation to the rest of the VOI. This is due to the small size of the original abnormality not producing a detectable decrease in activity. Abnormalities were easily detected when neighbouring regions contained abnormalities, even when defined as low as 40%, particularly where the neighbouring regions were large. The most commonly missed abnormality was in the superior occipital lobe, and also the inferior occipital lobe (to a lesser degree). This is due to problems with the transformation between Talairach and MNI coordinate systems, which results in definition of occipital lobe regions partly outside of the cerebrum [Brett *et al.*, 2001], which are subsequently removed. This was not evident when using manually positioned VOI's as these were defined to be the correct size even after brain masking As expected, the main factor affecting the detectability of an abnormality was the deficit of activity contained in it and surrounding regions. The exception was where the region was sufficiently large. Secondary factors were the position and the influence of the partial volume effect. Inclusion of the warping algorithm in the spatial transformation of the VOI's to subject space could improve the sensitivity of detection by accounting for small anatomical differences.

The spread of the source activity, mainly due to the partial volume effect and scatter, is an issue with quantification where large, closely assembled and intense abnormalities create larger reductions, and small, sparse and less intense abnormalities cause the distribution to be dispersed. This effect can be seen when considering the mean simulated weight (Table 5-1 and Figure 5.2(a)). This value effectively quantifies how distributed an abnormality is, and a significant correlation

is evident between this value and the abnormality detection error. An approximate value of 0.17 (zero cross over point on Table 5-1) represents accurate estimation of the abnormality size, with deviation of approximately 0.02 above causing overestimation and below causing underestimation. This effect will also influence the results of VOI analysis when using small volumes, as an abnormality in a region will spread to neighbouring regions, creating the erroneous effect of hypoperfusion in these regions. Theoretically, this value could be approximated from the SPM distribution and iteratively applied to the same distribution in an attempt to correct for this error. Studies have demonstrated significant differences between scatter corrected and non scatter corrected images for normal subjects [Shiga *et al.*, 2002], and these effects could substantially influence the results of quantitative analysis. Lack of scatter correction has been found to be the largest single factor affecting the sensitivity of SPM [Van Laere *et al.*, 2002a]. These results indicate that the use of a scatter correction technique could improve quantification by reducing the spread of the source activity, which would lead to a more accurate detection of the extent of an abnormality. The results generated in this study show relatively low sensitivity, and is intentionally designed into the data set such that the simulated defects are not necessarily easily detectable. The sensitivity estimate will be less precise for the small number of controls and improvements to the accuracy of sensitivity of quantitative analysis would be expected when using a larger control database.

5.2 Analysis Using BRASS

Analysis of BRASS was performed to provide data that could be used to compare the results of two different techniques. Analysis was performed using standard methods to provide a useful comparison. The method is similar to SPM99 in that whole brain voxel-wise analysis is performed on registered data. VOI analysis is also available as a standard feature of BRASS, and was also assessed through comparison with the results from MarsBaR.

5.2.1 BRASS Analysis

BRASS analysis is performed using the same data set used for SPM99 analysis, acquired as described in section 3.2. This includes the standard acquisition, filtering,

reconstruction and masking. Output images are resampled and interpolated to have a standard image resolution of 64x64x64 voxels with voxel size of 3.5 x 3.5 x 3.0 mm. For analysis, image smoothing was carried out using a Butterworth filter of order 10, cut off 0.65 to give a FWHM of approximately 16mm (similar to standard SPM99 processing). Count normalisation is performed individually using the mean count in the cerebellum for all subjects, and including only voxels above 40%.

The BRASS software includes a standard region map that gives co-ordinate positions in three-dimensional Talairach space, and also provides the regions for VOI analysis. The regions in the standard template differ to those described above. For comparative analysis, the VOI's were replaced with the same model used in section 5.1. This was performed by resampling and interpolating the Talairach atlas to the same coordinate system describe above, and manually translating the database such that it aligned with the existing template image. The BRASS software also provides a standard ECD template for analysis of SPECT images, which is registered with the default region map. As there are differences in uptake between ECD and HMPAO in normal controls and AD [van Dyck *et al.*, 1996, Hyun *et al.*, 2001], it was necessary to generate a new HMPAO normal model from the audit control database for comparison with the controls.

5.2.1.1 Normal HMPAO Model Generation

The normal subject images (n=20) were individually spatially registered to the standard BRASS ECD template, using a 9-parameter transformation (3 parameters for each axis; scaling, translation and rotation), and maximising normalised mutual information. The registered images were count normalised and combined with the Talairach region map to generate the normal model using Modelgen (version 2.0) on HERMES. Analysis is performed without any correction for scatter or partial volumes.

5.2.1.2 Voxel-wise Analysis

Voxel-wise analysis was performed using the audit subject group, and assessed using the normal HMPAO model. Each abnormal image is analysed by comparison to the normal model mean and standard deviation images. A SD analysis threshold is defined, and abnormality is indicated by a voxel level above or below the threshold

value. This was assessed for sub-threshold clusters larger than 5 ml in volume. Only voxels above 50% of the maximum image intensity in the template image are included in the comparison. This is the standard value used for BRASS analysis, and is included such that analysis proceeds using only voxels within the cerebrum. A voxel-wise leave-one-out analysis was also performed on the data set using the normal HMPAO model.

5.2.1.3 Regional Analysis

Regional VOI analysis was performed using the generated model and template. For regional analysis, the sensitivity and specificity are assessed at different SD threshold values. A leave-one-out analysis was also performed on the audit control group using VOI analysis of the normal HMPAO model and template, at different threshold levels.

5.2.2 Results

Table 5-3 shows the results for leave-one-out analysis of the control group for both voxel-wise and VOI analysis, indicating the achieved level of sensitivity for different analysis thresholds.

Analysis Threshold (# SD)	2	2.5	3	3.5	4
Voxel-wise Specificity (%)	55	55	75	95	100
VOI Specificity (%)	25	55	70	85	90

Table 5-3. Leave-one-out analysis of the control group using the generated normal HMPAO model. The level of sensitivity achieved is reported for different analysis thresholds.

The results suggest that a threshold of at least 3.5 SD is required to obtain the required high level of specificity. At this threshold value, 95% specificity was achieved in the leave-one-out analysis of voxel-wise data, and 85% specificity for VOI analysis. Increasing this value to 3.75 SD's increased the VOI analysis specificity to 90%.

Analysis of the abnormal group at 3 SD using gyral regions yields a sensitivity and specificity of 74 % and 75 % respectively. At four SD these values were 48% sensitive and 100% specific. An optimum was found for 100 % specificity at 3.75 SD with 52% sensitivity. This analysis demonstrates that large increases in sensitivity can be achieved by reducing the detection threshold for BRASS. This increase is accompanied by a decrease in specificity. The method suggests an optimum of 3.75 SD for VOI analysis, which maintains 100% specificity while maximising sensitivity.

5.2.3 BRASS vs. SPM

Table 5-4 contains shows the summary sensitivity and specificity for the two equivalent analysis methods for SPM99 and BRASS. As the results show, both methods produce identical significance results, and no difference was witnessed between detected abnormal regions. Equivalent methods are used for both sets of results, i.e. 16 mm smooth, 3.75 SD threshold for BRASS, $p < 0.001$ for SPM, and show set level for voxelwise analysis and lobar level for VOI analysis.

Analysis Result	SPM99	BRASS
Voxel-wise Sensitivity (%)	67	67
Voxel-wise Specificity (%)	100	100
VOI Sensitivity (%)	52	52
VOI Specificity (%)	100	100

Table 5-4. Results for comparison of SPM99 and BRASS for voxelwise and VOI analysis. The results are indicated for analysis using 16 mm smoothing for both methods. Voxelwise results are for the entire volume using a threshold of $p < 0.001$ for SPM, and $SD > 3.75$ for BRASS. VOI results are at lobar level.

5.3 Discussion

Volume of interest (VOI) analysis was performed using both SPM (using MarsBaR toolbox) and BRASS analysis methods to assess the sensitivity and specificity of detection of abnormalities. Leave one out analysis was performed on the control data using the same VOI analyses. The threshold for abnormality detection for both methods was adjusted to give better than 90% specificity for the leave one out analysis.

For BRASS analysis, the leave one out analysis shows the production of a large number of false-positive results when using an analysis threshold at or below 3 SD. The results also suggest that this value should be above 4 SD for all analysis, to maintain the necessarily high level of specificity. However, several of the false-positive findings in the leave-one-out analysis appear to be edge effects. Voxel-wise analysis is particularly prone to registration errors, and tends to produce erroneous results around the surface of the brain. The edge effects in BRASS can be explained by errors in the registration process due to the low number of parameters used in the transform. Also, as the analysis threshold is set based on the normal template image, analysis may proceed where the original data is poorly registered leading to erroneous results.

The SPM VOI leave one out analyses showed only 2 false positives, while BRASS showed false positives in 6 of the control subjects at the default analysis threshold of 3 standard deviations (SD's). The BRASS threshold was adjusted to 3.75 SD's to achieve 90% specificity in the leave one out analysis. The abnormal VOI analyses showed BRASS to have a higher sensitivity than SPM at 3 SD's (74% vs. 52%), whereas the specificity was only 75% compared to 100% for SPM. Using a 3.75 SD threshold for BRASS, both methods produced identical results.

The creation of the normal model using BRASS requires reducing the resolution of the original data. As the template values indicating the region are discrete, it is not possible to correct the image for partial volumes as any given voxel requires that the value be interpolated from the original template. This results in error in the measurement of counts as the regions are of different shape and size.

SPM99 analysis uses a more complex model for statistical inference, with a multiple comparisons correction that is less severe than Bonferroni correction. BRASS does not use any correction for multiple comparisons on voxel-wise data, which partly explains the low level of specificity witnessed in the leave-one-out analysis.

The use of realistic ground truth allows for the assessment of the accuracy of analytical methods for real data. We have shown that both BRASS and SPM can produce similar results as long as the correct significance thresholds are identified. Care must be taken when selecting a threshold level for detection of abnormality for quantitative analyses methods. There is a trade-off when attempting to detect abnormal perfusion, and it is more important to maintain a high level of specificity while sacrificing sensitivity. It is difficult to obtain high sensitivity and specificity simultaneously due to the errors involved in SPECT imaging, particularly when dealing with mild disease. The results indicate that both methods require large or intense abnormalities to realise a high sensitivity, which is a physical property of the imaging system and subject, and not a property of the analysis technique.

The use of known ground truth allows an objective comparison of analysis methods, allowing decisions to be made on how to best maximise sensitivity and specificity simultaneously. These initial analysis results demonstrate how variations in the analysis technique can be evaluated and optimised using the simulated data. The

analysis of the data set using routine clinical methods highlights the need to update these analysis methods to obtain maximum efficacy, and suggests some such improvements.

Another important factor to consider is the nature of the software. SPM is a public domain package, which is supported entirely by the scientific community. BRASS is a commercial package, and an addition to the HERMES workstation. The cost of BRASS should be weighed up with respect to the dedicated support obtainable from commercial software, and the freely available SPM, as both packages perform equally well.

Chapter 6 Estimating and Simulating Brain Biodistribution of HMPAO

This chapter presents the methods used to obtain an estimate of ^{99m}Tc-HMAPO biodistribution within an anatomically accurate model of the normal human brain. A previously described standard anatomical model of the brain is used as a template. This is derived from a single normal MRI image, and was modified for use in this study due to limitations in accuracy. A varying level of activity is estimated for each anatomical region using iterative approaches. The estimated activity levels can then be used with the anatomical support to generate simulation objects that can be used with SimSET. A discussion of the application of the methods to normal brain modelling is also presented.

At this point, it is worth noting that these methods are designed to be specifically applicable to regional count distributions as opposed to voxelised activity distributions. The main aim is to generate a model that can provide the basis for normal modelling, with application in emission imaging of the brain. We are attempting to reduce the dimensions of the model and define regions of homogeneous tracer uptake, whereas full voxelwise reconstruction has been approached in other literature. [Floyd *et al.*, 1987, Kadrmas, 2001, Vandenberghe *et al.*, 2001].

6.1 Anatomically Accurate Normal Brain Phantom

The most important aspect for modelling in a study of this type is an accurate anatomical support. There currently exist several general-purpose digital representations of the human head that are freely available in the public domain, such as the digital Hoffman brain phantom [Hoffman *et al.*, 1991] and the Zubal phantom [Zubal *et al.*, 1994]. There also exists a complement of purpose made (usually segmented from MRI or CT) phantoms that have been incorporated into simulation systems [Evans *et al.*, 2001, Kim *et al.*, 1991]. Monte Carlo techniques have been used to perform simulation using these phantoms although quantitative evaluation in the literature is sparse.

Several different phantoms were originally evaluated for the creation of the SimSET activity and attenuation objects with the aim of simulating normal SPECT, with the priority being a realistic anatomical representation. Manual segmentations of CT or MRI data sets were also considered. While the digital Hoffman phantom is useful as it has a physical counterpart, the phantom could not be used due to the lack of realism and anatomical correctness. The visible human project (National library of medicine) [Ackerman, 1991] is a useful resource, but the phantom only contains intermittent slice data for the head, has a lower resolution than the Zubal phantom and lacks complete anatomical segmentation. The Talairach VOI's described in section 3.4 were also considered, but contains cerebral only regions, requiring complete modelling of extra-cerebral structures from a different source. The rest of this section concentrates on the Zubal head phantom as simulation object source, and presents the methods used for the implementation of the phantom in modelling normal cerebral HMPAO SPECT.

6.1.1 The Zubal Head Phantom

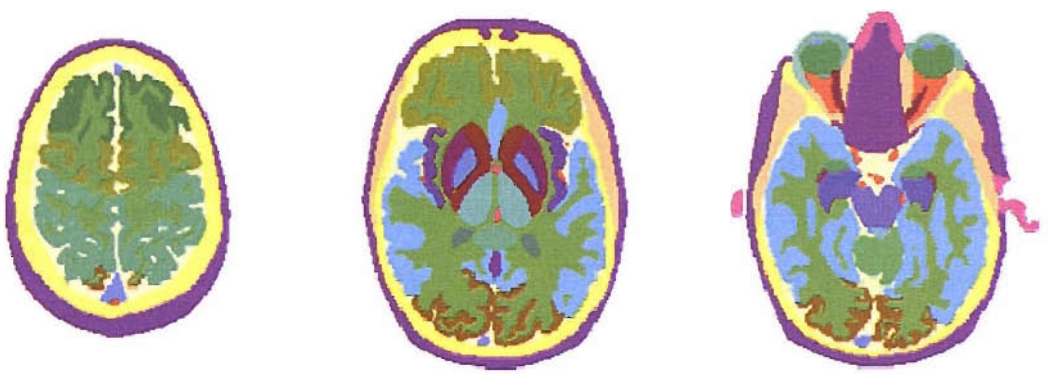

Figure 6.1. Three example slices from the segmented tomographic Zubal phantom of the head corresponding to slice numbers 30, 62 and 77. A high contrast colour map is used to highlight the different structures.

The Zubal head phantom was created by the Department of Diagnostic Radiology at Yale University with the intention of being applied to radiation transport calculations in nuclear medicine simulation. The head phantom is created from MRI data of a 35 year old healthy male, and has been manually segmented by clinical staff into 62 anatomical, neurological and taxonomical structures. The original MRI image has 124 slices of 256 x 256 voxels, which has been manually segmented to create a digital

phantom containing integer values representing the different structures of the head. The process used for segmentation involved manually outlining structures on transaxial slices and storing the results digitally. The slices start at the roof of the mouth and end at the top of the head, and have anisotropic voxel size of 1.1 mm x 1.1 mm x 1.4 mm. Figure 6.1 illustrates three slices taken from the dataset showing different structures as different colours.

6.1.2 *Zubal Phantom Validation Using SimSET*

The Zubal phantom was updated such that it was compatible with the SimSET package. Anatomical regions were extracted as necessary and combined into separate activity and attenuation objects

For the attenuation object, the index values representing the structures in the Zubal phantom were converted to SimSET material indexes representing the nearest equivalent material. The materials used were air, water, blood, bone, brain, muscle, gastrointestinal tract, connective tissue and fat, and Table 6-1 shows the relationship between original Zubal regions and the attenuation indexes used in SimSET. The region numbers shown are the same as those in Table 6-2, although several regions were removed from the phantom (see section 6.1.3).

Attenuating Material	SimSET Tissue Number	Included Zubal Regions
Air	0	0, 15, 16, 29
Water	1	2, 72, 74, 75, 92, 97, 115, 122, 123
Blood	2	23, 84
Bone	3	4, 5, 70, 71, 76, 81, 82, 99, 100, 102, 125
Brain	4	3, 77, 83, 85, 89, 91, 95, 96, 101, 103, 105, 107, 108, 109, 111, 112, 113, 114, 117, 118, 120, 124
Muscle	7	9, 78
Connective Tissue	15	1, 30, 106, 110, 116, 119, 121
Fat	23	22, 26, 98, 104

Table 6-1. SimSET attenuation indexes used for each Zubal phantom region. The numbers indicate the respective index number used from the original Zubal phantom.

Software was then used to generate a new image of the same dimensions as the Zubal phantom using the data above. The same procedure was carried out for the activity object, with relative activity values assigned to grey and white matter only in a ratio of 4 to 1, with the inclusion of the cerebro-spinal fluid (CSF) with no activity. The attenuation and activity objects were verified by comparison, to ensure correctly

defined regions and positioning. The two objects at this stage represent the initial model used for validation of the Zubal phantom within SimSET. Figure 6.2 shows the same example slice of both the attenuation and activity maps for the Zubal phantom, highlighting different activity levels, and attenuating structures according to the SimSET material index tables.

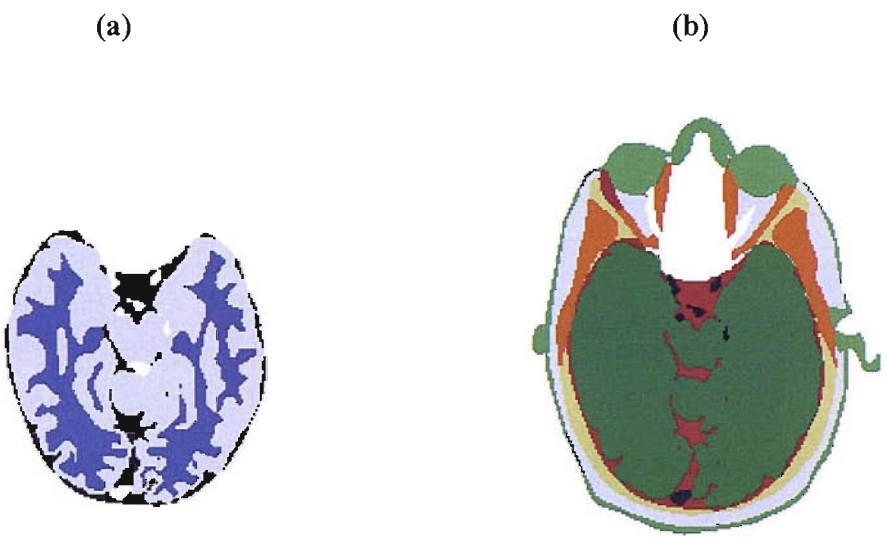

Figure 6.2. Example slices of the SimSET Zubal Phantom illustrating a) the activity map, and b) the attenuation map for the same slice. The different colours represent different levels of activity and different attenuating materials respectively, using a simple 4:1:0 combination for grey matter, white matter and CSF.

The Zubal phantom was incorporated into several initial simulation experiments using SimSET to attempt to validate the model and indicate limitations. Initially, this was carried out using empirical methods to obtain a source distribution based on the model described above, that provided a visually normal looking representation of the brain structures. This first stage of experimentation allowed the simulation parameters to be assessed and optimised, and insured that the phantom was being correctly interpreted by the software. One billion decays were simulated with a grey to white matter to CSF ratio of 4:1:0. Stratification was enabled and SPECT simulation was performed using the standard camera and collimator model as described in section 3.5.2. The initial simulations produce qualitatively normal data, and Figure 6.3 shows the reconstructed data generated using the standard visual processing method. The images illustrate variability in the perceived perfusion level around the cortex, and clearly indicate brain structures.

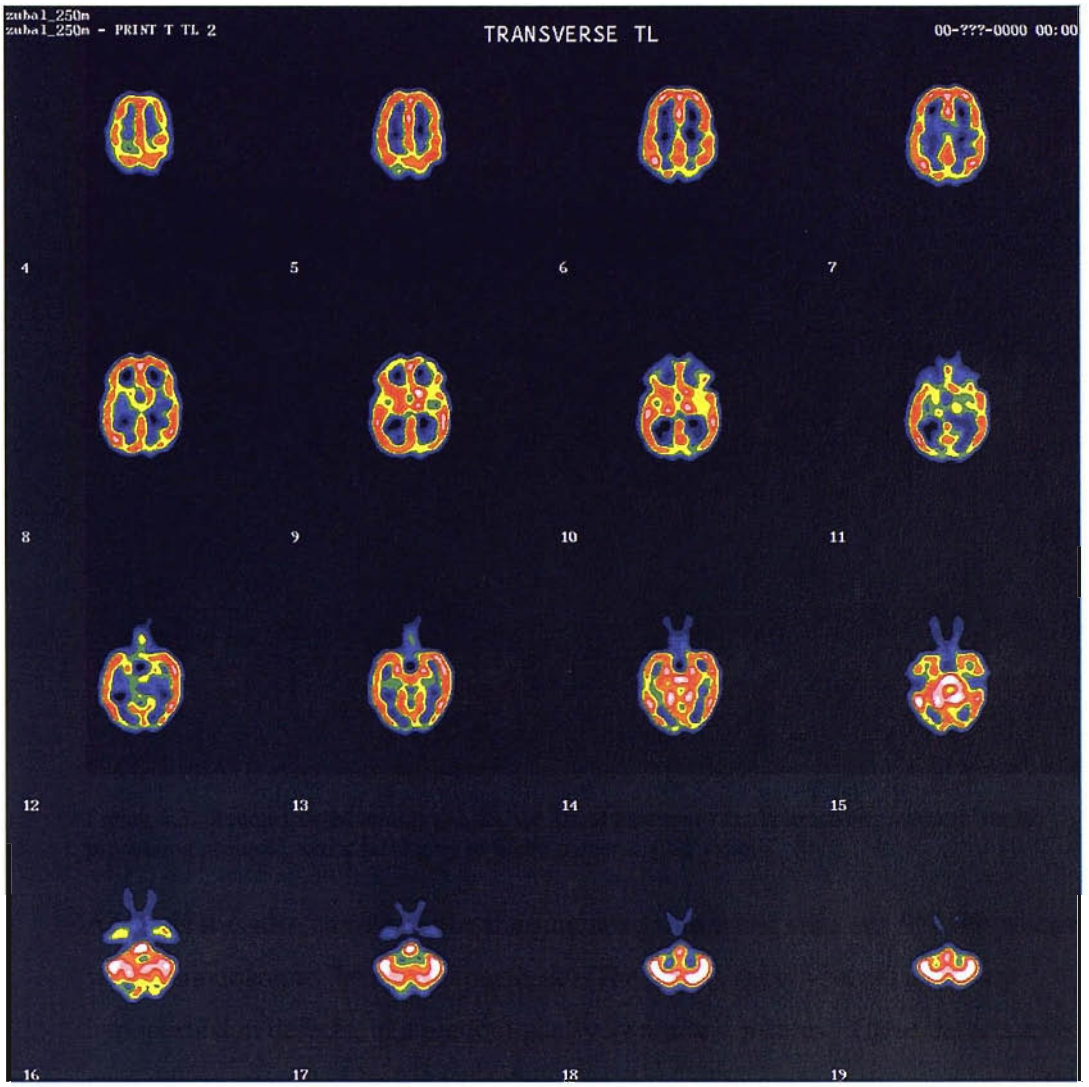

Figure 6.3. Reconstructed tomograph for the Zubal phantom simulation, using standard brain processing protocol, and a 4:1:0 grey to white matter to CSF ratio.

Analysis was also carried out on the simulated data using standard SPM99 processing, with comparison to the normal database. The results show severe significant hypoperfusion defects, in a predominantly symmetric pattern. These defects are particularly evident in and around the ventricles and in voxels near the edge of the brain. These abnormalities suggest the need for activity to be modelled in the CSF. Further simulations included the CSF with an activity of 10% of the grey matter activity, and shows marked reduction in the severity of hypoperfusion defects, although abnormalities are still evident. Figure 6.4 shows the results from SPM99 analysis with a grey matter to white matter to CSF ratio of 10:2.5:1, indicating regions of statistically significant hypoperfusion.

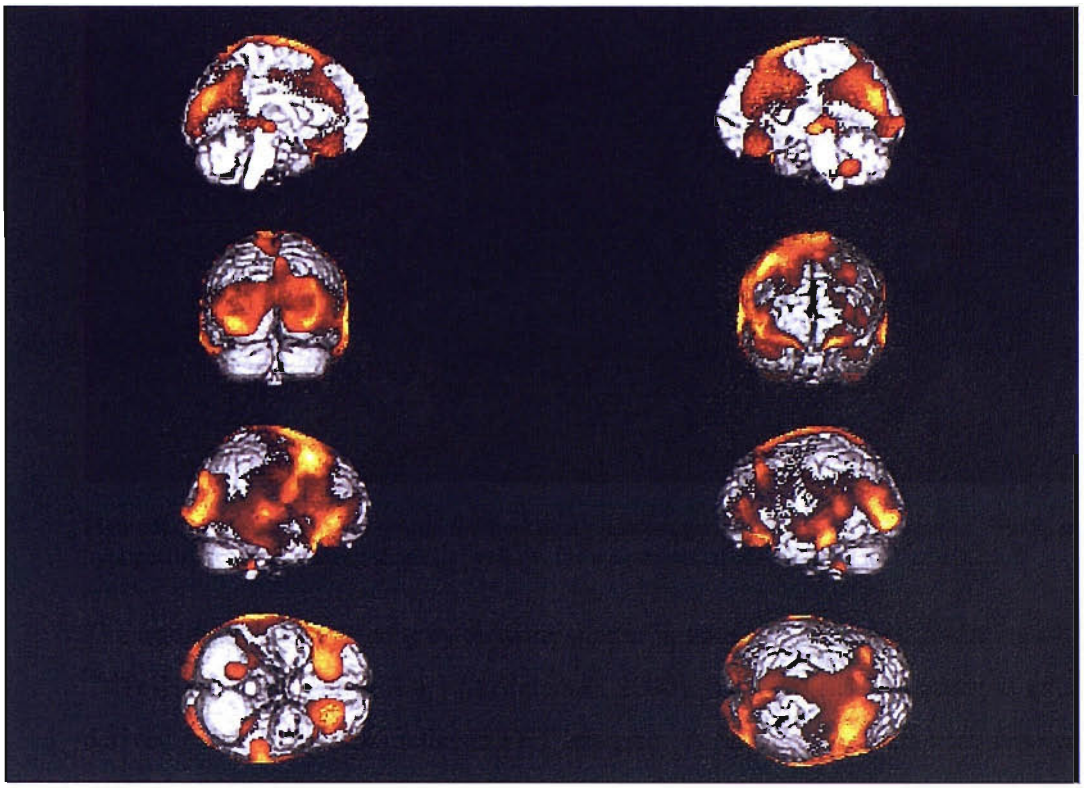

Figure 6.4. SPM99 analysis results for the Zubal phantom simulation, showing areas of significant hypoperfusion as increasing shades of yellow, for a distribution of GM/WM/CSF of 10:2.5:1

The traditionally reported grey to white matter uptake ratio used in simulation of ^{99m}Tc-HMPAO imaging is 4:1 [Arlig *et al.*, 2000]. This value is not accurate as it is derived from pharmacokinetics in PET imaging. A ratio of 2.2:1 has been reported for HMAPO studies in rat brains [Hoffman *et al.*, 1988], and experimentation shows a ratio of 2.5:1 produces more visually normal results.

While empirical methods are useful in obtaining qualitative results, quantification requires advanced methods to obtain a realistic and heterogeneous biodistribution in the normal brain.

6.1.3 The Updated Zubal Phantom

Empirically derived ratio combinations, as discussed above, were simulated but found to lack realism, indicating that a more heterogeneous model of biosdistribution was required. The results also suggest that the original anatomical model used was producing artefacts due to incorrectly segmented anatomy. While the Zubal Phantom provides an accurate anatomical model for cerebral structures, the model has several

limitations created predominantly by MRI imaging, that limit its use as a support in the modeling described herein. As these anomalies can adversely affect quantitative analysis, an attempt has been made to provide more accurate approximations where anatomical data is incomplete or does not exist. These changes are described here. Most of the changes were empirically implemented while performing the validations described in section 6.2, and implemented due to obvious perfusion differences with the control database.

One major limitation of the phantom was a lack of segmentation information for the facial region. The entire facial region below the frontal lobe and above the roof of the mouth is defined as a single region, with the exception of the turbinates and the nasal septum. This region also contains a mis-segmented part of the inferior frontal cortex, surrounding cerebrospinal fluid, skull and other anatomically distributed regions that fall into the same taxonomy. This is illustrated in Figure 6.5.

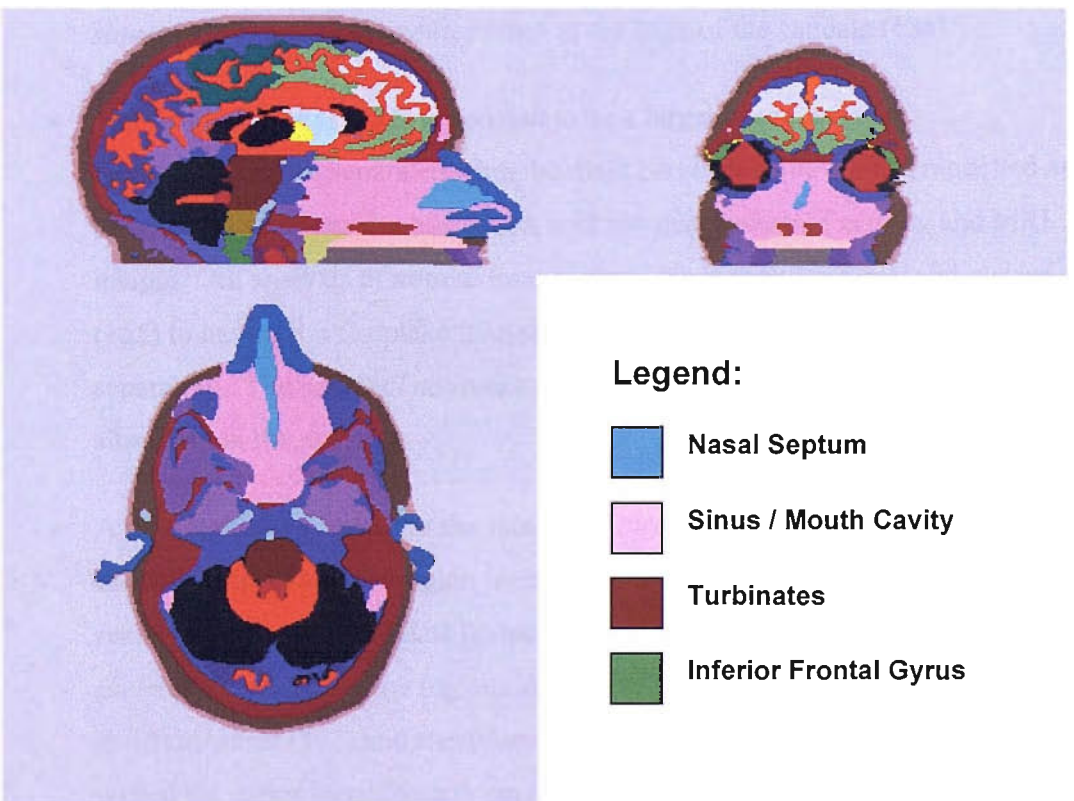

Figure 6.5. Orthogonal views of the original Zubal phantom illustrating the limitation of the segmentation of the facial region.

This causes problems when simulating as the anatomy and physiology in this region has a high inter-subject variability which creates errors when using automatic

registration. Furthermore, attenuation effects in the region are complex due to the anatomy and modeling the whole region as air can cause large variation in perceived activity levels. In [Grova *et al.*, 2003], measurement errors in the facial region are incorrectly assumed to be an effect of registration, and the subject sinuses in the Zubal phantom have been reported to be larger than normal anatomy [Stodilka *et al.*, 2000]. Both these findings can be explained by inaccurate segmentation. The model was updated to more accurately define the facial region using the MRI image as a guide, and included the following changes;

- The *frontal lobe* grey matter (89) has been extended into the *sinus / mouth cavity region*, and an additional layer of *CSF* (2) approximately 1 mm thick has been added around this to extend the existing region.

- *Cerebellar sinuses* (or *sigmoid sinuses*) are segmented from the *sinus / mouth cavity* region and assigned an independent region (133), as are the *frontal sinuses* (134) and the *unnamed sinus* at the back of the caudate (136).

- The *cerebellar WM* (132) is updated to be a larger, more accurate representation and separated from the main *cerebral white matter*, modelled as brain. This is due to an observation with the distribution of activity and MRI images. An analysis of normal images show the *cerebellar tonsil* and *cistern* (155) to have a lower uptake than the *cerebellum*, and thus it is defined separately. The *cerebral aqueduct* (122) is added to *CSF* (2) due to the similarity in the anatomy.

- A new region is created for the *nasal and throat cavity* (140) segmented from the MRI image, and the region is extended into the *pharynx* (15). The remaining unsegmented data (extraneous) in the *pharynx* (15) is joined with *skeletal muscle* (9). New regions are also segmented for *ethmoid sinus* (141), *sphenoid sinus* (142) and *maxillary sinus* (143), all modelled as air and defined within the major *sinus / mouth cavity* region. This operation removes the remaining *sinus/mouth cavity* region from the phantom.

- *Mastoid air cells* (135) are lattice-like, open, air-containing spaces in the *skull*, adjacent to the *cerebellum*. This is modelled entirely as *skull* in the Zubal

phantom, and has been updated and a new region created to reduce the attenuation effect.

- The *nasal septum* (82) and *turbinate* (100) regions within the sinuses are combined with the segmented *concha* and added as a new region: *concha, turbinates and septum* (150), modelled as bone.

Figure 6.6 shows graphically the major updates made to the Zubal phantom, Figure 6.7 and Figure 6.8 show a 3D rendering with spatial relationship to the skull, and Table 6-2 is a complete list of the regions used for modelling the updated phantom.

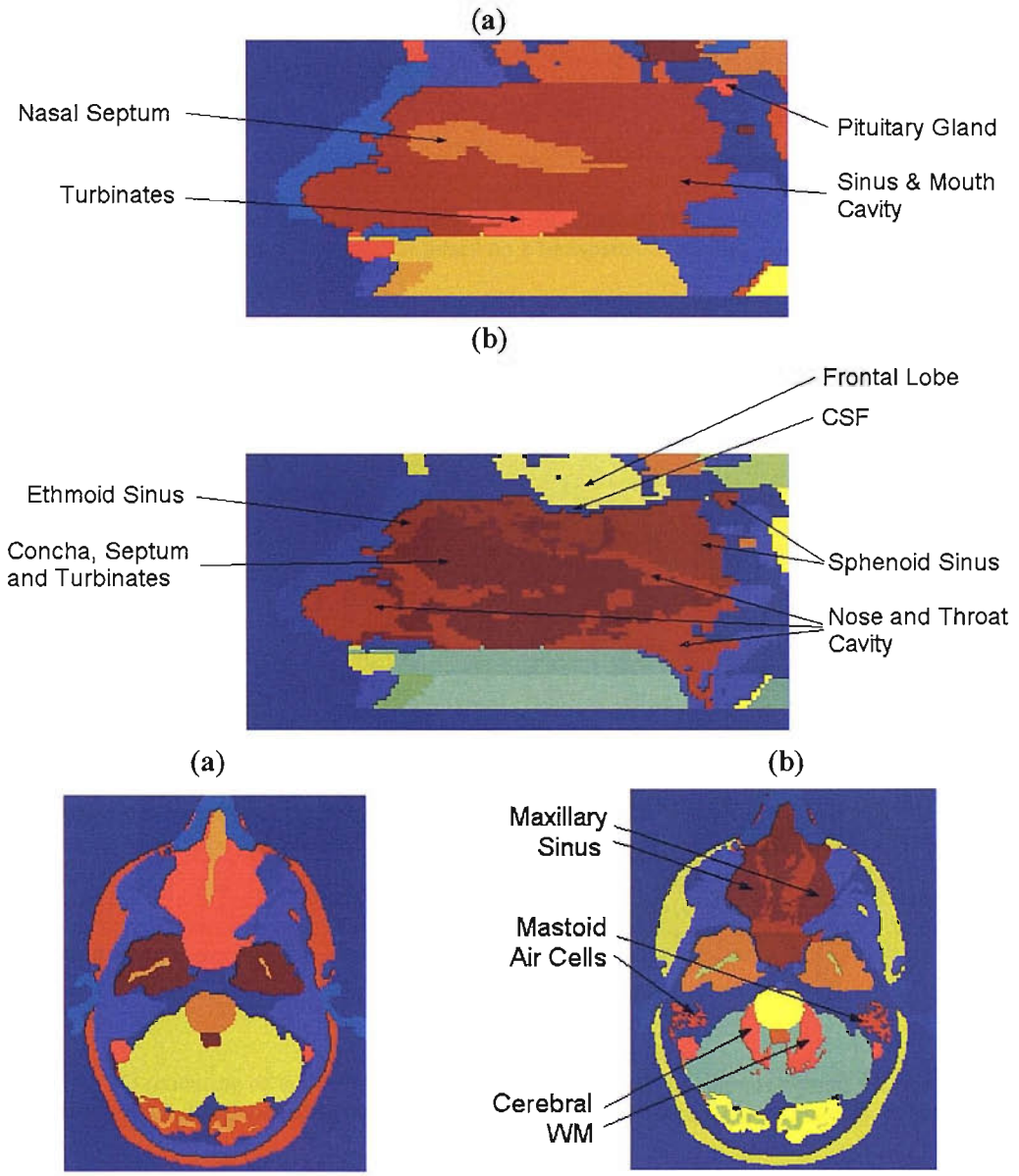

Figure 6.6. Illustration of the major Zubal phantom updates. (a) is the original Zubal image and (b) is the updated phantom image. The text in the images indicates regions that have been updated.

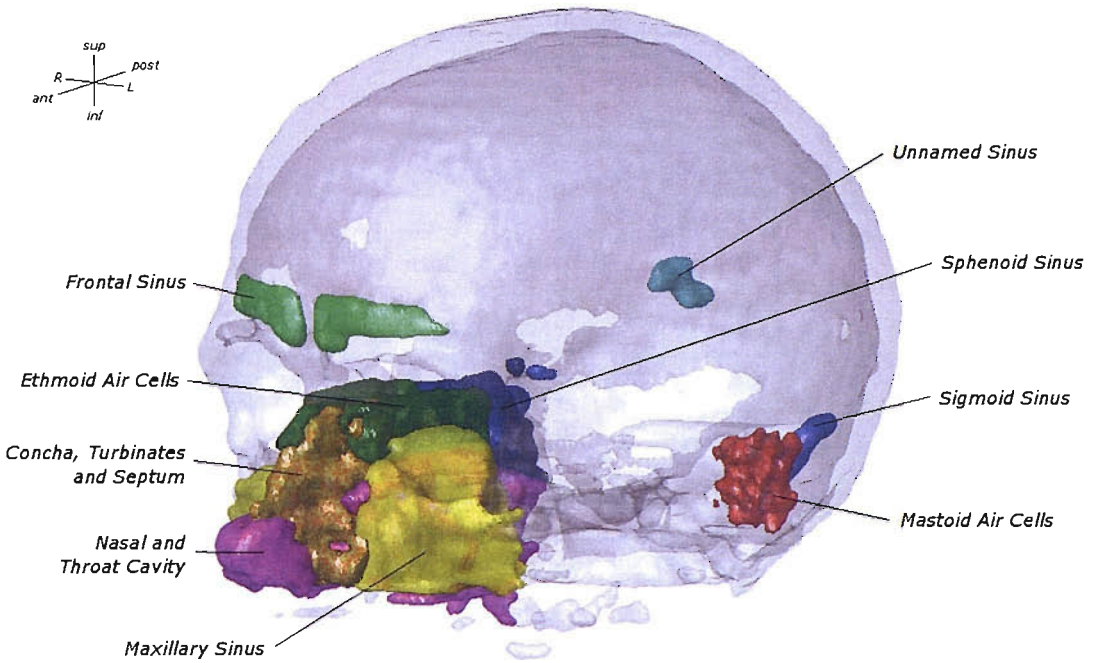

Figure 6.7. A 3D rendering of the updated Zubal phantom, showing regions that have been updated/segmented. The regions are superimposed on a transparent rendering of the skull region.

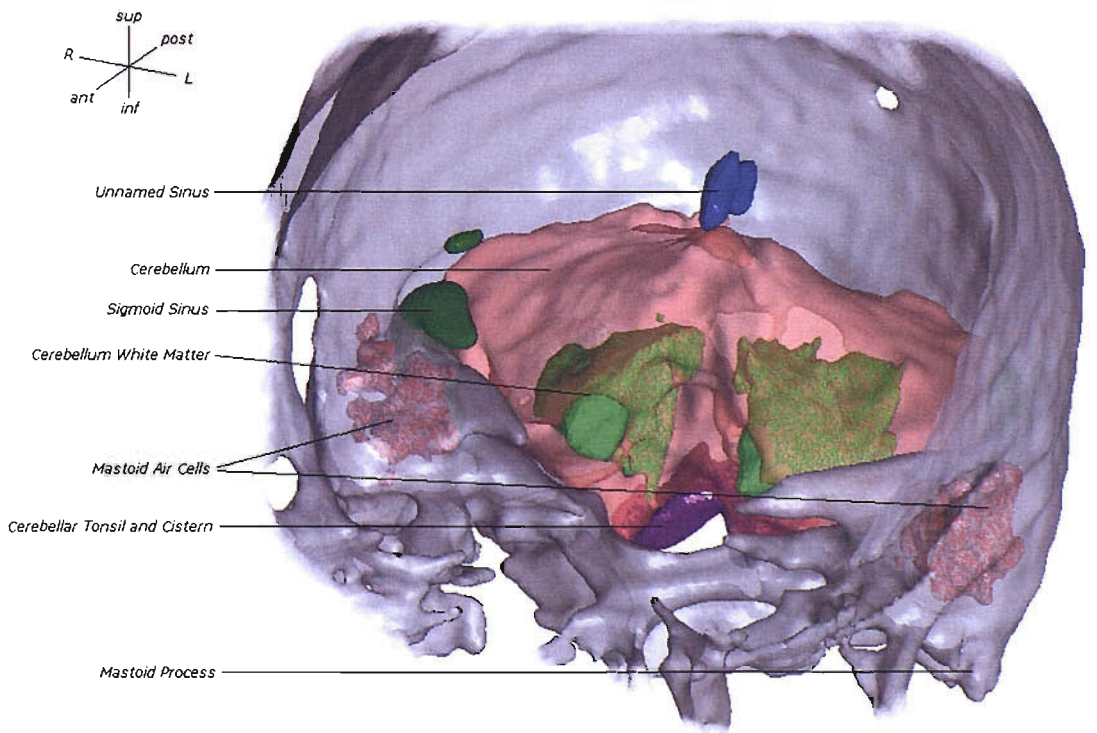

Figure 6.8. A 3D rendering of the updated Zubal phantom, showing the regions around the cerebellum that have been updated/segmented. The regions are superimposed on transparent cutaway of the *skull* region.

Seq. #	Name	Number	Attenuation Material	Index
1	Outside Phantom	0	Air	0
2	Skin	1	Connective Tissue	15
3	Cerebral Fluid (CSF)	2	Water	1
4	Spinal Cord	3	Brain	4
5	Skull	4	Bone	3
6	Spine	5	Bone	3
7	Skeletal Muscle	9	Muscle	7
8	Fat	22	Fat	23
9	Blood Pool	23	Blood	2
10	Bone Marrow	26	Fat	23
11	Cartilage	30	Connective Tissue	15
12	Dens of Axis	70	Bone	3
13	Jaw Bone	71	Bone	3
14	Parotid Gland	72	Water	1
15	Lacrimal Glands	74	Water	1
16	Spinal Canal	75	Water	1
17	Hard Palate	76	Bone	3
18	**Cerebellum**	77	**Brain**	**4**
19	Tongue	78	Muscle	7
20	Horn of Mandible	81	Bone	3
21	**Cerebral WM**	**83**	**Brain**	**4**
22	**Superior Sagittal Sinus**	**84**	**Blood**	**2**
23	**Medulla Oblongata**	**85**	**Brain**	**4**
24	**Frontal Lobes**	**89**	**Brain**	**4**
25	**Pons**	**91**	**Brain**	**4**
26	**Third Ventricle**	**92**	**Water**	**1**
27	**Occipital Lobes**	**95**	**Brain**	**4**
28	**Hippocampus**	**96**	**Brain**	**4**
29	Fat	98	Fat	23
30	Uncus (ear bones)	99	Bone	3
31	**Caudate Nucleus**	**101**	**Brain**	**4**
32	Zygoma	102	Bone	3
33	**Insula Cortex**	**103**	**Brain**	**4**
34	**Putamen**	**105**	**Brain**	**4**
35	Optic Nerve	106	Connective Tissue	15
36	**Internal Capsule**	**107**	**Brain**	**4**
37	Septum Pellucidium	108	Brain	4
38	**Thalamus**	**109**	**Brain**	**4**
39	Eyeball	110	Connective Tissue	15
40	**Corpus Collosum**	**111**	**Brain**	**4**
41	**Special Region Frontal Lobes**	**112**	**Brain**	**4**
42	Cerebral Falx	113	Brain	4
43	**Temporal Lobes**	**114**	**Brain**	**4**
44	**Fourth Ventricle**	**115**	**Water**	**1**
45	Frontal Portion of Eyes	116	Connective Tissue	15
46	**Parietal Lobes**	**117**	**Brain**	**4**
47	**Amygdala**	**118**	**Brain**	**4**
48	Eye	119	Connective Tissue	15
49	**Globus Pallidus**	**120**	**Brain**	**4**
50	Lens	121	Connective Tissue	15
51	**Lateral Ventricles**	**123**	**Water**	**1**
52	**Prefrontal Lobes**	**124**	**Brain**	**4**
53	**Cerebellum WM**	**132**	**Brain**	**4**
54	Cerebral (Sigmoid) Sinuses	133	Blood	2
55	Frontal Sinuses	134	Air	0
56	Mastoid Air Cells	135	Air	0
57	Unnamed Sinuses	136	Blood	2
58	Nasal and Throat Cavity	140	Air	0
59	Ethmoid Sinuses	141	Air	0
60	Sphenoid Sinuses	142	Air	0
61	Maxillary Sinuses	143	Air	0
62	Concha, turbinates & septum	150	Bone	3
63	Cerebellar Tonsil and cistern	155	Brain	4

Table 6-2. Description of the updated Zubal phantom regions. The table displays the sequential region number, the region name, the region number in the phantom, the material used in the attenuation object and the attenuation index used in SimSET. The regions marked in bold are those within the cerebrum.

Wherever possible, semi-automatic segmentation techniques were applied to the MRI images using MRIcro, in an attempt to extract more anatomical information and

update the phantom. For models where real anatomical data is unavailable due to either limited or poor information content, an approximation was sought (e.g. the facial sinus groups). For all such regions, this was achieved by using MRI and HMPAO images from several normal subjects. These images contain sufficient structural information to allow anatomy to be inferred. This data provides enough information to support model optimisation, based on information on the normal anatomy. The updated model is not intended to be an accurate representation of the individual subject anatomy, but uses normal supports to guide an approximation to average subject anatomy. This is valid as subject averaging is performed in the presence of large anatomical variation, and the approach is to provide a general model that is more biased towards the average. Table 6-2 contains a complete list of the updated phantom regions and their associated attenuation material and index. Note that all future references are made to the sequential region numbers.

6.2 Deriving the Activity Distribution

Early simulation experiments with simple GM/WM/CSF ratios show hypoperfusion almost continuously around the cerebrum, when compared to normal controls. It is thought that the hypoperfusion witnessed in the simulated results at the edge of the cerebrum is caused by a lack of contribution from extra-cerebral activity in the CSF, meninges, skull and fat surrounding the brain, and also by circulating blood in these regions. This normal tissue uptake is assumed to be caused by interaction with fat due to the lipophilic nature of the tracer used. Analysis of the SPECT template revealed that there was a level of activity of around 25% of the reference (cerebellar) activity in this region, and simulating this additional activity level improved the results markedly. Further empirical simulation and analysis revealed tracer uptake in other brain structures, at varying concentrations. It is for this reason that a quantitative reconstruction process was implemented to attempt to quantify tracer uptake within the heterogeneous brain phantom.

The approach taken to obtain an estimated activity distribution is based on the updated anatomical support described previously: Each region is assumed to be independent and have uniform distribution (albeit variable between regions), with emissions that can be characterised by the SimSET model for the imaging system. The

biodistribution is estimated from either measured or simulated perfusion data. A transfer function is then derived mapping the input activity level to the measured count level in a reconstructed tomograph, which accounts for system dependent parameters and errors introduced by the tomographic reconstruction process. The activity distribution can then be estimated by using the derived transfer function.

6.2.1 The Model

Estimating activity in such a complex source model using empirical methods is very difficult due to the heterogeneity of the biodistribution and the large number of parameters involved. One of the major limitations for using full MLEM reconstruction is the size of the transition matrix required. For our configuration, a full MLEM transition matrix (for phantom source voxel to detector projection bin) would require 256x256x128 x 128x128x128 elements to model the source to projector model; assuming a single byte per element would require approximately 17.6 T bytes (1.76×10^{13} bytes) of memory to store the transition matrix alone. Thus a simplification of the transition matrix is required that reduces the complexity of the model, and is achieved by using an anatomical support to define regions of homogeneous tracer uptake within a heterogeneous distribution. The proposed model, rather than describing a source voxel to projection element count level, instead describes a source regional activity level to reconstructed output region counts. Equation 6.1 describes the model employed, where estimated count level in a region is the sum of the contribution from all regions in the image.

$$\tilde{\lambda}_j = \sum_i f_{ij} \lambda_i \qquad \textbf{(6.1)}$$

$\tilde{\lambda}_j$ is the expected count level in a reconstructed region, λ_i is the activity level in the voxelised source region, and f_{ij} is the transition matrix. Thus we attempt to define the complete forward-back projection in f_{ij}, including imaging effects such as scatter and partial volumes, plus the effects of the reconstruction process. If f_{ij} is estimated from analytical simulation experiments and $\tilde{\lambda}_j$ is estimated from reconstructed tomograph data, we can solve for λ_i to provide a regional activity distribution using classical

iterative reconstruction techniques. The resulting activity distribution data can then be used as an activity model for simulation.

A regional support is provided by the updated Zubal phantom (section 6.1.3) as described in Table 6-2. This model assumes that the activity distribution is heterogeneous across all regions, but homogenous within the region. The number of source and destination elements is the same and equal to the number of anatomical regions used. In the case of our phantom with 63 independent regions, we would require only 30 k bytes of storage space for a double precision floating-point transition matrix.

6.2.2 Model Training; Estimating f_{ij}

Two simulation methods are proposed for generating the transition matrix, f_{ij}, being different only in the simulation method used to generate the training data. Original f_{ij} measurements incorporated the experimentally measured PSF described in section 4.1, and used this to simulate activity in each region by convolution with the VOI. The major advantage is the speed of the simulation, but the simulated result is spatially uniform and not variable with subject anatomy or location, thus variable attenuation is not simulated. Monte Carlo methods were also used, and both methods produced comparable results.

To generate training data for both methods, each source region, i, with uniform mean activity, $\bar{g}_i$, was simulated independently. For the Monte Carlo simulations, a set of projection images are produced which are then reconstructed using standard methods. Each region is then registered back to the phantom space for counting, using an automatic simplex search based on maximising coincident voxel intensities for a rigid body transform. The registration method also allows the high resolution regions to be used for counting by interpolation of the low resolution reconstructed images. A normalised count value, c'_j, is extracted for each output region, j, by masking the simulated image with the VOI and normalising using equation 6.2, such that the measured counts are a factor of the total counts with $\sum c'_j = 1$.

$$c'_j = \frac{c_j}{\sum_j c_j} \qquad \textbf{(6.2)}$$

The SimSET simulation system has no concept of time, and thus it is difficult to quantitatively assess the output count level. Geometric collimator modelling further complicates the issue as it requires the manual addition of Poisson noise. The collimator modelling also requires collection of weights and variance as opposed to actual count levels, and results in a level of uncertainty in the estimates (see section 2.5.1.1). Performing this normalisation here simplifies modelling as the transformation is scaled to unity ($\overline{g}_i = 1$). Furthermore, the PSF simulation technique uses this form by default as no quantitative method exists and thus both techniques are directly comparable.

f_{ij} is then multiplied by the number of voxels in the input region, N_i, and divided by the number of voxels in the output region N_j, to obtain a correctly scaled model that maps a mean input activity level to a mean output count level. The f_{ij} matrix is now calculated from equation 6.3.

$$f_{ij} = \frac{N_j . c'_j}{N_i} \tag{6.3}$$

The matrix can then be used to perform a regional convolution on an arbitrary source distribution using equation 6.1, and calculates a relative perfusion value for arbitrary input. While this relationship is strictly linear, non-linear effects can be incorporated into the model by including additional parameters. However, linear reconstruction algorithms depend only on the point response of a system (which is largely linear), and not on additional factors [Du *et al.*, 2005], and therefore there is no modelling requirement.

As mean values are used to calculate the f_{ij} matrix, the result is quantitative and no scaling of f_{ij} is required. Furthermore, if we assume anatomical segmentation is functionally defined and homogeneous, then image noise will be effectively attenuated. On this assumption, other degrading effects such as scatter, imaging and reconstruction artefacts are modelled as a combined linear effect, and expressed by f_{ij}.

As the region outside of the phantom is largely empty, the f_{ij} matrix is altered for both methods such that the contribution from this region to all other regions is zero. This

avoids the estimation procedure using an activity level in this region to improve the results.

6.2.3 Parameter Estimation, λ_i

Two different methods are presented for solving equation 6.1 to provide an estimate for λ_i. The MLEM and ART methods are applied and presented here. These methods produce the relative activity distribution required to obtain the pattern of perfusion specified.

6.2.3.1 Stopping Criteria

Both estimation methods have the property of systematically reducing the errors between the projected and actual measurements at the cost of increasing the image noise on each iteration. The first few iterations of the MLEM algorithm recover the lower frequency structures of the image [Kadrmas, 2001], and are thus more likely to be applicable to the parameters under study. Subsequent iterations provide more accuracy on a smaller spatial scale, and are likely to increase the noise in the image. To ensure accuracy in the results, it is desirable to stop the estimator when the errors between the measured and projected data can be explained within the normal variation of the data set. The results are assumed accurate when errors between the projected and measured results can be explained by the normal distribution, with mean and standard deviation equal to that of the control group. This imposes the assumption that the count levels within a region are homogeneous and normally distributed, as would be expected for a random variable.

For each measured region, j, the variance, σ_j^2, is also calculated from the distribution of counts within the region. On each iteration of the algorithm, the forward projected mean estimate, $\hat{\lambda}_j$, is assumed to be the mean of a normally distributed count level across the region, with variance equal to that of the measured data. The t-statistic is then calculated from equation 6.4.

$$t = \frac{\hat{\lambda}_j - \tilde{\lambda}_j}{\sqrt{2\sigma_j^2 / N_j}} \tag{6.4}$$

Where N_j is the number of voxels in region j. The probability associated with the t-statistic can then be calculated. The algorithm is assumed to have converged when all regions are within the normal distribution using a probability threshold of $p < 0.05$.

When estimating counts in a normal distribution, unlike when using a simulated result, the count distribution can only be assumed to be normally distributed for regions that are included in the registration. Physiological and anatomical variations, as well as large registration errors result in the assumptions being violated outside of the cerebrum. Therefore, only cerebral regions are included in the stopping criteria when applying the methods to normal controls. These regions are indicated in bold in Table 6-2

6.2.3.2 *Algebraic Reconstruction Technique (ART)*

ART is a useful reconstruction technique as it is relatively straight forward to implement and easy to understand conceptually and mathematically.

ART can be implemented to solve equation 6.1 by substituting the forward projector for as_i^n, and the measured counts for at_i into equation 2.2, and weighting the update variable with the relative contribution as shown in equation 6.5;

$$\lambda_i^{n+1} = \lambda_i^n + r.\lambda_i^n \sum_j f_{ij} \frac{\left(\tilde{\lambda}_j - \sum_i f_{ij}\lambda_i^n\right)}{\sum_i f_{ij}\lambda_i^n} \qquad \textbf{(6.5)}$$

For each iteration, the estimator updates the estimated count level in a region by adding or subtracting a proportion of the current estimate for each region. The proportion is calculated from the difference between a measured and projected value, which is weighted by the contribution of the source region to the destination. As equation 6.5 contains weighting by the current estimate, if an estimate starts at or becomes zero, subsequent iterations will not alter the estimate and it will remain at zero.

6.2.3.3 *Maximum Likelihood Expectation Maximisation (MLEM)*

MLEM offers a similar method to the ART method described above in that a weighted difference measure is used to update the current estimate. The MLEM formula in equation 2.3 can be altered to solve equation 6.1 as shown in equation 6.6:

$$\lambda_i^{k+1} = \frac{\lambda_i^k}{\sum_j f_{ij}} \sum_j \left(\frac{f_{ij} \tilde{\lambda}_j}{\sum_i f_{ij} \lambda_i^k} \right) \tag{6.6}$$

The estimator in MLEM provides the update as a weighted ratio of the measured to forward projected count level for all regions. The estimator is very similar to ART, but also normalises each update by the total contribution of the source activity. As with ART, regions with zero activity will not change on subsequent iterations.

6.2.4 Generating Simulation Objects

The estimated activity levels produced by these methods can be used as the input activity levels for Monte Carlo simulation. As the activity levels in each region can be potentially very small when expressed in Ci/cc (the default for SimSET), one must ensure that sufficiently precise representation is used. In our case we represent each number with 10 decimal places. The total input activity over all input regions is normalised to 25MBq by linear scaling, which corresponds to 5% of a 500MBq administered dose (see Table 1-2), and converted to a Ci/cc measurement for SimSET input. SimSET index and translation tables are then generated for the regional distribution, and included in the main simulation parameter files.

6.3 Normal Brain Modelling

The methods described above can be applied to the estimation of the activity distribution for arbitrary images. Of particular importance is the application to normal data, where the resulting biodistribution could be used as the basis of the production of normal data sets. While the phantom model is adequate to describe a single subject and the subject distribution, it is limited in that the simulation of the distribution does not account for other effects, such as the effect of anatomical and physiological variation that is present between subjects in a group. If this variation can be characterised for normal parameters, then this data can be randomly sampled to provide variation in the data set that corresponds to real world (or at least group) variation. In the simplest sense, these parameters can be derived from individual subjects during pre-processing. The inclusion of these variations prior to simulation

will allow for the generation of a model that is capable of describing normal data within normal inter-subject variability.

This section describes methods that can be applied, along with those discussed above, to generate normal data sets from the standardised phantom image.

6.3.1 Counting the Controls, $\tilde{\lambda}_j$

Accurate count measurements for all phantom regions are required for all control subjects for maximum efficacy. This requires firstly that we have good quality input data, free from external influences such as age and disease. Secondly, the data should be processed using the same method applied to the training data. Thirdly, we require an accurate spatial transformation so that the normal images can be aligned with the regions for counting. Finally, we require valid data for all regions to be counted.

A subset of the normal control database was used. Only normal subjects under 70 years of age were considered, as studies suggest no significant correlation between age and perfusion level below this age (see section 2.1.5). A leave-one-out analysis was also performed on the control sub-group using SPM99, and any subject exhibiting significant abnormal characteristics compared to the rest of the group were omitted. The resulting control group contained 15 subjects below the age of 70.

The standard SPM99 bounding box is extended as the existing bounding box is defined to contain brain only. To obtain the best quantitative measure, extension is essential such that normalisation of control subjects (and phantom regions) produces images that contain the entire head and face. This is particularly true for close cerebral proximity as uptake in extra-cerebral structures can directly influence the measured count level within the cerebrum.

The Zubal MRI image is spatially registered to the SPM MRI template using a 12 parameter affine transform, followed by iterative (12 iterations) non linear warping using 4x5x4 basis functions with linear interpolation. The resulting transformation is then applied to each of the phantom regions independently using linear interpolation. Individual regional transformation is performed to account for partial volumes by weighting partial volume voxels by their size, allowing image counts to be collected

over part of a voxel (also commonly called fuzzy regions). Normal SPECT images are masked to remove non-brain activity before being spatially registered, as above, to the standard template. The derived transformation is then applied to original unmasked data to provide the images for counting. The resulting image is in the same template space as the Zubal phantom regions and counting can proceed directly by using the phantom regions as a mask for the control images.

Scatter correction is not applied to the normal images. While the technique has been shown to improve quantitative analysis for SPECT images [Buvat *et al.*, 1995], the effect of scatter can be accurately modelled in the transformation matrix.

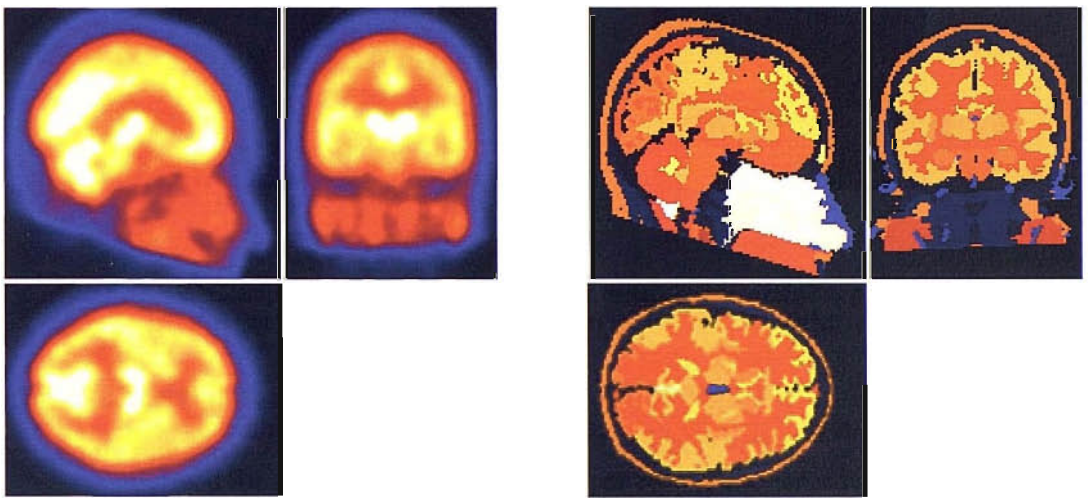

Figure 6.9. Example orthogonal slices of (left) the mean control image (template), smoothed using an 8 mm FWHM isotropic Gaussian kernel and (right) the updated Zubal phantom registered to template space.

The control subject images were updated to correct problems in regions where data is not defined for all subjects due to imaging or reconstruction effects. The data were synthesised by randomly selecting a control with valid data in the region and sampling the voxel value after count normalisation. This provides a within group estimate of count level for incomplete data sets. Where no data exists for any control, the phantom is updated to remove any voxels that lie within this area. Figure 6.9 shows three orthogonal slices of the control normal template and the registered Zubal phantom, and illustrates the spatial extent of the data set.

Count normalisation uses a modified version of the normalised cerebellum grey and white matter regions (regions 18 and 53 in Table 6-2). The regions are combined and

eroded using neighbourhood operators to reduce the cross-talk from adjacent regions. Each subject image is then masked with the reference region, and the average counts within the region are normalised to 100 counts/cc.

After count normalisation, an average count value, $\bar{\lambda}_{lj}$, is calculated for each region, j, of each of L normal images, l. The value is then averaged across all normal images to give the expected count value, $\tilde{\lambda}_j$, as shown in equation 6.7, and a standard deviation value, σ_j, as shown in equation 6.8.

$$\tilde{\lambda}_j = \frac{\sum_l \bar{\lambda}_{lj}}{L} \tag{6.7}$$

$$\sigma_j = \sqrt{\frac{\sum_l \left(\bar{\lambda}_{lj} - \tilde{\lambda}_j\right)^2}{L-1}} \tag{6.8}$$

6.3.2 Physiological Variation

Due to cerebral interconnections between (possibly) remote regions, it is not possible to simply randomly sample a distribution. In this case, correlations between biodistribution in distinct regions will be ignored, and the resulting distribution is likely to be in error. This section details a method for expressing the correlations between regions and incorporating this as a variance parameter to allow variation to be applied to the extracted biodistribution. This is achieved by using principal component analysis (PCA) to define the data set as a mean image and a set of correlated normal deviations on a regional basis. An important property of the principal components is that they are orthogonal and hence independent, thus random sampling can be effectively applied.

The kth principal component can be extracted for each region j, c_{kj}, from the normal data set. For the ith image, a_{ij}, we can extract a mean activity level, $\bar{a}_j$, across the entire group. Each normal image can then be approximated by assigning a coefficient, w_{ik}, to each principal component image, c_{kj}, and adding these images to the mean image whilst minimising the sum of squared differences, $\sum\sum e_{ij}^2$, between the approximated and the original image:

$$a_{ij} = \overline{a}_j + \sum_{k=1}^{p} w_{ik} c_{kj} + e_{ij} \quad \textbf{(6.8)}$$

Where p is the number of principal components (which is also equal to the number of regions).

PCA is commonly used to reduce the dimensionality of a data set by using a number of the largest components (determined from the Eigen value). In this implementation, all components are used to ensure maximum available variability in the production of artificial data sets. As the component images are highly correlated with dataset variation, we can define the normal distribution by describing the variation of the component coefficients across all controls, using the mean, $\overline{w}_k$, and standard deviation, σ_{w_k}. These distributions can then be randomly sampled for each k to produce an estimate, $\hat{w}_k$, that can be additively combined to create variation in each region, $\hat{a}_j$, using equation 6.9.:

$$\hat{a}_j = \overline{a}_j + \sum_{k=1}^{p} \hat{w}_k c_{kj} \quad \textbf{(6.9)}$$

The effect of age can also be incorporated by providing a model and a linear scaling coefficient that can be applied to the data set prior to the addition of Poisson noise. Thus the noise effects due to the reduction in activity are also modelled.

6.3.3 Anatomical Variation

Anatomical variation is incorporated into the model using spatial transformations that allow an image defined in standard space to be transformed to any subject space. As each image is transformed to template space, a best fit spatial transformation matrix is saved that maps the subject image into the template space, as derived using SPM99. This transformation can be reversed and combined with a mapping from Zubal phantom space to template space to provide a mapping for the Zubal phantom space into known subject space. These methods are described here.

6.3.3.1 Affine Transformation

The affine transformation can be expressed in matrix form using 12 parameters (4 x 4 matrix). The affine transformation, *TF*, can be inverted simply by obtaining the inverse transform and multiplying with coordinates, as shown in equation 6.10.

$$\begin{aligned}[x \quad y \quad z \quad 1]TF &= [x' \quad y' \quad z' \quad 1] \\ [x' \quad y' \quad z' \quad 1]TF^{-} &= [x \quad y \quad z \quad 1]\end{aligned} \tag{6.10}$$

6.3.3.2 Non-linear Deformations

Non-linear deformations are applied in SPM through constrained warping based on regional basis functions. The basis functions used are those of the discrete cosine transform (DCT), and the deformation field is applied as a linear combination of these basis functions.

The transformation between three-dimensional coordinates *m(x,y,z)* and *n(x,y,z)* is given by the following equation.

$$\begin{aligned}n_x &= m_x + \sum_l t_{lx} b_{lx}(m) \\ n_y &= m_y + \sum_l t_{ly} b_{ly}(m) \\ n_z &= m_z + \sum_l t_{lz} b_{lz}(m)\end{aligned} \tag{6.11}$$

Where t_{lr} is the *l*th coefficient for dimension *r* and $b_{lr}(m)$ is the *l*th basis function for dimension *r*, at position *m*. SPM uses an iterative algorithm to provide estimates for the parameters *t* and *b(m)* within a Bayesian framework. To reverse the transformation, the transforms are calculated from the saved coefficients and the warps are subtracted from the deformation field.

As the transformations are based on Cartesian coordinates, both the affine transformation and the basis function transformation can be carried out sequentially prior to resampling the source volume. Furthermore, several sets of transformations can be carried out sequentially without loss of information, allowing transformation to a standard template space followed by transformation from template space to the Zubal phantom space, and finally sampling the volume.

Chapter 7 Parameter Estimation Results

This chapter details the results of applying the methods described in Chapter 6 for parameter estimation, and concentrates on validation of the methods for the calculation of regional activity. The method is firstly applied to a known distribution and then to the estimation of normal parameters.

7.1 Extracted Transfer Functions

The transfer function (f_{ij}) is calculated for the two simulation methods as described in section 6.2.2. A uniform activity distribution is simulated within each region of the updated Zubal phantom described in section 6.1.3 by using either (i) convolution with the point spread function (PSF) or (ii) using SimSET and reconstructing using FBP, incorporating attenuation correction using a uniform attenuation map.

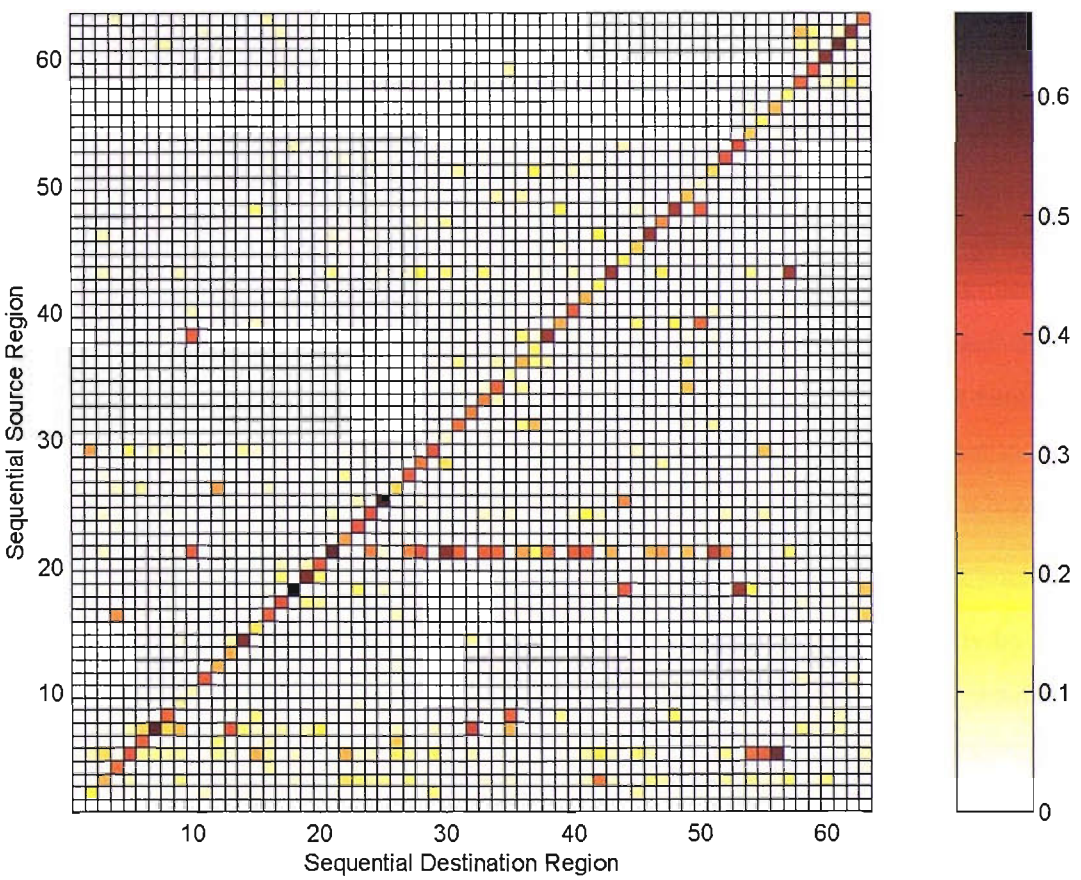

Figure 7.1. The f_{ij} matrix derived using the PSF simulation method shown in graphical format. The colours represent the change in the destination region mean count for unit source activity.

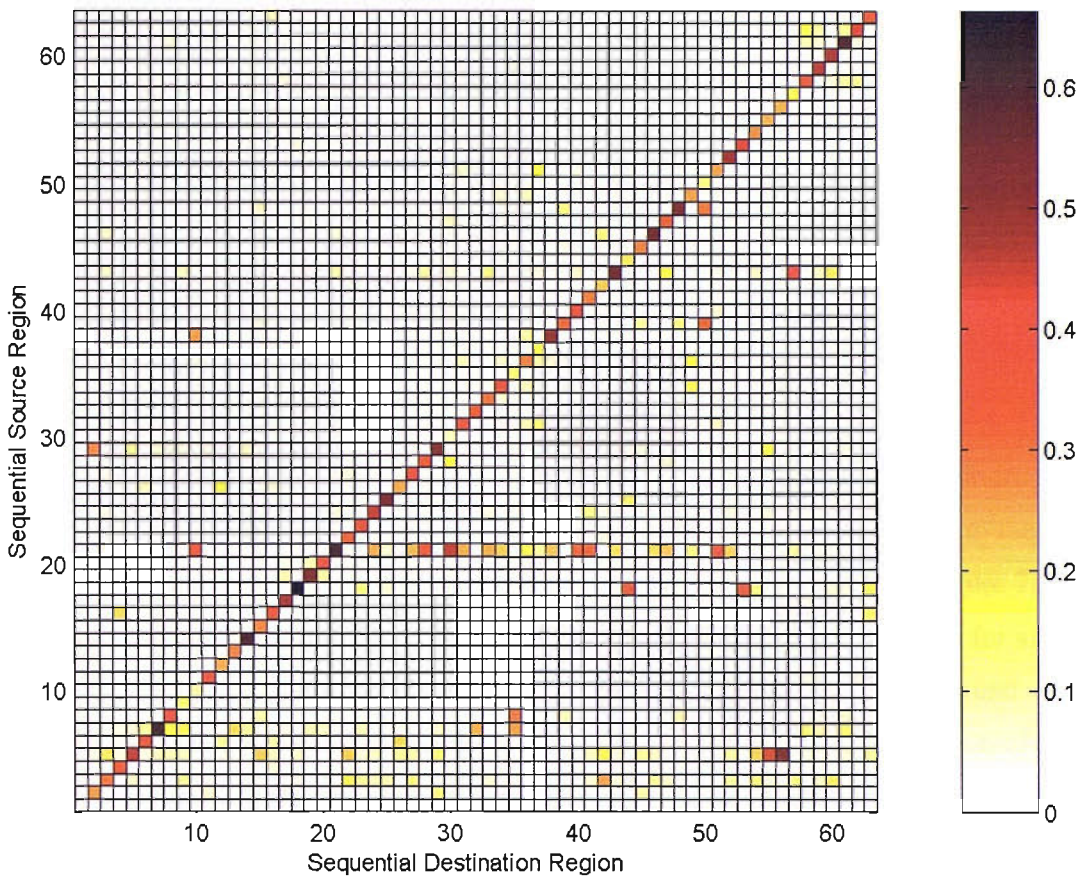

Figure 7.2. The f_{ij} matrix derived using the SimSET simulation method shown in graphical format. The colours represent the change in the destination region mean count for unit source activity.

Figure 7.1 shows the extracted transfer function in graphical form for the PSF method and Figure 7.2 shows the same result for the SimSET method. The region numbers are the sequential region numbers shown in Table 6-2, and the colours represent the destination region mean count distribution for mean unit source activity. The sum of each column of the matrices should be equal to 1, i.e. normalised, although due to averaging across all voxels in a region and differences between region sizes, a region may contribute more than summed unit counts to all regions (i.e. $\sum$ row $\neq 1$).

Both transfer functions have similar patterns of contribution, defined primarily by regional spatial extent and proximity. The major difference between the two results is the relative magnitude of a regional contribution to adjacent regions. The *cerebral white matter* (region 21) is clearly visible as contributing the most overall activity due to its size, spatial extent and proximity to other regions. This region will therefore have the greatest direct influence on the image. Other regions with a large spatial influence include the *CSF* (3) and *skull* (5). Regions modelled as air (e.g. *sigmoid*

sinus (54), *frontal sinus* (55) and *mastoid air cells* (56)) have a particularly small effect on detected count rate in the region and are more influenced by the activity in adjacent regions (i.e. the regions mentioned above are all affected more by activity in the *skull* than themselves). One interesting point is that no region contributes more than approximately 70% of its own activity to counts in itself for either method of deriving the f_{ij} matrix. This is a direct result of the partial volume effect.

7.1.1 Uniform Forward Projections

While it is clear that the SimSET method for deriving the transfer function is more representative of the imaging and processing system, the question remains as to the suitability of the PSF generated method for the estimation of parameters. Figure 7.3 shows a graph of the projected count levels for a uniform activity distribution for all regions of the phantom (excluding the outside phantom region) using the PSF and SimSET generated transfer functions. This is achieved by matrix multiplication of a uniform unity activity distribution by the f_{ij} matrices shown above.

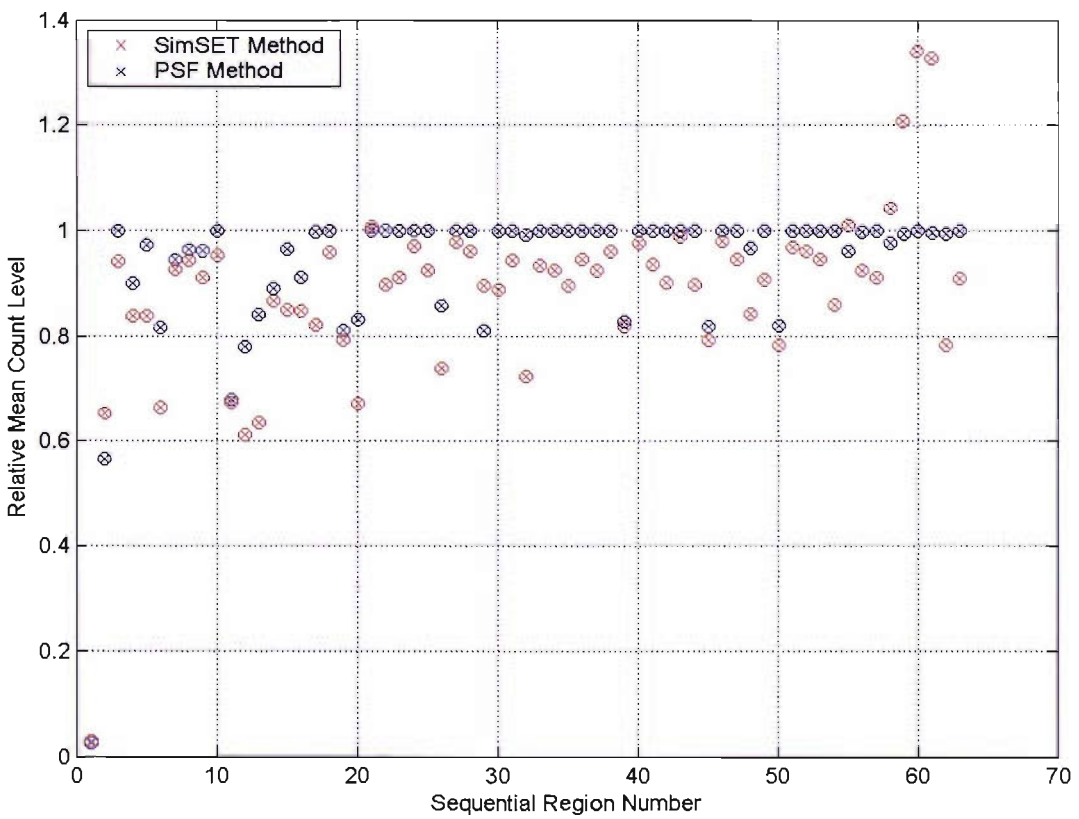

Figure 7.3. Uniform forward projection for the two f_{ij} *matrices*. The graph shows the relative mean count level in each region following forward projection of a uniform activity distribution using the f_{ij} matrix. Shown are PSF method (blue circles) and the SimSET method (red circles).

For the SimSET model, the majority of the regions are not equal to one due to imperfect reconstruction and attenuation correction. The regions below 1 indicate an under-correction for the attenuation effect (i.e. too small an attenuation coefficient), whereas the regions above 1 indicate and over-correction (i.e. too large an attenuation coefficient), during generation of the transfer function. The PSF distribution is almost entirely uniform, and considerably different to the projected levels for the SimSET f_{ij} matrix. The majority of the projected values for the PSF method are very close to unity. The PSF method is the perfect case, and this is as would be expected for perfect reconstruction and attenuation correction.

Comparing both methods, it is clear that the SimSET method will produce results that are more representative of the real world (imperfect) case, as it models system inaccuracies that are not modelled using the PSF method (see section 7.4 for a full discussion). The results indicate that the PSF method generated transfer function would not be suitable for deriving accurate estimates of the biodistribution in the presence of imperfect reconstruction and attenuation correction algorithms. Thus, the SimSET method is the 'Gold Standard' method, and used for all further studies.

7.2 Validation of the Regional Deconvolution Methods

Parameter estimation where the production of test data can be controlled (i.e. simulation) is useful in validation of the basic principles of estimation. In the case where the f_{ij} matrix accurately models the simulation, and the counting methods are the same, the estimator should naturally converge to the correct solution. This is not true for SimSET simulation as FBP reconstruction introduces inaccuracies dependent on the distribution of activity, and thus differences will be subjective. The PSF method uses a reconstructed PSF, and reconstruction is simulated and the same for any distribution. Thus the estimation methods described in section 6.2.3 can be validated using this special case by simulating by convolution with the PSF and performing deconvolution using the PSF method. Validation is straightforward and iterates to the correct result in a single iteration for MLEM. For the ART method, convergence is slower and estimates are within 7% after one iteration and reach 1% within 10 iterations.

To assess the use of ART and MLEM estimation for the SimSET method, a known uniform distribution is simulated using SimSET. Estimation is then applied to the reconstructed and pre-processed output. This was performed for the following reasons: (i) To evaluate the performance and characteristics of the ART and MLEM iterative algorithms, allowing a study of the actual errors produced and a validation of the performance by iteration number. (ii) To allow an objective comparison of the two methods, illustrating any differences in the two algorithms. (iii) To allow an effective validation of the proposed estimation methods.

The updated Zubal phantom was simulated using a uniform activity level of 0.1 μCi per cc for all regions (apart from the *outside phantom* region). $6x10^9$ decays were simulated to obtain relatively noise-free projections. The images are reconstructed and counted using the standard methods as described in section 6.2.2, effectively minimising the errors associated with registering the phantom to a template. The flood source activity is normalised such that there is an average of 100 counts per cc for the *cerebellum* (region 18). This is equivalent to a count level of 0.8 counts per voxel for 2 mm isotropic cubic voxels. For accurate estimation, the MLEM and ART algorithms should converge to this activity level for all regions.

7.2.1 Simulated Regional Distribution

Figure 7.4 shows the extracted regional count level for the reconstructed and processed uniform activity simulation. Comparison of the image to Figure 7.3 shows that the relative distribution of counts is similar to the distribution for the SimSET forward projection. However, there are obvious differences, leading to the conclusion that differences exist between the regional convolution and the back projected simulation, and therefore errors will exist in the estimated results. The count values generated using f_{ij} regional convolution are smaller than those measured when performing the SimSET simulation. This is an effect of the reconstruction methods, as counts are collected in the *outside phantom* region for all individual region simulations. This is partly due to the large number of simulated photons and partly due to the steak artifact when performing FBP. The results also show that the distribution is quite different to the expected PSF method regional convolution.

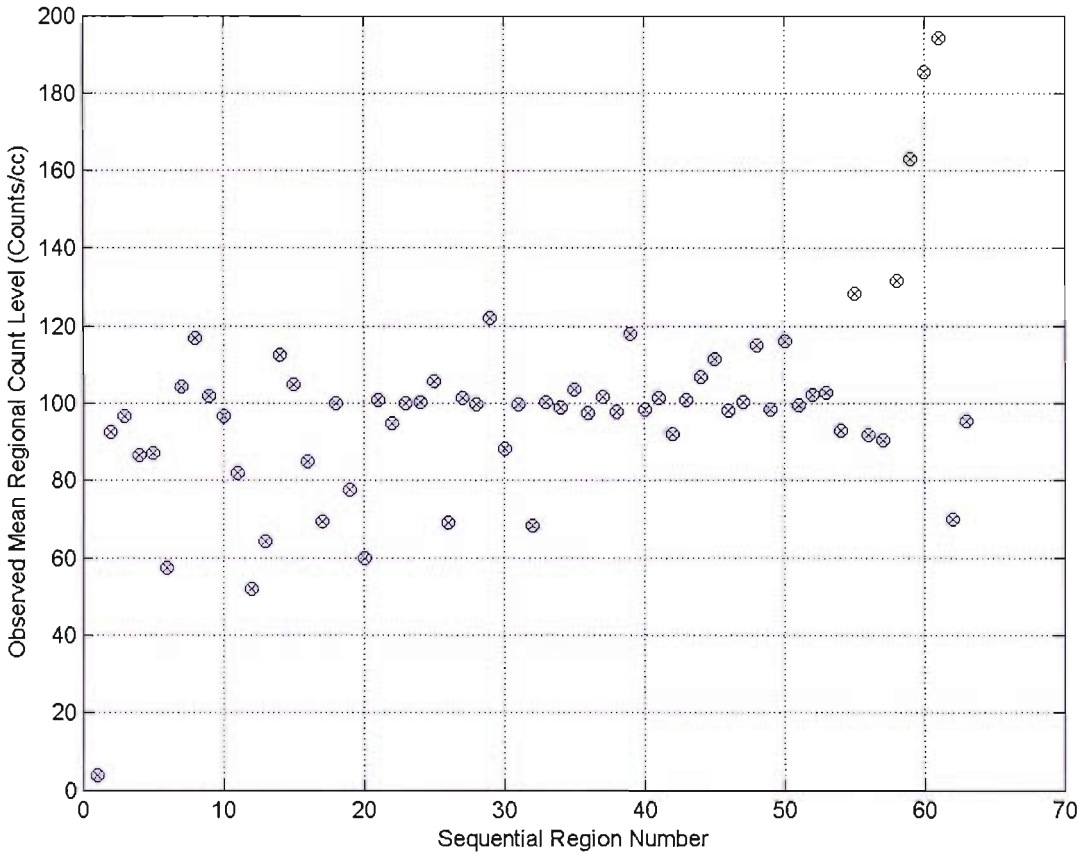

Figure 7.4. Extracted regional count levels for a SimSET simulated flood activity distribution. Activity is uniform and 0.1μCi / cc in every region except the outside phantom region, which is zero. Counts are normalised to 100 counts/cc for the *cerebellum* region (region 18).

7.2.2 MLEM

The MLEM algorithm was applied to the known simulated distribution described above by substituting for $\tilde{\lambda}_j$ in equation 6.6, using the SimSET generated f_{ij} matrix as described in section 6.2.3.3. 1000 iterations were performed to ensure the maximum likelihood estimate was found, and twelve iterations were required to fulfil the stopping criteria. The estimated activity results are shown in Figure 7.5 for the first twenty iterations of the algorithm.

The graph shows that after twelve iterations, all regions are within normal limits of the measured count level according to the t-test, except the outside phantom region (region 1). The outside phantom region is constrained to have zero activity, and as such is updated by connected regions whose primary influence is their own measured activity level. This also clearly illustrates a need for a stopping criterion, as subsequent iterations further increase this error. The graph also shows that the

number of significant regions is monotonic with iteration number, indicating that each iteration reduces the overall error (which is a property of MLEM). There is a visible difference between the rates at which some of the regions converge.

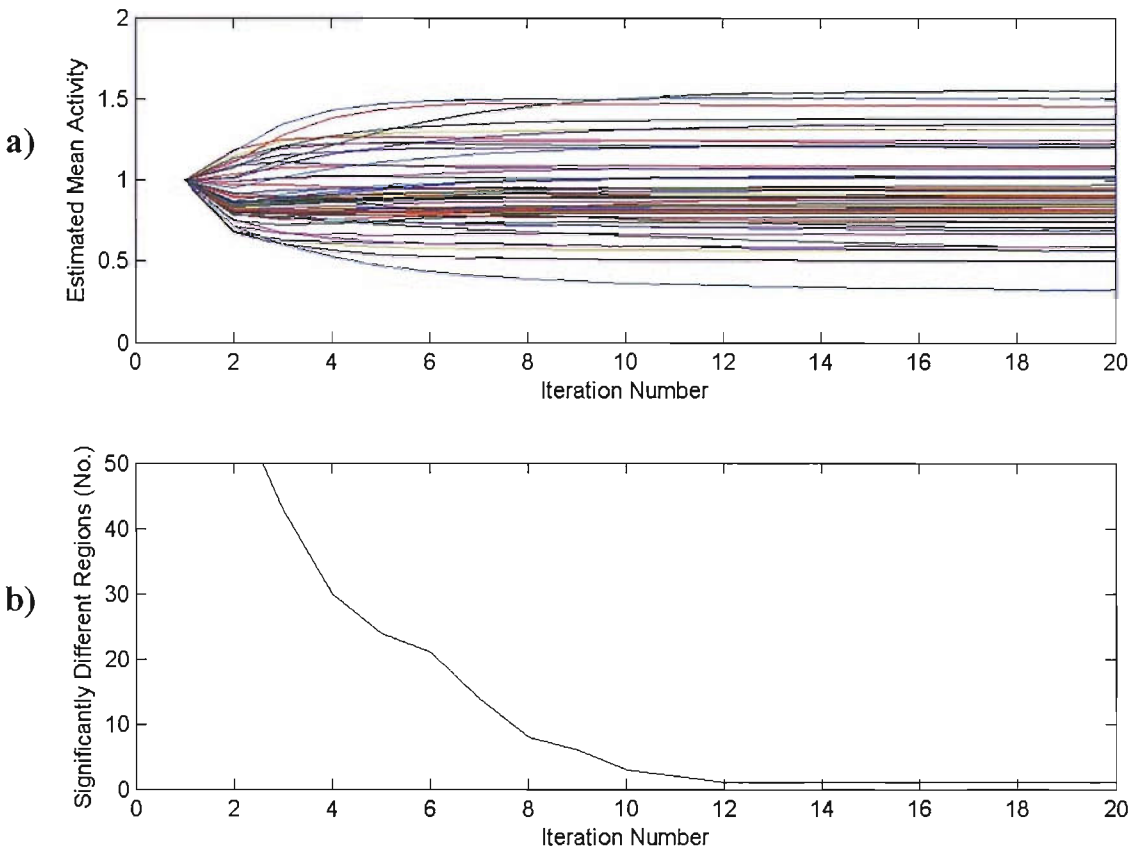

Figure 7.5. Convergence characteristics and stopping criteria for MLEM estimation of a uniform distribution. a) the estimated activity level for all regions plotted against the iteration number, and b) the number of regional distributions that are deemed to be significantly different from the control image distributions.

7.2.3 ART

The ART algorithm was applied to the known simulated distribution described in section 7.2.1 by substituting for $\tilde{\lambda}_j$ in equation 6.5, using the SimSET generated f_{ij} matrix as described in section 6.2.3.2. 10,000 iterations were performed to ensure convergence. Figure 7.6 shows the convergence characteristics for ART reconstruction using the SimSET forward projector for 50 iterations. The algorithm achieves the stopping criteria at iteration 47. Once again, the outside phantom region remains significantly different from the measured distribution, even at convergence. As with the MLEM method, there is a visible difference between the rates at which

the regions converge. The number of significantly different regions is not monotonic with respect to iteration number as with the MLEM algorithm, suggesting that subsequent iterations do not necessarily reduce the overall error.

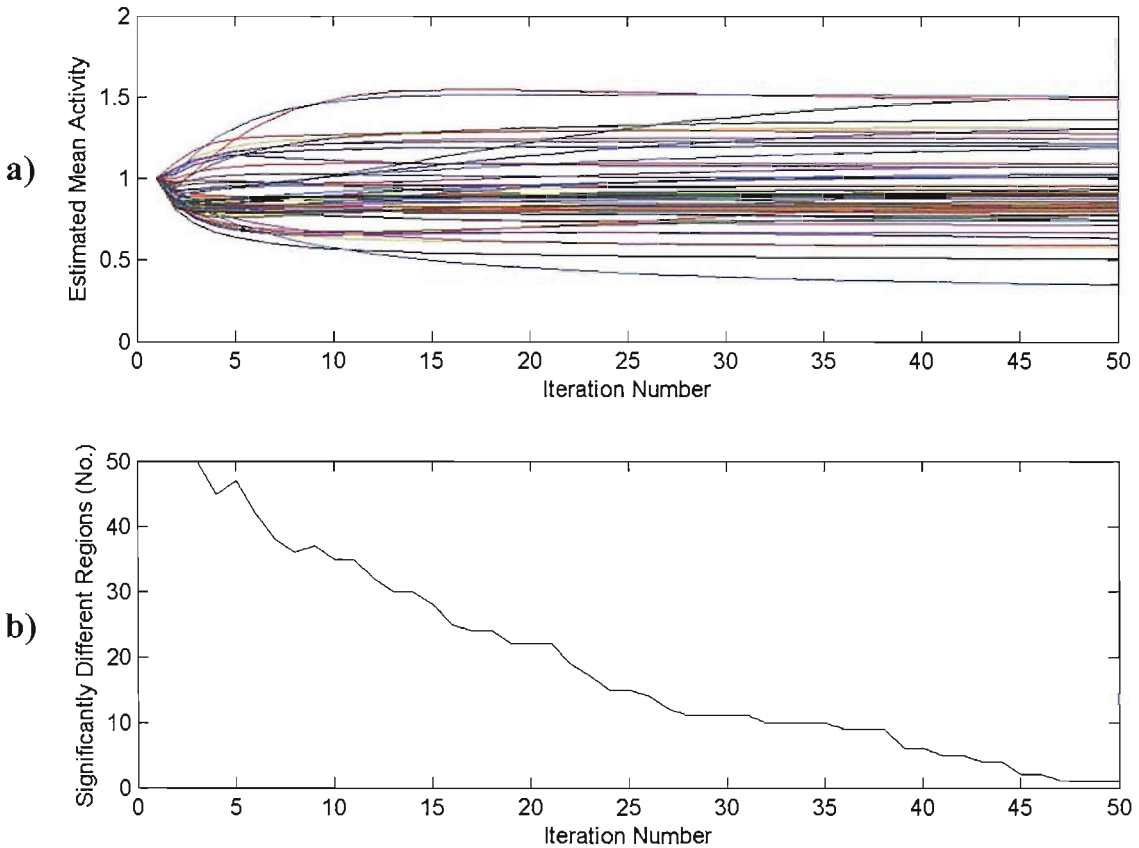

Figure 7.6. Convergence characteristics and stopping criteria for ART estimation of a uniform distribution. a) the estimated activity level for all regions plotted against the iteration number, and b) the number of regional distributions that are deemed to be significantly different from the control image distributions.

7.2.4 MLEM vs. ART Estimation

The ART and MLEM algorithms were compared at convergence, representing 10,000 iterations of the ART algorithm and 1000 iterations of the MLEM algorithm. After performing the reconstruction, the derived activity levels were compared. The maximum absolute regional difference was 7.4×10^{-15} for the Uncus region. This demonstrates that both methods converge to the same result, and illustrates that the ART algorithm is also capable of converging on the maximum likelihood estimate, albeit over a larger number of iterations.

The results show that the estimator convergence is much slower for ART, taking 47 iterations before fulfilling the stopping criteria, as opposed to 12 for MLEM. Figure 7.7 shows the estimated mean regional activity values for both ART and MLEM at convergence and after fulfilling the stopping criteria.

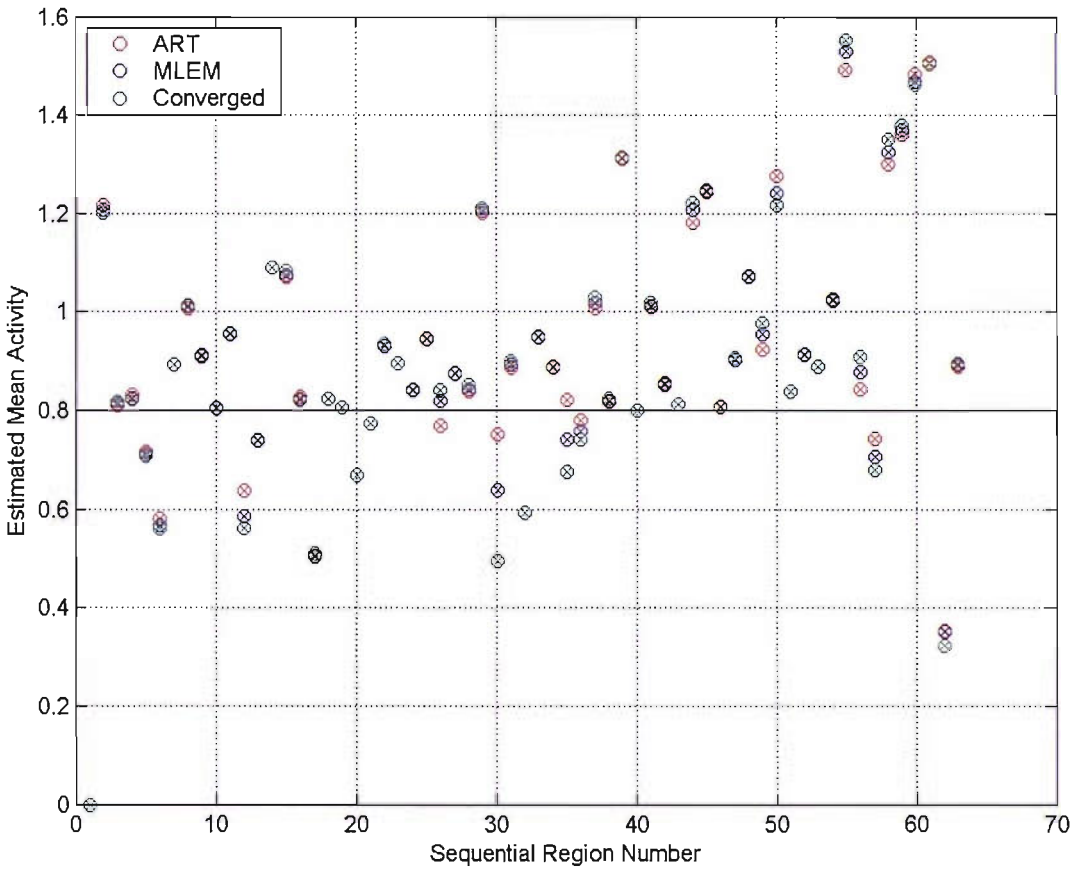

Figure 7.7. The estimated activity levels for all regions for ART (red) and MLEM (blue) after fulfilling the stopping criteria (iteration 45 and 12 for ART and MLEM respectively). Also shown is the result for both regions at convergence (green, iteration 10,000 and 1,000 for ART and MLEM respectively). The black line represents the expected estimated activity level.

Good agreement is shown for most regions. Variation is evident in the values at stopping and those at convergence. Several of the regions are diverging from their known activity value of 0.8. The MLEM estimator tends to iterate to its solution more quickly, whereas the ART estimator remains closer to the original distribution value and iterates more slowly. This result indicates that the MLEM method quickly approaches the convergence point, that both ART and MLEM solutions are erroneous, and that the stopping criterion should be used for both methods.

Of the regions shown above, all cerebral and closely connected regions show very good agreement, and all are within 25% of the original distribution. As expected, the activity distribution is overestimated for the majority of regions as the regional convolution requires an increase in activity to produce the same count levels. The difference can be partly explained by the f_{ij} matrix errors (Figure 7.3 and Figure 7.4), and partly by differences in the reconstruction process.

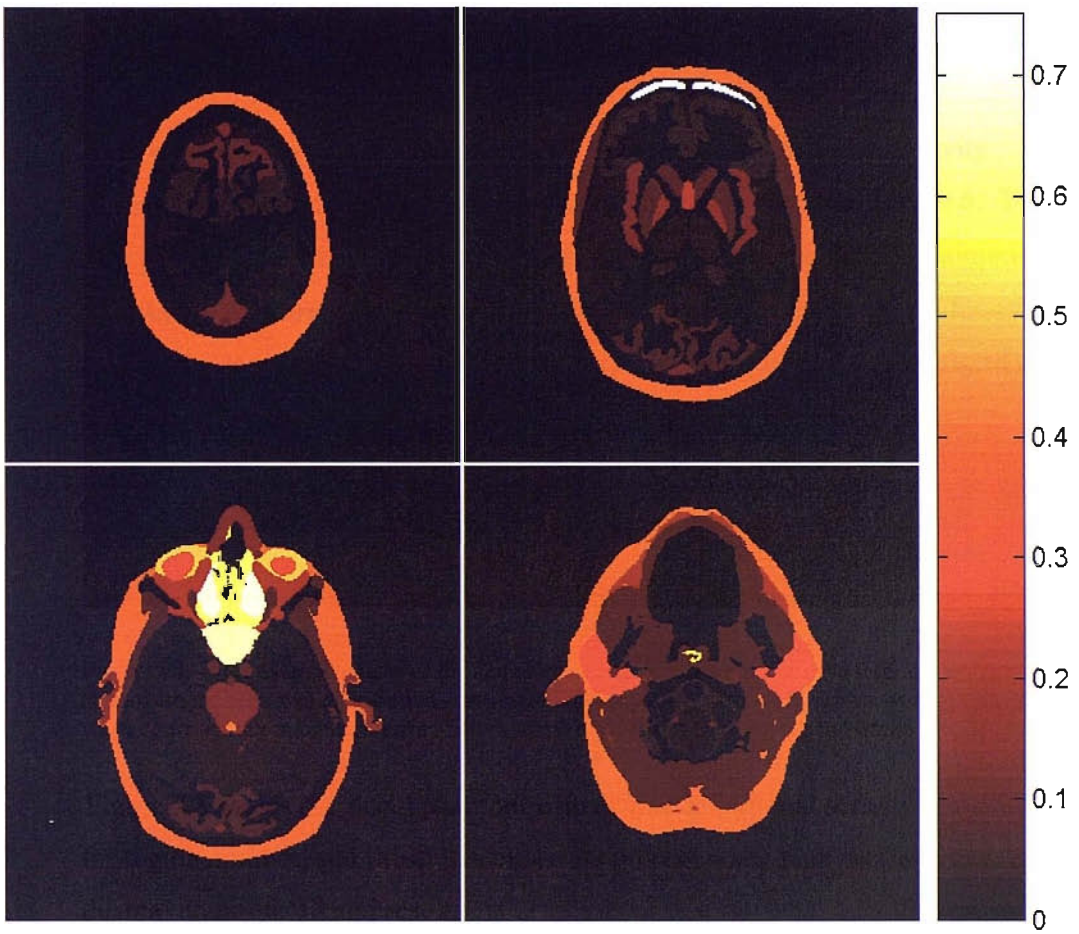

Figure 7.8. Four example slices of the Zubal phantom, coloured by absolute regional estimation error at convergence (known distribution – estimated distribution), with black representing no error and white representing maximum error. Slices numbers are (left to right, top to bottom) 25, 59, 83 and 118.

Figure 7.8 shows the Zubal phantom with estimated regional activity error substituted for region number, and illustrates the errors present when both methods converge to the maximum likelihood result.

The illustration shows that the errors are correlated with regions of high or low attenuation. That is deep cerebral regions, regions modeled as bone (skull, nasal septum) and regions modeled as air (sinuses, nasal and throat cavity), with the largest

errors in the sinus and facial regions. The images show low errors for cerebral regions, but demonstrate a level of error in and around several of the midbrain regions. Also, estimation error seems to be higher for regions nearer the edge of the phantom than for central regions. These results indicate that the proposed method is valid for obtaining estimates of regional cerebral activity within well defined error limits.

7.3 Normal Model Estimation

The results presented in this section are for the extraction of the normal activity distribution using the methods and normal control data described in Chapter 6. The results are presented for using the SimSET MLEM method for parameter estimation, although other results are quoted for the purpose of comparison. Chapter 8 focuses on the use of the extracted activity distribution(s) for the production of simulated data sets.

7.3.1 Extracted Control Data

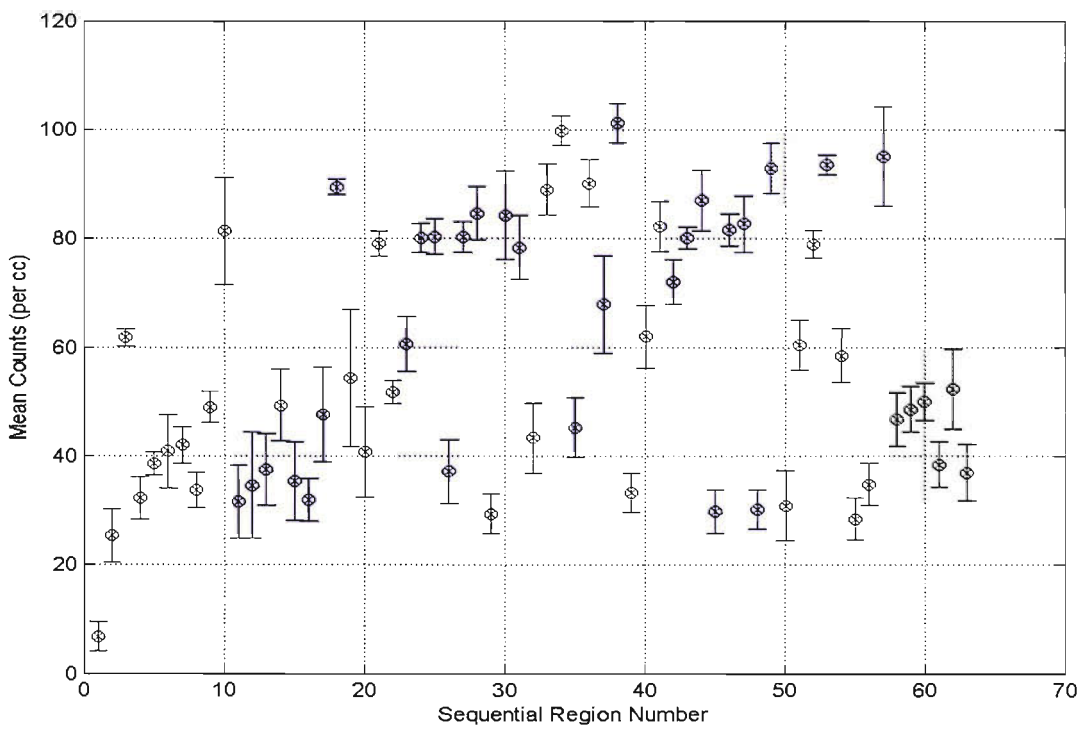

Figure 7.9. Control counts for each region within the updated phantom. The graph shows the mean counts per cc across the control group for each region, and the error bars represent +/- one standard deviation (inter-subject). The sequential region numbers are those shown in Table 6-2.

Num.	Name	cv_l	Num.	Name	cv_l
18	Cerebellum	0.016	**36**	Internal capsule	0.048
21	Cerebral WM	0.030	**38**	Thalamus	0.035
22	Superior sagittal sinus	0.041	**40**	Corpus Collosum	0.093
23	Medulla oblongata	0.084	**41**	Special region frontal lobes	0.057
24	Frontal lobes	0.032	**43**	Temporal lobes	0.025
25	Pons	0.039	**44**	Fourth ventricle	0.064
26	Third ventricle	0.156	**46**	Parietal lobes	0.036
27	Occipital lobes	0.035	**47**	Amygdala	0.061
28	Hippocampus	0.056	**49**	Globus pallidus	0.050
31	Caudate nucleus	0.074	**51**	Lateral ventricles	0.074
33	Insula cortex	0.053	**52**	Prefrontal lobes	0.033
34	Putamen	0.027	**53**	Cerebellum WM	0.020

Table 7-1. The coefficient of variation for the mean regional counts across the entire control sub-group. The regions shown are only those within the cerebrum.

All control images were spatially normalised to the SPM99 SPECT template and count normalised to the cerebellum region. Regional measurements are performed using the updated Zubal phantom, also registered to the SPM99 template, as described in section 6.3.1.

Figure 7.9 shows the regional distribution of counts across the control group for all regions in the updated phantom, along with the standard deviation values as error bars (+/- 1 SD), and Table 7-1 contains a list of all cerebral regions and their respective coefficient of variation.

All regions exhibiting high variability are outside of the cerebrum, in regions where the spatial normalisation and anatomical variation in known to introduce error to the estimates. The results show that all cerebral structures have a standard deviation value that is within 10% of the mean regional value, except for the third ventricle (problems with the modelling of this region are described in section 8.4).

7.3.2 Regional Homogeneity

When using a regional model to describe activity within the brain, it is important to ensure that the activity in each region is homogeneous across the region. This is essential to ensure that the segmentation and sub-divisions of the regions are themselves independent, and do not contain regions of varying activity levels. Homogeneous regions can be considered to be relevant to a study of brain perfusion. The measure for homogeneity is based on the coefficient of variation, as this has been shown to be particularly sensitive where regions contain voxels with extremely low

count levels [Lobaugh *et al.*, 2000]. A high coefficient of variation indicates that the region under study has a large variability between its voxels.

A similar method to that proposed by [Grova *et al.*] is used to assess the homogeneity of counts for each region, and to provide validation of the model for assessment of in-vivo distribution of activity. The population mean coefficient of variation, cv_i and standard deviation σ_i, was calculated for each region i, across all controls. The mean over all cv_i, $\overline{cv}$, was 0.11602, with SD 0.07669. [Lobaugh *et al.*, 2000] suggests using a threshold of 2 SD of the mean cv_i over all VOI's to give an indication of inhomogeneity, giving a 2 SD threshold for the homogeneity test of 0.2694.

Only three regions were above the homogeneity threshold. These were outside brain (region 0, $cv = 0.3782$) which is not modeled with a perfusion level, dens of axis (region 70, $cv = 0.2988$) which is not part of the cerebrum, and the eye lens (region 121, $cv = 0.3002$) which is a part of the eye. While it is true that error in any region will produce error in every other region, these regions are sufficiently remote (and too highly variable) to add meaningful bias to the regional estimates.

The perfusion model can therefore be assumed to be sufficiently homogenous within the brain and head region to enable a study of regional activity.

7.3.3 The Normal Activity Distribution

Activity levels were estimated for the normal control template image described in section 6.3.1 using the methods described in section 6.2.3. The MLEM algorithm reached the stopping criteria for all cerebral regions at iteration 28. The ART algorithm reached the stopping criteria for all cerebral regions at iteration 156. The results show variation in distributions upon reaching their respective stopping criteria. The number of parameters used for both methods is low and therefore the time required for estimation is small, although MLEM converges more quickly.

Table 7-2 shows the extracted mean regional counts and associated standard deviation for the control template image, for all phantom regions using the MLEM algorithm and stopping criteria.

Region	Mean	SD	Region	Mean	SD
1	0.00	0.00	**33**	125.02	14.20
2	51.58	15.62	**34**	141.01	8.13
3	53.39	4.05	**35**	113.65	31.53
4	36.41	9.18	**36**	92.06	16.72
5	41.05	4.63	**37**	63.54	36.77
6	78.80	16.29	**38**	133.12	6.26
7	45.08	4.98	**39**	44.60	8.82
8	23.81	6.14	**40**	50.11	11.31
9	40.64	11.48	**41**	120.77	13.98
10	62.13	48.89	**42**	136.15	15.59
11	45.45	13.56	**43**	92.34	2.92
12	63.62	30.95	**44**	118.87	30.01
13	71.18	18.65	**45**	27.81	9.03
14	64.60	10.36	**46**	98.98	4.71
15	50.72	24.13	**47**	102.99	14.90
16	25.30	6.93	**48**	33.29	6.05
17	61.29	15.15	**49**	108.56	20.53
18	105.59	2.32	**50**	51.18	40.33
19	76.21	20.50	**51**	29.29	9.56
20	62.29	14.95	**52**	100.91	4.71
21	72.22	3.34	**53**	107.74	5.74
22	49.71	6.14	**54**	74.76	17.66
23	69.91	13.95	**55**	3.09	2.82
24	101.64	4.79	**56**	15.55	10.32
25	98.03	6.19	**57**	208.47	45.80
26	40.08	8.73	**58**	28.68	6.50
27	105.01	6.03	**59**	15.27	5.56
28	106.90	12.76	**60**	4.04	2.41
29	20.76	3.61	**61**	5.34	2.48
30	208.35	99.00	**62**	96.49	15.09
31	96.07	16.16	**63**	16.97	11.35
32	73.32	15.63			

Table 7-2. The estimated activity mean and standard deviation values for all regions using the MLEM algorithm at stopping criteria, for the control template image described in section 6.3.1.

The regions with the highest count levels and variability are all small regions and outside of the cerebrum. Three regions iterate to zero for some controls. These are the frontal sinuses (55), the sphenoid sinuses (60) and the maxillary sinus (61), and are additional regions and modelled as cavity. These regions are subject to high anatomical inter-subject variability and registration errors, and while the model for the frontal sinuses is known to be accurate for the Zubal phantom subject, this variation dominates the estimated activity levels within these regions. Furthermore, the facial regions including the maxillary and sphenoid sinus are modelled as air and lack the inclusion of the complex structure of the sphenoid and facial bones along with its associated attenuation.

The coefficient of variation was calculated for the estimated activity levels for each region within the cerebrum from Table 7-2, to allow a comparison between the

variation when counting and that for the estimated activity levels. The results are presented in Table 7-3. All regions within the cerebrum had a coefficient of variation of under 0.33, with the largest variation measured in the lateral ventricles. When compared to Table 7-1, it can be seen that the variation within the estimated activity level is higher than the variation in the measured counts. This is as expected, as the variation in the measured count levels will be propagated to the estimated values. An important result is that the variation in the estimated values is correlated with the original counting variation ($r = 0.74$ over 24 cerebral regions). This indicates that while the method increases the variation in the original count, little unexplained variation is introduced by performing the extraction. This result seems to indicate that there could be an applicable diagnostic capability for the extracted values, although variation is still above that for extracted count levels. These results also suggest that the estimation process is robust to variation in the original data.

Num.	Name	*cv*	Num.	Name	*cv*
18	Cerebellum	0.022	**36**	Internal capsule	0.182
21	Cerebral WM	0.046	**38**	Thalamus	0.047
22	Superior sagittal sinus	0.123	**40**	Corpus collosum	0.226
23	Medulla oblongata	0.200	**41**	Special region frontal lobes	0.116
24	Frontal lobes	0.047	**43**	Temporal lobes	0.032
25	Pons	0.063	**44**	Fourth ventricle	0.252
26	Third ventricle	0.218	**46**	Parietal lobes	0.048
27	Occipital lobes	0.057	**47**	Amygdala	0.145
28	Hippocampus	0.119	**49**	Globus pallidus	0.189
31	Caudate nucleus	0.168	**51**	Lateral ventricles	0.327
33	Insula cortex	0.114	**52**	Prefrontal lobes	0.047
34	Putamen	0.058	**53**	Cerebellum WM	0.053

Table 7-3. The coefficient of variation for activity levels derived using the MLEM SimSET method. The regions shown are only those within the cerebrum, and are calculated from Table 7-2

7.3.4 Group Analysis

The MLEM method was applied individually to each spatially and count normalised control subject within the normal database. The count distribution is estimated from regional mean levels for each control and applying the MLEM technique with stopping criteria. A measure of the inter-subject regional variation is calculated across each region for each of the controls. These results are useful in assessing how well a selected region is defined in terms of how consistent the distribution of counts within the region is across the control group. It is worth pointing out that partial

volume effects, differences in anatomy and differences in image registration will always dominate and produce high variation within a region.

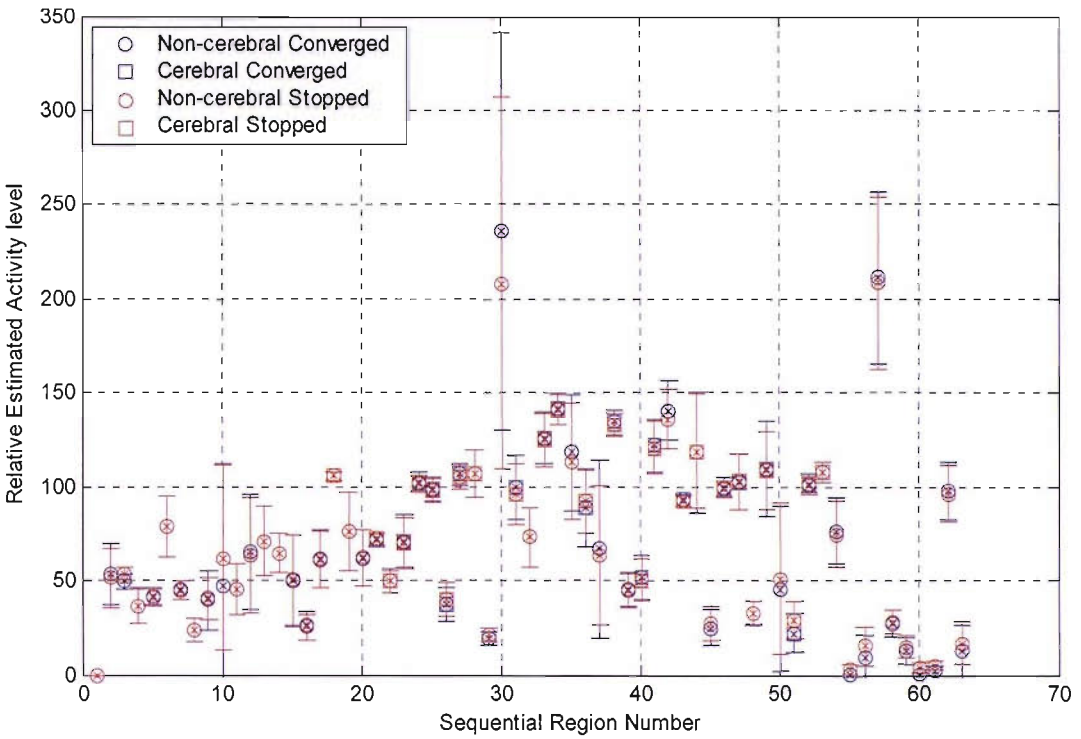

Figure 7.10. Summary data for estimated activity levels derived using MLEM with the SimSET f_{ij} forward projection, for each normalised control individually. The values represent the mean estimated activity values across the entire control group, and the bars are the inter-subject SD. The results are shown for the estimated value at convergence and upon fulfilling stopping criteria. The boxes represent cerebral structures. All control subjects are spatially normalised and count normalised to the cerebellum region prior to estimation.

Figure 7.10 shows the mean and variation in the estimated activity levels when applying MLEM to each of the control subject individually. The results indicate differences in variation of the estimated values between the stopping and converged activity levels. It can be seen that the inclusion of the stopping criteria reduces the variance of the estimate, which demonstrates that the inclusion of the stopping criterion is producing more consistent quantitative estimates.

7.4 Discussion

Figure 7.1 and Figure 7.2 show how the distribution of counts depends on the distribution of activity. While the results indicate that the counts in a region are influenced by adjacent regions, they also suggest that the major contribution to most regions is the activity in that region. The major factor influencing the distribution is

the partial volume effect. The extraction of the f_{ij} matrix and regional counts also has a useful side effect. Model based partial volume correction is inherent in the extraction of transfer matrix and the regional count levels, and the experiment therefore accounts, in a general sense, for the PV effect. This has been shown to improve results for quantitative imaging [Du *et al.*, 2005].

The results for the PSF method clearly highlight the need to incorporate an accurate model for attenuation in the simulation to provide accurate parameter estimation for real data. When performing regional convolution of a uniform distribution, the measured distribution within the head will also be uniform (for a spatially uniform PSF). The exception is in regions that are connected to the outside phantom region by the voxelised PSF (i.e. $\text{region}_{\text{outside},j} \otimes PSF > 0$), which is not simulated in the training data (see section 6.2.2). The estimator will attempt to converge on a solution that depends only on the size and shape of a region, and not on its relative attenuation. This is a major limitation of the PSF method.

The Monte Carlo methods for generating the forward projector are more accurate due to the inclusion of the attenuation effect, and inaccuracies resulting from imperfect correction are more likely to be systematic and similar to those found in physical imaging. As with physical imaging, the distribution of regional counts is correlated with the attenuation coefficient and regions with very little attenuation result in an increase in the total forward projected counts, as demonstrated by Figure 7.3 (e.g. region 5 is modelled as skull, and region 58-61 are modelled as air). Monte Carlo methods for generating the forward projector are also preferred for the following reasons: (i) As the PSF system is dependent on an experimentally measured PSF, any change in the imaging system requires performing new experimental measurements, (ii) while the SimSET forward projector needs to be simulated and calculated for any given implementation, this only needs to be carried out once, and (iii) the model used for the generation of Monte Carlo data is an accurate model of the system, and accounts for effects such as attenuation.

The third option would be to simulate the distribution using full Monte Carlo simulation to forward project the distribution on each iteration of the ART or MLEM algorithm. This offers the most accurate forward transformation including full simulation of the data for each iteration. The stopping algorithm and source

distribution is also optimised as stopping can be subjectively and actively enforced. The disadvantage is the time required to perform estimation. For convergence of the MLEM algorithm (28 iterations) on dual processor 2GHz AMD PC's, simulating 6 billion decays per iteration with stratification and working with good input data (i.e. section 6.3.1), would require 630 CPU hours of processing to complete. This timing is based on the current grid networking capability described in section 3.5.3, and without adding the necessary intermediary steps (e.g. iterating the algorithm and setting up the simulation).

Validation was performed on the methods to test their ability to estimate a known result. The results presented in sections 7.2 and 7.3 show that the methodology is robust enough to be directly applicable to a number of simulation systems. Application using PSF simulation demonstrated that by using an f_{ij} matrix that is an accurate transfer function of the imaging and reconstruction process, then precise activity estimates can be achieved in few iterations. Thus, it is important to ensure that the transfer function accurately defines the underlying system. Any approximation or inaccuracies in the model produces errors in the derived activity distribution while still providing an optimal solution.

Results for Monte Carlo simulation of the flood source indicate that the estimated activity in cerebral regions are within 25% of the true distribution. The MLEM estimator converges more quickly and most of the regions are close to optimum when applying the stopping criteria. For ART, the regions converge more slowly and small but tangible errors are evident for many iterations of the algorithm. Running ART, while using the SimSET generated transfer function produces identical results at convergence to the MLEM method. However, the method converges more slowly, is less consistent and more variable than MLEM when using the stopping criteria. The MLEM algorithm with stopping criteria is therefore adopted as the 'gold standard' for parameter estimation.

One major limiting factor in achieving zero error is the image reconstruction method (FBP) and the applied attenuation correction when generating the tomograph for counting. The results of errors in the estimation of the attenuation map, and inter-image differences, have a meaningful and direct effect on the measured perfusion level. The FBP reconstruction algorithm generates a uniform attenuation mask based

on the collected count distribution. Although the effect of attenuation is known to be effectively averaged across the projections, regions with a very high or low level of attenuation are likely to be in error, as are their reconstructed values. Furthermore, regions that are close to the edge of the phantom may be partly excluded from the generated attenuation mask for low count images, or high activity levels may result in an artificially large attenuation map. As the forward and back projections for the experiment are effectively the same, and this case provides precise estimates (this result is proven by experiment using the PSF method), then differences must exist in the processing and reconstruction method. It is the combination of these factors and the original forward projector generation errors that produce the error witnessed in Figure 7.7. This results in a loss of information that is closely related the differences in the generated attenuation map, or specifically to; (i) the difference between calculated and actual attenuation coefficients of a region and (ii) its proximity to the edge of the phantom.

These techniques effectively highlight regions within the phantom that are in error due to reconstruction and processing differences, as shown in Figure 7.8, and highlight the importance of limiting inter-subject variability by using accurate and repeatable methods. Several techniques could be employed to obtain a more accurate reconstructed value. Accuracy could be improved by using model based attenuation correction based on coefficients derived from the phantom as described in [Zaidi *et al.*, 2004, Arlig *et al.*, 2000, Stodilka *et al.*, 2000]. All studies reported positive benefits in terms of accuracy when inferring attenuation maps from the phantom, and the latter study suggests that using the Zubal phantom to infer attenuation coefficients results in a mean error of 7.5% when compared to using an attenuation map generated from transmission imaging. This would provide accurate attenuation correction for the generation of the transfer function and a normal approximation for subject imaging. This would greatly improve the estimation accuracy for the activity distribution, and realise lower variance in the estimated values.

The variation across the extracted counts for all subjects was shown to be correlated with the measured count level variation (Table 7-1 and Table 7-3), which shows that the extraction process is robust in the presence of variation. However, when counting in the presence of real anatomical variation, it is unlikely that the activity model is an

accurate representation of the real subject image even after spatial normalisation, and hence errors will always exist. The extracted activity levels for the simulated database show good agreement with the cerebellum and cortex measures reported in a recent study that incorporated voxel-based morphology for measurement of HMPAO distribution [Ito *et al.*, 2006].

Chapter 8 Toward An Artificial Normal Control Database

A major goal of this study was to improve simulation of voxelised and segmented models of human head anatomy by incorporating a normal model of brain perfusion. The simulation model then describes both the activity and attenuation correctly and provides a useful baseline result from which many different variations of anatomy and physiology can be generated. This would allow the production of arbitrary datasets that could be applied to many facets of the radionuclide imaging process. Of particular importance is the use of the method to produce more realistic normal and abnormal data sets.

This chapter focuses on the application of the methods described previously to produce a model to be used for the production of normal SPECT images. The results presented in Chapter 7 are extended and applied to the SimSET model for the imaging system, to produce simulated data for analysis. It serves as an analysis of the normal subset of control data in terms of assessing the reproducibility of the biodistribution estimation for different subjects, and the effect on simulation. As the results discussed in Chapter 7 do not illustrate the errors in terms of normal modelling, the initial results presented are for (i) the ART method with stopping criteria, (ii) the MLEM with stopping criteria, and (iii) the MLEM method at convergence (both ART and MLEM produce the same results at convergence). The results reported herein, for reasons to be discussed, effectively constitute a feasibility study for the application of the methods to the production of normal data.

8.1 Simulated Normal Distribution

An analysis of the simulated data for the three algorithms is presented here, with the aim of defining the 'gold standard' method for providing the most accurate 'normal' simulations. Normal Control data was simulated for parameters derived from both the ART and MLEM algorithm at the stopping criteria, and at convergence.

Parameters were estimated for each subject in the normal control group as described in section 7.3.4, and the estimated activity levels were used to generate the activity model for full SimSET simulation. The activity and attenuation objects used in the simulations are all based upon the Zubal phantom in its original orientation, and are the same for each subject. $6x10^9$ decays were simulated for each subject using the standard model described in section 3.5.2, images are scaled to $5x10^6$ counts total and Poisson noise is added. Standard filtered back projection reconstruction is then performed on each image for comparison with normal data.

8.1.1 SPM99 Analysis

SPM99 pre-processing was carried out using the standard methods, to compare the estimated and simulated data to real patient data. The sensitivity is increased by smoothing using a smaller 12mm FWHM Gaussian kernel and using a smaller 14mm diameter ROI for cerebellar normalisation. Comparison was with the control sub-set described in 6.3.1 which were processed using the same methods. This is the group from which the data was derived and offers quantitative validation of the model accuracy. Any error witnessed in these results is a direct effect of the modeling, minus those errors discussed in Chapter 7.

SPM99 analysis is performed using the standard group analysis. Figure 8.1 shows the SPM99 hyperperfusion results for the normal simulated model generated using both the ART and MLEM algorithms with stopping criteria. No significant hypoperfusion clusters were detected for any method.

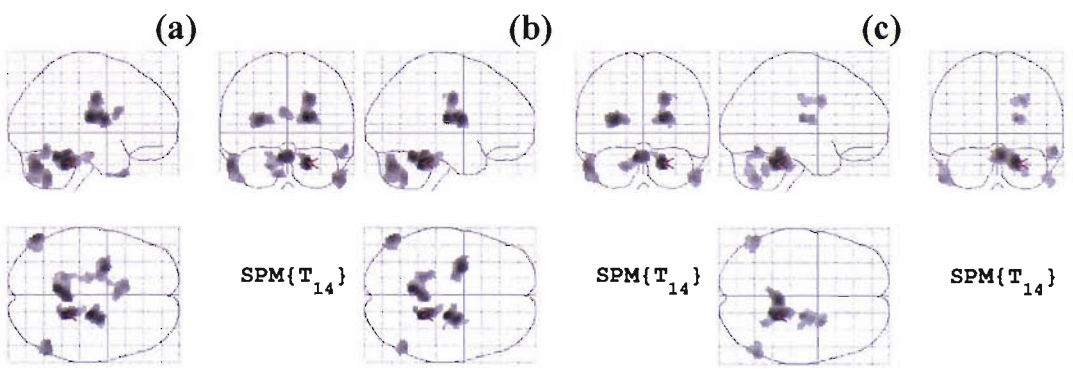

Figure 8.1. SPM99 analysis results for the estimated mean control distribution. a) the methods at convergence, b) the ART method, and c) the MLEM method. The images show significantly higher ($p > 0.001$) voxel intensities in the simulated image compared to the controls from which the activity distribution was derived, for clusters of $n > 100$ connected voxels.

The results show that the MLEM algorithm has a lower number of significant voxels compared to the ART method and both are lower than the converged result. Of the clusters shown, five were deemed significant at cluster level for the ART estimation compared to only one for the MLEM estimation values ($p<0.05$ corrected).

8.1.2 MarsBaR Analysis

As automatic spatial normalisation is only valid for cerebral regions, MarsBaR analysis VOI's were restricted to those within the cerebrum. Limiting the number of regions on which the comparison is performed also improves the power of the test by reducing the number of multiple comparisons. For all comparative analysis using MarsBaR, the mean regional count level was used as the summary function.

For both the ART and MLEM algorithm at stopping point, no regions were deemed to be significantly lower than the control distribution according to MarsBaR analysis, for either corrected or uncorrected p values. Table 8-1 shows the significantly hyperperfused regions for MarsBaR VOI analysis on the estimated and simulated distribution at convergence, and for ART and MLEM at stopping point. The table shows the uncorrected and corrected p-values (after applying a Bonferroni correction, n = 24), for VOI's with statistically significant higher count level than the control group.

Region	Converged		ART		MLEM	
No.	Uncorrected	Corrected	Uncorrected	Corrected	Uncorrected	Corrected
25	0.0020	**0.0475**	0.0035	0.0810	0.0116	0.2438
28	0.0371	0.5962	0.0392	0.6174	0.0587	0.7660
34	0.0167	0.3320	0.0175	0.3454	0.0263	0.4730
36	0.0391	0.6162	0.0514	0.7180	0.0710	0.8291
38	0.0433	0.6543	0.0562	0.7503	0.1768	0.9906
44	0.0008	**0.0195**	0.0013	**0.0316**	0.0014	**0.0325**
47	0.0155	0.3124	0.0261	0.4704	0.0102	0.2191
49	0.0121	0.2530	0.0180	0.3540	0.0108	0.2303
53	0.0006	**0.0132**	0.0009	**0.0209**	0.0023	0.0535

Table 8-1. The Zubal phantom regions deemed to have a significantly higher mean than the control group by MarsBaR analysis. Columns are for converged results, ART stopped and MLEM stopped. Results show all significant regions, using uncorrected and corrected p-values at a threshold of $p<0.05$. Bold values within the table indicate statistically significant differences for corrected p-values ($p<0.05$).

The converged result indicates that overestimation occurred in the *pons*, the *fourth ventricle* and the *cerebral white matter* regions. The results for ART are similar but

the *pons* region is still hyperperfused but not significantly different to the group. For MLEM, only the *fourth ventricle* is significantly different from the control group, although the *cerebral white matter* is still relatively hyperperfused. Both ART and MLEM estimations are more normal at the stopping point than at convergence. The MLEM algorithm results in the lowest average level of significance, and more normal looking data. The number of statistically significant regions is highest for the converged result.

8.1.3 Analysis Using Standard SPM99 Processing with Complete Database

To offer a more powerful statistical test, the simulated distribution is analysed using the complete routine analysis described in section 3.3.2, and using the larger database with the standard protocol. The full normal database has a higher level of uncertainty as the derived values are unlikely, statistically, to be equal due to less tightly controlled variation and effects such as the natural activity decline due to age (see section 6.3.1).

Figure 8.2 shows the voxel-wise significance maps for SPM99 analysis of the estimated and simulated data set at convergence, compared to the full control group. The graphs show clusters of 100 or more significant connected voxels at a corrected threshold of $p < 0.001$. At convergence, the simulated distribution shows significant hyperperfusion at cluster level for the largest cluster ($p = 0.000$), and also at set level ($p = 0.020$). Again, no significant hypoperfusion is detected.

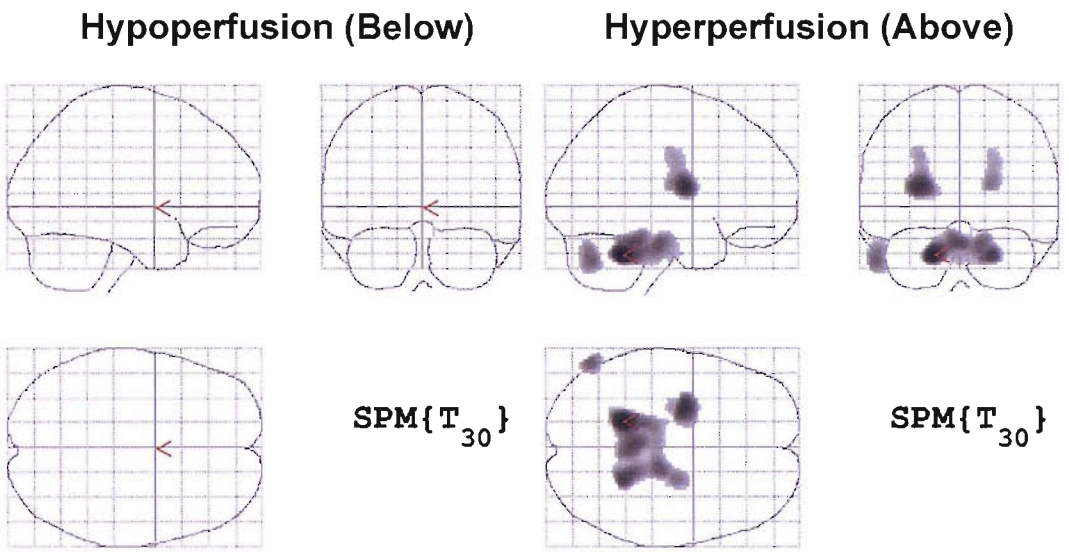

Figure 8.2. SPM99 output for the SimSET simulation at convergence for both the ART and MLEM estimated activity distributions. The results show statistically significant hypoperfusion and hyperperfusion for comparison with the full control group.

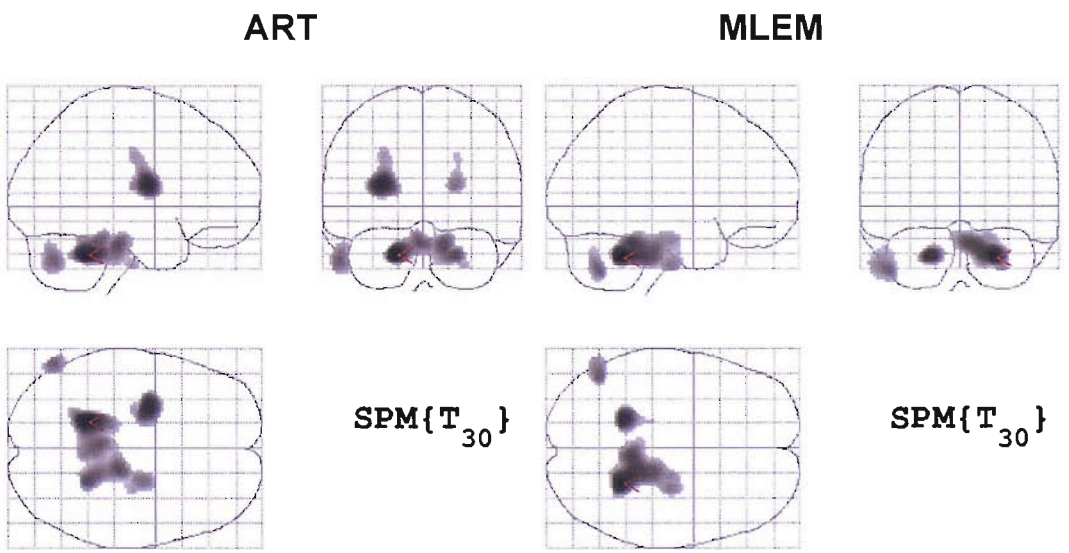

Figure 8.3. A comparison of the significant connected voxels detected when applying the standard SPM99 processing method. The results are shown for both ART and MLEM derived activity distributions, and show detected significant hyperperfusion.

Figure 8.3 shows the SPM99 output for ART and MLEM derived simulations at stopping point, when compared to the full normal database. No significant hypoperfusion was detected for either method. The largest detected cluster for the ART method (arrowed) is significant at cluster level ($p = 0.002$), and the data is also significant at set level ($p = 0.020$). The hyperperfusion is not significant at set level for the MLEM method ($p = 0.082$) although the largest cluster (arrowed) is significant

at cluster level ($p = 0.003$). The hyperperfusion is overall less significant for the MLEM method of estimating the distribution. The difference witnessed in the pattern of hyperperfusion also suggests that the MLEM method at stopping provides a different activity distribution to ART. These results also indicate that using the stopping criteria during estimation improves the estimated results.

8.2 Qualitative Analysis of the Current 'Gold Standard'

Parameter estimation using the SimSET generated forward projector and MLEM is the adopted 'gold standard' method. Figure 8.4 shows axial slices of the simulated normal image generated using this method (no added Poisson noise) and compares this to the normal template image from which the distribution was derived (section 7.3.1). The model shows good agreement across the entire cerebrum, although there are several qualitative differences between the patterns of perfusion.

There appears to be an attenuation effect in the template model, inferior and anteriorly to the temporal lobes and immediately inferior of the frontal lobe (slices 9 and 17), that is not present in the phantom. This would be consistent with the intricate structure of the *sphenoid sinus* and *Ethmoid sinus* and articulation with the frontal bone. The simulated data has an almost uniform distribution in this region with the exception of the *concha, turbinates and septum.*

The perfusion pattern for the simulated model is also different in the midbrain and cerebral peduncle (slices 33 and 41), and overestimation appears to be in a similar pattern to the overestimated regions shown in (the top right of) Figure 7.8. The midbrain contains a large number of small regions in close proximity, several of which are continuous with the *pons* and *brainstem* region (slices 25, 33, 41 and 49). Closer inspection reveals that the *Putamen* (34) is hyperperfused and the *thalamus'* (38) spatial extent appears to be different to the template.

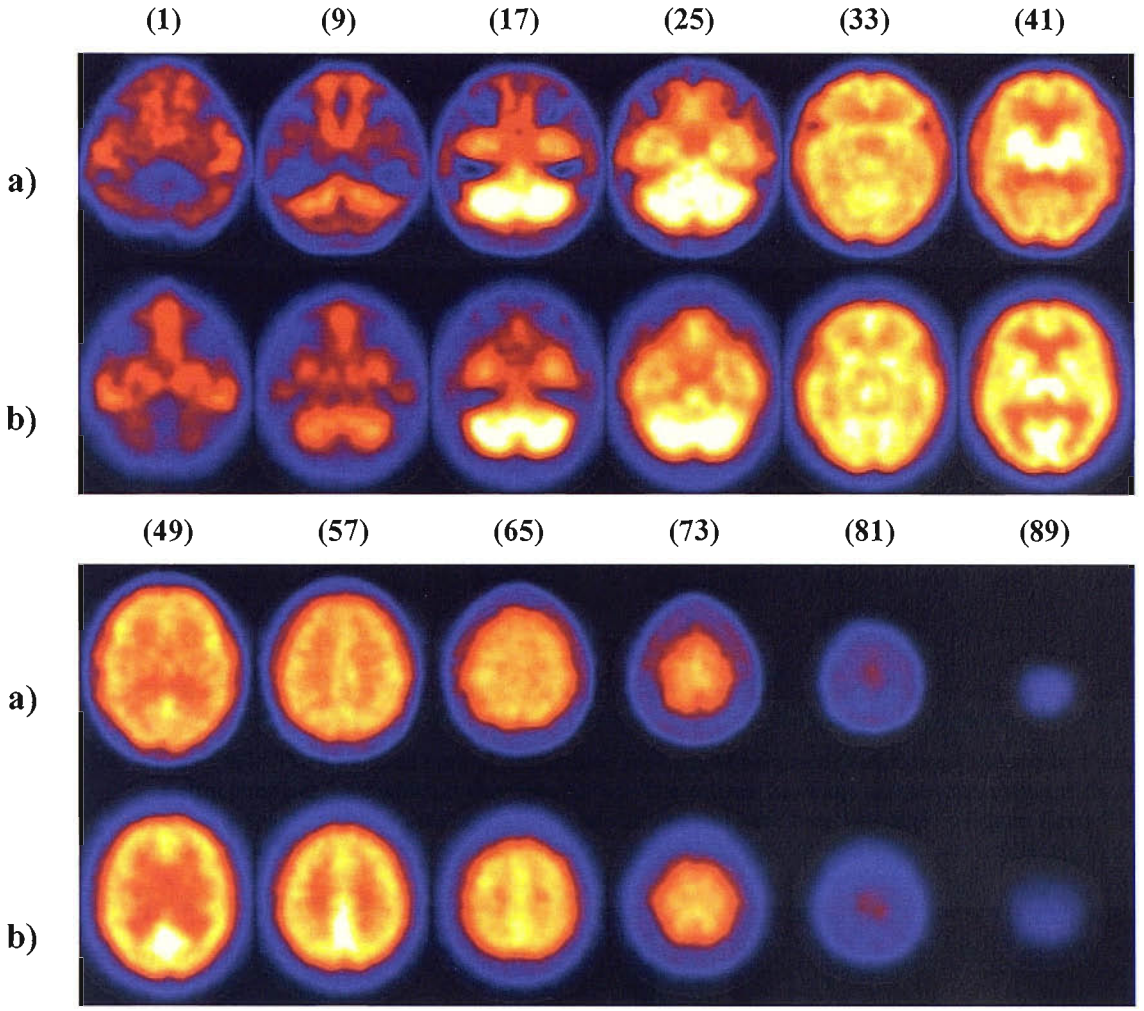

Figure 8.4. The simulated normal distribution for MLEM parameter estimation (a) compared to the control template from which it was derived (b). The column headings are the slice numbers for MNI template space. Images have no added Poisson noise and have been smoothed using an 8 mm FWHM Gaussian kernel.

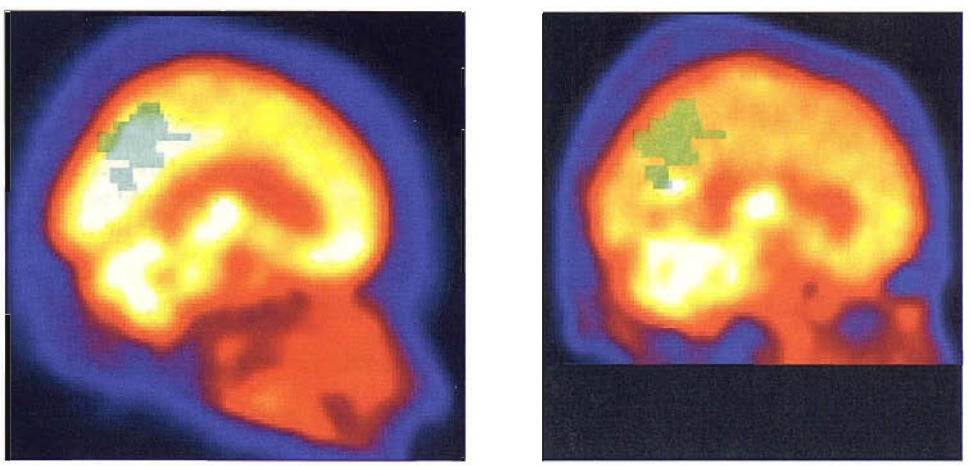

Figure 8.5. The control template image (left) and the simulated normal distribution (right). The precuneus region (extracted from the Talairach daemon) is overlaid and coloured in green.

The precuneus region of the *parietal lobe* appears to be hyperperfused in the template model (slice 41, 49 and 57), when compared to the simulated model. Figure 8.5 shows the two images with the precuneus from the Talairach atlas overlaid, and illustrates the difference in the level of perfusion. This is an example of a functionally distinct region that is not modeled separately in the phantom, and a recent study suggests that perfusion of the precuneus is as much as 35% more than surrounding regions [Cavanna and Trimble, 2006]. The precuneus in the Zubal phantom overlaps both the *parietal* and *temporal lobes*, which makes it more difficult to detect using VOI analysis and prone to larger error during estimation. The precuneus is likely to be directly responsible for a large part of the error and variability witnessed in these and connected regions.

A major difference in the pattern of perfusion is evident around the *cerebellum* and *brainstem* regions. The *cerebellum* is not easily distinguishable from the *brainstem*, *pons* and *fourth ventricle* in the simulated result; whereas it is clear in the template image. The *cerebellum* perfusion is also wider and narrower at the bottom in the simulated data. The *cerebral white matter* has a significantly higher perfusion level than the template image. Furthermore, the *skeletal muscle* immediately behind and inferior to the cerebellum appears to be hyperperfused in the simulated data.

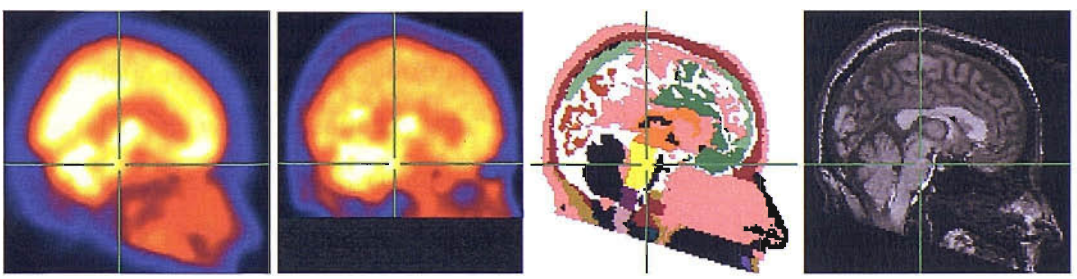

Figure 8.6. Example slices for the phantom simulation illustrating the problems with the segmentation of the cerebellum and surrounding regions. The crosshairs are centred on the pons. Images are, from left to right, the template Image, the simulated image, the Zubal phantom image, and the Zubal phantom MRI map.

Figure 8.6 shows the *cerebellum*, *brainstem* and *pons* region in more detail, using multiple different images. As can be seen, the *pons* (centre of cross-hairs) region has a higher perfusion level than the surrounding *brainstem*, although both are modeled as a single region in the phantom (yellow). The *third ventricle* running posterior to the brainstem should be continuous and create a divide between the *cerebellum*,

brainstem and *spinal cord* in the medial slices. Superiorly, the third ventricle joins the modified *CSF* which was originally the *cerebral aqueduct*. Also, there appears to be a lower level of perfusion immediately inferior to the *thalamus* at the top of the *brainstem* in the simulated image, that is not evident in the template.

8.3 Analysis of Simulated Normal Database

To assess the repeatability of the method, a leave-one-out analysis was performed for the entire simulated control group, by comparing each simulated control image with the remainder of the database. The SPM99 derived spatial normalisation parameters were also assessed. As there is no difference between the anatomies of each of the subjects, then the variation within the count distribution should have a negligible effect on the iteratively derived affine transformation parameters. Good agreement was shown across the spatial normalisation parameters for all simulated normal subjects. Of the group, only one image (simulated control 5) shows a significant set of hypoperfusion clusters ($p = 0.0021$), of which one is significant at cluster level ($p = 0.007$ corrected). The abnormalities are positioned at the posterior and anterior of the *corpus Collosum* on the left side of the brain. The abnormalities are small and do not appear to be associated directly with any anatomical structure. This error is assumed to be partly due to large variability in the extracted count levels, and partly due to segmentation of the *corpus Collosum* and surrounding area. As the variance is known to be relatively well controlled within the group, the results indicate that the method is both applicable to this entire control group, and is robust to normal variation within a dataset. This effectively illustrates the applicability of the method to the production of normal data sets within normal anatomical and physiological variation.

The simulated normal control subjects were individually compared to the original database (from which they were derived) using standard SPM99 processing. Figure 8.7 shows the summary results for the detected significant hypoperfusion and hyperperfusion for all subjects, overlaid on the Zubal phantom image, showing significant clusters of voxels ($n > 100$) at a threshold of $p < 0.001$. The significant voxel maps are averages across all subject analyses.

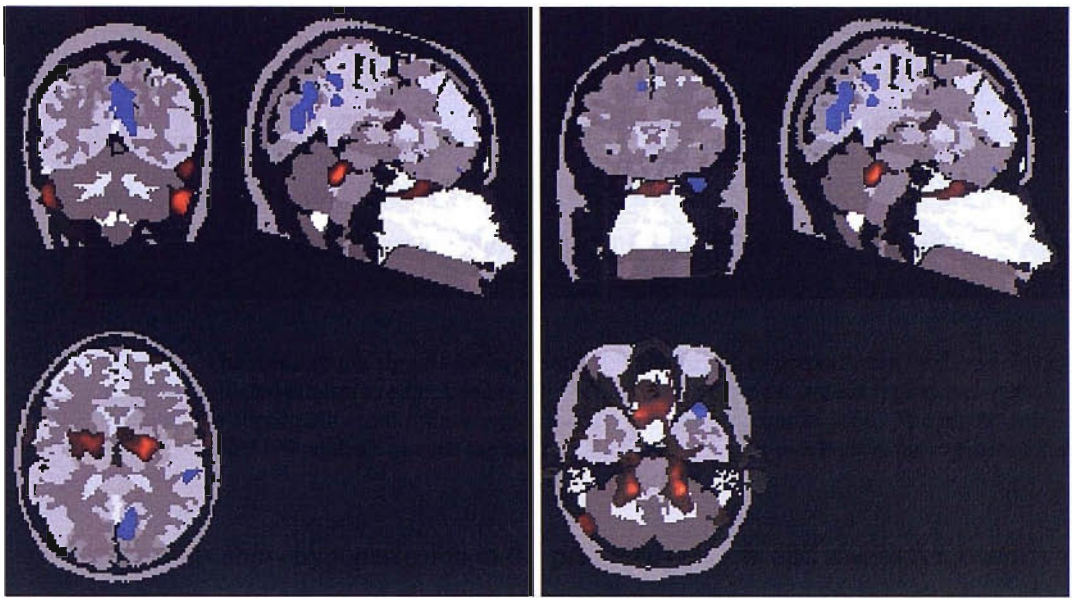

Figure 8.7. The mean of the significant hypoperfusion (blue) and hyperperfusion (red) voxel maps for the entire simulated control group. Images are (left) centred on the precuneus region and (right) centred on the abnormality in the sinus region at the inferior of the frontal lobe. The results are presented for SPM99 analysis against the control group sub-set, and overlaid on the registered Zubal phantom.

The results show hypoperfusion in the precuneus region, and also at the anterior of the *temporal lobe* on the right hand side of the brain. The precuneus was detected as significantly hypoperfused at cluster level ($p < 0.05$) in five of the simulated control subjects, and at voxel level ($p < 0.001$) in eight. Significant hyperperfusion is also shown around the *cerebellum* region (13/15 at cluster level, 15/15 at voxel level), centrally at the inferior aspect of the *frontal lobe* in the region of what should be the sphenoid bone (7/15 at cluster level, 12/15 at voxel level), and bilaterally in the region of the added *sigmoid sinus* (3/15 at cluster level, 14/15 at voxel level). The midbrain again shows hyperperfusion (8/15 at cluster level, 10/15 at voxel level), as does the temporal surface of the *skull* (1/15 at cluster level, 4/15 at voxel level).

8.4 Discussion

The MLEM method at stopping point using the SimSET generated forward projector is adopted as the 'gold standard'. This parameter estimation method has been shown to be useful and accurate, and a characterisation of the errors involved has been presented. Estimated parameters are shown to be more variable than the extracted count data although sources of errors are defined, and are controllable to some extent.

While the methods and measurements for incorporating anatomical and physiological variation are included here, none of these methods are actually implemented. This is due to modelling limitations and high estimated variance. If these methods were introduced at this stage, the variation would be further increased and the causes of variation would become indistinguishable from one another, particularly due to inaccurate demarcation of regional structures and the effect of this on automatic spatial normalisation.

The simulated 'normal' images are compared to normal distributions using a variety of approaches to assess different aspects of the methods. A qualitative analysis is presented that offers a general overview of the perfusion, and also allows assessment of extra-cerebral regions. VOI analysis is performed to indicate functionally mis-defined regions and voxel-wise analysis (SPM99) is performed to indicate regional errors that are not highly correlated with the VOI's. Both estimation methods are incredibly robust, and both are shown to converge to the same solution. The estimators will converge to a solution in the presence of error, although error will exist between the estimated result and the true activity distribution. This can be effectively validated using voxel-wise analysis, as ROI analysis is likely to produce false negatives. All three applied methods for estimating the activity distribution produce simulated data that is statistically different to the control database (according to SPM99 and MarsBaR analysis).

The SPM results show that there is no significant hypoperfusion in the simulated result for the model extracted from the normal template, although significant hyperperfusion abnormalities are present. Results for estimating the distribution using ART and MLEM with stopping criteria indicate that the MLEM results are closer to normal limits (i.e. the target levels). While the differences between the simulated results are small, the significance is altered by an appreciable level. Estimation using the MLEM algorithm consistently produces the most normal simulated data. The reason is that the MLEM algorithm converges more quickly and more uniformly by using parameter weighting. When the stopping criterion is successfully applied, a higher percentage of the estimations are likely to be closer to the correct value. Differences between the results of the two methods do however remain small.

Analysis shows several of the regions have (partly) statistically different simulated distribution to the original subset. The *pons*, *fourth ventricle* and the *cerebral white matter* regions were all deemed to be hyperperfused in the normal image simulation by VOI analysis. SPM analysis shows hyperperfusion in the *pons*, *brainstem*, *third ventricle*, *cerebral white matter*, *midbrain*, the *sphenoid sinus* and around the region of the *sigmoid sinus*. Unilateral and bilateral hyperperfusion was occasionally observed in the temporal bone of the *skull* region.

The count normalisation uses the *cerebellum* as a reference, eroded such that it contains little activity from surrounding regions. As this region is partly hyperperfused, there may be a small but significant shift in the measured count level in this region. However, count normalisation for SPM analysis uses a different search method based on the maximum count level, which is biased towards the large signal *cerebellum* activity. Any change introduced by this method is therefore negligible.

Several problems were found when quantitatively assessing the simulated output. While the MLEM method is successful in estimating a distribution that solves equation 6.1, and this result holds up for voxelwise analysis, the solution is not the optimum one. Using VOI's to describe the parameters reduces the complexity of the model, but as such it is very robust to errors. Where errors exist they are masked by the estimation procedure making them difficult to assess. Where regions are not correctly (anatomically and functionally) defined due to model inaccuracies, the estimation procedure will still converge to a valid solution, although the solution will be in error. Automatic spatial normalisation procedures will attempt to compensate for the difference in anatomy and produce undefined error. The underpinning assumption is that anatomical regions are functionally distinct in terms of rCBF, and care must be taken to ensure this assumption is as valid as possible.

Section 6.1.3 details the updates made to the Zubal phantom in order to facilitate its use as a model for normal brain anatomy in SPECT simulation. While these changes were incorporated to improve the model for use in this application, several problems still exist within the phantom.

The precuneus region is shown to be hypoperfused in one in three of the individually estimated and simulated subjects (Figure 8.7) although is not assessed as significantly

hypoperfused when the whole group is compared to either normal database (Figure 8.1 and Figure 8.3). As the variability in estimated activity levels is low in surrounding regions across the control group (regions 43 and 46 in Figure 7.10), it is thought that the problem is due to individual subject anatomical differences in these regions. An updated phantom should account for these differences and these regions should be further subdivided into smaller regions.

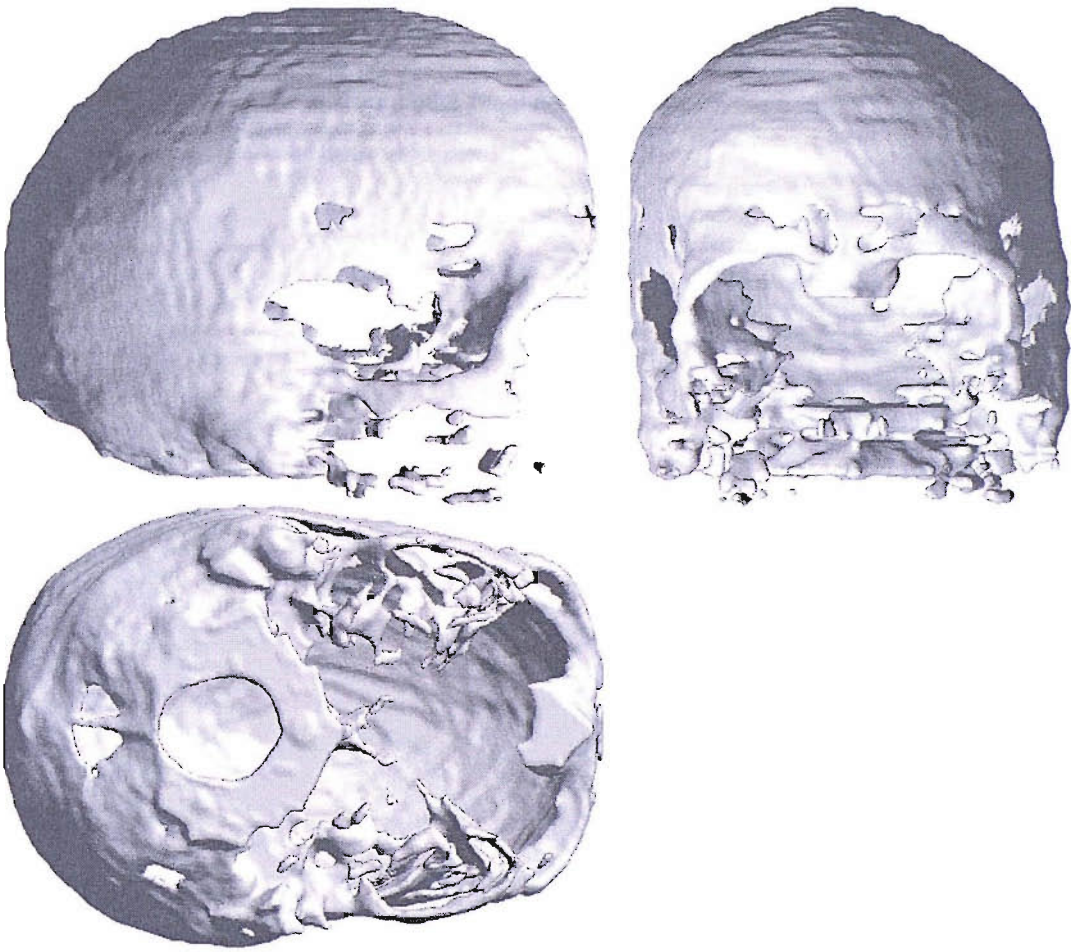

Figure 8.8. Three dimensional rendering of orthogonal views of the Zubal phantom *skull* region, showing problems with the modelling of the region.

Figure 8.8 is a three-dimensional image rendering of the current Zubal phantom *skull* showing orthogonal views and highlighting the problems with the model. Figure 8.9 shows a sagittal cross-section of the normal anatomy of the skull. As the images show, the *skull* is not completely defined within the facial regions, which is likely to be a feature of the median filtering applied to the original phantom segmentation. Thus we would expect to (and do) see hyperperfusion in these regions. The regions including the *frontal sinus, Ethmoid bone* and *sphenoid bone* are subject to large inter-

subject variation. As there is no *skull* defined in this region, parameter estimation errors are likely to be very high. There are clear and large discontinuities in the *skull* on the lateral walls of the temporal bone, and the inferior part of the temporal bone has no *skull* modelled. The modeling of the *skull* region immediately behind the *cerebellum* and slightly below its centre is broken. S*kull* discontinuities are also evident around the *frontal sinus* and occipital bone, and several regions of the *skull* are thinner than normal anatomy and/or have holes. The overall lack of attenuation resulting from the un-modelled *skull* could explain the overestimation of the activity in the sinus regions, at the side of the head and the back of the cerebellum. This also partly explains the cerebellum abnormalities.

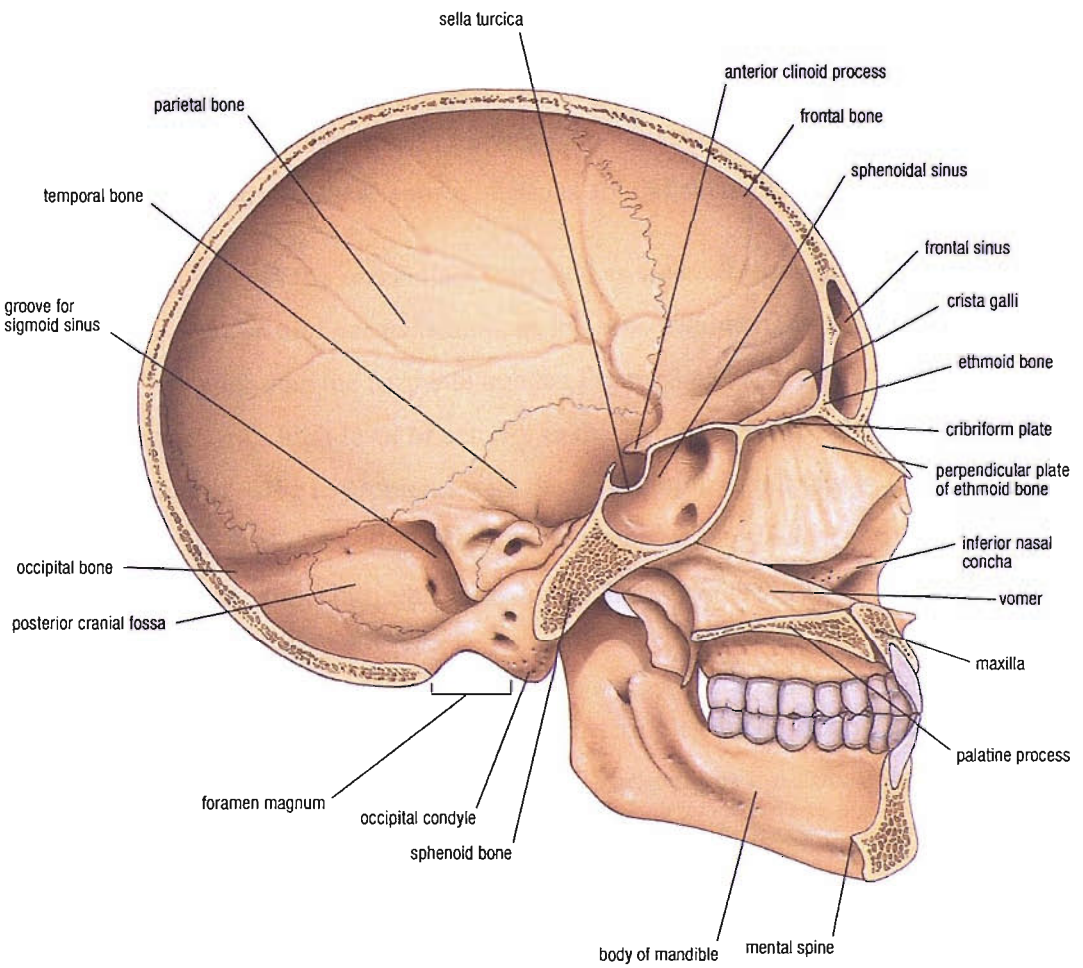

Figure 8.9. A sagittal cross-section of the normal human skull structure. Note the positioning of the sphenoid bone, sphenoid sinus and Ethmoid bone. Images are from [Gray *et al.*, 1918].

Accurate modeling is less important for cerebrally remote regions, but is paramount for regions in close proximity to the cerebral cortex (such as the *sphenoid, Ethmoid*

and *frontal* sinuses). The combination of these errors in terms of functional demarcation and attenuation levels produces errors in VOI measurements, and increases the registration error during automatic spatial normalisation.

Much of the detected hyperperfusion can be explained by limitations of the Zubal phantom segmentation of the *skull*. The amount of *skull* anterior to the *pons* and *brainstem* which articulates with the inferior of the sphenoid bone is small compared to normal anatomy, and is instead modeled entirely as *CSF*. *Skull* is not defined at the inferior of the *frontal lobe* or in the face surrounding the various sinus regions. The sphenoid / frontal bone should be modeled between this and the *Ethmoid sinuses*, and articulate with the frontal bone that currently stops immediately above the sinus region at the top of the nose. The sphenoid bone should articulate laterally with the temporal bone, and anteriorly and inferiorly with *turbinates, nasal septum and concha*. These facial bones all add to the attenuation effect within and around the region and cause errors where approximations are not accurate.

The hyperperfusion in the *cerebellum* (reported as *sigmoid sinus*) appears to be due to a difference in the spatial normalisation, as the *cerebellum* on the normalised image appears to be wider than the template image (Figure 8.4, slices 17 and 25). This could be caused by a high level of activity in the *sigmoid sinuses* which is not present in normal images. Due to problems with the distribution of activity in these regions, the highly active *sigmoid sinuses* may be interpreted as *cerebellum* activity by the spatial normalisation routine, which would attempt to compensate by reducing the width of the region.

Figure 8.10 shows the normal anatomy of the ventricles and midbrain regions of the cerebrum. Figure 8.11 is a three dimensional rendering of the Zubal phantom showing the midbrain, ventricle system and *cerebellum*, *brainstem* and *pons*. Figure 8.12 is a three dimensional rendering of the individual components of these regions. The images together illustrate the differences between the phantom image and normal anatomy. The detected problems with the midbrain are due to the size of the regions, the segmentation of the regions and their non-functional demarcation in the phantom. As the regions are small, registration errors between them will be large where not functionally distinct. This large variation will produce inaccuracy in extracted count levels and make statistical tests weak.

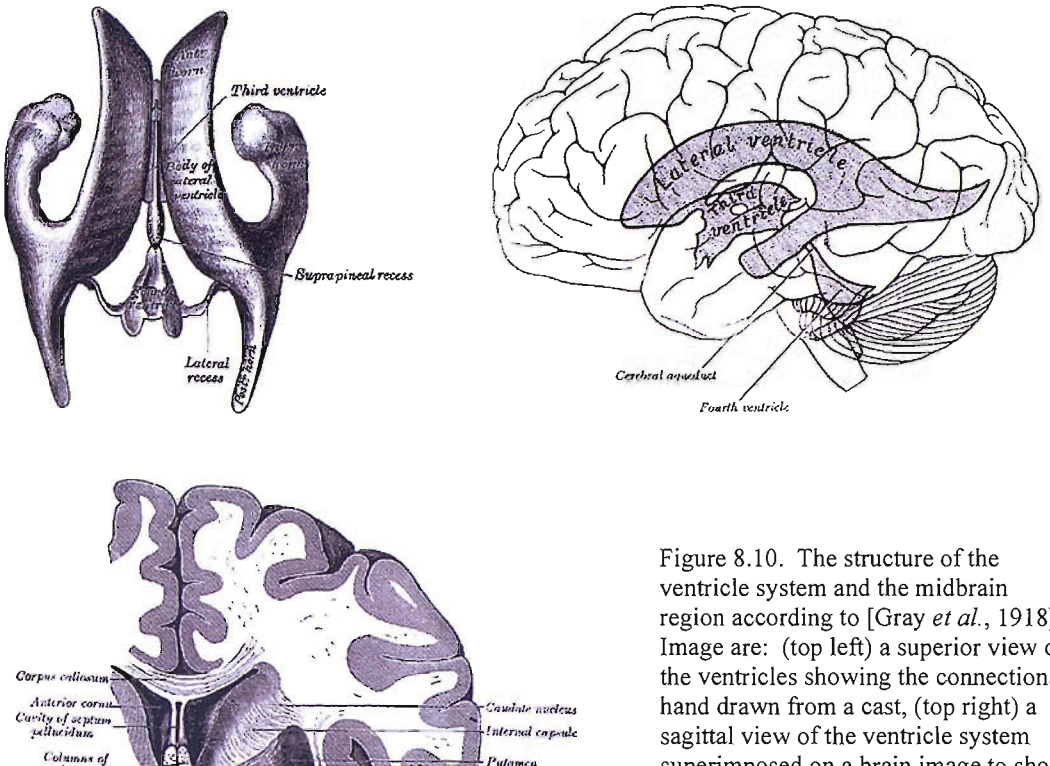

Figure 8.10. The structure of the ventricle system and the midbrain region according to [Gray *et al.*, 1918]. Image are: (top left) a superior view of the ventricles showing the connections, hand drawn from a cast, (top right) a sagittal view of the ventricle system superimposed on a brain image to show approximate location and extent. (bottom left) a coronal section of the mid brain region, indicating the various structures of the midbrain.

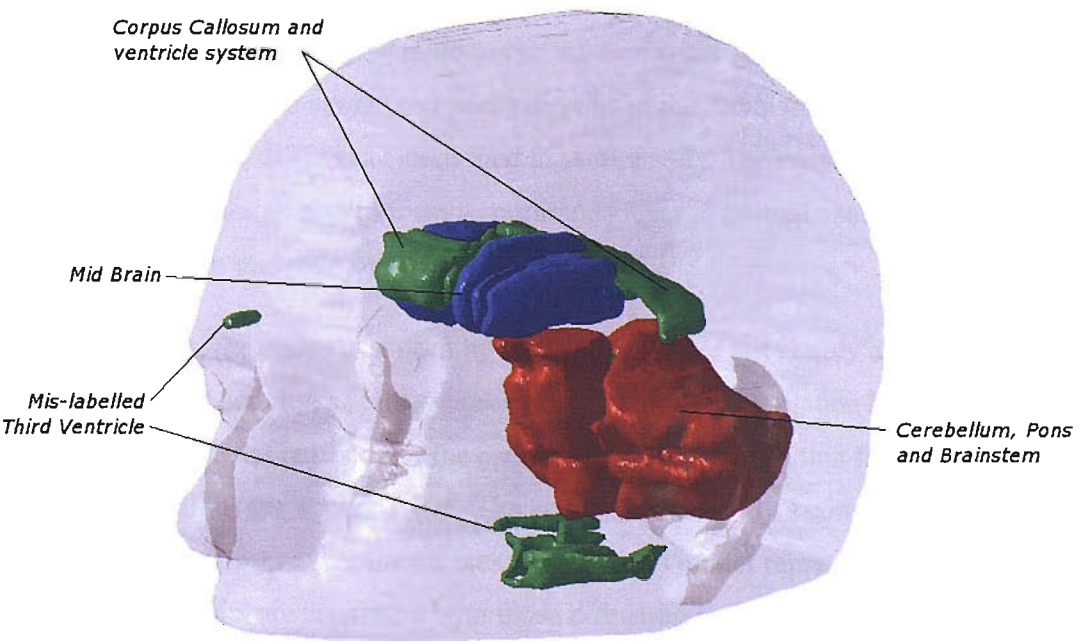

Figure 8.11. A three dimensional rendering of the updated Zubal phantom showing an overview of segmentation for midbrain and connected regions.

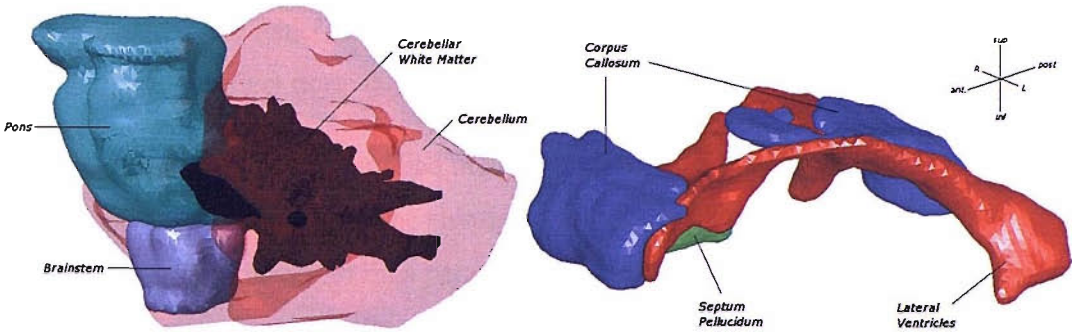

Figure 8.12. A three dimensional rendering showing the segmentation of (left) the *pons*, *brainstem*, *cerebellum* and *cerebellar white matter*, and (right) the *corpus callosum*, *lateral ventricles* and *septum pellucidum* according to the Zubal phantom.

The *third ventricle* is mislabelled as *temporal lobe* in the phantom image, and is incorrectly defined at the bottom of the phantom (Figure 8.11). The *third ventricle* should be defined in the medial slices immediately below the *septum pellucidum*. The *ventricles* in the phantom are also smaller than normal anatomy, and do not include an inferior and posterior horn. As the *third ventricle* is not correctly defined, there is no connection between the *lateral ventricles* and the *fourth ventricle*. The *pons* is not functionally defined, and the original pituitary gland has been removed due to its small size. However, these two regions appear to be functionally distinct from surrounding regions of the *brainstem* in normal perfusion. It can also be seen that there is discontinuity between the *brainstem/pons* and the midbrain region. In normal anatomy, this region contains the cerebral peduncle which is medially inferior to the *third ventricle*, and connects the midbrain to the *brainstem* and *pons*. This region is modelled partly as *white matter* and partly as *pons* in the Zubal phantom, and is the cause of some of the differences described in section 8.2. The *corpus callosum* is discontinuous, although should form a continuous layer in normal anatomy, separated inferiorly from the midbrain by the *lateral ventricles*.

As this indicates, the errors produced by these methods are not simply a result of overestimation of activity, as there appears to be very little correlation between statistically significant regions and the estimated activity distribution for obtaining the known distribution (see Figure 7.10). The errors are caused by a combination of factors including errors in parameter measurement and model representation. However, the results are consistent with those discussed in Chapter 7, and confirm that the errors are indeed within controllable limits and not likely to affect the

methods used in the generation of normal data, provided the phantom model can be updated to truly reflect normal anatomy.

The results indicate that the applied method is directly applicable to the extraction of the true activity distribution. The simulated activity distribution created from the averaged controls converges on a parameter estimate that solves equation 6.1. The voxelwise comparison between the dataset and the data from which it was derived shows that the activity model and segmentation is also a good approximation. Errors are evident, but these errors are completely explained by differences between the anatomical support and normal anatomy. Analysis was more normal for the estimated template model, compared to the average model for individual subjects. This suggests that the estimation procedure is sensitive to input image noise. This is expected as individual anatomical differences are averaged across many subjects when creating the template, thus averaging registration and counting errors. Wherever possible, to maximise efficacy data extraction should be carried out on averaged groups after pre-processing, as opposed to extracting parameters for each subject independently and averaging these.

Chapter 9 Conclusions and Future Work

9.1 Conclusions

Imaging and analysis is a powerful tool in dementia research. Molecular imaging using radiotracers gives useful insight into the mechanisms behind dementia. However, the imaging method is only as powerful as the methods used to detect abnormal data. An early and defining goal of this study was to create a method of effectively allowing a comparison of imaging systems and analysis methods. The emphasis has changed due to lack of support data and problems with creating data that is applicable to all instances of an imaging and analysis system. However, the validation still remains a long term goal of the project, and a lot of the work has focused on the production of ground truth models that can be used in this task.

The brain can be analysed using a large number of different approaches based on anatomy or function. Functional SPECT imaging using ^{99m}Tc is a particularly convenient and useful one for studies of rCBF, and has far reaching implications in dementia research. The stochastic nature of the emissions can be exploited through statistical testing to provide a level of interpretation that is far more powerful than visual inspection alone. However, to validate and compare these quantitative approaches, ground truth has to be established to allow an effective comparison.

Both Monte Carlo and analytical simulations have been used in the generation of normal and abnormal SPECT imaging data. The real power of analytical simulation is that it is easily characterised by experimental measurements, and simulation time is generally very short. Monte Carlo methods are preferred, however, as true system modelling is performed, and the data produced is directly applicable to a wide variety of imaging configurations.

Analytical simulation has been successfully used to generate a complete audit data set that is to be used to test the efficacy and perform a cross comparison of analysis methods in ^{99m}Tc-HMPAO SPECT imaging. The dataset has been specifically designed to test the analysis methods used in dementia research, by simulating realistic representations of disease in normal subjects. Images have been distributed

to participating centres for analysis, and a full study of the results will ensue. The major long term goal is to provide a unified comparative method to allow characterisation of the analysis process, and provide ground truth data that can be used to compare these methods. The complete audit data set is described in detail in [Ward *et al.*, 2005]. Initial analysis using SPM99 shows the dataset is valid, and a cross comparison of SPM99 with BRASS shows that both methods can detect abnormalities with the same level of accuracy. However, the dataset is limited to analysis of reconstructed data using a particular gamma camera, and not directly applicable to other cameras.

Monte Carlo methods are preferred for modelling, as the random nature of radiation can be accurately modelled macroscopically. While the developed simulation method is adequate for simulating abnormalities in normal images, a spatially invariant PSF is used for simulation which results in a lack of realism if applied to heterogeneous attenuators. Furthermore, Monte Carlo methods can be applied to any number of simulation systems or camera configurations. SimSET has been experimentally validated for use as a model for our gamma camera, and a shared access Beowulf cluster was used to perform multiple parallel simulations and vastly improve simulation speed. Monte Carlo simulation is however dependent on an accurate models for the imaging system and source objects. An accurate source activity model needs also be derived which represents the underlying attenuation distribution and biodistribution, without the confounding effects of imaging. This distribution can then be applied to any number of simulation configurations, which has application in the unification of normal databases.

The Zubal phantom is adopted as the anatomical support for the source object, supporting regional count level simulation. The original model required some modifications for use as a functional head phantom, and the updated phantom was validated as a model for rCBF. Combined with accurate simulation, this leads to the production of 'gold standard' data that can be used to assess any aspect of the imaging process, be it before, during or after acquisition. The phantom was combined with iterative algorithms and simulated object dependent regional convolution methods to estimate the activity distribution with an acceptable level of accuracy (maximum 25% error in cerebral structures). The MLEM based estimator is validated as the 'gold

standard' for parameter extraction, and was shown to be in error at convergence. While errors are evident in the estimated values, these are well defined. The estimator is applied to a low variance subset of normal control images, and results are validated as a normal model for the anatomical support.

Monte Carlo simulation of parameters shows that the model is adequate for normal simulation, as the simulated distribution is largely within normal limits. However, several distinct errors are observed and highly correlated with phantom discrepancies, which limits the use of the simulated normal database for comparison to real subjects. We conclude that the method is feasible for the production of normal data sets, and suggest that providing an accurate and functionally defined anatomical support will achieve this goal. Also, the method is shown to be repeatable and robust to normal (and well controlled) variation. How the method performs with high, or indeed abnormal variation remains to be seen.

A large amount of the project emphasis has been put on the simulation of images using different methods to achieve the same goal; an image that represents a known distribution. This image can be analysed and the results of the analysis can be compared with the original data to obtain an analysis efficacy rating. The use however is not limited to analysis, as the system will allow simulation of SPECT for any source object using an array of different camera configurations, and extending easily to PET and possibly other imaging modalities. The application of the method is also not confined to quantitative analysis, and has immediate implication and application in any method where it could be useful to provide an accurate baseline measurement (e.g. dosimetry calculations, targeted radiotherapy etc.). The Zubal head phantom is only part of the whole body Zubal phantom that is freely available, and the methods could be adapted and applied to the study of function for many different systems.

In conclusion, we have proven the basis for performing simulation based on regional MLEM estimated parameters and an accurate anatomical support. All aspects of the method have been validated for use in the current implementation, and results are very encouraging. The phantom requires work, although a framework for the accurate estimation of regional distributions has been generated that is directly applicable to the estimation of normal biodistribution in normal subjects. This method should be

fully validated on a larger database including more variable results, before being implemented as the basis of a system for generating anatomically and physiologically accurate brain SPECT simulation.

9.2 Future Work

The audit data is currently being evaluated by several different centres. Once analysis results have been collected and collated, the results will need to be analysed and published. With continued interest and growth of public domain software like SPM, a comparison should also be sought between different versions to assess relative gain in terms of accuracy. This is a major goal of the data set, and an effective comparison has been enabled.

The analytical simulation system has also been reasonably successful in early evaluation and experiment involving MLEM and ART estimation, due to its speed in forward projecting data and absolutely quantifiable nature. However, the use of the system has been shown to be limited for full brain SPECT simulation. It is not expected that any more general release data sets will be created using these methods, as the method is expected to be superseded by SimSET in the future. However, the method is still useful in the fast production of abnormal data sets for qualitative validation purposes, and for the simple creation of voxel based simulated data.

The SimSET system has been fully validated for use as a model of the gamma camera used for the experimental work. Various validation tasks have been performed to ensure its accuracy, and all have proven the system accuracy within acceptable limits. Further updates are planned by the authors of the SimSET software, including full Monte Carlo based collimator modelling and improved variance reduction techniques. Once these updates have been released, the system should be validated using the new methods, and a comparison should be made to assess the updated simulation system in this context. Of particular note is the Monte Carlo modelling of the collimator, as this was found to be a fundamental limitation of the simulation system.

The Zubal head phantom has been continually evolving through eleven in house updates to date. At the current update, the estimation results are almost normal, and all remaining error is well characterised. The final update required, as described in

section 8.4, should resolve all remaining error in the phantom distribution. It is believed that this model will be a great benefit to research using simulation and quantification, and provide a true representation of normal head anatomy. This would have immediate implications on previously published studies using the Zubal phantom. However, the physiological segmentation of the phantom is still open to interpretation.

The phantom development could take one of several different but related routes. The extracted count levels have been shown to have a high variability. The source of this variability is well defined, and if controlled could warrant a study of the diagnostic capability of the derived activity levels. The back projection performed during parameter estimation should effectively compensate for the effect of the imaging process and attenuation and also increase the image resolution. Thus derived activity levels should be compatible across different imaging systems for the same radiolabel. This could provide justification for creating a separate and completely functionally defined activity map with more disease specific regions. The results suggest that this should at least be partly incorporated into the next update to account for large spatial differences in haemodynamic response (e.g. precuneus). While the segmentation used in the phantom is based on anatomy rather than physiology, many alternative segmentations of the data may be performed to provide models that are particular to a large number of imaging tasks. For example, the medial temporal lobe structures are useful in epilepsy studies, or segmentation could be based on inferred cytoarchitecture for maximum functional demarcation. Validation should be performed on any new model for its specific application.

Attenuation correction based on the head phantom should be assessed using an updated model with the additional skull regions described in section 8.4. Model based partial volume correction and attenuation correction based on inferring attenuation distributions (IAD) would provide a very good approximate correction for image reconstruction. Recent study results [Zaidi *et al.*, 2004, Stodilka *et al.*, 2000] suggest accurate attenuation approximation using the Zubal phantom was, on average, within 7.5 % of that measured from transmission scanning. As the attenuation model is known to be different to normal anatomy, these results are expected to improve significantly, particularly in light of the effect on the cerebellum counts. A re-analysis

using the same methods should yield better results, and also provide a better understanding of the effects of the updated phantom models.

While every effort was made to keep the phantom regions within original demarcations and/or anatomical constraints, a certain amount of estimation was applied to the definition of new phantom regions. The updates were all implemented as a matter of cause and in the interest of simulating a normal distribution, and only implemented where deemed necessary due to the lack of formal anatomical education of the author. The updates that have been implemented, and those that still require implementing, should be verified by a properly qualified person to ensure correct anatomical and physiological segmentation. While this process has been started, time constraints have restricted its development and hence its implementation. However, the current work is presented below.

Figure 9.1 and Figure 9.2 show a three dimensional rendering of the current work on the updated Zubal skull region. The skull segmentation is based upon inferring normal structure and outlining regions of low signal intensity in the Zubal phantom MRI image, based on anatomical models [Gray *et al.*, 1918]. The addition of the extra skull can be seen in comparison with Figure 8.8, and comparison to normal anatomy (Figure 8.9) shows that the updates are a more accurate model of normal skull anatomy. Fortunately, the Zubal phantom skull structure of the *sphenoid sinus* is normal, and the MRI images contains enough information for good approximate demarcation, as shown by the highlighted region in Figure 9.3. However, the data is still lacking much of the skull structure of the paranasal anatomy and sphenoid, temporal and frontal bone structures. The phantom segmentation requires more work in consultation with external sources, using three dimensional renderings to improve modelling.

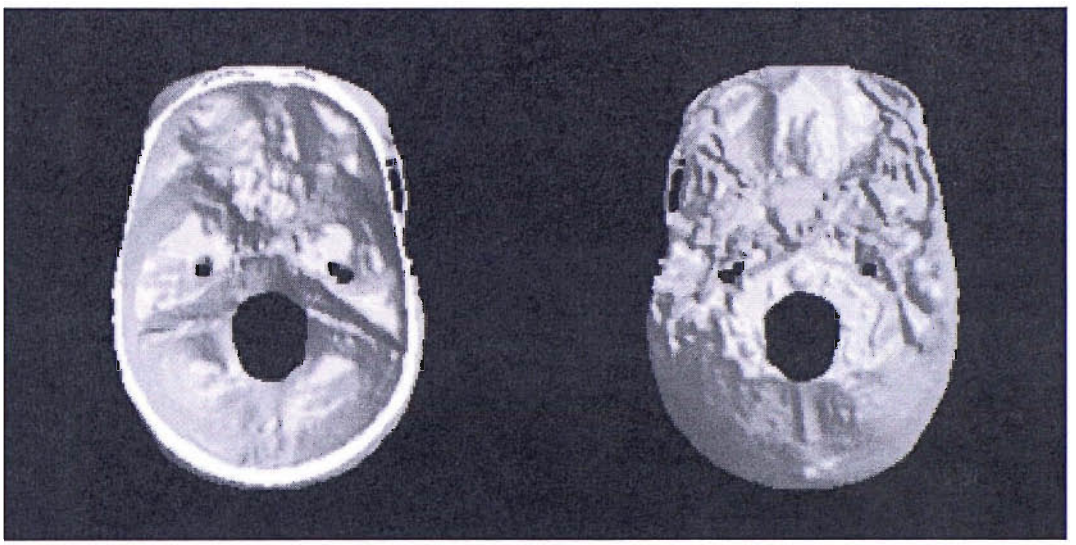

Figure 9.1. The inferior (left) and superior (right) view of a 3D rendering of the updated Zubal phantom skull region. The rendering contains only tranaxial slices 1-50.

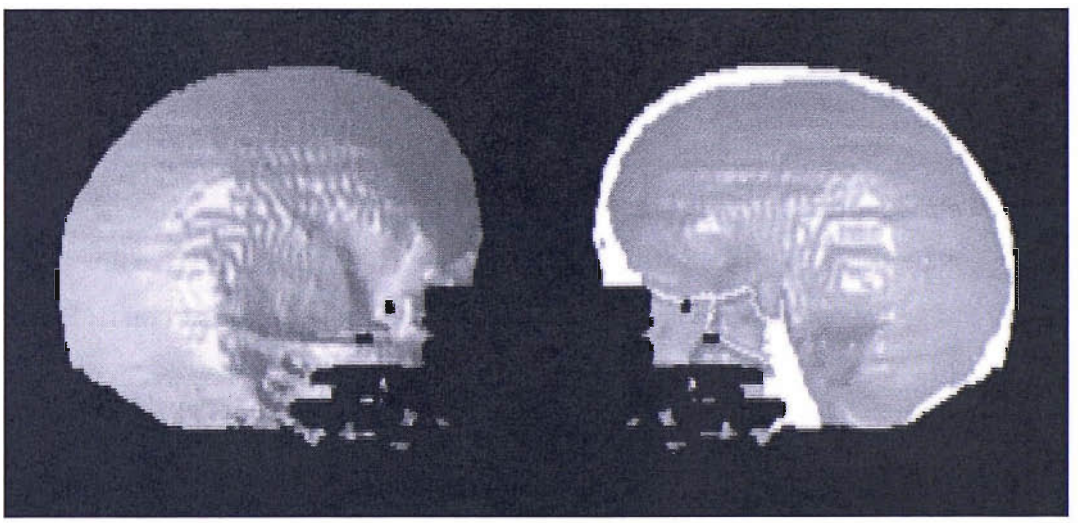

Figure 9.2. The inferior (left) and superior (right) view of a 3D rendering of the updated Zubal phantom skull region. The rendering contains only transaxial slices 1-50.

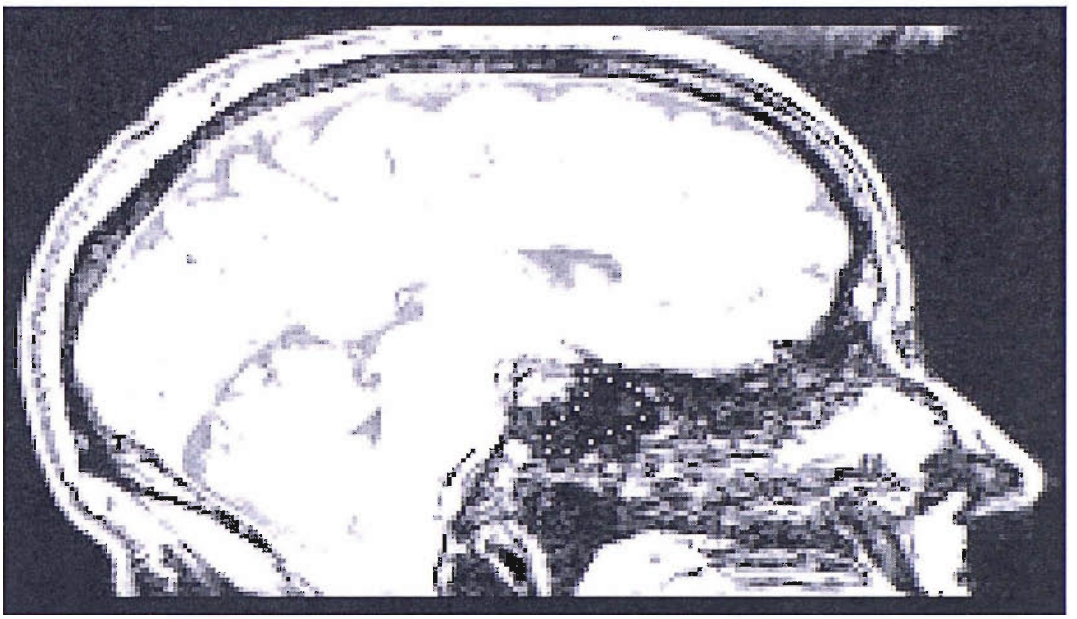

Figure 9.3. The Zubal phantom MRI image, showing the approximate inferred location of the sphenoid sinus. The dotted green line is the sphenoid sinus.

If normal parameters derived from control subjects can reproduce normal data, then this provides the foundation for simulating complete artificial normal datasets. The results do not completely validate this as a method for simulating normal data as errors still exist. However, it does show that the method could be successfully applied to extract normal distributions, with more accurate source object modelling both in terms of segmentation and metabolic function. If this could be reproduced by simulation, then the method could be employed to generate large volume data sets for comparative studies. As we are able to accurately extract activity parameters for different cameras using implementation specific forward projectors, then the results could be pooled and compared in a standardised space. Any derived parameter set is then directly applicable to any imaging system for which a simulation model exists.

If a normal model can indeed be created, the first task would be performing a cross-camera comparison with simulated data. This could be achieved by simulating the same distribution using two different cameras or processing methods, and extracting the transfer function. Arbitrary data could then be used as the input model and the MLEM estimator results should be compared to see if there is any real variation. The results would provide an insight into the performance of the transfer function for modelling different imaging systems. The validated method could be used to assess many other aspects of the imaging and analysis procedure using the baseline result.

For example, the effect of different count levels on the automatic registration procedure could be evaluated using realistic data.

Once the model is validated as accurate, the statistical properties of the methods should be assessed and characterised. This should be followed by a performance analysis for the estimators when estimating activity in the presence of error, and a systematic evaluation of the effect of disease specific abnormalities.

Physiological and anatomical variation can be estimated to model real subject variation, and methods are described. Its implementation and validation is currently limited by the phantom modelling, as these problems need to be rectified before increasing the variance of the image by adding artificial variation. This technique allows descriptions of variations through the use of normal subjects and parameters extracted to describe these. These parameters should be applied to produce realistic simulation with real variation, and to assess the effect of this transformation on the baseline result.

Movement is an undesirable effect in SPECT and PET imaging that is difficult to predict and even more difficult to correct. A normal simulation system incorporating movement can offer information on its effect on imaged data, and allow a method of assessing correction techniques. The incorporation of movement could be performed without alteration of the SimSET code. The simplest method would be to perform temporal partitioning, with each partition having a discrete model representing some rigid body transform of the baseline model, and simulation parameters that define the temporal range of the partition. Multi-processor environments are particularly suited to this task of multiple discrete simulations as execution can be run in parallel, resulting in a reduction in simulation time. Also, as the radiation is discrete and predictable over time, dynamic activity with a high temporal frequency could be simulated by averaging activity levels across the range of motion, hence limiting the required number of partitions. However, this method does not extend so easily to the inclusion of dynamic attenuation. SPECT and PET studies of organs such as the heart or kidney would require many partitions that explicitly model movement over its normal range of motion, using highly deformable elastic models. The ideas suggested above would be directly applicable to the dynamic simulation of such organs, which could provide a method of extending the capabilities of the simulation system. The

implication of being able to provide such data is huge, as movement is a major problem in most nuclear medicine studies. In SPECT brain studies, motion correction has been experimentally shown to be non-deterministic and subject to large variation. Thus, application where the movement is known prior to analysis offers great benefits in understanding its effect on the imaging and analysis procedure.

The project emphasis is now firmly on improving the phantom model to an acceptable level, such that it can be used to generate normal data. The baseline model can then be applied to a large number of studies through the modelling of normal variation. The results presented here all indicate that if the required updates are implemented, then accurate normal models can be extracted. If this can be achieved, the methods have immediate application in the production of an updated audit group, as well as many other validation studies.

References

Ackerman, M. J. (1991) The Visible Human Project. *J Biocommun,* 18, 14.

Anger, H. O. (1958) Scintillation Camera. *Rev Sci Instr,* 29, 27-33.

Arlig, A., Gustafsson, A., Jacobsson, L., Ljungberg, M. & Wikkelso, C. (2000) Attenuation correction in quantitative SPECT of cerebral blood flow: a Monte Carlo study. *Phys Med Biol,* 45, 3847-59.

Baete, K., Nuyts, J., Van Laere, K., Van Paesschen, W., Ceyssens, S., De Ceuninck, L., Gheysens, O., Kelles, A., Van Den Eynden, J., Suetens, P. & Dupont, P. (2004) Evaluation of anatomy based reconstruction for partial volume correction in brain FDG-PET. *Neuroimage,* 23, 305-17.

Bailey, D. L., Hutton, B. F. & Walker, P. J. (1987) Improved SPECT using simultaneous emission and transmission tomography. *J Nucl Med,* 28, 844-51.

Beekman, F. J., Kamphuis, C. & Frey, E. C. (1997) Scatter compensation methods in 3D iterative SPECT reconstruction: a simulation study. *Phys Med Biol,* 42, 1619-32.

Berr, C., Wancata, J. & Ritchie, K. (2005) Prevalence of dementia in the elderly in Europe. *Eur Neuropsychopharmacol,* 15, 463-71.

Brambilla, M., Cannillo, B., Dominietto, M., Leva, L., Secco, C. & Inglese, E. (2005) Characterization of ordered-subsets expectation maximization with 3D post-reconstruction Gauss filtering and comparison with filtered backprojection in 99mTc SPECT. *Ann Nucl Med,* 19, 75-82.

Brett, M., Christoff, K., Cusack, R. & Lancaster, J. (2001) Using the talairach atlas with the MNI template. *NeuroImage,* 13, 85.

Brett, M. A., J., Valabregue, R. & Poline, J. (2003) Region of interest analysis using an SPM toolbox (abstract). *Neuroimage,* 16, suplement (CD-ROM).

Buvat, I. & Castiglioni, I. (2002) Monte Carlo simulations in SPET and PET. *Q J Nucl Med,* 46, 48-61.

Buvat, I., Castiglioni, I., Feuardent, J. & Gilardi, M. C. (2005) Unified description and validation of Monte Carlo simulators in PET. *Phys Med Biol,* 50, 329-46.

Buvat, I., Rodriguez-Villafuerte, M., Todd-Pokropek, A., Benali, H. & Di Paola, R. (1995) Comparative assessment of nine scatter correction methods based on spectral analysis using Monte Carlo simulations. *J Nucl Med,* 36, 1476-88.

Cavanna, A. E. & Trimble, M. R. (2006) The precuneus: a review of its functional anatomy and behavioural correlates. *Brain,* 129, 564-83.

Chang, L. T. (1978) A Method for Attenuation Correction in Radionuclide Computed Tomgoraphy. *IEEE Trans. Nucl. Sci.,* 25, 638-43.

Cot, A., Falcon, C., Crespo, C., Sempau, J., Pareto, D., Bullich, S., Lomena, F., Calvino, F., Pavia, J. & Ros, D. (2005) Absolute Quantification in Dopaminergic Neurotransmission SPECT Using a Monte Carlo-Based Scatter Correction and Fully 3-Dimensional Reconstruction. *J Nucl Med,* 46, 1497-504.

Darambara, D. G. & Todd-Pokropek, A. (2002) Solid state detectors in nuclear medicine. *Q J Nucl Med,* 46, 3-7.

Dougall, N. J., Bruggink, S. & Ebmeier, K. P. (2004) Systematic review of the diagnostic accuracy of 99mTc-HMPAO-SPECT in dementia. *Am J Geriatr Psychiatry,* 12, 554-70.

Du, Y., Tsui, B. M. & Frey, E. C. (2005) Partial volume effect compensation for quantitative brain SPECT imaging. *IEEE Trans Med Imaging,* 24, 969-76.

Evans, J. F., Blue, T. E. & Gupta, N. (2001) Absorbed dose estimates to structures of the brain and head using a high-resolution voxel-based head phantom. *Med Phys,* 28, 780-6.

Fleming, J. S. (1989) A technique for using CT images in attenuation correction and quantification in SPECT. *Nucl Med Commun,* 10, 83-97.

Fleming, J. S., Kemp, P. M., Bolt, L. & Goatman, K. A. (2002) Measurement of cerebral perfusion volume and 99mTc-HMPAO uptake using SPECT in controls and patients with Alzheimer's disease. *Nucl Med Commun,* 23, 1057-64.

Fleming, J. S. & Simpson, D. E. (1994) A technique for simulation of the point spread function of a gamma camera. *Phys Med Biol,* 39, 1457-73.

Fleming, J. S., Whalley, D. R., Skrypniuk, J. V., Jarritt, P. H., Houston, A. S., Cosgriff, P. S. & Bailey, D. (2004) UK audit of relative lung function measurement from planar radionuclide imaging. *Nucl Med Commun,* 25, 923-34.

Floyd, C. E., Jr., Jaszczak, R. J. & Coleman, R. E. (1987) Convergence of the maximum likelihood reconstruction algorithm for emission computed tomography. *Phys Med Biol,* 32, 463-76.

Folstein, M. F., Folstein, S. E. & Mchugh, P. R. (1975) "Mini-mental state". A practical method for grading the cognitive state of patients for the clinician. *J Psychiatr Res,* 12, 189-98.

Fotenos, A. F., Snyder, A. Z., Girton, L. E., Morris, J. C. & Buckner, R. L. (2005) Normative estimates of cross-sectional and longitudinal brain volume decline in aging and AD. *Neurology,* 64, 1032-9.

Frackowiak, R. S. J. (1997) *Human brain function,* San Diego; London, Academic Press.

Gray, H. F. R. S., Blake, A. J. J. & Fedden, W. F. (1918) *Anatomy,* London, Longmans & Co.

Greitz, T., Bohm, C., Holte, S. & Eriksson, L. (1991) A computerized brain atlas: construction, anatomical content, and some applications. *J Comput Assist Tomogr,* 15, 26-38.

Grova, C., Jannin, P., Biraben, A., Buvat, I., Benali, H., Bernard, A. M., Scarabin, J. M. & Gibaud, B. (2003) A methodology for generating normal and pathological brain perfusion SPECT images for evaluation of MRI/SPECT fusion methods: application in epilepsy. *Phys Med Biol,* 48, 4023-43.

Hanyu, H., Shimuzu, T., Tanaka, Y., Takasaki, M., Koizumi, K. & Abe, K. (2003) Effect of age on regional cerebral blood flow patterns in Alzheimer's disease patients. *J Neurol Sci,* 209, 25-30.

Haynor, D. R., Harrison, R. L. & Lewellen, T. K. (1991) The use of importance sampling techniques to improve the efficiency of photon tracking in emission tomography simulations. *Med Phys,* 18, 990-1001.

Hirsch, C., Bartenstein, P., Minoshima, S., Mosch, D., Willoch, F., Buch, K., Schad, D., Schwaiger, M. & Kurz, A. (1997) Reduction of regional cerebral blood flow and cognitive impairment in patients with Alzheimer's disease: evaluation of an observer-independent analytic approach. *Dement Geriatr Cogn Disord,* 8, 98-104.

Hoffman, E. J., Cutler, P. D., Guerrero, T. M., Digby, W. M. & Mazziotta, J. C. (1991) Assessment of accuracy of PET utilizing a 3-D phantom to simulate the activity distribution of [18F]fluorodeoxyglucose uptake in the human brain. *J Cereb Blood Flow Metab,* 11, A17-25.

Hoffman, T. J., Corlija, M., Chaplin, S. B., Volkert, W. A. & Holmes, R. A. (1988) Retention of [99mTc]-d,l-HM-PAO in rat brain: an autoradiographic study. *J Cereb Blood Flow Metab,* 8, S38-43.

Houston, A. S., Kemp, P. M. & Macleod, M. A. (1994) A method for assessing the significance of abnormalities in HMPO brain SPECT images. *J Nucl Med,* 35, 239-44.

Hutton, B. F., Braun, M., Thurfjell, L. & Lau, D. Y. (2002) Image registration: an essential tool for nuclear medicine. *Eur J Nucl Med Mol Imaging,* 29, 559-77.

Hyun, Y., Lee, J. S., Rha, J. H., Lee, I. K., Ha, C. K. & Lee, D. S. (2001) Different uptake of 99mTc-ECD adn 99mTc-HMPAO in the same brains: analysis by statistical parametric mapping. *Eur J Nucl Med,* 28, 191-7.

Imran, M. B., Kawashima, R., Awata, S., Sato, K., Kinomura, S., Ono, S., Yoshioka, S., Sato, M. & Fukuda, H. (1999a) Parametric mapping of cerebral blood flow

deficits in Alzheimer's disease: a SPECT study using HMPAO and image standardization technique. *J Nucl Med,* 40, 244-9.

Imran, M. B., Kawashima, R., Sato, K., Kinomura, S., Ono, S., Qureshy, A. & Fukuda, H. (1999b) Detection of CBF deficits in neuropsychiatric disorders by an expert system: a 99Tcm-HMPAO brain SPET study using automated image registration. *Nucl Med Commun,* 20, 25-32.

Ito, H., Inoue, K., Goto, R., Kinomura, S., Taki, Y., Okada, K., Sato, K., Sato, T., Kanno, I. & Fukuda, H. (2006) Database of normal human cerebral blood flow measured by SPECT: I. Comparison between I-123-IMP, Tc-99m-HMPAO, and Tc-99m-ECD as referred with O-15 labeled water PET and voxel-based morphometry. *Ann Nucl Med,* 20, 131-8.

Ito, H., Kawashima, R., Awata, S., Ono, S., Sato, K., Goto, R., Koyama, M., Sato, M. & Fukuda, H. (1996) Hypoperfusion in the limbic system and prefrontal cortex in depression: SPECT with anatomic standardization technique. *J Nucl Med,* 37, 410-4.

Ito, K., Morrish, P. K., Rakshi, J. S., Uema, T., Ashburner, J., Bailey, D. L., Friston, K. J. & Brooks, D. J. (1999) Statistical parametric mapping with 18F-dopa PET shows bilaterally reduced striatal and nigral dopaminergic function in early Parkinson's disease. *J Neurol Neurosurg Psychiatry,* 66, 754-8.

Kadrmas, D. J. (2001) Statistically Regulated and Adaptive EM Reconstruction for Emission Computed Tomography. *IEEE Trans Nucl Sci,* 48, 790-8.

Kemp, P. M., Holmes, C., Hoffmann, S. M., Bolt, L., Holmes, R., Rowden, J. & Fleming, J. S. (2003) Alzheimer's disease: differences in technetium-99m HMPAO SPECT scan findings between early onset and late onset dementia. *J Neurol Neurosurg Psychiatry,* 74, 715-9.

Kim, H. J., Zeeberg, B. R., Fahey, F. H., Bice, A. N., Hoffman, E. J. & Reba, R. C. (1991) Three-dimensional SPECT simulations of a complex three-dimensional mathematical brain model and measurements of the three-dimensional physical brain phantom. *J Nucl Med,* 32, 1923-30.

Lancaster, J. L., Rainey, L. H., Summerlin, C. S., Freitas, C. S., Fox, P. T., Evans, A. C., Toga, A. W. & Mazziotta, J. C. (1997) Automated Labeling of the Human Brain: A Preliminary Report on the Development and Evaluation of a Forward-Transform Method. *Hum Brain Mapp,* 5, 238-42.

Lancaster, J. L., Woldorff, M. G., Parsons, L. M., Liotti, M., Freitas, C. S., Rainey, L., Kochunov, P. V., Nickerson, D., Mikiten, S. A. & Fox, P. T. (2000) Automated Talairach atlas labels for functional brain mapping. *Hum Brain Mapp,* 10, 120-31.

Larsson, S. A., Jonsson, C., Pagani, M., Johansson, L. & Jacobsson, H. (2000) A novel phantom design for emission tomography enabling scatter- and attenuation-"free" single-photon emission tomography imaging. *Eur J Nucl Med,* 27, 131-9.

Lewellen, T., Harrison, R. & Vannoy, S. (1998) The SimSET Program. IN LJUNGBERG, M., STRAND, S.-E. & KING, M. A. (Eds.) *Monte Carlo calculations in nuclear medicine: applications in diagnostic imaging.* Bristol, Institute of Physics Pub.

Ljungberg, M. & Strand, S. E. (1989) A Monte Carlo program for the simulation of scintillation camera characteristics. *Comput Methods Programs Biomed,* 29, 257-72.

Lobaugh, N. J., Caldwell, C. B., Black, S. E., Leibovitch, F. S. & Swartz, R. H. (2000) Three brain SPECT region-of-interest templates in elderly people: normative values, hemispheric asymmetries, and a comparison of single- and multihead cameras. *J Nucl Med,* 41, 45-56.

Ma, Y., Kamber, M. & Evans, A. C. (1993) 3D simulation of PET brain images using segmented MRI data and positron tomograph characteristics. *Comput Med Imaging Graph,* 17, 365-71.

Meltzer, C. C., Cantwell, M. N., Greer, P. J., Ben-Eliezer, D., Smith, G., Frank, G., Kaye, W. H., Houck, P. R. & Price, J. C. (2000) Does cerebral blood flow decline in healthy aging? A PET study with partial-volume correction. *J Nucl Med,* 41, 1842-8.

Metz, C. E., Atkins, F. B. & Beck, R. N. (1980) The geometric transfer function component for scintillation camera collimators with straight parallel holes. *Phys Med Biol,* 25, 1059-70.

Minoshima, S., Frey, K. A., Koeppe, R. A., Foster, N. L. & Kuhl, D. E. (1995) A diagnostic approach in Alzheimer's disease using three-dimensional stereotactic surface projections of fluorine-18-FDG PET. *J Nucl Med,* 36, 1238-48.

Minoshima, S., Koeppe, R. A., Frey, K. A., Ishihara, M. & Kuhl, D. E. (1994) Stereotactic PET atlas of the human brain: aid for visual interpretation of functional brain images. *J Nucl Med,* 35, 949-54.

Nagao, M., Murase, K., Kikuchi, T., Ikeda, M., Nebu, A., Fukuhara, R., Sugawara, Y., Miki, H. & Ikezoe, J. (2001) Fractal analysis of cerebral blood flow distribution in Alzheimer's disease. *J Nucl Med,* 42, 1446-50.

Pagani, M., Gardner, A., Salmaso, D., Sanchez Crespo, A., Jonsson, C., Jacobsson, H., Lindberg, G., Wagner, A., Hallstrom, T. & Larsson, S. A. (2004) Principal component and volume of interest analyses in depressed patients imaged by 99mTc-HMPAO SPET: a methodological comparison. *Eur J Nucl Med Mol Imaging,* 31, 995-1004.

Pagani, M., Kovalev, V. A., Lundqvist, R., Jacobsson, H., Larsson, S. A. & Thurfjell, L. (2003) A new approach for improving diagnostic accuracy in Alzheimer's disease and frontal lobe dementia utilising the intrinsic properties of the SPET dataset. *Eur J Nucl Med Mol Imaging,* 30, 1481-8.

Pagani, M., Salmaso, D., Jonsson, C., Hatherly, R., Jacobsson, H., Larsson, S. A. & Wagner, A. (2002) Regional cerebral blood flow as assessed by principal component analysis and (99m)Tc-HMPAO SPET in healthy subjects at rest: normal distribution and effect of age and gender. *Eur J Nucl Med Mol Imaging,* 29, 67-75.

Pickut, B. A., Dierckx, R. A., Dobbeleir, A., Audenaert, K., Van Laere, K., Vervaet, A. & De Deyn, P. P. (1999) Validation of the cerebellum as a reference region for SPECT quantification in patients suffering from dementia of the Alzheimer type. *Psychiatry Res,* 90, 103-12.

Radau, P. E., Slomka, P. J., Julin, P., Svensson, L. & Wahlund, L. O. (2001) Evaluation of linear registration algorithms for brain SPECT and the errors due to hypoperfusion lesions. *Med Phys,* 28, 1660-8.

Salmon, E., Collette, F., Degueldre, C., Lemaire, C. & Franck, G. (2000) Voxel-based analysis of confounding effects of age and dementia severity on cerebral metabolism in Alzheimer's disease. *Hum Brain Mapp,* 10, 39-48.

Shiga, T., Kubo, N., Takano, A., Kobayashi, J., Takeda, Y., Nakamura, F., Katoh, C., Koyama, T., Tsukamoto, E. & Tamaki, N. (2002) The effect of scatter correction on 123I-IMP brain perfusion SPET with the triple energy window method in normal subjects using SPM analysis. *Eur J Nucl Med Mol Imaging,* 29, 342-5.

Slomka, P. J., Radau, P., Hurwitz, G. A. & Dey, D. (2001) Automated three-dimensional quantification of myocardial perfusion and brain SPECT. *Comput Med Imaging Graph,* 25, 153-64.

Soonawala, D., Amin, T., Ebmeier, K. P., Steele, J. D., Dougall, N. J., Best, J., Migneco, O., Nobili, F. & Scheidhauer, K. (2002) Statistical parametric mapping of (99m)Tc-HMPAO-SPECT images for the diagnosis of Alzheimer's disease: normalizing to cerebellar tracer uptake. *Neuroimage,* 17, 1193-202.

Stamatakis, E. A., Glabus, M. F., Wyper, D. J., Barnes, A. & Wilson, J. T. (1999) Validation of statistical parametric mapping (SPM) in assessing cerebral lesions: A simulation study. *Neuroimage,* 10, 397-407.

Stamatakis, E. A., Wilson, J. T., Hadley, D. M. & Wyper, D. J. (2002) SPECT imaging in head injury interpreted with statistical parametric mapping. *J Nucl Med,* 43, 476-83.

Stapleton, S. J., Caldwell, C. B., Leonhardt, C. L., Ehrlich, L. E., Black, S. E. & Yaffe, M. J. (1994) Determination of thresholds for detection of cerebellar blood flow deficits in brain SPECT images. *J Nucl Med,* 35, 1547-55.

Stodilka, R. Z., Kemp, B. J., Prato, F. S., Kertesz, A., Kuhl, D. & Nicholson, R. L. (2000) Scatter and attenuation correction for brain SPECT using attenuation distributions inferred from a head atlas. *J Nucl Med,* 41, 1569-78.

Takeuchi, R., Yonekura, Y., Matsuda, H. & Konishi, J. (2002) Usefulness of a three-dimensional stereotaxic ROI template on anatomically standardised 99mTc-ECD SPET. *Eur J Nucl Med Mol Imaging,* 29, 331-41.

Talairach, J. & Tournoux, P. (1988) *Co-planar stereotaxic atlas of the human brain: 3-dimensional proportional system: an approach to cerebral imaging,* Stuttgart, Thieme.

Thomason, M. G., Longton, R. F., Gregor, J., Smith, G. T. & Hutson, R. K. (2004) Simulation of emission tomography using grid middleware for distributed computing. *Comput Methods Programs Biomed,* 75, 251-8.

Todd, R. W., Nightingale, J. M. & Everett, D. B. (1974) A Proposed Gamma Camera. *Nature,* 251, 132-4.

Tsui, B. M. & Gullberg, G. T. (1990) The geometric transfer function for cone and fan beam collimators. *Phys Med Biol,* 35, 81-93.

Van Dyck, C. H., Lin, C. H., Smith, E. O., Wisniewski, G., Cellar, J., Robinson, R., Narayan, M., Bennett, A., Delaney, R. C., Bronen, R. A. & Hoffer, P. B. (1996) Comparison of technetium-99m-HMPAO and technetium-99m-ECD cerebral SPECT images in Alzheimer's disease. *J Nucl Med,* 37, 1749-55.

Van Laere, K., Versijpt, J., Audenaert, K., Koole, M., Goethals, I., Achten, E. & Dierckx, R. (2001) 99mTc-ECD brain perfusion SPET: variability, asymmetry and effects of age and gender in healthy adults. *Eur J Nucl Med,* 28, 873-87.

Van Laere, K. J., Versijpt, J., Koole, M., Vandenberghe, S., Lahorte, P., Lemahieu, I. & Dierckx, R. A. (2002a) Experimental performance assessment of SPM for SPECT neuroactivation studies using a subresolution sandwich phantom design. *Neuroimage,* 16, 200-16.

Van Laere, K. J., Warwick, J., Versijpt, J., Goethals, I., Audenaert, K., Van Heerden, B. & Dierckx, R. (2002b) Analysis of clinical brain SPECT data based on anatomic standardization and reference to normal data: an ROC-based comparison of visual, semiquantitative, and voxel-based methods. *J Nucl Med,* 43, 458-69.

Vandenberghe, S., D'asseler, Y., Van De Walle, R., Kauppinen, T., Koole, M., Bouwens, L., Van Laere, K., Lemahieu, I. & Dierckx, R. A. (2001) Iterative reconstruction algorithms in nuclear medicine. *Comput Med Imaging Graph,* 25, 105-11.

Varrone, A., Pappata, S., Caraco, C., Soricelli, A., Milan, G., Quarantelli, M., Alfano, B., Postiglione, A. & Salvatore, M. (2002) Voxel-based comparison of rCBF SPET images in frontotemporal dementia and Alzheimer's disease highlights the involvement of different cortical networks. *Eur J Nucl Med Mol Imaging,* 29, 1447-54.

Ward, T., Fleming, J. S., Hoffmann, S. M. & Kemp, P. M. (2005) Simulation of realistic abnormal SPECT brain perfusion images: application in semi-quantitative analysis. *Phys Med Biol,* 50, 5323-38.

Yokoi, T., Shinohara, H. & Onishi, H. (2002) Performance evaluation of OSEM reconstruction algorithm incorporating three-dimensional distance-dependent resolution compensation for brain SPECT: a simulation study. *Ann Nucl Med,* 16, 11-8.

Yoshikawa, T., Murase, K., Oku, N., Imaizumi, M., Takasawa, M., Rishu, P., Kimura, Y., Ikejiri, Y., Kitagawa, K., Hori, M. & Hatazawa, J. (2003a) Heterogeneity of cerebral blood flow in Alzheimer disease and vascular dementia. *AJNR Am J Neuroradiol,* 24, 1341-7.

Yoshikawa, T., Murase, K., Oku, N., Kitagawa, K., Imaizumi, M., Takasawa, M., Nishikawa, T., Matsumoto, M., Hatazawa, J. & Hori, M. (2003b) Statistical image analysis of cerebral blood flow in vascular dementia with small-vessel disease. *J Nucl Med,* 44, 505-11.

Zaidi, H. (1999) Relevance of accurate Monte Carlo modeling in nuclear medical imaging. *Med Phys,* 26, 574-608.

Zaidi, H., Montandon, M. L. & Slosman, D. O. (2004) Attenuation compensation in cerebral 3D PET: effect of the attenuation map on absolute and relative quantitation. *Eur J Nucl Med Mol Imaging,* 31, 52-63.

Zubal, I. G., Harrell, C. R., Smith, E. O., Rattner, Z., Gindi, G. & Hoffer, P. B. (1994) Computerized three-dimensional segmented human anatomy. *Med Phys,* 21, 299-302.